Making and Manipulating Nanowires inside Carbon Nanotubes

Karwei So



A Thesis Submitted in Partial Fulfillment of the Requirements for the Degree of Doctor of Philosophy in Materials Science

Department of Materials - Wolfson College
University of Oxford
December 2017

I confirm that the work presented in this thesis is my own work and I have indicated all information which has been derived from other sources.

Abstract

This thesis summaries the study of various aspects related to the growth of multi-wall carbon nanotubes (MWCNTs) filled with metals and their post-synthesis processing to form macroscopic papers, known as buckypapers (BPs). Fe-filled MWCNTs (Fe@MWCNTs) and Fe/Co-filled MWCNTs (Fe/Co@MWCNTs) were produced by chemical vapour deposition (CVD), with the objective of growing sufficient quantities of these materials, whilst retaining their quality. A systematic study was carried out to investigate the effects of changing the synthesis parameters (sublimation and pyrolysis temperature, furnace gap and Ar flow) on the quality of Fe@MWCNTs produced. Crucially, this systematic study revealed the conditions to produce Fe@MWCNTs of high enough quality and quantity for post-synthesis processing. *In situ* residual gas analysis (RGA) revealed that regardless of pyrolysis temperature, the detected high mass fragments were broken down over the course of the reaction to ethene and methane, which continued to break down and release H_2 even after exhaustion of ferrocene. *In situ* TEM studied passing current through a Co-NP decorated Fe@MWCNT and emphasised the importance of discerning the affects of current on the structure of the metal filling before utilising them in electrical applications. Fe@MWCNTs were processed to form BPs (4 cm diameter), constructed by depositing layers of Fe@MWCNTs and conventional MWCNTs. Strips of these BPs were successfully prototyped as the moving component in a non-metallic electromechanical relay. I/V measurements showed these ferromagnetic BPs were capable of consistently carrying the same current at a given voltage, up to 3 V, for a minimum of 50 cycles. Selectively depositing the Fe@MWCNTs produced BPs which responded in pre-selected regions to external magnetic stimuli. Tensile tests performed on BPs formed of conventional and N-doped MWCNTs, of two different lengths each, revealed that CNT length and type influence different aspects of the BP's mechanical properties.

Acknowledgements

So here it is, the thesis! I don't think I quite knew what I was signing up for when I first decided to do a DPhil; there's been so many ups and and I have definitely learnt a lot throughout this experience. I doubt I would have survived without the support and guidance from a bunch of absolutely fantastic people. First and foremost, I would like to thank my supervisor and co-supervisor Prof Nicole Grobert and Dr Frank Dillon for being amazing mentors during my time in Oxford. Without your strong words of encouragement and nudges into the right direction I would have struggled to stay on track.

A very special mention to Dr Shayan Meysami for reading my thesis and never getting fed up my endless questions. I'm so grateful for all your advice and for continuously believing in me even when I had my doubts, your positivity definitely spurred me on through my gloomy moments. Thank you for your patience and for supplying me with various types of CNTs for making BPs!

I would like to thank the DPhil candidates, Part II students and post-docs in the *Nanomaterials by Design* group for all their valuable contributions and for being great people to hang out with. Shoutouts go to Dr Vitaly Babenko for his Matlab scripts and scientific discussions, Mr Jesus Acapulco for creating amazing schematics for me and Mr Matt Robson for answering all my Materials Science related questions. Thanks to Ms Sarah Connolly and Mr Matthew Blackmur for assisting me with Rietveld refinements.

I had the amazing opportunity to work at the Bio-Nano Electronics Research Centre (BNERC), in Japan, over the course of my DPhil and I am thankful to Prof Toru Maekawa for supervising me over my time there, Prof Takashi Uchida for training me to take contact angle measurements, Dr Yutaka Nagaoka for teaching me how to use the SQUID and for looking out for me during my stay and Mr Seiki Iwai for carrying out cell proliferation tests for me. I'd like to thank everyone at BNERC for being so kind and welcoming whilst

I was there. Thank you to Dr Shunji Kuroso and Dr Tomofumi Ukai for continuing to take SQUID measurements for me after I had left.

I would like to thank my collaborators, Prof Clive Siviour, Dr Kalin Dragnevski and Ms Marzena Tkaczyk at the Department of Engineering, Oxford University. I am grateful for their advice on conducting tensile tests, scientific discussions and for helping me with the digital image correlation work.

I am grateful to Dr Neil Young, Dr Alison Crossley, Dr Phil Holdway, Dr Colin Johnstone and Mr Greg Cook from the Oxford Materials Characterisation Services (OMCS) for training me in microscopy and helpful advice on characterising my samples. Thank you to Dr Phil Holdway for carrying out XRD and XPS measurements and to Mr Greg Cook for your help with the carbon coater and I/V measurements setup. Many thanks to Dr Juan Lozano for carrying out Nanofactory work for me on the Fe/Co@MWCNTs.

I've had four unforgettable years at Wolfson College, full of fond memories and I am so fortunate to have met so many wonderful people there. Thank you to Dr Tom Coxon, Ms Nina Klein and Mr James Holt-Martyn for sticking with me to the end and for being wonderful housemates. I wish to show appreciation to Prof Dame Hermione Lee, the president, Ms Gillian Hamnett, the senior tutor and Prof Feliciano Giustino, my college advisor, for their support throughout my time at Wolfson.

I would like to thank the Engineering and Physical Sciences Research Council (EPSRC) for funding my DPhil and to the Japanese Society for the Promotion of Science (JSPS) for selecting me for their Summer Fellowship Program, which enabled me to conduct my research at BNERC.

Thank you to Mr Johnny Luk for being my sounding board, your cheesy words of advice and optimistic view on life, and Mr Duo Zhang for your words of encouragement and for letting me use your gym.

Finally, I am deeply indebted to my family, Kam, Mei Lan, Chiwei and Chiho for always being there for me and putting up with me, despite my quirks. I am so incredibly fortunate to have such a loving family and I wouldn't be where I am today without you guys.

Fellowships

Engineering and Physical Sciences Research Council (EPSRC) Doctoral Training Award (DTA) D.Phil Fellowship

Japanese Society for the Promotion of Sciences (JSPS) Summer Fellowship Selected as one of ten students in the UK for the Summer Fellowship to conduct research in Japan for 10 weeks. I worked at the Bio-Nano Electronics Research Centre (BNERC), Toyo University, where I conducted the SQUID and contact angle measurements presented in this thesis, as well as collaborating with researchers at BNERC on multidisciplinary projects. This involved working on using leaf extracts to improve the biocompatibility of buckypapers, investigating the effect of external magnetic field on coffee ring experiments using Fe@CNTs and studying cell proliferation of cancerous and normal cells on the surface of magnetic buckypapers.

Publications

Smart ferromagnetic carbon nanotube buckypaper as corrosion-free switches for low signal relays *Karwei So, Seyyed Shayan Meysami, Vitaly Babenko, Greg Cook, Benoit Grosjean, Jonathan Quinson, Yutaka Nagaoka, Toru Maekawa, Frank Dillon, Nicole Grobert*, Applied Materials Today. **In review**

Buckypaper for tension sensing applications *Karwei So, Seyyed Shayan Meysami, Benoit Grosjean, Kalin Dragnevski, Marzena Tkaczyk, Frank Dillon, Clive Siviour, Nicole Grobert* **Written up**

Time dependent decomposition of ammonia borane for the controlled production of 2D hexagonal boron nitride *Vitaly Babenko, George Lane, Antal Koos, Adrian Murdock, Karwei So, Jonathan Moffat, Jude Britton, Seyyed Shayan Meysami, Nicole Grobert*, Scientific Reports, 2017. Contributed to the paper carrying out IR analysis on the samples.

Oral Presentations

Carbon 2016 (13/7/16 State College, USA) *Karwei So, Seyyed Shayan Meysami, Vitaly Babenko, Greg Cook, Benoit Grosjean, Jonathan Quinson, Yutaka Nagaoka, Frank Dillon, Toru Maekawa, Nicole Grobert* Designing Magnetic Buckypapers towards Electronics Applications

Invited Speaker to the LIMA Annual Users Club Meeting 2016 (20/5/16, Oxford, UK) *Karwei So, Benoit Grosjean, Seyyed Shayan Meysami, Kalin Dragnevski, Frank Dillon, Clive Siviour, Nicole Grobert* Mechanical Testing of Buckypapers

Invited Speaker to the Bio-Nano Electronics Research Centre International Symposium on Bioscience and Nanotechnology 2015 (28/11/15, Kawagoe, Japan) *Karwei So, Benoit Grosjean, Seyyed Shayan Meysami, Yutaka Nagaoka, Seiki Iwai, Frank Dillon, Toru Maekawa, Nicole Grobert* Routes towards Magnetic Buckypapers and their Application

NanoteC 2015 (16/9/15, Oxford, UK) *Karwei So, Benoit Grosjean, Jonathan Quinson, Kalin Dragnevski, Clive Siviour, Yutaka Nagaoka, Frank Dillon, Toru Maekawa, Nicole Grobert* Moving towards Macroscopic Carbon Buckypapers

Oxford Department 2nd Year DPhil Presentation 2015 (4/3/15, Oxford, UK) *Karwei So, Frank Dillon, Nicole Grobert* Magnetic Carbon Nanotubes towards Selective Response Macrostructures?

Invited Speaker to the Bio-Nano Electronics Research Centre International Symposium on Bioscience and Nanotechnology 2014 (14/11/14, Kawagoe, Japan) *Karwei So, Benoit Grosjean, Seyyed Shayan Meysami, Frank Dillon, Nicole Grobert* Magnetic Carbon Nanotube Materials

Poster Presentations

Carbon 2016 (13/7/16 State College, USA) *Ana M. Perez-Mas, Karwei So, Seyyed Shayan Meysami, Nicole Grobert, Ricardo Santamaria, Patricia Alvarez, Rosa Menendez* Improvement of buckypaper structure and properties by using CNT/GO hydbrids

7th UK- Japan Symposium of Fundamental Research Advances in Carbon Nanomaterials 2016 (13/6/16, London, UK) *Karwei So, Seyyed Shayan Meysami, Vitaly Babenko, Greg Cook, Benoit Grosjean, Jonathan Quinson, Yutaka Nagaoka, Frank Dillon, Toru Maekawa, Nicole Grobert* Smart Magnetic Buckypapers for Electronics Applications

Oxford Department 3rd Year DPhil Poster Session (24/2/16, Oxford, UK) *Karwei So, Frank Dillon, Nicole Grobert* What are Carbon Nanotubes?

Microscience Microscopy Congress 2015 (29/6/15, Manchester, UK) *Karwei So, Benoit Grosjean, Seyyed Shayan Meysami, Kalin Dragnevski, Frank Dillon, Clive Siviour, Nicole Grobert In situ* scanning electron microscopy observations of the mechanical behaviour of buckypapers

Contents

List of Figures **xxv**

List of Tables **xxviii**

1 Introduction **1**

1.1 Outline 1

1.2 Literature Review 3

1.2.1 The Carbon Nanotube 3

1.2.2 CVD MWCNT growth 4

1.2.3 Mechanism for CNT growth via CVD 5

1.2.4 Filled Carbon Nanotubes 8

1.2.5 Magnetic Properties and Structure of Ferromagnetic Metal-Filled CNTs 12

1.2.6 Post-Synthesis Processing of CNTs Towards Macrostructures 15

1.3 Conclusions 18

2 *In situ* Mass Spectroscopy Study of Fe@MWCNT Growth **20**

2.1 Introduction 20

2.2 Experimental 23

2.2.1 Furnace Temperature Profiles 23

2.2.2 Procedure for Synthesis of Fe@MWCNTs 23

2.2.3 Monitoring Synthesis with Mass Spectrometry 24

2.2.4 Characterisation 25

2.3 Results and Discussion 26

2.3.1 Furnace Gap 26

2.3.2 Mass Spectrometry 28

2.3.3 Monitoring H_2 Evolution 44

2.4 Conclusions . . . 64

3 Producing Fe/Co@MWCNTs 67

3.1 Introduction . . . 67

3.1.1 Structure of FeCo Alloy Materials . . . 68

3.1.2 Bulk FeCo Alloy Materials . . . 68

3.1.3 Structure of Nanoscale Magnetic Alloy Materials . . . 69

3.1.4 Magnetic Properties of Alloy Materials . . . 70

3.1.5 Bulk Magnetic Alloys . . . 70

3.1.6 Nanoscale Magnetic Alloys . . . 71

3.2 Experimental . . . 72

3.2.1 Fe/Co@MWCNT Synthesis Procedure . . . 72

3.2.2 Characterisation . . . 74

3.3 Results and Discussion . . . 75

3.3.1 Structure and Morphology of Fe/Co@MWCNTs . . . 75

3.3.2 TEM and EDX . . . 78

3.3.3 Purity of Fe/Co@MWCNTs and Structure of Filling . . . 85

3.3.4 Magnetic Properties of Fe/Co@MWCNTs . . . 94

3.3.5 Evaluating the Effect of Current on Fe/Co@MWCNTs . . . 97

3.4 Conclusions . . . 101

4 Manipulation of Magnetic Buckypapers 103

4.1 Introduction . . . 103

4.2 Experimental . . . 106

4.2.1 MWCNT and Fe@MWCNT Synthesis . . . 108

4.2.2 Magnetic Buckypaper . . . 108

4.2.3 Buckypaper with Selective Magnetic Regions . . . 109

4.2.4 Relay and I/V Measurements . . . 111

4.2.5 Characterisation . . . 112

4.3 Results and Discussion . . . 113

4.3.1 Structure of Magnetic Buckypaper . . . 113

4.3.2 Magnetic Properties of BP . . . 115

4.3.3 Relay and I/V Measurements . . . 117

4.3.4 Synthesis of BPs with Selective Magnetic Regions . . . 128

4.4 Conclusions . . . 132

5 Mechanical Properties of Buckypapers 134

5.1 Introduction . . . 134

5.2 Experimental . . . 140

5.2.1 Preparation of MWCNTs and N-doped MWCNTs . . . 140

5.2.2 Preparation of Buckypapers . . . 140

5.2.3 Characterisation . . . 140

5.2.4 Mechanical Tests and Strain Maps . . . 141

5.3 Results and Discussion . . . 142

5.3.1 Synthesis of Doped- MWCNT BPs, and their Properties . . . 142

5.3.2 Contact Angle Measurements . . . 146

5.3.3 XPS and FTIR Spectra of BPs . . . 151

5.3.4 Mechanical Testing of BPs . . . 154

5.4 Conclusions . . . 163

6 Summary and Future Research 165

6.1 Summary of Research . . . 165

6.2 Future Work . . . 168

7 Appendix 198

List of Abbreviations

AAO Anodic Aluminium Oxide

AACVD Aerosol Assisted Chemical Vapour Deposition

BCC Body Centred Cubic

BNERC Bio-Nano Electronics Research Centre

BNNT Boron Nitride Nanotube

CNT Carbon Nanotube

CVD Chemical Vapour Deposition

Co@MWCNT Co-filled Multi-Wall Carbon Nanotube

DIC Digital Image Correlation

DWCNT Double-Wall Carbon Nanotube

FCC Face Centred Cubic

FCCVD Floating Catalyst Chemical Vapour Deposition

Fe@MWCNT Fe-filled Multi-Wall Carbon Nanotube

Fe/Co@MWCNT Fe and Co-filled Multi-Wall Carbon Nanotube

FWHM Full Width Half Maxima

H_c Coercivity

MWCNT Multi-Wall Carbon Nanotube

M_s Magnetisation Saturation

RMS Root Mean Square

SWCNT Single Wall Carbon Nanotubes

SFE Surface Free Energy

VANTAs Vertically Aligned Nanotube Arrays

Chemicals

DCB Dichlorobenzene

EG Ethylene Glycol

F Formamide

H Hexadecane

IPA Isopropanol

PTFE Polytetrafluoroethylene

PDMS Polydimethylsiloxane

SDS Sodium Dodecyl Sulfate

TCB Tricholorobenzene

Characterisation Techniques

AGM Alternating Gradient Magnetometry

EDX Energy Dispersive X-ray Spectroscopy

EELS Electron Energy Loss Spectroscopy

ETEM Environmental Transmission Electron Microscopy

FTIR Fourrier Transform Infra-Red Spectroscopy

MS Mass Spectroscopy

RGA Residual Gas Analysis

SEM Scanning Electron Microscope

SQUID Superconducting Quantum Interference Device

TEM Transmission Electron Microscope

TGA Thermogravimetric Analysis

XRD X-ray Diffraction

PXRD Powder X-ray Diffraction

XPS X-ray Photoelectron Spectroscopy

Units

sccm Standard Cubic Centimetres per Minute

SLM Standard Litres per Minute

List of Figures

1.1 Flow chart of the PhD project and proposed future work. 3

1.2 TEM images showing MWCNTs first imaged by Iijima [16], showing a and c) MWCNTs, and b) double-wall carbon nanotube (DWCNT). 4

1.3 Schematic, adapted from [30] showing a typical setup used for AACVD. The aerosol created by the aerosol generator is carried into the furnace by an inert gas flow, where it decomposes to form MWCNTs on the substrates. 5

1.4 Schematics showing a) the VLS model, image modified from [61]. The precursor gas decomposes on the catalyst particle to form C atoms, which diffuse through the particle as a solid solution. Eventually, the particle becomes saturated and C precipitates out of the particle following the temperature gradient within the particle. b) tip growth, and root growth mechanisms for MWCNT growth, which occur for unfavourable, and strong interactions between the substrate and the particle, respectively [58]. 6

1.5 Schematic showing a) an open tip mechanism [62] and b) combined tip and base growth mechanisms for growing filled MWCNTs [58]. 8

1.6 Schematics showing a) a typical MWCNT formed by CVD, with a catalyst particle inside the MWCNT, b) a partially filled MWCNT, and c) a continuously filled MWCNT. The black lines represent graphitic layers and grey shows the filled regions [58]. 8

1.7 Schematics showing a 2-stage furnace setup typically used for growth of metal-filled MWCNTs by CVD of metallocenes [8]. 11

1.8 Schematics showing ways in which surfactants can bind with CNTs, show formations of a) a cylindrical micelle (front and side views), b) hemimicelle and c) random surfactant adsorption [144]. 16

1.9 Schematics showing the domino push method used in [146], showing a) a cylinder being used to push down an aligned MWCNT array, b) peeling of the aligned BP from the silicon substrate, and c) spraying ethanol on the micropore membrane to allow the BP to be peeled off the membrane. . . . 17

2.1 Schematics showing a) the basic setup used for CVD growth of Fe@MWCNTs and b) the modified setup for experiments with *in situ* MS. The lengths of the furnaces are 21 and 31 cm for the the sublimation and pyrolysis furnaces, respectively. 23

2.2 Graphs showing the furnace temperature profiles obtained with the distances of a) 0 cm, b) 1 cm, c) 2 cm, d) 3 cm, e) 4 cm, and f) 5 cm between the sublimation and pyrolysis furnaces. 27

2.3 SEM images showing the material produced from syntheses with a gap between the sublimation and pyrolysis furnaces of a) 0 cm, b) 1 cm, c) 2 cm, and d) 3 cm. As observed, the syntheses produced high amount of agglomerates with varying amounts of MWCNTs. 28

2.4 MS scan cycles from synthesis carried out with a pyrolysis temperature of 750 °C for a) background scan, taken whilst purging the furnace with Ar at room temperature, b) 0.08, c) 1.34, d) 3.01, e) 4.27, f) 5.54, g) 7.20, h) 8.47 minutes into the reaction. 31

2.5 MS scan cycles from synthesis carried out with a pyrolysis temperature of 850 °C for a) background scan, purging with Ar, b) 0.10, c) 1.41, d) 3.12, e) 4.42, f) 6.13, g) 7.44, h) 9.15 minutes into the reaction. 33

2.6 Mass spectrum for ferrocene, taken at room temperature from the NIST database [179]. 34

2.7 Mass spectrum for naphthalene, taken at room temperature from the NIST database [180]. 36

2.8 Normalised mass fractions of cyclopentadiene and major products (indene, benzene and naphthalene) as a function of temperature [178]. 37

2.9 Graphs showing the % abundance of N_2 and C_2H_4 (partial pressure) making up the peak at 28 m/z in the MS scans per cycle for a pyrolysis temperature of a) 750 °C and b) 850 °C. 38

2.10 Zoomed in MS scan cycles from synthesis carried out with a pyrolysis temperature of 750 °C for a) background scan, purging with Ar, b) 0.08, c) 1.34, d) 3.01, e) 4.27, f) 5.54, g) 7.20, h) 8.47 minutes into the reaction.. . . 41

2.11 Zoomed in MS scan cycles from synthesis carried out with a pyrolysis temperature of 850 °C for a) background scan, purging with Ar, b) 0.10, c) 1.41, d) 3.12, e) 4.42, f) 6.13, g) 7.44, h) 9.15 minutes into the reaction. . . 43

2.12 H_2 evolution graphs showing the abundance of H_2 relative to ^{36}Ar obtained for differing T_{sub} and T_{pyro} with a) 100 sccm Ar flow and 2 cm furnace gap, b) 100 sccm Ar flow and 3 cm furnace gap, c) 50 sccm Ar flow and 2 cm furnace gap, and d) 50 sccm Ar flow and 3 cm furnace gap. The dashed lines indicate the period in which the alumina crucible was pushed into the middle of the sublimation furnace. The labels are as follows: A= 200/ 750, B=200/850, C= 250/750, D= 250/850 °C for T_{sub}/T_{pryo}, 1= 100, 5= 50 sccm Ar flow and 2 and 3 indicates the furnace gap in cm. 45

2.13 SEM images showing the material produced from syntheses monitored with MS. Syntheses were carried out with T_{sub} and T_{pyro} of 200/750 °C with a) 100 sccm, 2 cm gap, b) 100 sccm, 3 cm c) 50 sccm, 2 cm, and d) 50 sccm and 3 cm. The product for syntheses carried out with T_{sub} and T_{pyro} of 200/850 °C with e) 100 sccm, 2 cm gap, f) 100 sccm, 3 cm g) 50 sccm, 2 cm, and h) 50 sccm and 3 cm. 51

2.14 SEM images showing the material produced from syntheses monitored with MS. Syntheses were carried out with T_{sub} and T_{pyro} of 250/750 °C with a) 100 sccm, 2 cm gap, b) 100 sccm, 3 cm c) 50 sccm, 2 cm, and d) 50 sccm and 3 cm. The product for syntheses carried out with T_{sub} and T_{pyro} of 250/850 °C with e) 100 sccm, 2 cm gap, f) 100 sccm, 3 cm g) 50 sccm, 2 cm, and h) 50 sccm and 3 cm. 52

2.15 TEM images showing the material produced from syntheses monitored with MS. Syntheses were carried out with T_{sub} and T_{pyro} of 200/750 °C with a) 100 sccm, 2 cm gap, b) 100 sccm, 3cm c) 50 sccm, 2 cm, and d) 50 sccm and 3 cm. The product for syntheses carried out with T_{sub} and T_{pyro} of 200/850 °C with e) 100 sccm, 2 cm gap, f) 100 sccm, 3cm g) 50 sccm, 2 cm, and h) 50 sccm and 3 cm. 53

2.16 TEM images showing the material produced from syntheses monitored with MS. Syntheses were carried out with T_{sub} and T_{pyro} of 250/750 °C with a) 100 sccm, 2 cm gap, b) 100 sccm, 3cm c) 50 sccm, 2 cm, and d) 50 sccm and 3 cm. The product for syntheses carried out with T_{sub} and T_{pyro} of 250/850 °C with e) 100 sccm, 2 cm gap, f) 100 sccm, 3cm g) 50 sccm, 2 cm, and h) 50 sccm and 3 cm. 54

2.17 TEM image showing an example Fe NP coated in graphitic C, as confirmed by XRD. 55

2.18 XRD patterns for a) a majority agglomerate Fe NP coated in C sample (B53) and b) a majority Fe@MWCNT sample (C53), where T_{sub}/T_{pyro} are B= 200/850 and C= 250/750 °C. The agglomerate particles consisted of α-Fe phases, whilst the Fe@MWCNTs were filled with a mixture of Fe-phases and Fe_3C. 57

2.19 TGA graphs showing the mass loss profiles for the material produced with varying T_{sub} and T_{pyro} with a) 100 sccm Ar flow and 2 cm furnace gap b) 100 sccm Ar flow and 3 cm furnace gap, c) 50 sccm Ar flow and 2 cm furnace gap, and d) 50 sccm Ar flow and 3 cm furnace gap. The labels are as follows: A= 200/ 750, B=200/850, C= 250/750, D= 250/850 °C for T_{sub}/T_{pryo}, 1= 100, 5= 50 sccm Ar flow and 2 and 3 indicates the furnace gap in cm. 58

2.20 Rate of mass loss graphs for the material produced with varying T_{sub} and T_{pyro} with a) 100 sccm Ar flow and 2 cm furnace gap b) 100 sccm Ar flow and 3 cm furnace gap, c) 50 sccm Ar flow and 2 cm furnace gap, and d) 50 sccm Ar flow and 3 cm furnace gap. The labels are as follows: A= 200/ 750, B=200/850, C= 250/750, D= 250/850 °C for T_{sub}/T_{pryo}, 1= 100, 5= 50 sccm Ar flow and 2 and 3 indicates the furnace gap in cm. 59

2.21 Graphs showing the magnetic hystereses syntheses carried out with Ar flows and furnace gaps of a) 100 sccm, 2 cm and b) 100 sccm, 3 cm, c) 50 sccm, 2 cm, and d) 50 sccm, 3 cm, respectively. SQUID measurements were carried out at 4 K. The labels are as follows: A= 200/ 750, B=200/850, C= 250/750, D= 250/850 °C for T_{sub}/T_{pryo}, 1= 100, 5= 50 sccm Ar flow and 2 and 3 indicates the furnace gap in cm. 61

2.22 Graphs showing the coercive forces for syntheses carried out with Ar flows and furnace gaps of a) 100 sccm, 2 cm and b) 100 sccm, 3 cm, c) 50 sccm, 2 cm, and d) 50 sccm, 3 cm, respectively. SQUID measurements were carried out at 4 K. The labels are as follows: A= 200/ 750, B=200/850, C= 250/750, D= 250/850 °C for T_{sub}/T_{pryo}, 1= 100, 5= 50 sccm Ar flow and 2 and 3 indicates the furnace gap in cm. 62

3.1 Phase diagram for Fe and Co [202]. Below 730 °C for a 50:50 Fe/Co mixture, the alloy undergoes a transition from a disordered αphase to an ordered CsCl α' phase. 68

3.2 Graph showing the variation in M_s with varying Co content, showing that an alloy with *ca.* 30 at.% Co in Fe should have the highest M_s value. 71

3.3 Schematic showing the position of the quartz substrates, placed 31-43 cm along the quartz tube, relative to the furnace temperature profile during the reaction, and in the full furnace setup (bottom). 74

3.4 SEM images showing the bulk products from a) FeCo-AB (75:25), b) FeCo-BB (50:50), and c) FeCo-CB (25:75), where the ratios in the bracket indicate the ratios of ferrocene and cobaltocene used in the synthesis and the B indicates bulk sample. 76

3.5 a) Graph showing the pyrolysis furnace temperature profile, alongside substrate position (black); the substrates are touching in the setup, but are shown separated in the graph. SEM images show the material grown on the substrates in positions b) 1, c) 2, and d) 3, for FeCoA (75:25), e) 1, f) 2, and g) 3, for FeCoB (50:50), and h) 1, i) 2, and j) 3, for FeCoC (25:75), where the ratios of ferrocene to cobaltocene used in the synthesis are in the brackets. 77

3.6 TEM image showing the filling of a Fe/Co@MWCNT produced for a and b) FeCo-AB (75:25), and c and d) FeCo-BB (50:50), e and f) FeCo-CB (25:75), with the brackets showing the ratio of ferrocene to cobaltocene used in the synthesis. 79

3.7 a) STEM image taken on the JEOL2100 of the site of EDX map collection. EDX maps showing the distribution of b) C, c) Fe, and d) Co within MWCNTs from FeCo-BB (50:50 ferrocene to cobaltocene synthesis). The EDX maps were taken by measuring the Kα emission for the elements listed above and show the random distribution of Fe and Co within the filled regions of the MWCNT. 80

3.8 a) STEM image collected from FeCo-AB sample (75:25 ferrocene to cobaltocene synthesis) and the corresponding EDX maps obtained for b) C, c) Fe and d) Co within the Fe/Co@MWCNT. The image is representative of the typical EDX maps collected for the FeCo-AB samples, which showed the even distribution of Fe and Co across the filled regions of the MWCNT. The average ratio of Fe:Co is 6:1, indicating that there was double the amount of Fe, compared to the originally intended Fe:Co ratio of 3:1. 81

3.9 a) STEM image collected from FeCo-CB (25:75 ferrocene to cobaltocene synthesis) and the corresponding EDX maps obtained for b) C, c) Fe and d) Co within the Fe/Co@MWCNT. The image is representative of the typical EDX maps collected for the FeCo-AB samples, which showed Fe and Co is evenly distributed across the filled regions of the MWCNT. The average ratio of Fe:Co is 2.7:1, indicating that there was a large excess in the amount of Fe, compared to the originally intended Fe:Co ratio of 0.33:1. 82

3.10 a) A dark field STEM image taken of the Fe/Co@MWCNT prior to applying bias to the MWCNT. The STEM image clearly shows a filled MWCNT decorated with NPs. EELS maps showing the distribution of b) Fe and c) Co within the Fe/Co@MWCNT. Measurements were taken by measuring the the L edge for EELS. The EELS maps suggest that the MWCNT is an Fe@MWCNT, decorated with Co NPs, based on the distribution of Fe and Co within the sample. Image taken on the JEOL-ARM by Dr. Juan Lozano. 84

3.11 TEM images from FeCo-BB (50:50 ferrocene to cobaltocene used in synthesis) showing a) a typical image obtained at lower magnification of the sample. However, the red ring shows an unusual MWCNT, which is highly decorated in NPs. b) A higher magnification image showing the decorated MWCNT, similar to the MWCNT imaged on the JEOL-ARM200F, suggesting it was an atypical MWCNT from the sample. 85

3.12 XRD patterns for FeCo-AB (25:75 (blue)), FeCo-BB (50:50 (red)) and FeCo-CB (75:25 (black)) samples, showing a) the entire 2θ range scanned, from 10 to 80 2θ and b) a close up of the 2θ range between 40-55 2θ. The Co peaks at *ca.* 43-45 2θ increase with increasing cobaltocene ratio in the precursor. 86

3.13 High angle XRD pattern, from 70-100 2θ, for FeCo-AB (25:75 (blue)), FeCo-BB (50:50 (red)) and FeCo-CB (75:25 (black)). The high angle measurements confirmed the presence of FeCo in the samples. 87

3.14 Graph showing trends in calculated Fe/Co values, obtained from EDX (black) and XRD (red), for the syntheses with varying ferrocene:cobaltocene ratio. 89

3.15 Graphs showing a) TGA mass loss curves for FeCo-AB (75:25 (black)), FeCo-BB (50:50 (red)), and FeCo-CB (25:75 (blue)). The first derivative shows changes in decomposition rate for b) FeCo-AB, c) FeCo-BB, and d) FeCo-CB. The ratio of ferrocene to cobaltocene given in brackets. TGA was carried out on bulk samples. 91

3.16 Graph showing the distribution of MWCNTs produced via CVD of a) FeCo-AB (75:25), b) FeCo-BB (50:50) and c) FeCo-CB (25:25), where the ratios in the brackets show the ratio of ferrocene to cobaltocene in the precursor mixtures. It is clear the the MWCNTs in FeCo-AB have a much larger range in diameters, compared to FeCo-BB and FeCo-CB. The modal diameter range is 50-60, 30-40, and 30-40 for FeCo-AB, FeCo-BB and FeCo-CB, respectively. 92

3.17 Graphs showing the hysteresis loops for Fe@MWCNTs (cyan), Co@MWCNTs (green), FeCo-AB (black (75:25)), FeCo-BB (red (50:50)), and FeCo-CB (25:75 (blue)) at a) 300 K and b) 4 K, where the ferrocene:cobaltocene precursor ratio is given in the brackets. H_c is shown more clearly for d) at 300 K and e) at 4 K. 95

3.18 *In situ* TEM images extracted from the video taken whilst passing an increasing current through an Fe@MWCNT decorated with Co NPs. The images show a) the initial structure of the MWCNT, b) the Co NPs starting to coalesce to form larger NPS, whilst the Fe filling starts to collect together, causing the inner diameter of the MWCNT to swell, c) complete movement of the Fe filling, such that it has collected in a large agglomerate at the top of the MWCNT, and d) MWCNT breakdown due to joule heating. 98

3.19 a) STEM image taken after bias was applied to the MWCNT. The red and green boxes show the two areas in which EELS maps were taken. EELS maps showing the distribution of b) Fe and c) Co within the red box, and d) Fe and e) Co within the green box. These EELS maps indicate that after applying bias, the Co NPs and the Fe filling have formed alloy NPs. 100

4.1 Schematic showing the set up used for vacuum filtration of the dispersions to obtain a BP. 104

4.2 SEM images extracted from [237] showing a-c) highly aligned MWCNTs within the BP, and d) the high amount of filling. 105

4.3 Image extracted from [236] of a magnetic BP being attracted to a magnet, showing its ferromagnetic behaviour. 106

4.4 Schematics of the different types of BPs, composed of a) only conventional MWCNTs, b) Fe@MWCNTs across the entire BP surface and c) Fe@MWCNTs localised to specific regions. Schematics b and c have a sandwich structure, shown in d) a magnetic layer is deposited between two layers of conventional MWCNTs. For design c), the magnetic Fe@MWCNTs are deposited at the edges of the BP. Image produced by Jesus Acapulco. . . . 107

4.5 Schematics showing the setup used for a) testing the magnetic BP in a relay, b) I/V characteristic measurements and c and d) photos showing the switch setup used. 111

4.6 Photograph showing the setup used for measurements carried out under vacuum and in N_2. The sample was carefully placed between the two tweezers. 112

4.7 a) Optical image of a solely Fe@MWCNT-BP. The BP flaked into small fragments and could not be peeled off the filter. b) SEM image showing the structure of the Fe@MWCNT-BP and shows a densely packed arrangement of very short Fe@MWCNTs. 113

4.8 SEM images taken of a) Fe@MWCNTs and b) conventional MWCNTs, showing the difference in length between the two CNT types. The conventional MWCNTs are noticeable much longer, compared to Fe@MWCNTs. 114

4.9 a) Optical image of a ferromagnetic BP, and SEM images showing b) the entangled MWCNTs, and c) edge-on image of a magnetic BP, used to estimate BP thickness. 115

4.10 Hysteresis loops obtained at 300 K for the magnetic BPs, measured the magnetic BP both parallel and perpendicular to the applied magnetic field. The hysteresis loop for the raw Fe@MWCNTs incorporated into the ferromagnetic BP shows a higher M_s than the BP. 116

4.11 Graph comparing the magnetic hysteresis obtained from SQUID measurements carried out at 300 K, for samples containing a majority of agglomerate C coated Fe NPs (D13) and Fe@MWCNT(C53). The temperatures of T_{sub}/T_{pyro} are C= 250/750, and D= 250/850 °C. 116

4.12 Graph showing the coercivity for the BPs with the magnetic field aligned parallel (blue) and perpendicular (black) to the BP, taken at 4 K (solid line) and 300 K (dashed line). 117

4.13 Graphs showing I/V curves obtained for conventional MWCNT BP (black) and magnetic BPs (red and blue). The two different batches of magnetic BPs are labeled FeBP1 (red) and FeBP2 (blue) for ease of discussion. Very similar I/V curves were obtained for FeBP2 and the conventional MWCNT BP, whilst FeBP1 carried much higher currents. 119

4.14 Graphs showing a) fluctuations in current over time, and b) I/V curves obtained for magnetic BP every 5 runs of 50. The consistency of I/V curves obtained over 50 cycles, disregarding the first run, is shown. 121

4.15 a) A comparison of the Raman spectra obtained pre (red) and post (black) I/V measurements. Close ups of the Raman spectra at low Raman shift for b) before, and c) after I/V measurements. The low angle peaks at 23-275 cm^{-1} are removed after 50 I/V measurements. 123

4.16 a) Comparisons of the I/V curves obtained for a Fe@MWCNT sandwich BP strip for measurements carried out in air, under vacuum and N_2 and b) graph showing the individual I/V curves obtained under vacuum over 5 cycles for **non-annealed** samples. All measurements were carried out on the same BP strip. 125
4.17 XRD patterns obtained from as produced BP (red) and following I/V measurements conducted under vacuum, then measurements in air (black), showing the formation of Fe_2O_3 following conductivity measurements. . . . 126
4.18 a) Comparisons of the I/V curves for measurements carried out in air, under vacuum and N_2 and b) graph showing the individual I/V curves obtained over 5 cycles for **annealed** samples. 127
4.19 Photograph showing the mixtures of water and P123 obtained after sonication for 2 h at 60 °C where the ratios of P123 to water are a)75:25, b)70:30, and c) 50:50. 129
4.20 Photographs showing the stages of creating a BP using the P123/Fe@MWCNT mixtures showing a) Pasting the P123/Fe@MWCNT mixture onto either side of the BP, b) pasting blank P123 (Solution 2) onto the centre of the BP, and c) the final selectively magnetic BP produced using this procedure. 130
4.21 Images extracted from a video showing the BP reacting to stimulation with a neodymium showing a) the BP at rest, and b) the edges of the BP bending as they are stimulated by the magnet. 131

5.1 SEM images, courtesy of Dr Shayan Meysami, showing the morphology of a) conventional MWCNTs, b) N-doped MWCNTs. TEM images showing the internal structure of c) conventional MWCNTs, and d) N-doped MWCNTs. 139
5.2 SEM images of the raw MWCNTs used for BP production. a) conventional MWCNTs (long), b) conventional MWCNTs (short), c) N-doped MWCNTs (long), and d) N-doped MWCNTs (short). 143
5.3 Optical image of a) conventional MWCNT BP produced from 'long' MWCNTs, and b) conventional MWCNT BP consisting of 'short' MWCNT on the polycarbonate filter. BPs were not successfully produced from short MWCNTs. 144

5.4 SEM images of a and b) long conventional MWCNT BP, and c, and d) attempts at producing BPs from short conventional MWCNTs, in which the majority of the surface appears to be messy bundle-like clusters. 145
5.5 SEM images taken for a and b) long N-doped MWCNT BP sample, and c and d) a short N-doped MWCNT BP sample. The long N-doped MWCNT BPs have a more uniform distribution, whilst bundles are observed on the surface of the short N-doped MWCNT BP. 146
5.6 Representative images captured during contact angle measurements showing a) a water droplet on the surface of a BP displaying hydrophobic behaviour, b) absorbing behaviour of the BPs, typically observed for the non-water solvent droplets on the surface of a BP sample. 147
5.7 An example of the graphs used to calculate the SFE of BPs, in this case for a conventional MWCNT BP. The large errors are a result of the absorbent behaviour of the BPs. 148
5.8 FTIR spectra obtained for raw MWCNTs, raw N-doped MWCNTs and N-doped and conventional MWCNT BPs. 151
5.9 XPS spectra obtained from N-doped MWCNT BP for a) C 1s, b) O 1s, and c) N 1s. 153
5.10 XPS spectra obtained from conventional MWCNT BP for a) C 1s, and b) O 1s. 154
5.11 Representative stress strain curves obtained for different batches of BP samples, where L stands for long, S for short, N for N-doped MWCNT, C for conventional MWCNT. The N-doped MWCNT BPs have sharp failures, whilst the conventional MWCNT BPs are less brittle. 155
5.12 SEM images taken of the tear edge of the BPs post mechanical testing of a and b) short N-doped MWCNT BP, c and d) long N-doped MWCNT BP. 156
5.13 SEM images extracted from a video taken during mechanical testing carried out on a conventional MWCNT BP showing, a) The intact BP, b) the start of a tear forming and thinning of the BP (circled in red), c) further BP tearing, and d) the torn BP. 158

5.14 a) Force/elongation curve for a short, N-doped MWCNT BP sample, showing the force required to reach BP failure. The corresponding displacement maps, obtained by DIC for b) point A, c) point B, and d) point C on the force/elongation curve. 159
5.15 a) Force/elongation curve for a long, N-doped MWCNT BP sample, showing the force required to reach BP failure, and the corresponding displacement maps, obtained by DIC for b) point A, c) point B, and d) point C on the force/elongation curve. 160
5.16 a) Force/elongation curve for a long, conventional MWCNT BP sample, showing the force required to reach BP failure, and the corresponding displacement maps, obtained by DIC for b) point A, c) point B, and d) point C on the force/elongation curve. The conventional MWCNT BP displays stable failure. 161
5.17 a) Force/elongation curve for a long, conventional MWCNT BP sample, showing the force required to reach BP failure and the corresponding correlation coefficient images, obtained by DIC for b) point A, c) point B, and d) point C, e) point D, and f) point E on the force/elongation curve. 162

6.1 Schematic taken from [153] showing the steps involved leading up to the UV irradiation activated MWCNT conjugational cross-linking reaction. . . 171
6.2 SEM images showing cells grown on the surface of ferromagnetic BPs, with the cells circled in red. The cells appear to have a preference for the slightly rougher surfaces of BPs, compared to smoother regions. 172
6.3 Graph showing the cell activity from Alamar Blue Assays over the course of 72 hours. The graph shows the cancer cells divide at a slower rate with increasing time, whilst the normal cells had a more steady cell division rate over the three days. 173

7.1 Phase diagrams for a) Fe, b) Co and c) Ni, showing the similar carbon solubilities of the three phase diagrams between 800-900 °C [44, 308]. 198
7.2 EDX spectra showing the key peaks detected from EDX of a) FeCo-AB, b) FeCo-BB, and c)FeCo-CB. Where A= 75:25, B= 50:50, and C= 25:75 ratios of ferrocene and cobaltocene used in the synthesis, and the second B= bulk sample. 199

7.3 Raman spectra obtained for a)FeCo-A1, b) FeCo-A2, c) FeCo-A3, d) FeCo-B1, e) FeCo-B2, f) FeCo-BB, g) FeCo-C1, h) FeCo-C2, i) FeCo-C3, where A= 75:25, B= 50:50, and C= .25:75 ferrocene:cobaltocene ratio and 1, 2, and 3 represent the substrate position. 202
7.4 Graph showing an estimate of local BP temperature with increasing currents. 203
7.5 Graphs showing the individual stress/strain curves obtained for multiple BP samples per BP batch for a) LCBP1, and b) LCBP2. 207
7.6 Graphs showing the individual stress/strain curves obtained for multiple BP samples per BP batch for a) SNBP1, b) SNBP2, c) SNBP3, and d) LNBP1. 208

List of Tables

1.1 Table showing the M_s and H_c values obtained for a range of syntheses. . . . 13

2.1 The experimental parameters investigated in the systematic study carried out in conjunction with monitoring H_2 evolution. The labelling system indicates: A) 200/ 750, B) 200/ 850, C) 250/ 750, and D) 250/ 850 °C for T_{sub} and T_{pyro}, respectively. The first number (i.e. A**5**2-200) corresponds to 5) for 50 and 1) for 100 sccm Ar flow. The second number (i.e. A5**2**-200) corresponds to 2) 2 cm and 3) 3 cm furnace gap. All syntheses were carried out for 10 minutes, with 200 mg of ferrrocene precursor. 25

2.2 Identification of the peaks that arise in the background MS scan. 34

2.3 The effects of different synthesis parameters on the properties of their corresponding synthesised Fe@MWCNTs. *indicates a mostly agglomerates sample. Labels: A= 200/750, B= 200/850, C= 250/750 and D= 350/850 °C for T_{sub}/T_{pyro}, 1 and 5 = 100 or 50 sccm Ar flow, respectively, and 2 and 3 = 2 or 3 cm furnace gap. 50

2.4 Values for the M_s, H_c and remanence for each sample in the systematic study. The labels are as follows: A= 200/ 750, B=200/850, C= 250/750, D= 250/850 °C for T_{sub}/T_{pryo}, 1= 100, 5= 50 sccm Ar flow and 2 and 3 indicates the furnace gap in cm. 63

3.1 The samples produced, using different ratios of ferrocene to cobaltocene, along with their unique reference code, which is used throughout the chapter. The final number/B in the reference code refers to substrate number or bulk sample (B) scraped out the quartz tube. 73

3.2 The average length of Fe/Co@MWCNTs, and NP diameter, where A= 75:25, B= 50:50, and C= 25:75 ferrocene:cobaltocene ratios used in the synthesis, the substrate position is given by 1= 31-35, 2= 35-39 and 3= 39-43 cm along the quartz tube, and B= bulk sample. 78

3.3 The average ratio of Fe:Co inside the filling, as calculated from taking the average of the Fe:Co from five EDX maps taken across the sample. The ratios show that there is a large excess in Fe in all cases. 82

3.4 The wt. % of Fe, Co and FeCo phases within the samples, calculated by Rietveld refinement, where FeCo-AB, FeCo-BB and FeCo-CB were synthesised using 75:25, 50:50 and 25:75 ratios of ferrocene to cobaltocene precursors, respectively. A good fit of the data to calculated XRD patterns was obtained for all PXRD patterns. XRD was carried out on bulk samples. . . 88

3.5 The $I_{D/G}$ obtained for different substrate positions for different ratios of ferrocene to cobaltocene precursor used during synthesis, where A= 75:25, B= 50:50, and C= 25:75 ferrocene:cobaltocene ratios used in the synthesis, the substrate position is given by 1= 31-35, 2= 35-39 and 3= 39-43 cm along the quartz tube, and B= bulk sample. 93

3.6 Table showing M_s and H_c at 300 and 4 K for Fe@MWCNTs, Co@MWCNTs and FeCo-AB, FeCo-BB and FeCo-CB, where the ratio in the brackets shows the ratio of Fe:Co, as calculated from XRD. A= 75:25, B= 50:50, and C= 25:75 ferrocene:cobaltocene ratios used in the synthesis. All SQUID measurements were taken on bulk samples. 95

4.1 Masses of P123 and distilled water investigated to obtain the ideal viscosity for dispersing Fe@MWCNTs in. 110

4.2 The $I_{D/G}$ ratios calculated from Raman spectra for conventional MWCNT and ferromagnetic (two different batches, labeled FeBP1 and FeBP2,) BPs, taken prior to and after I/V measurements. Five Raman measurements were taken per BP sample. 120

5.1 Table showing the approaches used to produce BPs, the type of CNT used, and the mechanical properties for each approach. The abbreviations HiPCO stands for high pressure CO, whilst SDS stands for sodium dodecyl sulfate, a surfactant used to disperse CNTs. 137

5.2 The short hand system used to label the samples. Following the code, a number is given to indicate different batches of BP samples, e.g. LCBP1. . 141

5.3 The total SFE, and the corresponding dispersive and polar components for both conventional and N-doped MWCNT BPs, calculated using the Fowkes equation. Top and bottom refer to the face of the BP, where the bottom face is the BP that was in contact with the filter paper. 149

5.4 The average contact angle for water, recorded for three batches, of N-doped or conventional MWCNT BPs. For the 'Face' column, T and B represent top and bottom faces, representative. For samples marked with a *, the needle was switched to a 32 G needle, and a droplet of size 4.5 μml was deposited on the BP surface. 150

5.5 The assignment to the key identified peaks present in all four FTIR samples.151

7.1 Table showing the average contact angles recorded for three batches, each, of N-doped or conventional MWCNT BPs. For the 'Face' column, T and B represent top and bottom faces, representative. The solvents are denoted as EG, F and H for ethylene glycol, formamide and hexadecane, respectively. For samples marked with a *, the needle was switched to a 32 G needle, and a droplet of size 4.5 ml was deposited on the BP surface. 204

7.2 Table showing the average contact angles recorded for three batches, each, of N-doped or conventional MWCNT BPs. For the 'Face' column, T and B represent top and bottom faces, representative. The solvents are denoted as EG, F and H for ethylene glycol, formamide and hexadecane, respectively. For samples marked with a *, the needle was switched to a 32 G needle, and a droplet of size 4.5 ml was deposited on the BP surface. 205

7.3 Table showing the average contact angles recorded for three batches, each, of N-doped or conventional MWCNT BPs. For the 'Face' column, T and B represent top and bottom faces, representative. The solvents are denoted as EG, F and H for ethylene glycol, formamide and hexadecane, respectively. For samples marked with a *, the needle was switched to a 32 G needle, and a droplet of size 4.5 ml was deposited on the BP surface. 206

Chapter 1

Introduction

1.1 Outline

Over the past few decades, intense research has been carried out on carbon nanotubes (CNTs) and their incredible properties, with a vast array of applications being proposed for these materials. Further, the hollow internal cavity of CNTs can be filled with different materials, including metals [1–4], fluorescent particles [5], fullerenes [6]. Specifically, the cavity can be filled with magnetic metals [7–13], which is the focus of this thesis. Coincidentally, chemical vapour deposition (CVD), arguably the most used synthesis method to produce MWCNTs, typically uses Fe, Co or Ni as the catalyst, with metallocenes being a commonly used catalyst source. By modifying the synthesis method to use the metallocene as both the carbon and catalyst source, multi-wall carbon nanotubes (MWCNTs) filled with these magnetic metals can be produced.

Despite the potential that these magnetic metal-filled MWCNTs offer by allowing individual MWCNTs to be controlled by external magnetic fields [14], ferromagnetic metal-filled MWCNTs have yet to be used in commercial applications. This lack of uptake into commercial use may be due to the limited quantity of these materials and to the impracticalities of manipulating individual Fe@MWCNTs on a large scale. Further, our current understanding of the growth mechanism for Fe@MWCNTs is incomplete.

In this work, different aspects of CVD of ferromagnetic metal-filled MWCNTs and their post-synthesis processing to form macroscopic structures was investigated. The project objective was to improve the quantity and quality of ferromagnetic metal-filled MWCNTs, whilst furthering our understanding of Fe@MWCNT growth, with the overall aim of cre-

ating smart materials which can be manipulated on the macroscopic scale. A review of the recent literature is first discussed in this chapter, and the gaps in the literature are identified. The growth of Fe-filled MWCNTs (Fe@MWCNTs) and the effect of changing synthesis parameters in a systematic study is discussed in chapter two. A number of *ex situ* characterisation techniques, such as Raman spectroscopy, electron microscopy, thermogravimetric analysis (TGA) and superconducting quantum interference device (SQUID) measurements were utilised to characterise the materials produced from the syntheses. Online monitoring of the reactor using *in situ* mass spectroscopy (MS) provided insight into the thermocatalytic cracking of ferrocene during synthesis. Chapter three covers the production of alloy-filled MWCNTs and assesses the viability of controlling the magnetic properties of these ferromagnetic alloy-filled MWCNTs by altering the ratio of the metal constituents making up the filling. The fourth chapter explores creating smart fabrics, buckypapers (BPs), from the Fe@MWCNTs produced using the optimised recipe from chapter two. Selectively depositing the Fe@MWCNTs in specific regions created BPs that were responsive to external magnetic stimulus only in those areas with Fe@MWCNTs. Strips of BPs with the Fe@MWCNTs deposited across the entire surface were used to create a non-metallic electromechanical switch prototype and the I/V characteristics of these BPs were investigated under air, N_2 and vacuum conditions. In the fifth chapter, the mechanical properties of BPs created using conventional and N-doped MWCNTs are discussed. The chapter examines the effect of BP type and length on tensile strength, and attempts to correlate surface chemistry, CNT length and type to the observed differences in stress/strain curves. The main research outcomes are summarised in chapter six, with a discussion of the proposed future works. These future works cover a range of research topics, towards the end goal of developing smart, multifunctional papers.

The work in chapter 4 resulted in a submitted article which is currently being reviewed. Each chapter consists of a dedicated introduction, experimental, results and discussion and conclusions. Figure 1.1 is a flow chart that shows how each chapter in this thesis is interconnected.

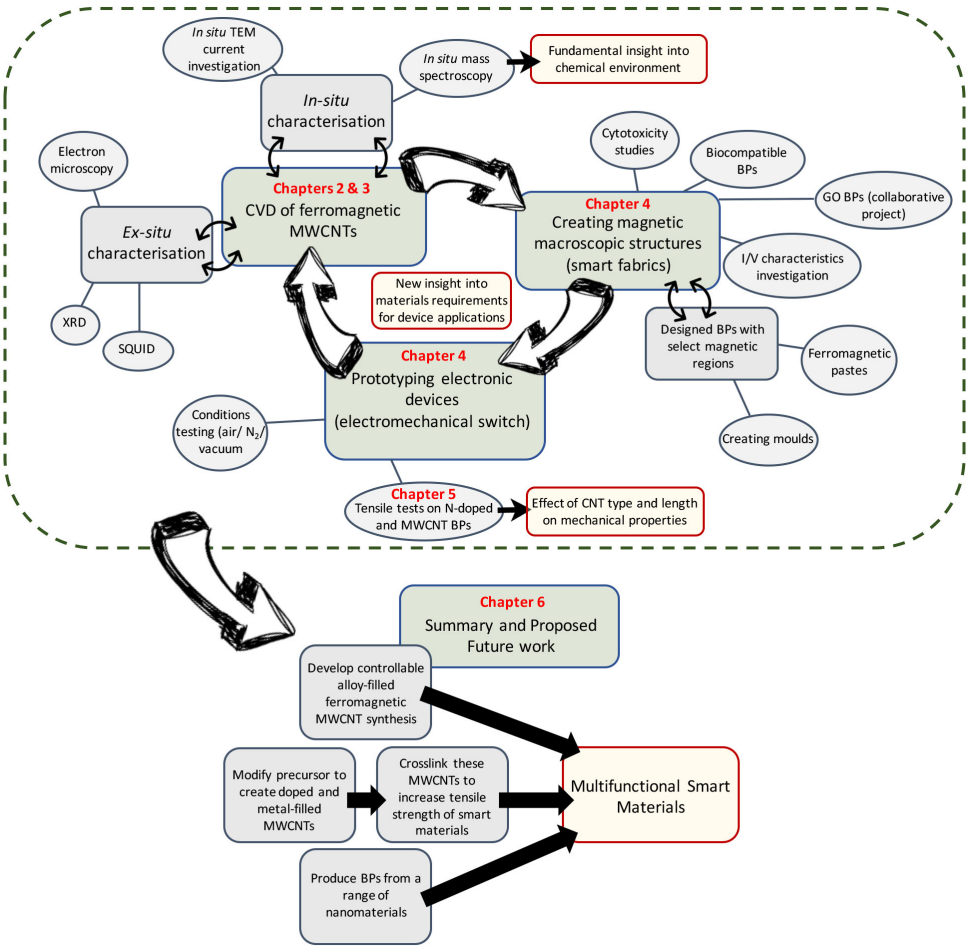


Figure 1.1: Flow chart of the PhD project and proposed future work.

1.2 Literature Review

1.2.1 The Carbon Nanotube

Carbon, C, is a versatile element, capable of bonding with up to 4 other atoms by hybridising into *sp*, sp^2 and sp^3 configurations. These different hybridised configurations explain why C can exist in a variety of allotropes; diamond, graphite, fullerenes, carbon nanotubes (CNTs) and graphene. Whilst diamond consists of sp^3 C, graphene related allotropes are formed of sp^2 C arranged in a 'honeycomb' lattice structure. Buckminsterfullerene, discovered in 1985 by Kroto *et al.* [15] are spherical structures with the arrangement of pentagons and hexagons providing its curvature. CNTs can be thought of as a rolled up sheet of graphene capped with a similar arrangement of pentagons and hexagons as fullerenes. Single-walled nanotubes (SWCNTs) consist of one C layer, whilst multi-wall nanotubes (MWCNTs) contain several C layers.

Iijima reported the structure of MWCNTs grown by arc discharge in 1991 [16] and showed their multi-wall structure in transmission electron microscopy (TEM) images (Figure 1.2). Besides arc discharge [17, 18], other approaches to producing CNTs include chemical vapour deposition (CVD) [19, 20] and laser ablation [21]. CVD is arguably the most popular approach used to grow CNTs, due to its scalability, hence this literature review focuses on the CVD approach for producing CNTs. Following this, the CNT growth mechanism is reviewed, before moving on to CNTs filled with metals and concluding with CNT processing methods to form macrostructures.

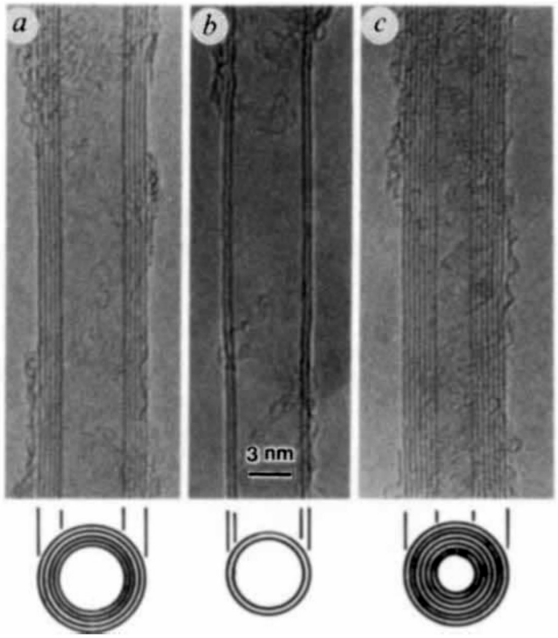


Figure 1.2: TEM images showing MWCNTs first imaged by Iijima [16], showing a and c) MWCNTs, and b) double-wall carbon nanotube (DWCNT).

1.2.2 CVD MWCNT growth

CVD is a versatile approach for growing MWCNTs, in which gaseous precursors, carried to the reactor under a controlled carrier gas flow, react together on a surface to form materials that are different from the precursor. Most CVD syntheses for MWCNT growth are based on pyrolysis of gaseous hydrocarbons such as alkanes [22–25], alkenes [25–27], and alkynes [20, 28, 29]. Liquid hydrocarbons are often vaporised or atomised before pyrolysis, typically using spray injectors or ultrasonic aerosol, known as spray pyrolysis (SPCVD) and aerosol assisted chemical vapour deposition (AACVD) (Figure 1.3), respectively.

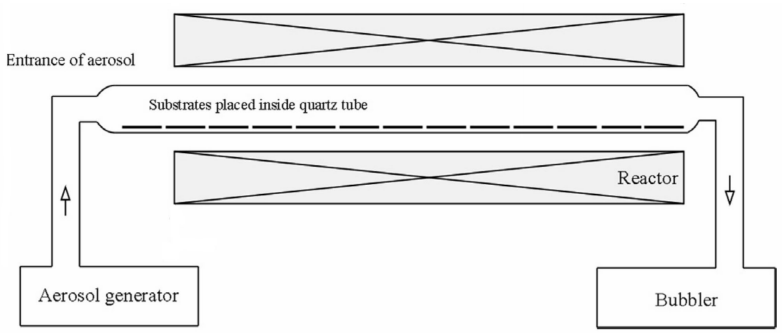


Figure 1.3: Schematic, adapted from [30] showing a typical setup used for AACVD. The aerosol created by the aerosol generator is carried into the furnace by an inert gas flow, where it decomposes to form MWCNTs on the substrates.

Often, catalysts, typically Fe, Ni, or Co, are used in CVD to increase hydrocarbon pyrolysis, and hence yields, this is more precisely known as catalytic chemical vapour deposition (CCVD). The catalyst particles can be deposited onto substrates prior to MWCNT synthesis [31–33] or introduced into the reactor simultaneously with the carbon precursor, as in AACVD [25, 30, 34]. Embedding the catalyst particles into the substrate allows the MWCNT diameter and intertube spacings to be controlled [32]. For AACVD, benzene derivatives and ferrocene are the most common carbon and catalyst sources, respectively [35–38]. Ferrocene is the Fe containing organometallic compound in the metallocene family, which have the general formula $(C_5H_5)_2M$, where M= Fe, Co and Ni.

Adjusting the CVD synthesis parameters such as furnace temperature, precursor species, reaction length and carrier gas, controls the materials produced [39]. Catalyst particle size defines the MWCNT diameter [20, 25, 36], whilst deposition time controls the MWCNT length, with longer reaction times producing longer MWCNTs [25, 34]. The MWCNT length is important for some processing methods (see section 1.2.7), and the effect of MWCNT length on the mechanical properties of macroscopic papers is discussed further in chapter 5. Increasing the metallocene to carbon source ratio, or pyrolysing the metallocene alone [40–42], produces MWCNTs with metal fillings, which are of interest due to their magnetic properties (sections 1.2.4-1.2.5), with the encapsulated metal nanowires/ nanoparticles being protected from oxidation by the MWCNT [8, 9, 43].

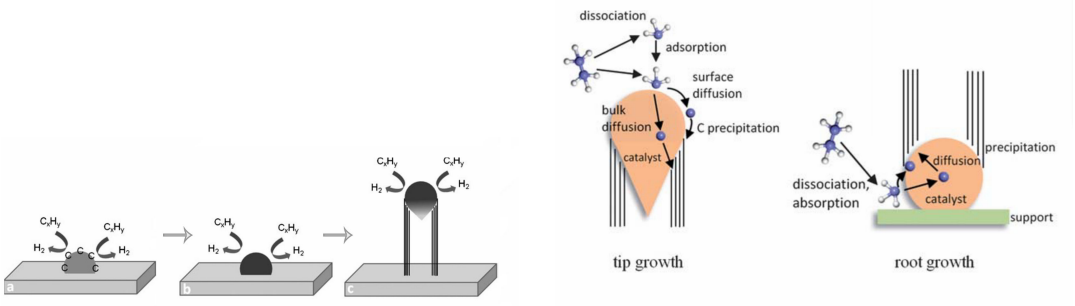
1.2.3 Mechanism for CNT growth via CVD

The CVD growth mechanism for both SWCNTs and MWCNTs is yet to be fully understood. Different aspects of the mechanism have been studied, including catalysts suitability

for MWCNT growth [44–46], whether the active catalyst is a carbide or metallic [45, 47, 48] and the C diffusion pathway [49, 50]. The solid nature of the catalyst particles during CVD was confirmed by *in situ* analytical studies [51–54].

The vapour-liquid-solid (VLS) model, developed to explain carbon nanofiber growth [55], was adapted by Baker *et al.* [56, 57] to explain MWCNT growth. In the VLS model, the gaseous precursor decomposes on the liquid catalyst particle to form C atoms which dissolve into the catalyst particles. The C precipitates when the particle becomes saturated, following the temperature gradient within the nanoparticle, to form MWCNTs [55, 58] (Figure 1.4a). The validity of a temperature driving force for carbon precipitation has been questioned for precursors with endothermic dissociations [59]. Tibbetts proposed chemical potential gradients as an alternative driving force [60], however this hypothesis breaks down for MWCNT growth from solid particles [61].

MWCNTs can grow by base or tip growth modes, the interactions between the catalyst particle and the substrate dictates whether the particle remains on the substrate with CNT growth [56, 57] (Figure 1.4b).



(a) (b)

Figure 1.4: Schematics showing a) the VLS model, image modified from [61]. The precursor gas decomposes on the catalyst particle to form C atoms, which diffuse through the particle as a solid solution. Eventually, the particle becomes saturated and C precipitates out of the particle following the temperature gradient within the particle. b) tip growth, and root growth mechanisms for MWCNT growth, which occur for unfavourable, and strong interactions between the substrate and the particle, respectively [58].

The VLS mechanism and base/tip growth modes have been extended to explain CVD growth of metal-filled MWCNTs. Zhang *et al.* [62] proposed an open tip mechanism, where an open tip forms until more catalyst particles fill the open MWCNT tip and rapid MWCNT growth encases the particles in C [62] (Figure 1.5a). However, theoretical studies show that open tips are energetically unfavourable compared to closed tips [63], which questions the validity of an open-tip mechanism for growth of filled MWCNTs.

Kunadian *et al.* [64] explains CVD metal-filled MWCNT growth by combining tip and base growth mechanisms (Figure 1.5b). The floating catalyst conditions allows for metal cluster formation and hydrocarbon decomposition to occur in the gas phase. Assuming initial base growth, catalytic metal clusters and C atoms land onto catalyst particles anchored to the substrate. These metal clusters modify the shape and C concentration of the rooted catalyst. It is likely that the growth mode will then switch to tip growth [58, 64]. Energy dispersive X-ray (EDX) studies observed changes from base to tip growth modes by carrying out CVD using ferrocene with a Co substrate layer, where no Co could be observed in the MWCNT filling. However Fe was found in the MWCNT filling for CVD with cobaltocene and a Fe substrate layer, which suggests that the growth mechanism had switched from root to tip growth [49]. Whilst the switch from root to tip growth was observed by altering whether Co and Fe were in the substrate layer or the metallocene, this does not confirm that switching growth mechanism occurs using just one metal, as the switch could be due to the poorer wettability between the Fe and the substrate, hence tip growth is preferred.

With our current knowledge, we are unable fully explain the formation of *in situ* filled CNTs. The influence of reaction conditions on MWCNT growth could mean that different conditions lead to different mechanisms for CNT growth. The range of growth conditions used by different research groups increases the difficulty in achieving a full understanding. *In situ* synthesis monitoring techniques could provide insight into the effects of different parameters on MWCNT growth environment. Understanding the reaction environment is the motivation behind chapter 2, where the effects of synthesis parameters on the reaction atmosphere is investigated by *in situ* mass spectroscopy (MS).

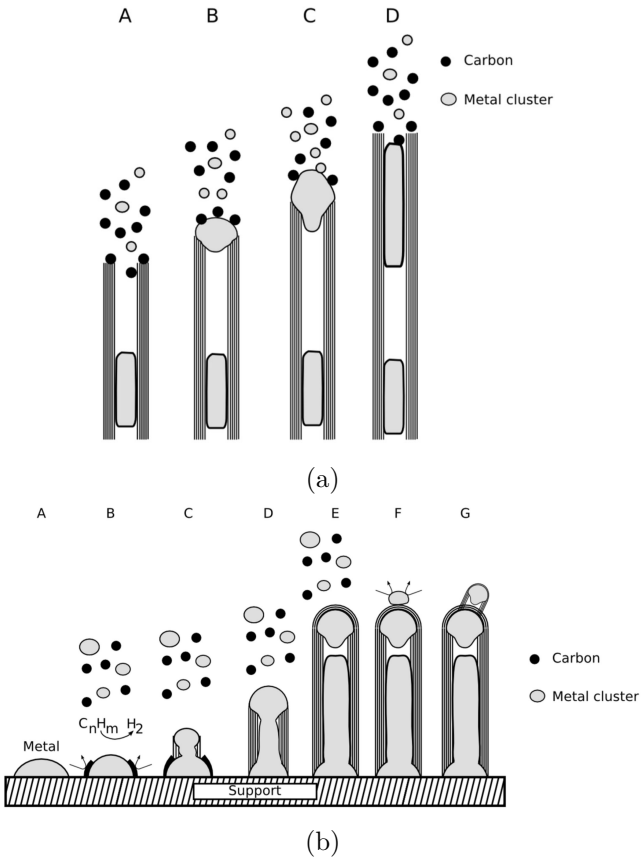


Figure 1.5: Schematic showing a) an open tip mechanism [62] and b) combined tip and base growth mechanisms for growing filled MWCNTs [58].

1.2.4 Filled Carbon Nanotubes

This section covers the methods used to produce metal filled-MWCNTs, covering *ex situ* and *in situ* techniques, with a section on ferromagnetic metal-filled MWCNT growth by CVD. MWCNTs can be filled with varying degrees and filling distribution within MWCNTs, as shown in the schematics in Figure 1.6.

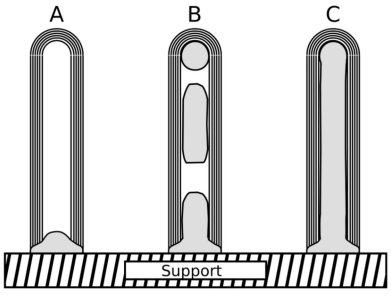


Figure 1.6: Schematics showing a) a typical MWCNT formed by CVD, with a catalyst particle inside the MWCNT, b) a partially filled MWCNT, and c) a continuously filled MWCNT. The black lines represent graphitic layers and grey shows the filled regions [58].

Whilst encasing metal nanowires in CNTs is the method of focus in this thesis, nanowires have been produced by other routes, such as electrodeposition and lithography [65, 66]. Nanolithography was the traditional approach used to create metal nanowire arrays [67]. Ordered, patterned arrays of nanomagnetic materials have been produced using lithographic methods such as interferometric lithography, or X-ray lithography and ion-beam etching. [66] In interferometric lithography, a resist layer, composed of an antireflective coating, is exposed to a standing wave fringe pattern generated by two laser beams. The fringe pattern leaves a pattern of holes or posts in the resist. [65] However, the lithography method is considered to be cumbersome compared to electrodeposition. Further, achieving large area, high aspect ratio nanowires is difficult with conventional lithography. [67]

Poissin first reported using a template and electroplating method to grow small diameter, 30 nm with lengths of up to 15 μm, Sn, In and Zn metal wires in 1969 [68]. Damage tracks in mica, created using high energy charged particles, were etched out using strong acids to form holes. The diameter of the holes directly affected the diameter of the metal.

Taking inspiration from Poissin's work, periodic and uniform arrays of Fe [69–71], Co [72, 73], Ni [72, 74] and alloy [73] metal nanowires have been produced. A popular approach to produce these nanowires is the direct electrochemical deposition of these metals into nanoporous anodic aluminium oxide (AAO) templates. AOA templates are particularly popular for the production of nanowires because of their high pore density, and the pores, which have a small pore size, are uniformly distributed [67]. The AAO templates are created by first anodising the Al in an acidic solution and applying a voltage, with a Pb sheet as the cathode. This process causes the aluminium oxide cell to grow in height. The pores inside these cells can then be widened to a chosen diameter by immersing the samples in phosphoric acid for a set amount of time. Finally, the anodised aluminium is placed inside an electrolyte containing metal ions for electrodeposition. An alternating current is applied between the aluminium oxide and a counterelectrode, the metal ions deposited inside the pores grow to form a metal nanowire from the bottom up. [69]

Whilst lithography and electrodeposition produces metal nanowires, encapsulating the nanowire inside CNTs enables the nanowire to be exceptionally stable. The C surrounding the nanowire prevents it from oxidation and the CNT also acts as a means to control the diameter of the nanowire, by controlling the diameter of the CNT [75].

Ex situ Approach to Metal Filled Carbon Nanotubes

Filled MWCNTs were first observed by Ajayan in 1993 [76], where molten Pb filled the inner cavity of the MWCNT by capillary suction. Other filled MWCNTs produced by capillarity include metal halides [77–79] florescent particles [80] and Fe [77, 81]. Capillarity is an *ex situ* filling method where the MWCNTs are fabricated separately to filling. Filling materials are limited to those with low surface tension, due to wettability [82] and the number of filled nanotubes depends on contact between the filling and MWCNT, with 1% of the MWCNTs being filled in Ajayan's experiments [76]. Tsang *et al.* [83] developed a single-step MWCNT opening and filling procedure using solutions of concentrated nitric acid and metal nitrates. This wet-chemical approach opened *ca.* 80% of the MWCNTs, and roughly 60-70% contained fillings of up to *ca.* 20 nm. Examples of the fillings that could fill MWCNTs using this method include oxides of Co, Ni, Ur and Fe [83].

In situ Approach to Metal Filled Carbon Nanotubes

In situ approaches for producing filled MWCNTs grow and fill the MWCNTs simultaneously. A study of metal-filled MWCNTs grown by arc discharge from composite metal-carbon electrodes found that high temperatures often favoured metal carbide fillings [84]. The formation of continuous nanowires inside MWCNTs was strongly correlated to the existence of an incomplete electronic shell, which affects the ability of the metal to act as a catalyst and form carbides [85]. However, the arc discharge method produces a large amount of byproducts, requiring additional purification steps to obtain the MWCNTs, hence CVD is typically the preferred method for metal-filled MWCNT growth.

CVD Method towards Ferromagnetic-Filled Carbon Nanotubes

As mentioned (Section 1.2.2), increasing the catalyst concentration or using the metallocene alone in CVD produces MWCNTs with a metal filling. Sen *et al.* [7] first synthesised MWCNTs using metallocenes in a two-stage furnace (Figure 1.7), with furnace temperatures of 200 and 900 °C. The metallocene sublimed in the first furnace, and decomposed in the second furnace to form MWCNTs. The MWCNTs were often completely filled with Fe, whilst syntheses with cobaltocene and nickelocene yielded MWCNTs containing Co and Ni particles. The magnetic nature of the catalyst was preserved in these metal-filled

MWCNTs, leading to interest in studying and controlling the magnetic properties of these ferromagnetic metal-filled MWCNTs.

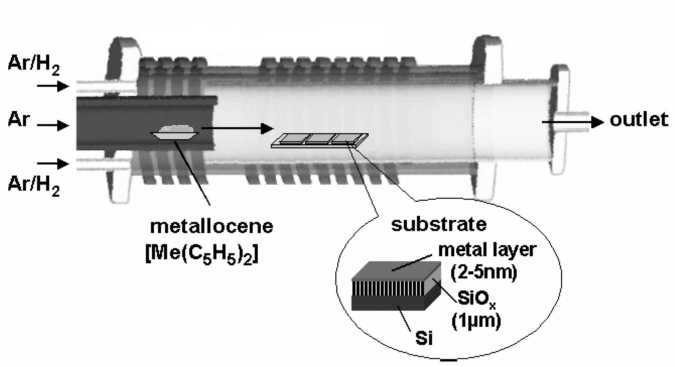


Figure 1.7: Schematics showing a 2-stage furnace setup typically used for growth of metal-filled MWCNTs by CVD of metallocenes [8].

Metallocenes have been used for CVD growth of MWCNTs filled with Fe [8–10, 42, 86, 87] and Co [88, 89]. Combinations of metallocenes can produce alloy-filled MWCNTs, using metallocene powders [12], or by dissolving them in hydrocarbons [13, 90, 91]. Most syntheses use a two-stage furnace (Figure 1.7) to improve control of precursor sublimation. However, there can be difficulties maintaining a constant sublimation rate throughout the sublimation furnace, due to steep temperature increases between the two furnaces. The effect of furnace gap on furnace temperature profiles is discussed in chapter 2.

Alternative precursors used to produce ferromagnetic metal-filled MWCNTs include phthalocyanines[92–94], $Co(CO)_3NO$ [95], or Fe_2O_3/SiO_2-Al_2O_3 powders [96], whilst alternative methods include heating $Co(CO)_3NO$ with Mg powder in a sealed chamber [97]. However, yields and filling lengths using these precursors can be limited, especially with phthalocyanines, which have a much higher carbon to metal ratio, resulting in lower filling lengths.

In situ metal filled-MWCNTs growth methods are preferred over *ex situ* ones, as it is a one-step MWCNT growth and filling procedure. Typically, higher filling % are achieved with *in situ* methods, with higher reproducibility as it does not rely on dipping MWCNTs evenly into a solution. For these reasons, metal filled MWCNTs were grown *in situ* by CVD in this thesis. Metallocene precursors were chosen due to their versatility; mixing these to grow alloy-filled MWCNTs was investigated (Chapter 3).

1.2.5 Magnetic Properties and Structure of Ferromagnetic Metal-Filled CNTs

Much of the research on ferromagnetic metal-filled MWCNTs has focused on understanding and controlling properties such as the magnetisation saturation (M_s) and coercivity (H_c) of the MWCNTs. Briefly, the M_s is the maximum applied external magnetic field, at which point all the magnetic dipoles within the material are aligned with the magnetic field, and H_c is the resistance of a material to changes in magnetisation [98].

Initial magnetic measurements showed the ferromagnetic nature of Fe@MWCNTs by applying alternating gradient magnetometry (AGM) to as grown Fe@MWCNT samples [8, 87]. These measurements also revealed the strong uniaxial magnetic anisotropy of Fe@MWCNTs, with the easy magnetic axis running parallel to the MWCNT axis [8]. The magnetic anisotropy is attributed to the large aspect ratio of the magnetic nanowires [58], however, this greater aspect ratio does not enhance H_c [99, 100]. Instead, nanowire diameter appears to be more important in determining H_c, with higher H_c observed for smaller diameters [100]. Magnetic dipole-dipole interactions between the Fe nanowires in individual MWCNTs depend on the alignment and density of the CNTs on the substrate, with decreasing interaction between Fe-nanowires for increasing MWCNT distances [101]. These dipolar interactions affect the magnetic data obtained by AGM, and should be taken into account [58]. Taking measurements on individual MWCNTs avoids problems with the degree of filling, MWCNT packing density and the dipolar interactions affecting the magnetic data obtained from bulk samples. Magnetic force microscopy measurements have measured the magnetic fluxes generated by individual Fe@MWCNTs, and showed the utility of using Fe@MWCNT as probes in the next generation of magnetic force microscopes [102–105].

Section 1.2.5 summarises some of the magnetic properties reported for ferromagnetic metal-filled MWCNTs. Enhanced H_c values were observed for Fe@MWCNTs at room temperature, with values typically being much higher than for bulk iron, which has a H_c of 9×10^{-3} mT [106]. Similar H_c increases have also been reported for Co- and Ni-filled CNTs (Section 1.2.5), compared to bulk hexagonal close pack (HCP) Co and Ni H_c values of 1 mT [88] and 0.7 Oe [107], respectively, suggesting that confining the magnetic elements inside MWCNTs shows a general trend of increasing H_c, which could be due to the size effect [88].

CNT Type	**Method**	**Precursor**	**Nanowire dimensions**	**M_s**	**H_c**	**Temp/ K**	**Ref**
Fe@MWCNT	CVD	Ferrocene	5-30 nm x 'a few' μm	750 μemu/mm^2	160 mT	300	[108]
Fe@MWCNT	CVD	Ferrocene	8-40 nm x ?	-	130 mT	300	[8]
Fe@MWCNT	CVD	Ferrocene, C_{60}		0.01 emu	800-1000 Oe	300	[41]
Fe@MWCNT	CVD (annealed)	Ferrocene	12-26 nm x ?	0.243 meum/mm$_2$	73 mT	300	[109]
Fe@MWCNT	Solid State Pyrolysis	Fe-phthalocyanine		3.5 emu/g	549 Oe	300	[110]
Fe@MWCNT	injection CVD	Ferrocene, xylene	10-20 nm x ?	-	732 Oe	RT	[111]
Co@MWCNT	CVD	Cobaltocene	15-30 nm x 'a few μm	-	59 mT	300	[88]
Co@MWCNT	CVD	$Co(CO)_3NO$	20 nm x 'a few μm	8.4 emu/g	-	300	[95]
Ni@MWCNT	Ni-Electroplating	nickel salts	11 nm x 215 nm	0.06 emu	40 Oe	300	[107]
Fe/Co@MWCNT	CVD	Ferrocene, cobaltocene	10-20 nm x 'a few μm'	-	126 mT	300	[12]
Fe/Co@MWCNT	AACVD	Ferrocene, cobaltocene, toluene	-	0.06 emu	900 Oe	300 K	[90]

Table 1.1: Table showing the M_s and H_c values obtained for a range of syntheses.

The structure of the filling in ferromagnetic metal-filled MWCNTs effects its magnetic properties. Fe@MWCNTs usually contain up to three Fe phases; α-Fe (ferrite), γ-Fe (austenite) and iron carbide (Fe_3C, cementite), which are responsible for the magnetic response [106, 112]. α-Fe and Fe_3 are ferromagnetic, with body centred cubic (BCC) and orthorhombic crystal structures, respectively, whilst γ-Fe, austenite, is paramagnetic, with a face centred cubic (FCC) structure [106, 113]. Shpak *et al.* [113] found that Fe@MWCNTs grown on silicon substrates formed the γ-Fe phase close to the top surface of the aligned MWCNTs whilst the α-Fe phase and Fe_3C were located closer to the silicon substrates. Similarly, Morelos-Gomez *et al.* [99] reported a coreshell nanowire structure with α-Fe surrounded by an Fe_3C shell.

The Fe phase encapsulated inside the MWCNTs can be selected by controlling furnace temperature and dwell time. Osorio *et al.* [106] linked the phase of the filling with the magnetic properties exhibited, reporting that high temperature syntheses with long dwell times resulted in higher compositions of α-Fe, which has a lower H_c than Fe_3C. Longer dwell times result in all of the carbon being expelled from the nanoparticles whilst a higher temperature provides more energy for the ejection of C from Fe_3C. Higher H_c values are achieved with lower temperatures and shorter dwell times as more Fe_3C is present in the MWCNTs, in agreement with work by Hampel *et al.* [87]. Controlling the amount of Fe_3C and metallic Fe present in the MWCNTs formed Fe@MWCNTs with intermediate H_c values; syntheses carried out at 1000 °C produced Fe@MWCNTs with a H_c of 445 Oe [106]. Similar H_c values were reported by Dillon *et al.* [40], with a H_c of 467 Oe for Fe@MWCNTs produced at 1050 °C. Dillon also found that increasing the temperature of the pyrolysis furnace led to an increase in the diameter of the outer wall of CNTs, whilst an increase in the sublimation temperature led to an increase in Fe@MWCNT diameter and hence, the Fe nanowire also increased in length. The magnetic properties were tuned by systematically varying the synthesis parameters; decreases in H_c of Fe@MWCNTs was observed with increasing pyrolysis temperature, whilst sublimation temperature controlled M_s [40].

Annealing Fe@MWCNT controls their magnetic properties by transforming the paramagnetic γ-Fe phase to the ferromagnetic α-Fe phase [109, 114, 115]. Leonhardt *et al.* [115] reported H_c values up to 130 mT and strong magnetic anisotropy for as-grown aligned Fe@MWCNT arrays grown by CVD of ferrocene. Annealing at 675 °C reduces H_c and removes the magnetic anisotropy by changing the filling from a mixture of α-Fe, γ-Fe and

Fe_3C to α-Fe [115]. Similar transformations from γ-Fe to α-Fe were observed by Gui *et al.* by annealing CVD Fe@MWCNTs produced using ferrocene in dichlorobenzene (DCB). Again, decreases in H_c and increases in M_s accompanied the increase in α-Fe phase within the Fe@MWCNTs.

1.2.6 Post-Synthesis Processing of CNTs Towards Macrostructures

CNT samples are often processed to remove impurities. Cleaning procedures are used to remove carbonaceous impurities, such as amorphous carbon and metal particles [116, 117]. Common treatments to remove carbonaceous impurities include chemical oxidation, acid treatment. These carbonaceous impurities are more reactive than the CNTs due to a higher presence of dangling bonds in amorphous carbon or the higher curvature of carbonaceous NPs. [117–119]. O_2, air and H_2O_2 are examples of typically used oxidising agents [117, 120, 121]. Chemical oxidation has the disadvantage of opening CNT ends and introducing oxygenated functional groups on the CNTs. Acid treatment using concentrated acids such as HNO_3 and H_2SO_4, or $KMnO_4$ can cut CNTs into shorter, open-ended CNTs and remove metal particles [122–124]. However, for Fe@MWCNTs, procedures such as acid treatment can remove the filling from the CNTs, which is counterproductive for syntheses aimed at growing Fe@MWCNTs.

Post-synthesis process can also be used to exploit the properties of CNTs in macrostructures, by taking them from the nanoscale to the macroscopic level. This processing produces freestanding structures such as buckypapers (BPs) [122, 125–128], fibres [129–133] and thin films [134–137]. BPs, are structures composed of entangled CNTs, first fabricated by Liu in 1998 [122]. Liu produced BPs by first cutting nearly endless and tangled SWCNTs into shorter, well-dispersed strands, using the surfactant sodium dodecyl sulfate (SDS) to assist with creating a homogenous dispersion. This solution was filtered to form a BP containing well-entangled SWCNTs. The centrifugation and filtration process not only produces BP, but also acts as a non-destructive method of removing byproducts from the samples [117, 122]. The resulting BP was mechanically strong, yet flexible and the conductive properties of the raw material was conserved in the BP.

One of the main challenges with creating BPs using a filtration method is achieving homogeneous and stable CNT dispersions. CNTs are attracted to one another by Van der Waals forces, whilst their high aspect ratios and flexibility leads to CNT entanglement

being increasingly probable [11]. Factors to consider for dispersing CNTs involve solvent type and choosing mechanical or chemical methods for dispersing the CNTs. However, both chemical an mechanical methods can change the CNT aspect ratio distribution by shortening, fragmenting or digesting the CNTs [138].

Chemical methods involve functionalising SWCNTs or MWCNTs using either covalent or non-covalent methods. Covalent functionalisation occurs preferentially at defect sites or CNT ends, and disrupts the delocalised electrons and bonds within the CNT structure by physically bonding to the C. Acid treatment is a commonly used chemical method that oxidises CNTs. However, oxidation often cuts the MWCNTs at high defect density sites, decreasing MWCNT diameter [138]. A combination of acid treatment and thermal oxidation can be used to purify and oxidise MWCNTs and SWCNTs [139–141]. For example, Muramatsu *et al.* [139] obtained stable suspensions of DWCNTs in EtOH without the aid of surfactants, by treating the DWCNTs with concentrated hydrochloric acid and oxidising them in air, which introduced oxide groups that increased their dispersibility.

Non-covalent functionalisation is a less destructive method that involves binding molecules to the surface of the CNT by ionic bonds, π- stacking or Van der Waals force. These molecules, such as DNA, polymers and surfactants like sodium dodecylbenzene sulfonate [142], Triton X-100 [136] and Gum Arabic [143] stabilise the CNTs to prevent aggregation. The most likely arrangements of the surfactant molecules, which are typically amphiphilic molecules, is shown in Figure 1.8. The main drawback to using surfactants is it is often difficult to remove them from the BP afterwards; these residual surfactant impurities could impede the properties of the BPs.

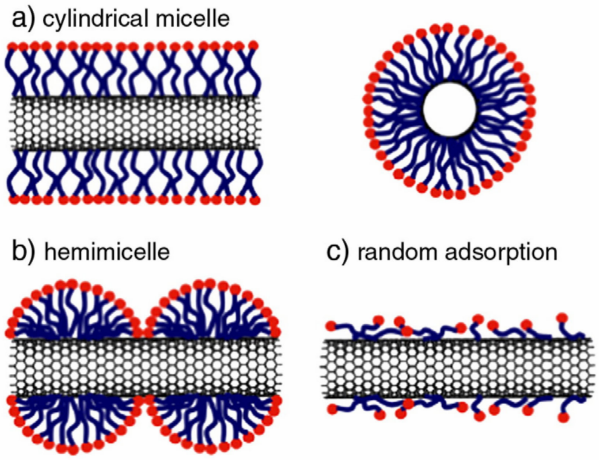


Figure 1.8: Schematics showing ways in which surfactants can bind with CNTs, show formations of a) a cylindrical micelle (front and side views), b) hemimicelle and c) random surfactant adsorption [144].

Mechanical methods, such as ultrasonication, shear mixing and milling, physically separate the CNTs bundles by using mechanical force to overcome the Van der Waals forces between CNTs. Ultrasonication relies on three mechanisms to break down CNT bundles in solvent; localised heating, formation of free radicals and cavitation. Cavitation involves nucleation and imploding of bubbles in the liquid [138]. Ultrasonication decreases both SWCNT and MWCNT length after bundle size has decreased. For MWCNTs, the nanotube layers are relatively independent of one another and sonication causes the layers to fractionate off leading to shorter and thinner MWCNTs with sonication time [138, 145].

Alternative BP synthesis routes include dry transfer [146], frit compression[147] and *in situ* BP production [148, 149]. Aligned BPs were produced by Wang *et al.* [146] using a dry transfer method (Figure 1.9). Large area, *ca.* 10 cm, MWCNT arrays with heights of >100 μm, were grown on silicon substrates by CVD, covered with a microporous membrane and pushed down by applying a constant force to a cylinder which was pushed across the aligned carpet. The BPs formed using this method displayed an improved thermal and electrical conductance performance, compared to MWCNT arrays. The BP displayed thermal and electrical conductances of 153 W m^{-1} K^{-1} and 2.0 x 10^4 S m^{-1} at room temperature, respectively, with the measurements carried out parallel to the MWCNT alignment in the BP.

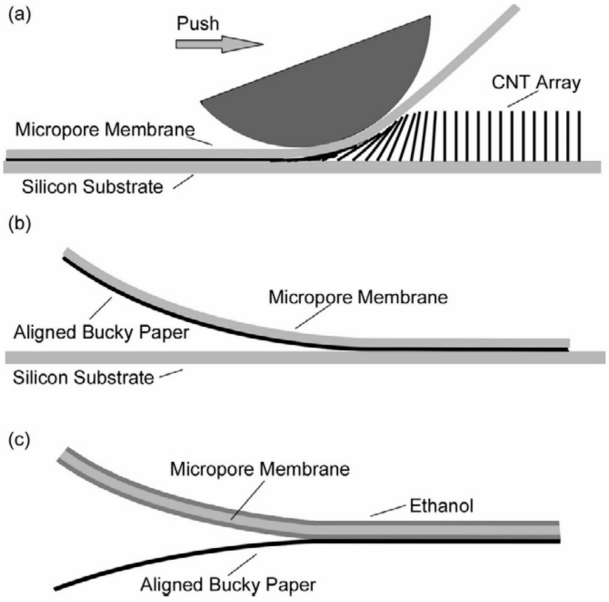


Figure 1.9: Schematics showing the domino push method used in [146], showing a) a cylinder being used to push down an aligned MWCNT array, b) peeling of the aligned BP from the silicon substrate, and c) spraying ethanol on the micropore membrane to allow the BP to be peeled off the membrane.

More recently, a continuous floating catalyst chemical vapour deposition (FCCVD) technique was developed by Xu *et al.* [150] to produce thin films. The FCCVD method produced MWCNTs, which continuously formed a hollow cylinder-like assembly. This cylinder was condensed and deposited onto a winding drum, under N_2, to form a continuous film. The winding rate controlled MWCNT alignment and densification, to form films that are well-aligned and contain highly packed MWCNTs. Fast removal of the MWCNT cylinder from the reactor and increasing spinning of the MWCNTs onto the drum were crucial for improving the alignment of the MWCNTs, resulting in tensile strengths of 9.6 GPa, the highest value recorded for MWCNT macroscopic assemblies. Previously, enhanced BP alignment was achieved either magnetically [151], or by mechanical stretching [152, 153].

Improvements to the mechanical properties of BPs has been achieved by densification [154] and conjugation cross-linking [153]. These cross-linked BPs had an increased electrical conductivity of 1.5 times compared to acid-treated BPs due to the conjugated cross-links increased electron transport. The Young's modulus increased from 1.91 GPa to 8.8 GPa for the pristine and cross-linked BPs, respectively.

1.3 Conclusions

MWCNTs filled with various magnetic metals have been successfully produced using CVD, with the use of metallocenes as the most popular precursor. Reports have explored how to control the magnetic properties of these metal-filled MWCNTs, with the sublimation and pyrolysis temperatures being the key parameters that affect H_c and M_s. However, it is not fully understood how changing the synthesis parameters alters the chemical environment during the reaction, which ultimately governs CNT growth. *In situ* approaches to monitor the reaction in real time, using techniques such as *in situ* mass spectroscopy, provides information on the chemical environment, which could lead to a method to predict the outcomes of the synthesis, and hence control the materials produced (chapter two).

The magnetic properties of ferromagnetic metal-filled MWCNTs are limited by the intrinsic properties of the metal. In the bulk, this problem is overcome by forming alloys, leading to enhanced characteristics, such as magnetic or mechanical properties. Producing alloy-filled MWCNTs may extend the M_s and H_c of Fe@MWCNTs, leading to ferromagnetic

metal-filled MWCNTs with reliably controlled magnetic properties (chapter three).

Post-synthesis CNT processing allows their properties to be translated into macroscopic structures. BPs have been produced from a variety of methods, with vacuum filtration being one of the most explored techniques. Improvements have been made to the electrical conductivity and mechanical behaviour of these BP materials, with current methods capable of continuously producing BPs with high mechanical strength. The majority of work has focused on SWCNTs, DWCNTs and conventional MWCNTs. However, a wide range of other CNTs, such as metal-filled MWCNTs or doped MWCNTs, are available. BPs have yet to be produced from these materials and there is a large scope for investigating how using different types of MWCNTs affects the mechanical or electrical conductivity of BPs.

Chapter 2

In situ Mass Spectroscopy Study of Fe@MWCNT Growth

In this chapter, the production of Fe@MWCNTs was studied using a combination of ex situ and in situ techniques. In situ residual gas analysis (RGA) mass spectrometry (MS) was used to monitor the key fragments evolved during chemical vapour deposition (CVD) of Fe@MWCNTs using a ferrocene precursor. A systematic study was conducted to understand how changing the synthesis parameters altered the evolution of specific gases and identify how the parameters affected the materials produced.

2.1 Introduction

As mentioned in Chapter 1, CVD of Fe@MWCNTs using a ferrocene precursor is a well-established method, first reported by Sen *et al.* [7]. The magnetic properties of these Fe@MWCNTs were investigated, with enhanced coercivities compared to Ni and Co nanowires observed by Grobert *et al.* [41]. A systematic study carried out by Dillon *et al.* [40] revealed the dependence of M_s and H_c on the sublimation furnace temperature (T_{sub}) and pyrolysis furnace temperature (T_{pyro}), respectively. To continue developing our understanding and control of Fe@MWCNT growth, *in situ* techniques can be utilised to collect real time data during MWCNT growth.

A broad range of *in situ* techniques are available, which can give insight into the properties of the catalyst, the CNTs or the chemical environment during reaction. For example, environmental transmission electron microscopy (ETEM) allows for observation of the catalyst

during nucleation and growth of MWCNTs, providing insight into the MWCNT growth mechanisms [52, 155–158], whilst *in situ* Raman [159–161] and laser reflection interferometry [162–164] monitor MWCNT properties, such as length and structural quality.

Integrating mass spectroscopy (MS) into setups allows the chemical environment during MWCNT growth to be evaluated [25, 30, 165–168]. Meshot *et al.* [169] used a hot plate CVD setup with a pre-heater for C_2H_2. The gas composition showed significant increases in methane concentration by preheating C_2H_2 [169, 170], with relative abundances of some hydrocarbon species increasing by orders of magnitude with marginal changes in pre-heater temperature [169]. Meysami *et al.* [34] monitored the thermocatalytic behaviour of 15 hydrocarbon precursors used in aerosol assisted chemical vapour deposition (AACVD) at high and room temperature. Hydrogen, methane, ethene and benzene were main intermediate fragments found across all 15 precursors investigated, with significantly increases in their abundance by heating. Tian *et al.* [171] observed similar hydrocarbon fragments from coupled thermal analysis with MS (TA-MS) to study CVD MWCNT growth from benzene.

Whilst ferrocene is a commonly used precursor for CVD of Fe@MWCNTs, little is known about the thermocatalytic cracking of ferrocene, which could provide crucial information towards further understanding the growth mechanism for Fe@MWCNT. The kinetic behaviour of ferrocene during thermocatalytic cracking is not well understood, as it involves a combination of reactions that occur consecutively, in parallel and catalytically, with the products from decomposition catalysing further decomposition [172]. Studies by Dyagileva *et al* [172] revealed that the kinetic pyrolysis curve for up to 25 % ferrocene decomposition fitted a first order reaction, with a rate constant of $1.6\text{x}10^{-5}$ s^{-1}.

Lewis *et al.* [173] measured the thermal decomposition of ferrocene using a low-pressure pyrolysis method. The mechanism of decomposition followed Equation (2.1), and a rate constant of $2.19\text{x}10^{16}$ s^{-1} $e^{(-382\ kJ/mol/RT)}$ was obtained. No thermal decomposition occurred below *ca.* 850 °C [173].

$$Fe(C_5H_5)_{2(s)} \rightarrow Fe_{(l)} + 2C_5H_{5(g)} \tag{2.1}$$

However, Leonhardt *et al.* [8] state that ferrocene decomposition occurs at temperatures above *ca.* 500 °C following Equation (2.2) for growth of Fe@MWCNTs, although the equation was not backed up by experimental evidence.

$$Fe(C_5H_5)_{2(s)} \rightarrow Fe_{(l)} + C_5H_{5(g)} + CH_{4(g)} + H_{2(g)} + ... \quad (2.2)$$

Carrying out *in situ* MS studies during CVD of Fe@MWCNTs using ferrocene would provide insight into the thermocatalytic cracking of ferrocene and may further our understanding of the kinetics involved. This information can be used to enhance the quality and yield of the products, as well as the design aspects of future MWCNT CVD reactors. Monitoring the effect of altering the synthesis parameters on the chemical environment, i.e. changes in the gases evolved, is important, as the chemical environment ultimately controls the reaction taking place. The key parameters that influence Fe@MWCNT growth in a two-stage furnace are temperatures of T_{sub} and T_{pyro}, the distance between the furnaces, the identity and mass of the precursor, flow rate, and deposition time [58]. It is known that changing these parameters alters the material produced, with changes in T_{sub} controlling the nanomaterial produced [174], whilst increasing T_{pyro} increases Fe@MWCNT diameter [8, 40, 46, 175, 176]. The amount of filling, and the Fe-phase encapsulated depends on carrier gas flow rate [7], Boi *et al.* [177] reported higher flow rates decreased the relative abundance of Fe_3C in the filling. Dillon *et al.* [40] found the magnetic properties of Fe@MWCNTs was tuned by T_{sub} and T_{pyro}. H_c decreased with increasing T_{pyro}, whist the M_s was strongly affected by variations in T_{sub}.

This chapter studies Fe@MWCNTs growth using a combination of *ex situ* and *in situ* methods to simultaneously gain an improved understanding of the chemical environment during CVD and optimise the growth conditions. It aims to answer questions regarding the thermocatalytic cracking of ferrocene by using *in situ* RGA MS to monitor the species evolved during the reaction.Identifying the exhaust fragments produced during CVD allows us to establish how ferrocene cracks during pyrolysis. By studying the fragments produced, we can identify the intermediate hydrocarbon fragments responsible for CNT growth. The effect of changing the synthesis parameters on the evolution of gases, detected in MS, was investigated and attempts were made to correlate this to the properties of the material produced, such as their magnetic properties, morphology and their defectiveness.

2.2 Experimental

This section first discusses the procedure followed to obtain furnace temperature profiles of the sublimation and pyrolysis furnaces. These profiles provided invaluable information on the plateau regions of the furnace, and established the ideal gap between the two furnaces. The method used for producing Fe@MWCNTs, with MS attached is covered, as well as the parameters investigated in the systematic study.

2.2.1 Furnace Temperature Profiles

The sublimation and pyrolysis furnaces were set to 300 and 800 ° C, respectively. Individual temperature profiles were measured with furnace gaps of 0 to 5 cm, in 1 cm gap intervals. The temperature was taken every 0.5 cm along the entirety of both furnaces, including the gap using a thermocouple. For accuracy, the thermocouple was allowed to stabilise for *ca.* 1 minute between readings. Measurements were taken in open air. Temperature readings were repeated three times.

2.2.2 Procedure for Synthesis of Fe@MWCNTs

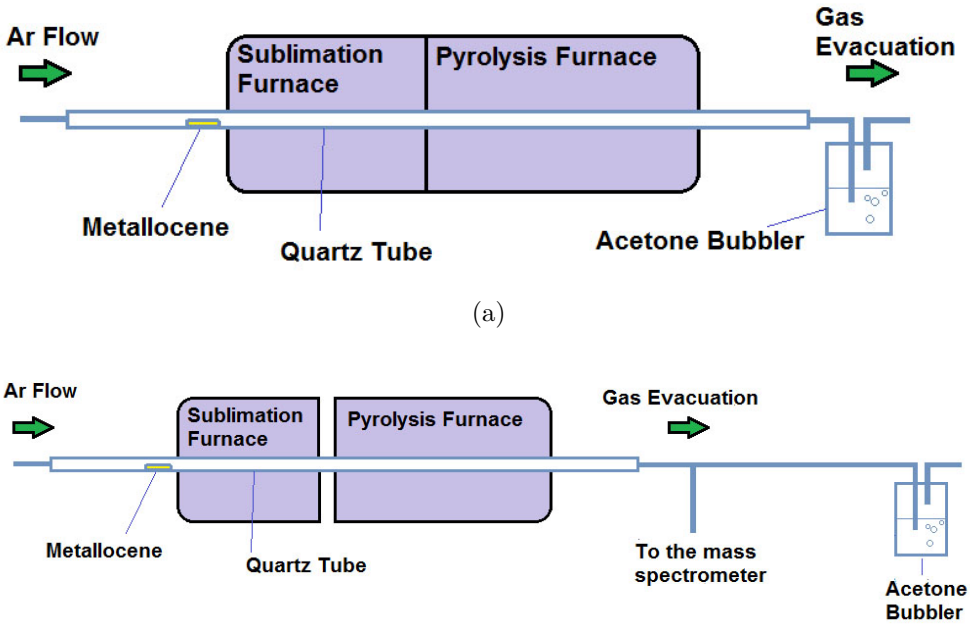


Figure 2.1: Schematics showing a) the basic setup used for CVD growth of Fe@MWCNTs and b) the modified setup for experiments with *in situ* MS. The lengths of the furnaces are 21 and 31 cm for the the sublimation and pyrolysis furnaces, respectively.

Figure 2.1a shows the basic setup for producing Fe@MWCNTs using a two stage furnace (INSTRON SFL), of lengths 21 and 31 cm, for the sublimation and pyrolysis furnaces, respectively. New quartz tubes of diameter 2 cm and length 80 cm were used as the reaction chamber. Ferrocene was weighed into a crucible and placed in the quartz tube 13.5 cm along. A marking at 3 cm ensured that the ferrocene was in the centre of the sublimation zone when the quartz tube was slid into the furnace. The quartz tube was attached to the gas line, and connected at the other end to an acetone trap.

The system was flushed with Ar at 1 SLM, controlled by a mechanical gas flow controller, for 5 minutes prior to switching the furnaces on. The furnaces were set to the required temperatures and the Ar flow was decreased to 100 sccm during heating. The precursor remained out of the furnace during heating to ensure it did not sublime before the furnaces were at the desired temperature. Once the furnaces were at temperature, the Ar flow was set to the required value and the quartz tube was slid into the furnace up to the 3 cm mark. After the 10 minute reaction time, the furnace was switched off and cooled under 100 sccm Ar flow to room temperature.

2.2.3 Monitoring Synthesis with Mass Spectrometry

A Hiden Analytical Quadrupole Mass Spectrometer (MS) (HPR-20 *QIC* was used to monitor the progress of the reaction (Figure 2.1b). The MASsoft *Professional* software programmed to obtain mass spectra in the range of 1-200 mass-to-charge ratio (m/z) and to monitor O_2, Ar, H_2 and a background scan, over the course of the experiments. The different m/z ratios were filtered and counted by a Faraday cup.

The vacuum on the MS was kept between 2-3 x10^{-6} Torr. Prior to heating, the MS was used to check the system was leak free by ensuring N_2 (28 m/z) and O_2 (36 m/z) had a lower abundance than ^{36}Ar isotope, which has a natural abundance of 0.334 %. The data was processed to establish the rate of H_2 evolution.

The Ar flow, furnace gap, T_{sub} and T_{pyro} were varied systematically (Table 2.1) to understand how they affected evolution of H_2 over the course of the reaction.

Label	Ar Flow/ sccm	Furnace Gap/ cm	T_{sub}/ °C	T_{pyro}/ °C
A52	50	2	200	750
B52	50	2	200	850
C52	50	2	250	750
D52	50	2	250	850
A53	50	3	200	750
B53	50	3	200	850
C53	50	3	250	750
D53	50	3	250	850
A12	100	2	200	750
B12	100	2	200	850
C12	100	2	250	750
D12	100	2	250	850
A13	100	3	200	750
B13	100	3	200	850
C13	100	3	250	750
D13	100	3	250	850

Table 2.1: The experimental parameters investigated in the systematic study carried out in conjunction with monitoring H_2 evolution. The labelling system indicates: A) 200/ 750, B) 200/ 850, C) 250/ 750, and D) 250/ 850 °C for T_{sub} and T_{pyro}, respectively. The first number (i.e. A**5**2-200) corresponds to 5) for 50 and 1) for 100 sccm Ar flow. The second number (i.e. A5**2**-200) corresponds to 2) 2 cm and 3) 3 cm furnace gap. All syntheses were carried out for 10 minutes, with 200 mg of ferrrocene precursor.

2.2.4 Characterisation

The JEOL-840F SEM, operated at 5 V, was used to investigate the morphology of the materials produced. The internal structure and Fe@MWCNT diameter was imaged using the JEOL-2100, operated at 200 kV

Superconducting quantum interference device (SQUID) measurements were carried out using the Quantum Design MPMS®3 at 4 K to investigate the magnetic properties of all samples produced in the systematic study. The SQUID sample preparation was carried out as follows; *ca.* 1 mg of sample was placed on a pre-weighed square of aluminium foil (*ca.* 2 cm x 2 cm). The foil was folded to encase the sample and slid into a straw to a

set position. The straw was capped at both ends and screwed onto the sample mount, which was placed into the SQUID. The MPMS®3 Multivu software was used to program the measurement conditions.

Thermogravimetric analysis (TGA) was performed using a PerkinElmer®Pyris 1 thermogravimetric analyser on *ca.* 5 mg of sample to estimate the relative abundance of Fe and Co in the sample. The measurements were carried out between 50 to 900 °C, under a synthetic air flow of 80 ml/min.

2.3 Results and Discussion

2.3.1 Furnace Gap

Mapping the furnaces was carried out to find the ideal temperature profiles for both furnaces before the systematic studies. The ideal profile has two independently controllable furnace profiles with a minimal temperature decrease in the gap between the furnaces; too large a temperature decrease could lead to condensation and recrystallisation of the sublimed ferrocene. This behaviour is not desirable as it would cause an uneven flow rate of ferrocene vapour, as well as reducing the mass of ferrocene that is available for pyrolysis. Mapping the furnace temperature profiles with 0-5 cm distances between the sublimation and pyrolysis furnace revealed the large influence T_{pyro} had on T_{sub} (Figure 2.2a). With a 0 cm furnace gap, the clear incline in T_{sub} means that the set furnace temperature will not be the actual temperature of the furnace. To achieve controllable synthesis temperatures, T_{sub} has to be independent of T_{pyro}.

The individual furnace temperatures profiles are independent with furnace gaps of 4 and 5 cm (Figure 2.2e and f). However, the temperature at the end of the sublimation furnace starts to decrease, with further decreases in temperature to *ca.* 50 °C within the furnace gap region with a 5 cm gap (Figure 2.2f). At this lower temperature, some sublimed ferrocene may condense between the two furnaces, which is undesirable. The ideal furnace gap is likely to be either 2 or 3 cm; the majority of T_{sub} is constant with minimal temperature decrease in the gap. To further limit the temperature decrease between the two furnaces, insulating material was wrapped around the quartz tube between the two furnaces.

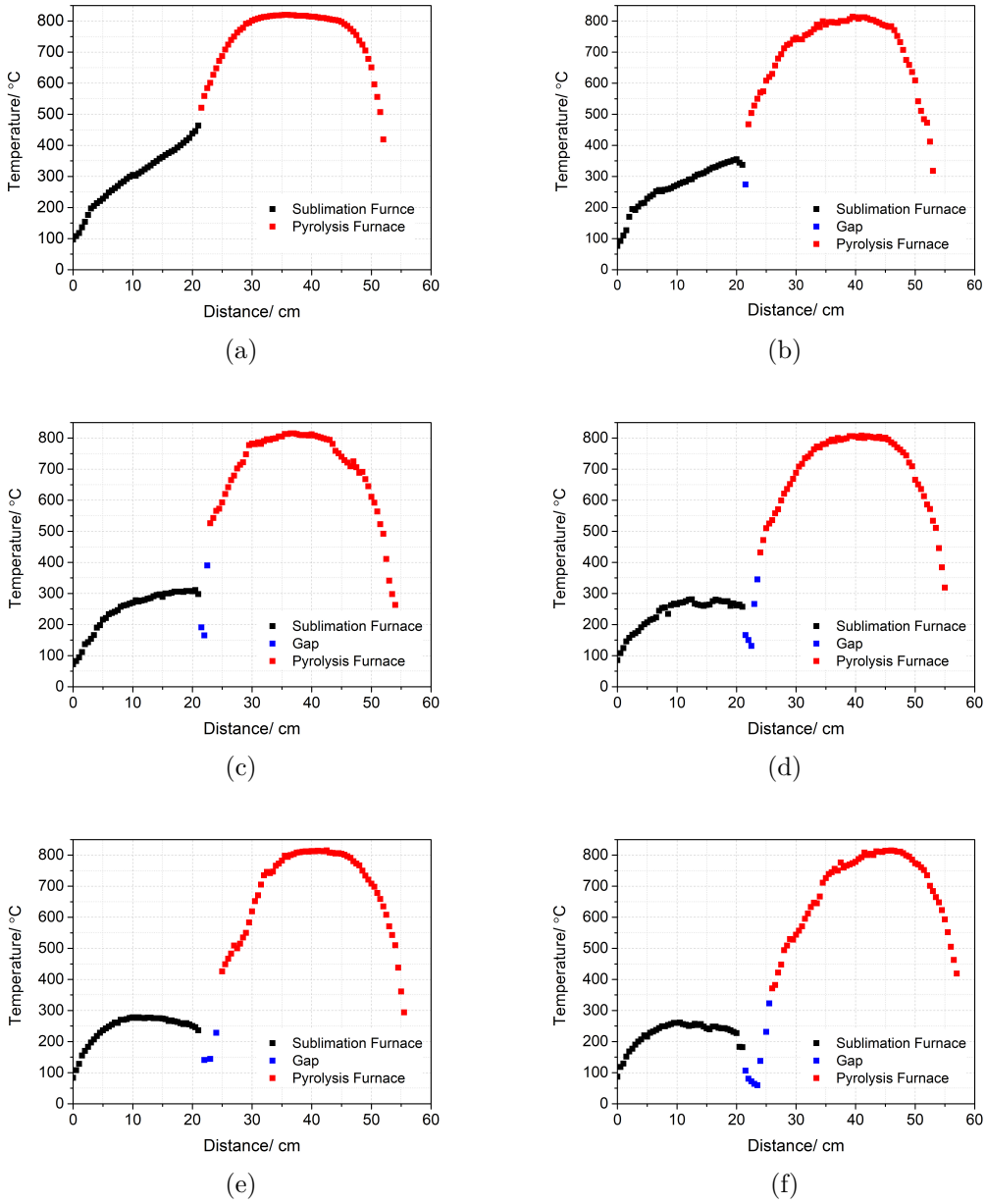
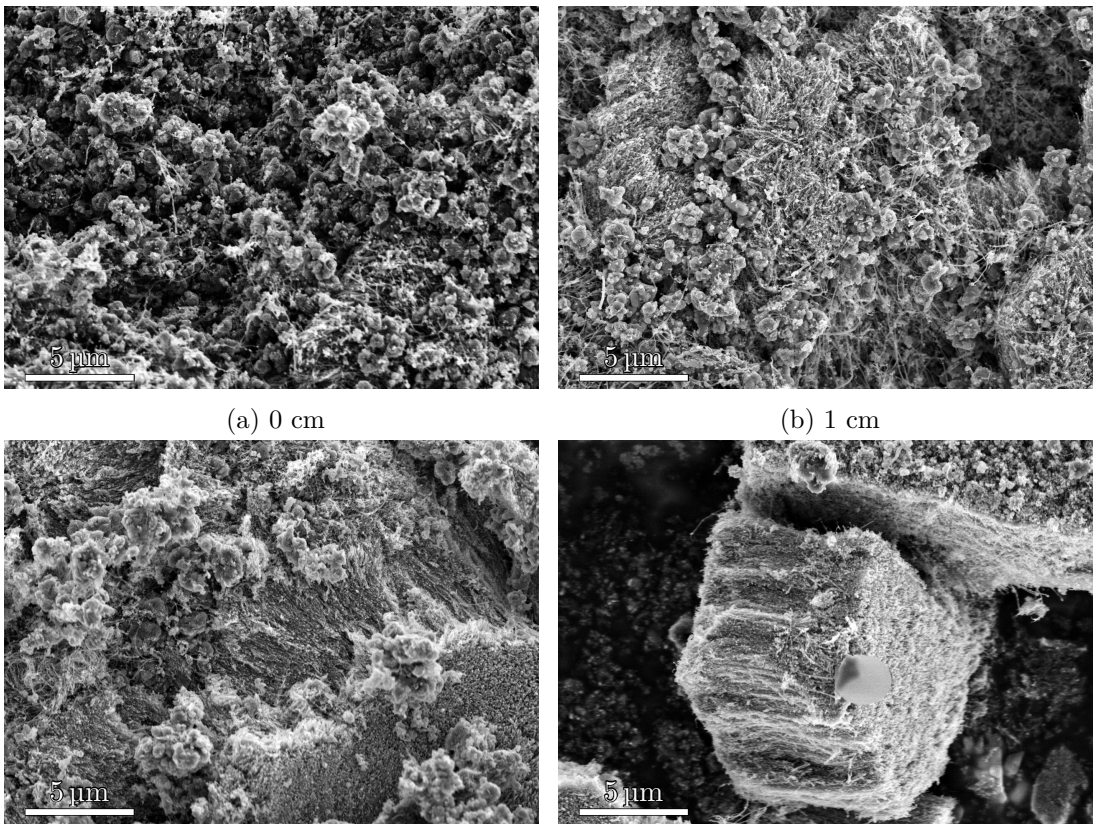


Figure 2.2: Graphs showing the furnace temperature profiles obtained with the distances of a) 0 cm, b) 1 cm, c) 2 cm, d) 3 cm, e) 4 cm, and f) 5 cm between the sublimation and pyrolysis furnaces.

The effect of furnace gap (0-3 cm) on the products from CVD is highlighted for syntheses carried out at T_{sub} and T_{pyro} of 250 and 750 °C, respectively, under an Ar flow of 100 sccm (Figure 2.3). Increasing the furnace gap reduces the amount of agglomerate material produced at 0 cm (Figure 2.3a), with the MWCNTs appearing to be more aligned with 2 and 3 cm furnace gaps. Whilst a 1 cm furnace gap produced MWCNTs, the sublimation furnace temperature was affected by the pyrolysis furnace (Figure 2.2 b). As the sublimation temperature could not accurately be controlled, the furnace gap of 1 cm was not studied further.



(a) 0 cm (b) 1 cm

(c) 2 cm (d) 3 cm

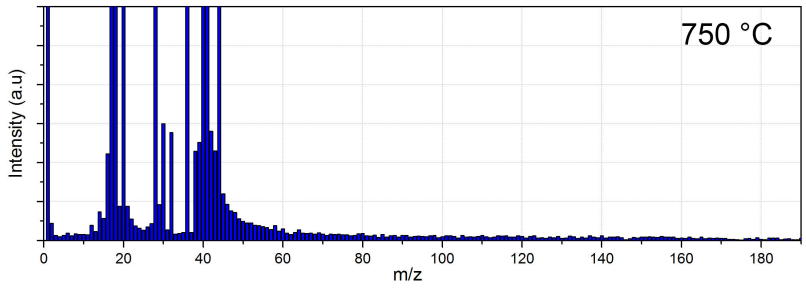
Figure 2.3: SEM images showing the material produced from syntheses with a gap between the sublimation and pyrolysis furnaces of a) 0 cm, b) 1 cm, c) 2 cm, and d) 3 cm. As observed, the syntheses produced high amount of agglomerates with varying amounts of MWCNTs.

2.3.2 Mass Spectrometry

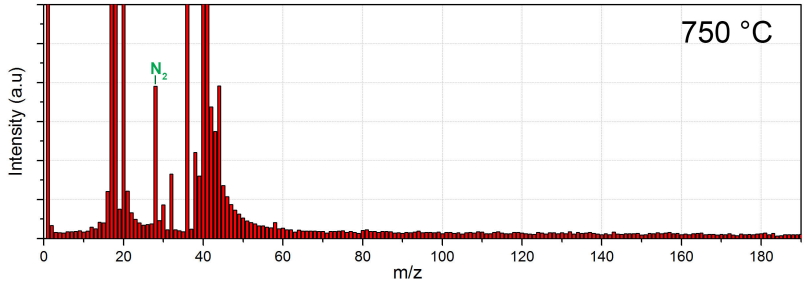
Full residual gas analysis (RGA) mass spectra scans were collected for ferrocene pyrolysis at T_{sub} of 250 °C and T_{pyro} of 750 and 850 °C (Figure 2.4 and Figure 2.5). Full RGA mass spectra were not collected for T_{sub} of 200 °C as T_{sub} is unlikely to have a significant effect on ferrocene pyrolysis. A higher T_{sub} may result in a higher concentration of ferrocene molecules in the pyrolysis furnace which could lead to a larger range of fragments and higher reaction rates [178], however the key pyrolysis fragments are not likely to change. Collecting full RGA mass spectra for all experiments and conducting a complete analysis of each individual fragment formed under different conditions was beyond the scope of this investigation.

The RGA mass spectra collected during ferrocene pyrolysis was compared to the standard mass spectrum of ferrocene at room temperature (Figure 2.6) [179]. The spectra obtained at room temperature and during pyrolysis show significant differences; the fragments obtained at room temperature are caused by ionisation-induced fragmentation inside the ion source of the mass spectrometer. At high temperature, the fragments are a result of ferrocene pyrolysis in the reactor. The absence of the molecular ion peak for ferrocene (128 m/z) indicates that pyrolysis occurs very quickly, and that ferrocene is unable to escape the pyrolysis furnace unreacted. The peak at 186 m/z is indistinguishable from the background noise. By comparing spectra at room and high temperature, the fragments caused by ionisation-induced cracking can be excluded. The main fragments observed at room temperature (Figure 2.6) are of very low abundance at high temperature.

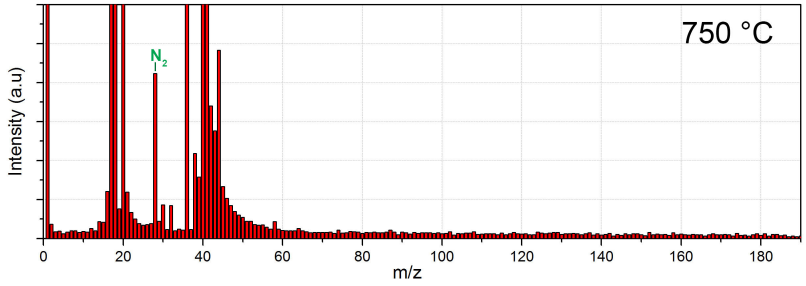
Background scans were taken whilst purging the reaction vessel prior to heating the furnace (Figure 2.4a and Figure 2.5a), to check that the setup was not leaking and to identify which peaks arose during pyrolysis. Table 2.2 shows the peaks that were identified in the background, these peaks are also present in the MS collected during ferrocene pyrolysis. The peaks at 17 and 18 m/z correspond to adsorbed water inside the fused silica capillary of the analyte transfer line and the stainless steel fittings that attach the transfer line to the quartz reactor. To minimise the adsorbed water signal, the capillary line was heated using a DC generator to >150 °C.



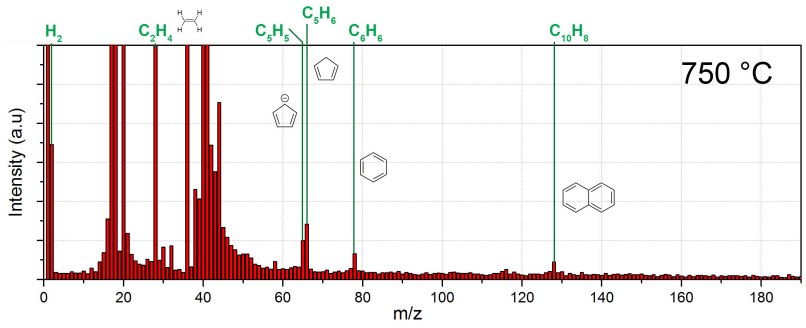
(a) Background



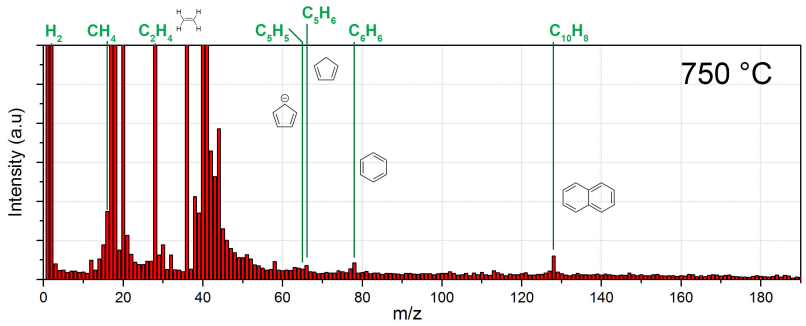
(b) 0.08 mins



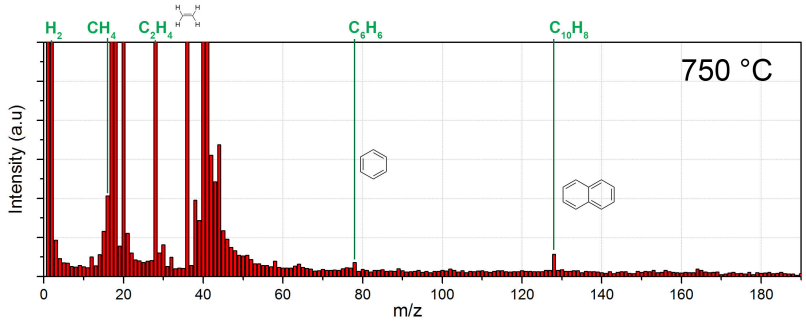
(c) 1.34 mins



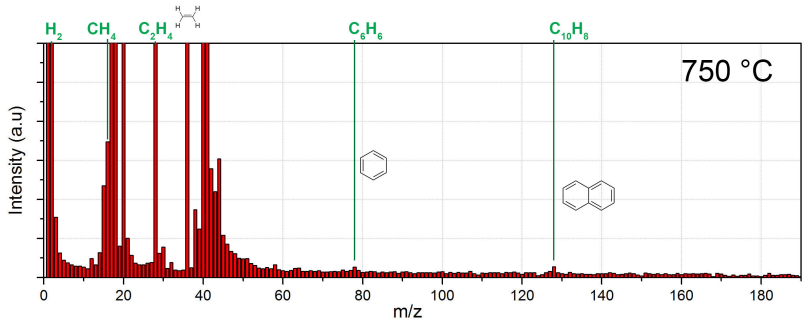
(d) 3.01 mins



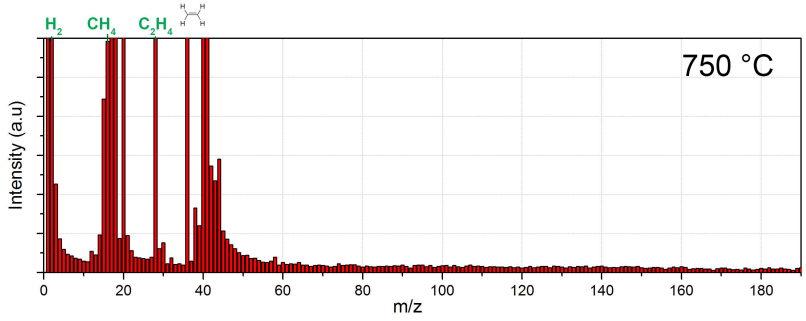
(e) 4.27 mins



(f) 5.54 mins

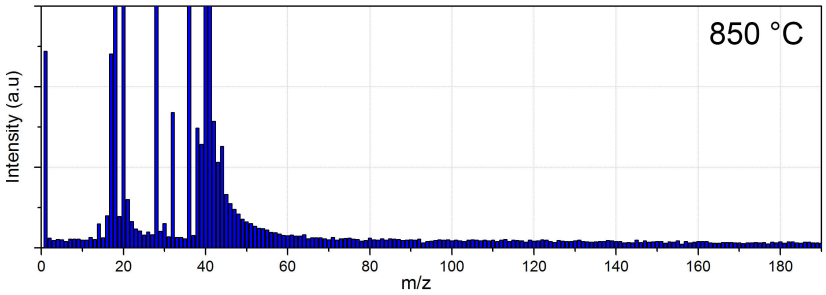


(g) 7.20 mins

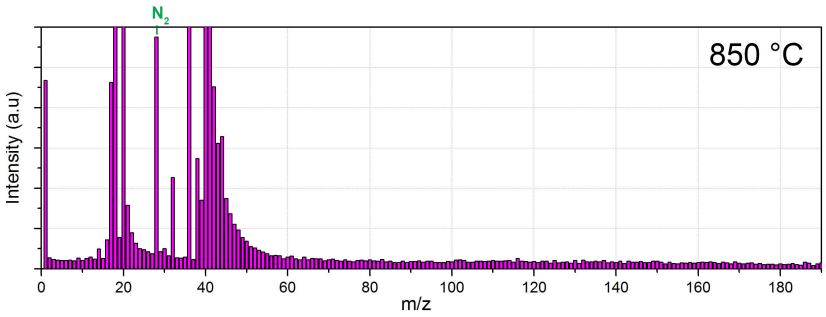


(h) 8.47 mins

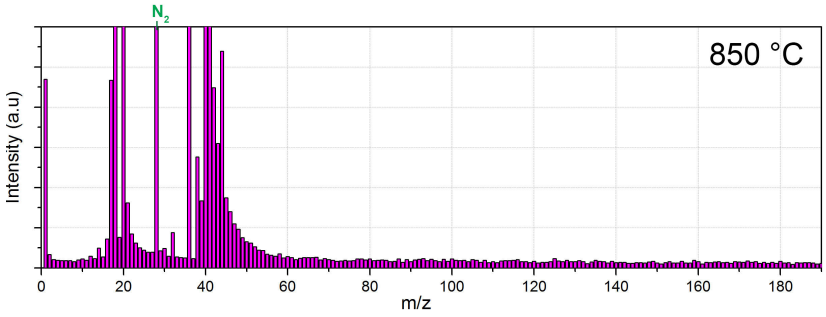
Figure 2.4: MS scan cycles from synthesis carried out with a pyrolysis temperature of 750 °C for a) background scan, taken whilst purging the furnace with Ar at room temperature, b) 0.08, c) 1.34, d) 3.01, e) 4.27, f) 5.54, g) 7.20, h) 8.47 minutes into the reaction.



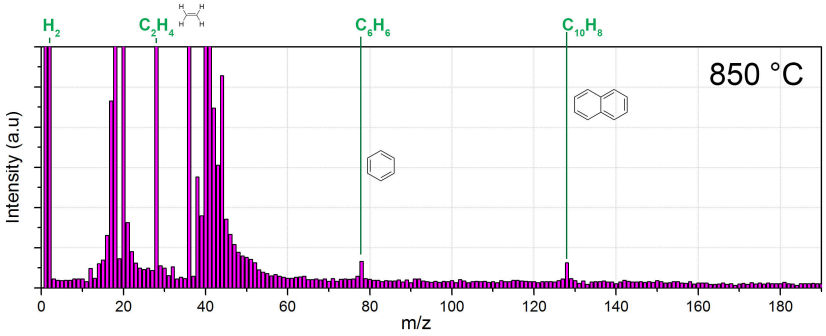
(a) Background



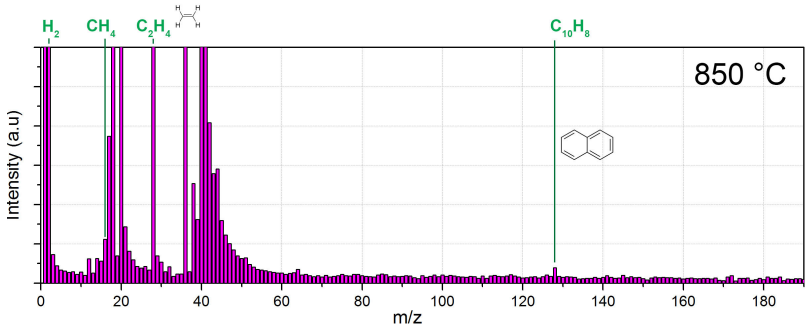
(b) 0.10 mins



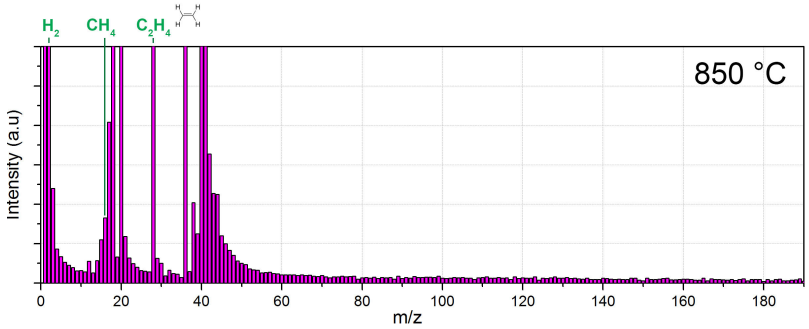
(c) 1.41 mins



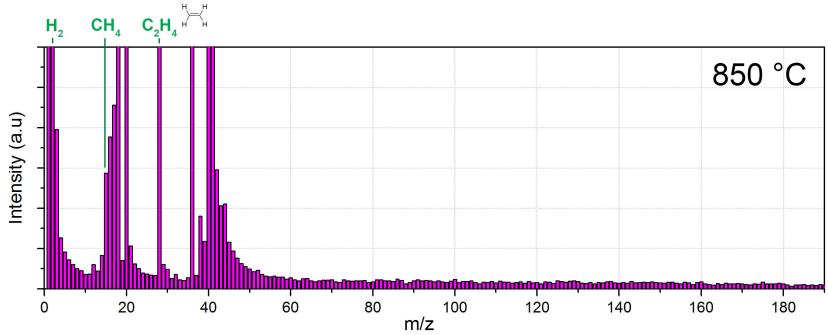
(d) 3.12 mins



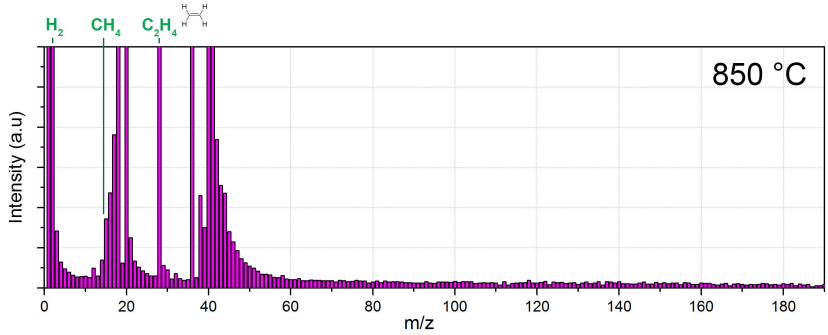
(e) 4.42 mins



(f) 6.13 mins



(g) 7.44 mins



(h) 9.15 mins

Figure 2.5: MS scan cycles from synthesis carried out with a pyrolysis temperature of 850 °C for a) background scan, purging with Ar, b) 0.10, c) 1.41, d) 3.12, e) 4.42, f) 6.13, g) 7.44, h) 9.15 minutes into the reaction.

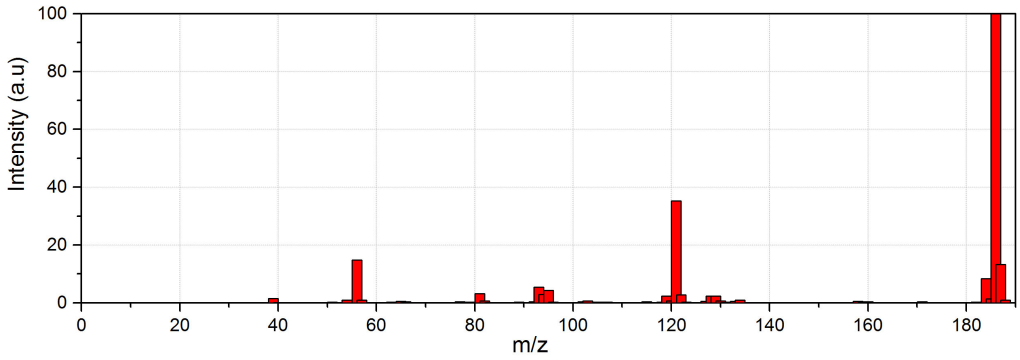


Figure 2.6: Mass spectrum for ferrocene, taken at room temperature from the NIST database [179].

m/z	**Possible Formula**
2	H_2
17 and 18	adsorbed water
20	doubly ionised Ar
28	N_2
32	O_2
36, 38 and 40	Ar isotopes
44	CO_2

Table 2.2: Identification of the peaks that arise in the background MS scan.

Transfer of the analytes from the exhaust of the CVD reactor, along the capillary line to the Faraday detector typically took less than a second. Running each MS scan in the range of 1-200 m/z at a high resolution, with a 10^{-8} Torr detection limit took *ca.* 86 seconds. As each CVD reaction was carried out for 10 minutes, this allowed for seven scans to be obtained within the reaction time. Striking a balance between scan resolution and the length of time per scan was crucial to allow for a low noise to signal ratio, whilst having as many cycles as possible within the timeframe to monitor the species released in the exhaust. The Hiden Analytical HPR-20 QIC quadrupole mass spectrometer has a detection limit of 5 parts per billion. Figure 2.4b-h and Figure 2.5b-h show the RGA mass spectra obtained, identifying the species released during CVD at T_{pyro} 750 and 850 °C, respectively. The key intermediate fragments for the thermocatalytic cracking of ferrocene are labelled in the mass spectra. The first two mass spectra scans (b and c) for both pyrolysis temperatures show no significant species are evolved. This delay

is likely to be due to the time taken for the ferrocene to reach the temperature of the sublimation furnace, sublime, and then travel to the pyrolysis furnace under the Ar flow. Once in the pyrolysis furnace, the ferrocene has to then break down and form Fe particles, releasing hydrocarbons simultaneously. However, as no ferrocene molecules are detected, the pyrolysis of ferrocene is very quick. As ferrocene decomposes at temperatures >500 °C [172], the delay is likely to be related to ferrocene reaching sublimation temperature and travelling to the pyrolysis furnace.

The most notable heavier hydrocarbon species (>60 m/z) observed in the mass spectra at both pyrolysis temperatures are naphthalene (128 m/z) and benzene (78 m/z). The peak at 128 m/z could also correspond to propylbenzene, however the likelihood of this is small considering the higher structural stability and lowered energy through electron conjugation of naphthalene. However, labelling the molecular ion peaks for naphthalene compared to propylbenzene based solely on their fragmentation signature is not entirely accurate as RGA involves pyrolysis-induced fragmentation, rather than from electron ionisation alone. The benzene peak (78 m/z) is likely to be formed by thermocatalytic cracking of naphthalene inside the pyrolysis furnace, and not by electron ionisation from the mass spectrometer, as evidenced by the abundance of benzene in the standard mass spectrum of naphthalene being not as significant as in the RGA obtained for both pyrolysis temperatures during the CVD reaction. Meysami *et al.* [34] studied the mass spectra obtained for thermocatalytic cracking of 5 wt% ferrocene dissolved in a range of cyclic, acyclic and aromatic hydrocarbons in AACVD of MWCNTs. The peak at 128 m/z was detected for solvents such as methylcyclohexane, 1,2,4-trimethylbenzene and isopropylbenzene and assigned as C_9H_{20}. It is unlikely that the peak at 128 m/z is C_9H_{20} due to the limited abundance of H_2 in ferrocene alone, which would be insufficient to account for the large increase in H_2 evolved during CVD and formation of C_9H_{20}. Further, naphthalene has been reported as a species formed during pyrolysis of cyclopentadiene [178].

The mechanism for naphthalene formation from ferrocene is not understood. However, the catalytic formation of benzene from a range of acyclic and monocyclic saturated hydrocarbon solutions was reported by Meysami *et al.* [34], reflecting the high structural stability of benzene. It is interesting that the key fragments detected in this study are the same as for pyrolysis of ferrocene alone, with the presence of the peak at 78 m/z, for all hydrocarbon solutions investigated [34]. This may suggest that ferrocene, the only constant species in all the hydrocarbon solutions surveyed, is primarily responsible for

the consistent peaks detected in this study. Whilst the mechanism for benzene formation was not elucidated, it was suggested that it may involve recombination of fragments and radicals. A similar mechanism is likely to be responsible for the formation of benzene and naphthalene observed here.

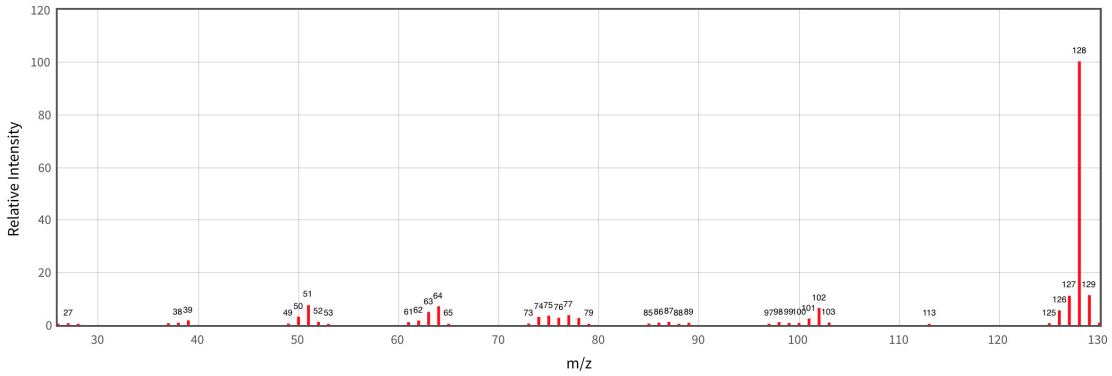


Figure 2.7: Mass spectrum for naphthalene, taken at room temperature from the NIST database [180].

Peaks at 65 and 66 m/z are also present in the mass spectra for a pyrolysis temperature of 750 °C (Figure 2.4d and e). The peak at 66 m/z is likely to correspond to cyclopentadiene, rather than cyclopropylacetylene due to the high ring strain in 3 membered rings [181], as well as cyclopentadiene being the hydrocarbon in the organometallic ferrocene compound. The peak at 65 m/z is likely to be cyclopentadienyl. Despite naphthalene and benzene fragments being present in mass spectra for both pyrolysis temperatures, cyclopentadiene and cyclopentadienyl are not detected at 850 °C. The absence of these peaks at 65 and 66 m/z at a pyrolysis temperature of 850 °C could be due to the shorter lifetime of cyclopentadiene at higher temperatures, which reacts quickly to form benzene and naphthalene. Djokic *et al.* [178] found that temperature and dilution of cyclopentadiene has a direct impact on the reaction rates of its conversion to other hydrocarbons, with benzene, naphthalene and indene being key products. At temperatures of 850 °C, the mass fraction of cyclopentadiene decreased significantly (*ca.* 35 %), whilst the mass fraction of naphthalene, indene and benzene increased (Figure 2.8). At 750 °C, a much larger mass fraction of cyclopentadiene was observed (*ca.* 90 %), which explains why cyclopentadiene was detected in the RGA for a pyrolysis temperature of 750 °C, but not for 850 °C.

Exhaustion of these heavier fragments occurred much quicker at a T_{pyro} of 850 °C (present Figure 2.5d and e), compared to 750 °C (present Figure 2.4d-g). The shorter time period for detection of these heavier fragments at 850 °C is likely because of the faster thermo-

catalytic cracking of these heavier fragments at the elevated T_{pyro}.

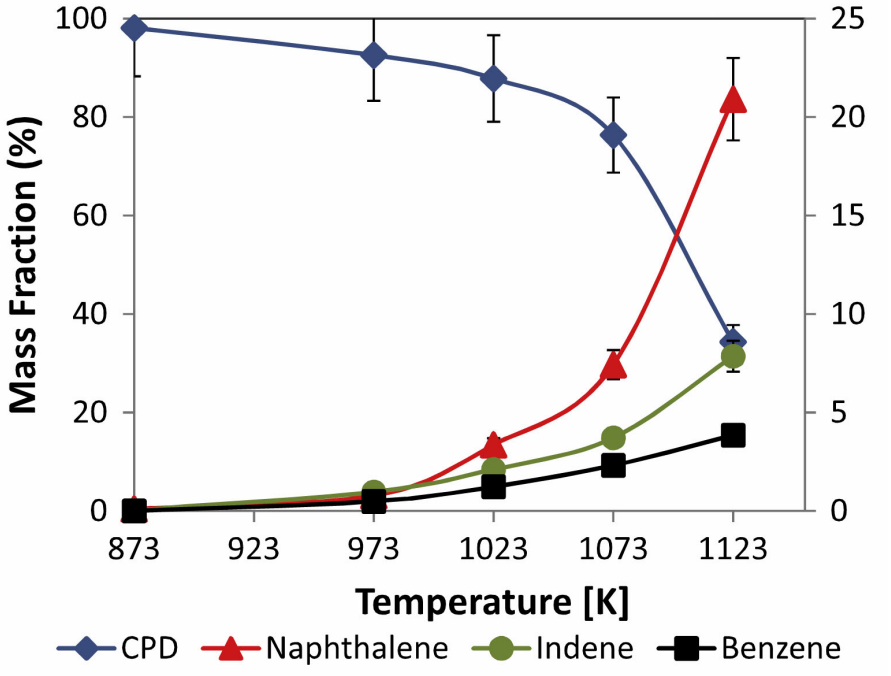
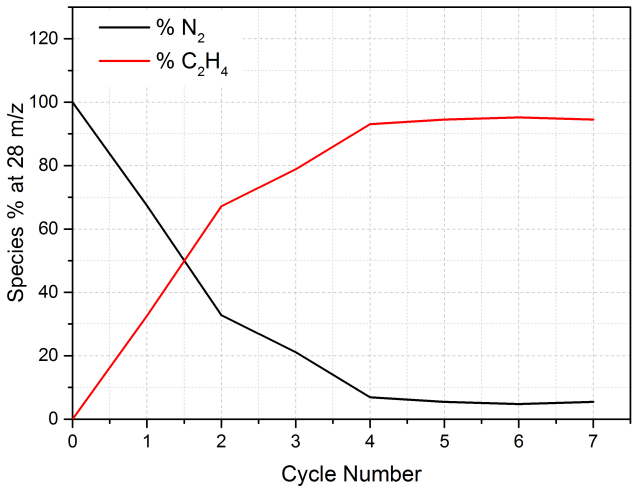


Figure 2.8: Normalised mass fractions of cyclopentadiene and major products (indene, benzene and naphthalene) as a function of temperature [178].

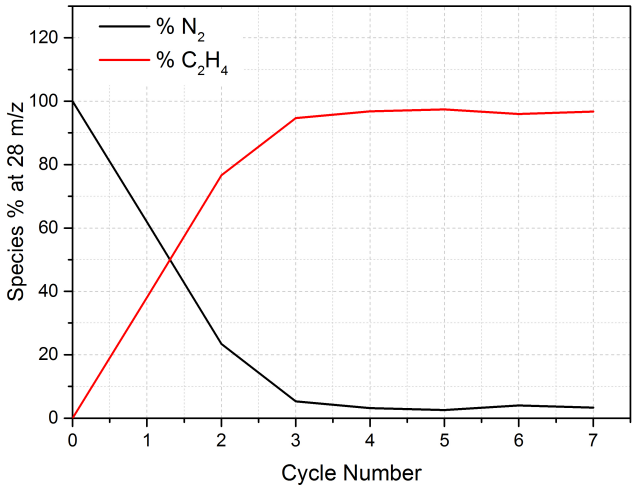
Initially, the peak at 28 m/z corresponds to N_2 from the atmosphere, however, during CVD, the abundance of O_2 and N_2 that leaked into the system declined significantly. This is particularly evident from the time resolved molecular ion peak for O_2 at 32 m/z. Conversely, the peak at 28 m/z increases in abundance over the course of the reaction, which is attributed to release of C_2H_4 from ferrocene pyrolysis. C_2H_4 has previously been reported to be an important hydrocarbon in AACVD of MWCNTs, along with CH_4 and benzene [34]. As the system is not completely leak free, the peak at 28 m/z could be from N_2 or C_2H_4, hence it was necessary to calculate the partial pressures of both components. The relative % of N_2 (28 m/z) and C_2H_4 (32 m/z) was estimated by comparing the ratio of O_2 and N_2 from atmospheric MS scans to the ratio of the same peaks obtained from the RGA of the reaction.

The % contributions of N_2 and C_2H_4 to the peak at 28 m/z was plotted against cycle number for both pyrolysis temperatures (Figure 2.9). The relative % of C_2H_4 increases significantly over the course of the CVD reaction, such that the peak at 28 m/z is predominantly C_2H_4 by MS cycle 4 and 3 with T_{pyro} of 750 and 850 °C, respectively. It should be noted that the absolute quantity of N_2 leaking into the system remains constant, however the partial pressure of N_2 decreases in Figure 2.9 because of the evolution

of C_2H_4, which dilutes the N_2 contribution to the peak at 28 m/z. Figure 2.9 shows that the amount of C_2H_4 increases rapidly over the first 3-4 cycles (*ca.* 3-5 mins of the reaction), before reaching a plateau. The amount of C_2H_4 does not decrease towards the end of the reaction. This observation of high C_2H_4 abundance despite full consumption of ferrocene, indicated by exhaustion of benzene and naphthalene (Figure 2.4h and Figure 2.5f-h), implies that Fe@MWCNT growth could have been sustained even after full ferrocene evaporation.



(a) 750 °C

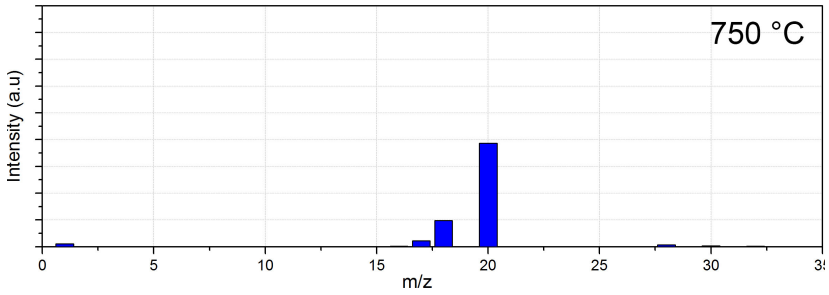


(b) 850 °C

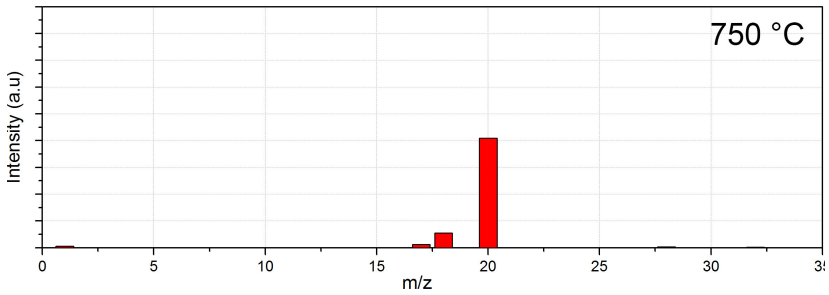
Figure 2.9: Graphs showing the % abundance of N_2 and C_2H_4 (partial pressure) making up the peak at 28 m/z in the MS scans per cycle for a pyrolysis temperature of a) 750 °C and b) 850 °C.

The lightest hydrocarbon fragments observed in the RGA mass spectra obtained at both pyrolysis temperatures are methane (16 m/z) and methyl (15 m/z). The abundance of these light hydrocarbon fragments increases towards the end of the reaction (Figure 2.4e-h and Figure 2.5e-h). Interestingly, these lighter hydrocarbon fragments are not as abundant at T_{pyro} of 850 °C, compared to 750 °C. This increase in abundance of lighter hydrocarbons coincides with the progressive exhaustion of the heavier hydrocarbon fragments, thus indicating that the heavier hydrocarbons are effectively cracked down to form simple carbon species that are required for bottom-up synthesis of sp^2 carbon nanomaterials [182–185].

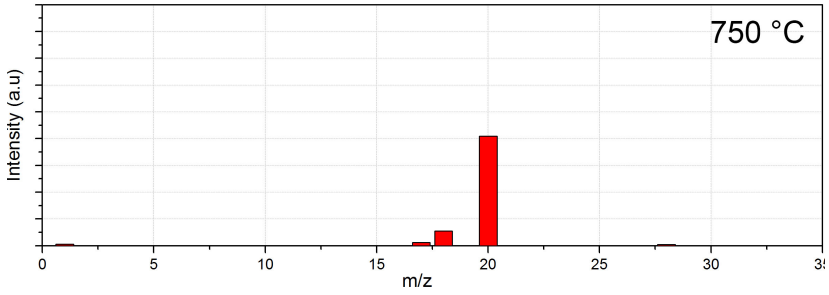
H_2 and C_2H_4 showed the largest increase in abundance over the course of the CVD reaction. Figure 2.10 and Figure 2.11 show close up mass spectra in the region of 0-35 m/z and highlights the substantial increase in H_2 for both T_{pyro} over the duration of the syntheses. H_2 and C_2H_4 do not follow the same evolution trends; whilst C_2H_4 reaches a plateau towards the end of the reaction, H_2 evolution continues to increase through to the end of the reaction at T_{pyro} of 750 °C. With a T_{pyro} of 850 °C, there was a decrease in the abundance of both H_2 and CH_4 released at 9.15 mins (Figure 2.11h and Figure 2.5h). This decrease in H_2 could suggest a decrease in Fe@MWCNTs growth, as H_2 is only released once C has adsorbed onto the surface of the catalyst particles. The similar decrease in abundance of both H_2 and CH_4 could imply that the evolution of H_2 is strongly effected by the abundance of CH_4 which could be the dominant species from which H_2 is released.



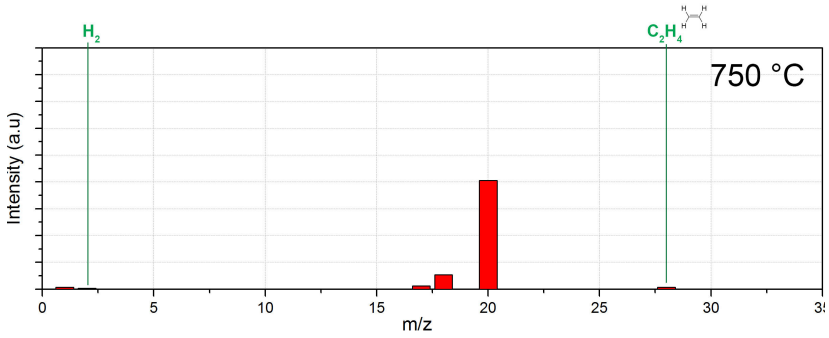
(a) Background



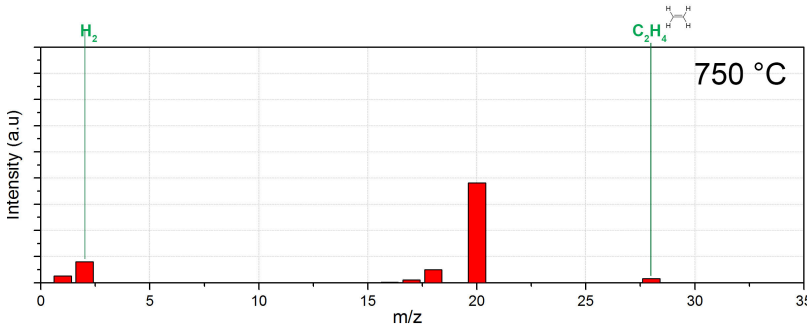
(b) 0.08 mins



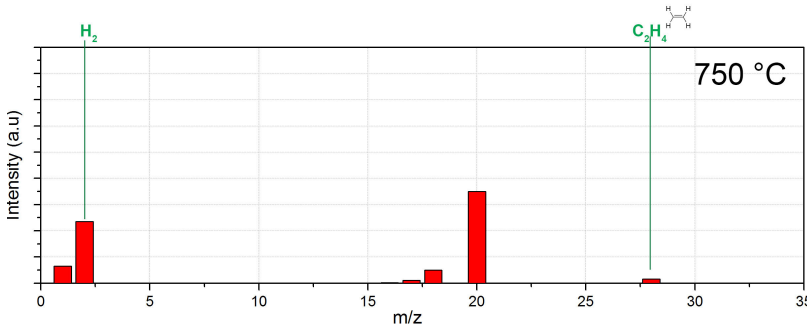
(c) 1.34 mins



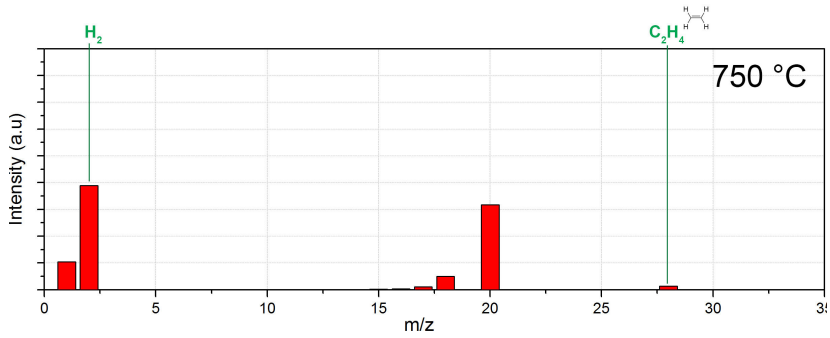
(d) 3.01 mins



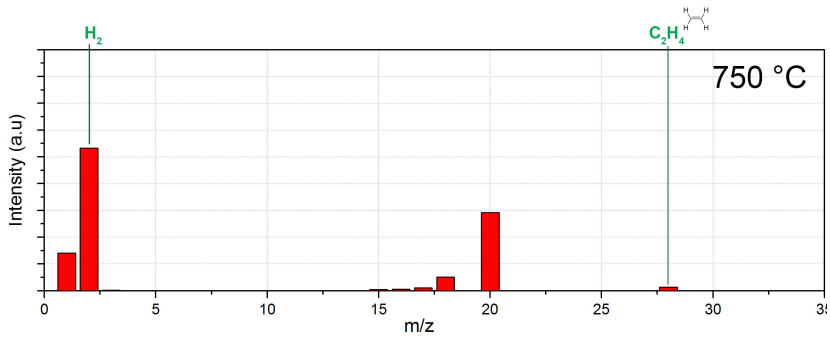
(e) 4.27 mins



(f) 5.54 mins

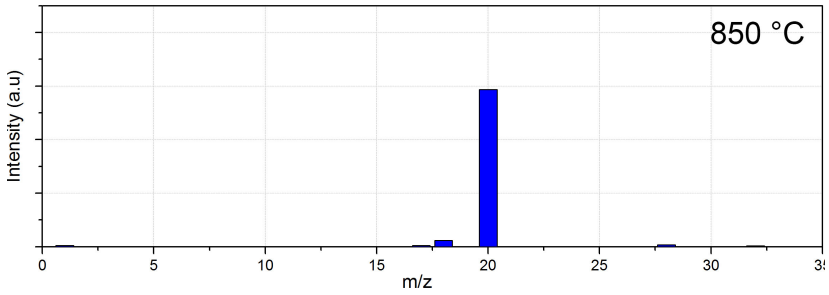


(g) 7.20 mins

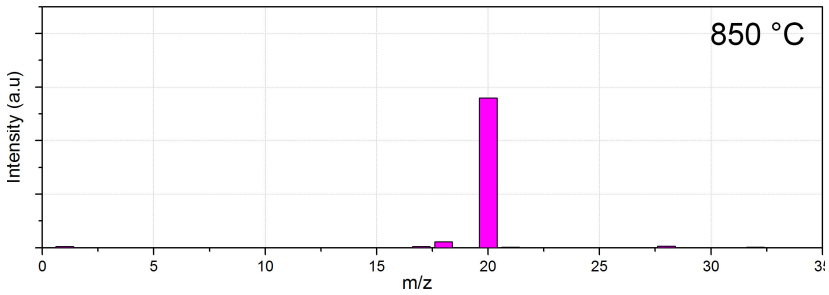


(h) 8.47 mins

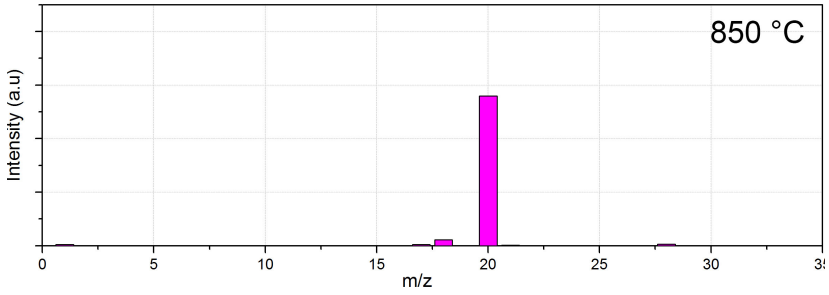
Figure 2.10: Zoomed in MS scan cycles from synthesis carried out with a pyrolysis temperature of 750 °C for a) background scan, purging with Ar, b) 0.08, c) 1.34, d) 3.01, e) 4.27, f) 5.54, g) 7.20, h) 8.47 minutes into the reaction..



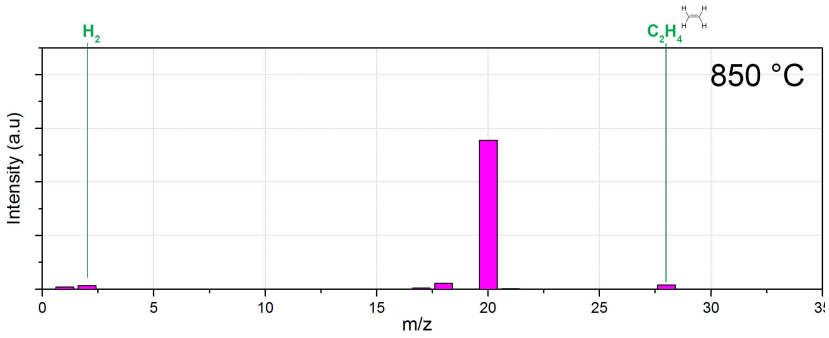
(a) Background



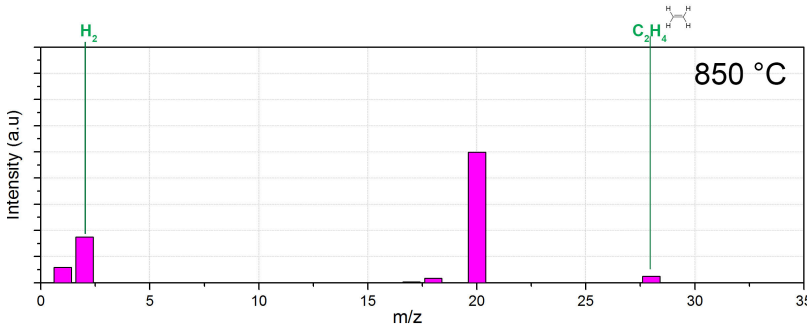
(b) 0.10 mins



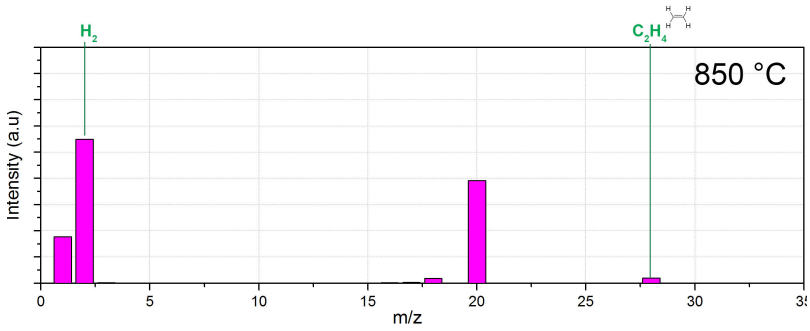
(c) 1.41 mins



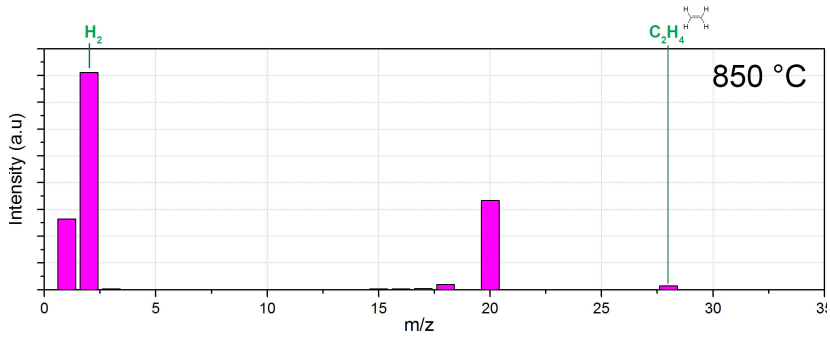
(d) 3.12 mins



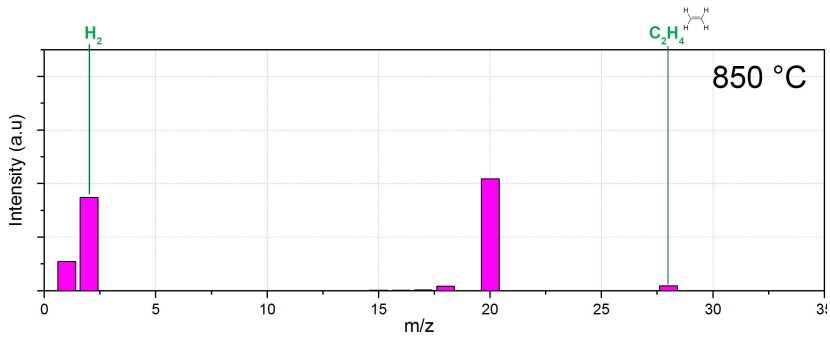
(e) 4.42 mins



(f) 6.13 mins



(g) 7.44 mins



(h) 9.15 mins

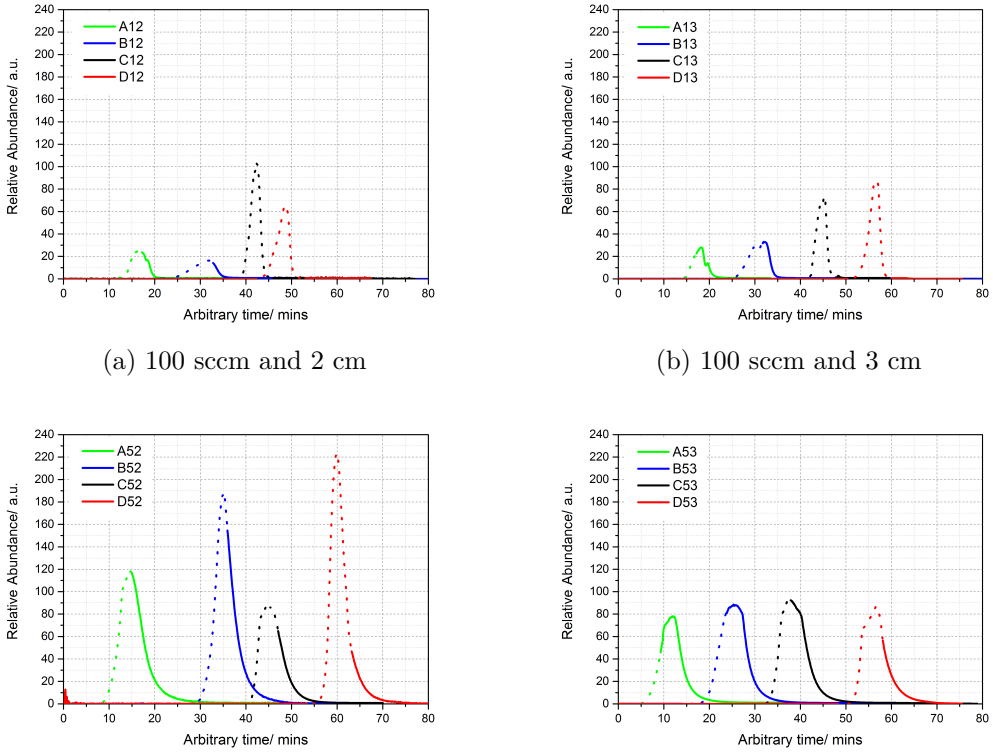
Figure 2.11: Zoomed in MS scan cycles from synthesis carried out with a pyrolysis temperature of 850 °C for a) background scan, purging with Ar, b) 0.10, c) 1.41, d) 3.12, e) 4.42, f) 6.13, g) 7.44, h) 9.15 minutes into the reaction.

The evolution of H_2 follows a similar increasing evolution trend as observed for methane, suggesting that the quantity of methane and methyl fragments should be relatively high at the end of the 10 minute reaction. The presence of these single-carbon species means that it is likely that Fe@MWCNT growth could be sustained despite the full consumption of ferrocene. To verify this hypothesis, an experiment was carried out in which the H_2 evolution peak was monitored until it decreased down to initial levels, which took 35 minutes. Interestingly, the quantity of Fe@MWCNTs deposited was significantly higher for the 35 minute reaction (30.72 mg) compared to the 10 minute experiment (4.12 mg) carried out otherwise identical synthesis parameters. Based on these observations, full exhaustion of ferrocene may not immediately stop the growth of Fe@MWCNTs.

Due to the relationship between rate of H_2 evolution and the rate of Fe@MWCNT growth, a systematic study was conducted exclusively monitoring the release of H_2 to understand how changing the synthesis parameters affects H_2 release. Attempts were then made to correlate the rate of H_2 production with the materials produced with varying synthesis parameters.

2.3.3 Monitoring H_2 Evolution

The relative abundance of H_2, normalised against the abundance of ^{36}Ar for each experiment was plotted against time to give an indication of how H_2 evolved during the CVD reaction (Figure 2.12). ^{36}Ar was selected as the species to normalise H_2 against as it has an intensity in the same order of magnitude as H_2 and because of its known abundance, relative to ^{40}Ar. The reaction time, i.e. when the crucible was slid into the pyrolysis furnace, is represented by the dashed lines. Upon introduction of ferrocene into the system, H_2 starts to be detected after an initial delay of 1-4 minutes, depending on the synthesis parameters, as previously observed for the RGA study (Figure 2.4 and Figure 2.5). Monitoring H_2 provides an indication of when thermocatalytic cracking of the hydrocarbon species detected in the RGA study has been exhausted, however Fe@MWCNT growth is still likely to occur for a short period after exhaustion of H_2 because C will still be diffusing through the Fe particles. The H_2 evolution peaks give an indication of the lifetime of hydrocarbon species remaining within the system following the full consumption of ferrocene.



(a) 100 sccm and 2 cm

(b) 100 sccm and 3 cm

(c) 50 sccm and 2 cm

(d) 50 sccm and 3 cm

Figure 2.12: H_2 evolution graphs showing the abundance of H_2 relative to ^{36}Ar obtained for differing T_{sub} and T_{pyro} with a) 100 sccm Ar flow and 2 cm furnace gap, b) 100 sccm Ar flow and 3 cm furnace gap, c) 50 sccm Ar flow and 2 cm furnace gap, and d) 50 sccm Ar flow and 3 cm furnace gap. The dashed lines indicate the period in which the alumina crucible was pushed into the middle of the sublimation furnace. The labels are as follows: A= 200/ 750, B=200/850, C= 250/750, D= 250/850 °C for T_{sub}/T_{pryo}, 1= 100, 5= 50 sccm Ar flow and 2 and 3 indicates the furnace gap in cm.

After reaching a maximum, $H_{2\ max}$, H_2 evolution decreases, which may be caused by the catalyst particles becoming deactivated. This phenomenon is observed in the growth of conventional MWCNTs by CVD of benzene [186–188], where catalyst deactivation was thought to be caused by decreases in the number of active sites, their quality and the accessibility to the active sites, with increased length of the MWCNTs.

Three types of H_2 evolution curves are observed; evolved H_2 reaches $H_{2\ max}$, and back to *ca.* initial levels within the reaction time, t_{cru}, (profile 1), $H_{2\ max}$ is reached but H_2 concentration does not decrease back to initial levels within t_{cru} (profile 2), and $H_{2\ max}$ is reached after t_{cru} (profile 3).

The synthesis parameters with profile 1 H_2 evolution curves all have an Ar flow of 100 sccm and T_{sub} of 250 °C (Figure 2.12 a and b, red and black). Profile 2 is typically observed for 100 sccm Ar flow, with T_{sub} of 200 °C. Combined, these observations suggest that

at higher gas flow, T_{sub} plays an important role in determining if the majority of H_2 is produced within t_{cru}. Profile 3 H_2 evolution is likely associated to the onset of H_2 release. Increasing the furnace gap or decreasing the Ar flow rate increased the delay before H_2 was first released from *ca.* 135 to 200 seconds for Ar flows of 100 and 50 sccm, respectively, and 150 to 185 seconds for furnace gaps of 2 and 3 cm, respectively. These delays in onset for H_2 evolution likely increases the time it took to reach $H_{2\ max}$ relative to starting the experiment (compare Figure 2.12a to c, and b to d).

Evaluating the mass balance between the amount of H_2 evolved and the mass of ferrocene required to achieve this provides *in situ* diagnostics of the efficiency of the CVD reaction, which could be used to improve reactor design. For example, if a lower mass of ferrocene is required than inputted to generate the amount of H_2 detected, this suggests that the reactor design is poor; increasing the length of the furnace may improve this. Attempts to estimate the mass per minute of H_2 evolved and perform mass balance calculations were unsuccessful due to the large amount of assumptions made, resulting in the calculated ferrocene mass being an order of magnitude larger than used experimentally to achieve the estimated mass of H_2.

The ideal gas law (Equation (2.3)) was used to estimate the mass per minute of H_2 evolved from the mg/min flow of ^{36}Ar, where P is the pressure (1 atm), V is the volume (L/min), n is the number of mols of the species, R is the ideal gas constant (0.0821 L atm K^{-1} mol^{-1}), and T is the temperature (K). Using the ideal gas law to calculate the mg/min flow of H_2 is invalid for numerous reason, most crucially, the ideal gas law is for a closed thermodynamic system, which is not true of the experimental setup used. The exchange of gases and the evolution of H_2 during the reaction means that the ideal gas law is not applicable. Further assumptions include presuming the pressure during CVD was at atmospheric pressure and that Ar flow was laminar and constant at 1.0 or 0.5 L/min. Further, the temperature inputted into Equation (2.3) was constant at either 1023 or 1123 K, which is inaccurate as the Ar gas flow starts at room temperature, then 473 or 523 K in the sublimation furnace, before reaching 1023 or 1123 K in the pyrolysis furnace.

$$PV = nRT \tag{2.3}$$

The mg/min of H_2 evolved was calculated by taking the ratio of ^{36}Ar to H_2 (Equation (2.4)), where M is the real molar abundance, I is the intensity and K is the correction factor. In an ideal scenario, the intensity directly translates into the real molar abundance, meaning the molar abundance of analytes with the same peak intensity would have the same real molar abundance. However, this situation is not always the case, hence a correction factor is needed. In this calculation, the correction factor was assumed to be one, which may be incorrect, leading to large errors with mg/min of evolved H_2 values.

$$\frac{M_{\mathrm{H2}}}{M_{\mathrm{36Ar}}} = K\frac{I_{\mathrm{H2}}}{I_{\mathrm{36Ar}}} \tag{2.4}$$

The Effect of Synthesis Parameters on the Properties of Fe@MWCNTs

The properties of materials produced from the systematic study are displayed in Table 2.3. The errors for the Fe@MWCNT length, outer lengths and filling length were calculated by measuring *ca.* 500 CNTs per sample. The materials produced for the systematic study were far from single phase, with samples containing a mixture of Fe@MWCNTs and clusters of C coated Fe NPs of varying ratios. Some syntheses contained a significantly higher density of agglomerated clusters of NPs of Fe coated in C than MWCNTs, these samples are loosely termed agglomerate samples. Attempts to correlate the gas analysis data to the properties of the Fe@MWCNTs were difficult, with no clear correlation between H_2 evolution profile and the material produced. The materials produced from syntheses with T_{pyro} of 850 °C consistently contained a large amount of C-coated Fe agglomerates, independent of T_{sub} (Figure 2.14). SEM images commonly consisted mainly of these agglomerates, however TEM revealed MWCNTs amongst these (Figure 2.16). The higher T_{pyro} may cause the Fe particles to be more mobile, hence they collide to form larger clusters, which form agglomerates preferentially over Fe@MWCNTs. Syntheses with a T_{pyro} of 750 °C typically formed MWCNTs.

The effect of Ar flow and furnace gap on the properties of Fe@MWCNTs is unclear, with no obvious trends observed by changing either synthesis parameter. This may be due to the changes in Ar flow and furnace gap being too small to have a significant affect, perhaps increasing the parameter space would provide a clearer picture. No significant trends were observed between changes in synthesis parameters and MWCNT diameter and Fe filling lengths, due to the large range in Fe@MWCNT diameter and filling lengths,

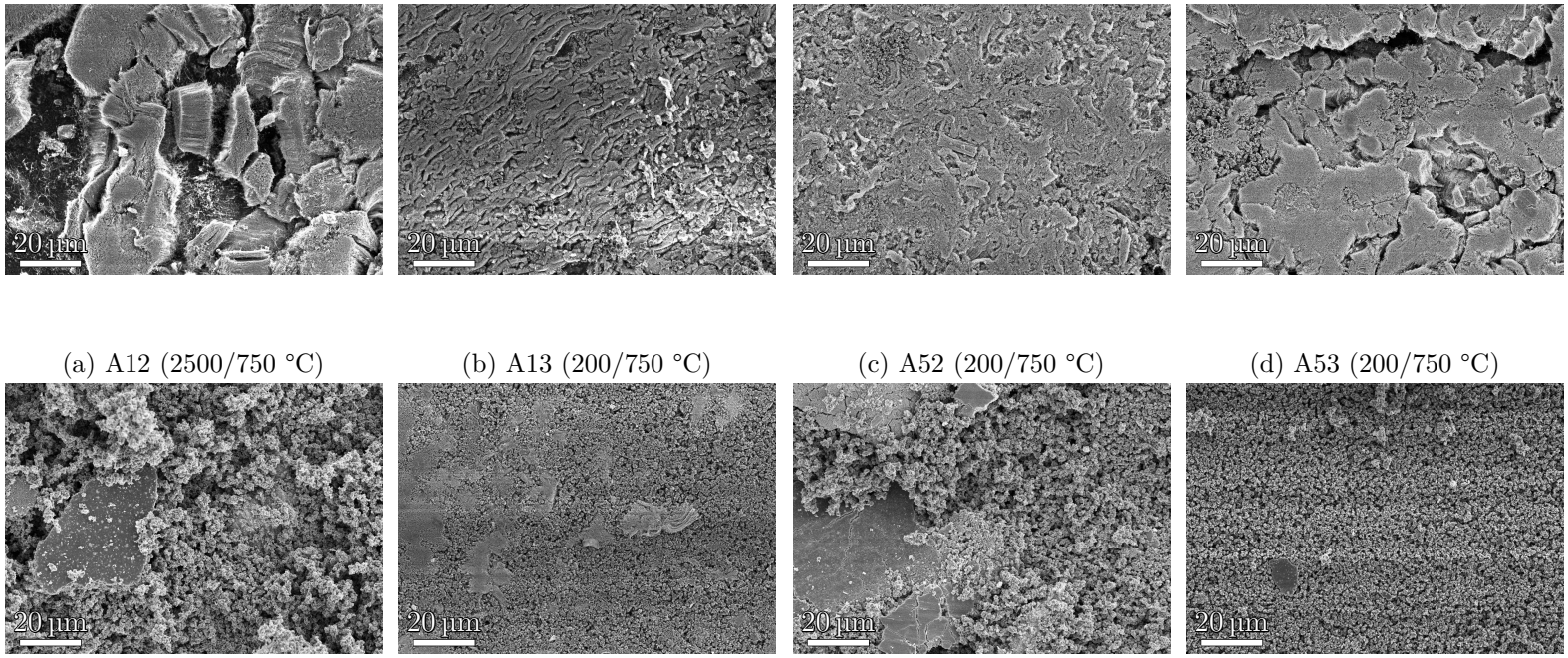
with some filling lengths in the μm range. The Fe-fillings were not continuous, further lowering the Ar flow may result in continuous fillings, as previously reported [189]. Despite the lack of significant trends between the changes in synthesis parameters and the Fe@MWCNT properties, the study did isolate the best combination of parameters that yielded the highest quantity of Fe@MWCNTs, with fewest quantity of by-products. These parameters were T_{sub}, T_{pyro}, Ar flow and furnace gap of 250 °C, 750 °C, 50 sccm and 3 cm, respectively.

The fact that the samples are inhomogeneous is likely to have a strong effect on the properties of the materials, such as their magnetic properties. It is difficult to estimate the ratio of CNTs to NPs, as simply counting the number of each within TEM images would not be meaningful, due to the difference in size, shape and Fe content for the two materials. The best approach to estimating the contribution of each would be to weigh the masses of each material. Establishing the Fe and C content of both materials would also be useful information. This would involve separating the NPs from the CNTs and running TGA on these individually. Exploring this further in the future would provide more insight into whether controlling the synthesis parameters affects the properties of the CNTs without interference from the presence of NPs within the samples.

Ref	H_2 Profile	Fe@MWCNT Length/ μm	Outer diameter/ nm	Inner diameter/ nm	Filling Length/ nm	NP diameter/ nm
A52	2	8.77 ±4.0	25.4 ±9.8	10.6 ±5	244 ±200	30 ±17
B52	2	*	49.01 ±26.7	28.1 ±13	210 ±202	53 ±29
C52	2	19.74 ±6.3	27.6 ±12.1	11.2 ±9	144 ±108	29 ±19
D52	2	*	43.6 ±21.3	31.1 ±18	512 ±333	81 ±52
A53	3	2.16 ±0.5	26.5 ±11.1	17.2 ±16	262 ±229	25 ±14
B53	3	*	33.9 ±17.0	18.9 ±11	210 ±200	41 ±29
C53	2	7.99 ±1	28.5 ±13.2	17.4 ±8	167 ±142	34 ±14
D53	2	*	42.7 ±22.9	25.1 ±7	201 ±147	67 ±60
A12	2	8.72 ±2.1	52.4 ±10.6	39.4 ±8	131 ±111	39 ±16
B12	2	*	10.51 ±9.4	4.4 ±2	108 ±133	36 ±22
C12	1	6.16 ±0.9	29.6 ±11.1	13.7 ±3	203 ±172	17 ±10
D12	1	14.28 ±1.3*	22.4 ±13.5	14.6 ±2	227 ±159	39 ±34
A13	3	7.30 ±1.8	54.4 ±10.5	30.8 ±5	223 ±148	48 ±15
B13	3	*	33.8 ±19.9	15.4 ±7	116 ±111	37 ±22
C13	1	25.97 ±7.4	33.1 ±11.8	13.2 ±3	323 ±331	18 ±8
D13	1	9 ±1.8*	51.1 ±29.7	28.8 ±4	473 ±409	49 ±38

Ref	Raman $I_{D/G}$	TGA T_{50} (°C)	Fe concentration from TGA (wt.%)
A52	0.661	635	19.0
B52	0.480	635	17.9
C52	0.732	633	19.5
D52	0.414	648	17.5
A53	0.671	645	16.5
B53	0.561	645	18.0
C53	0.659	572	19.0
D53	0.400	647	17.8
A12	0.691	639	18.1
B12	0.482	635	18.4
C12	0.689	675	18.2
D12	0.367	645	18.9
A13	0.546	614	16.8
B13	0.451	642	17.6
C13	0.570	571	17.9
D13	0.418	645	18.0

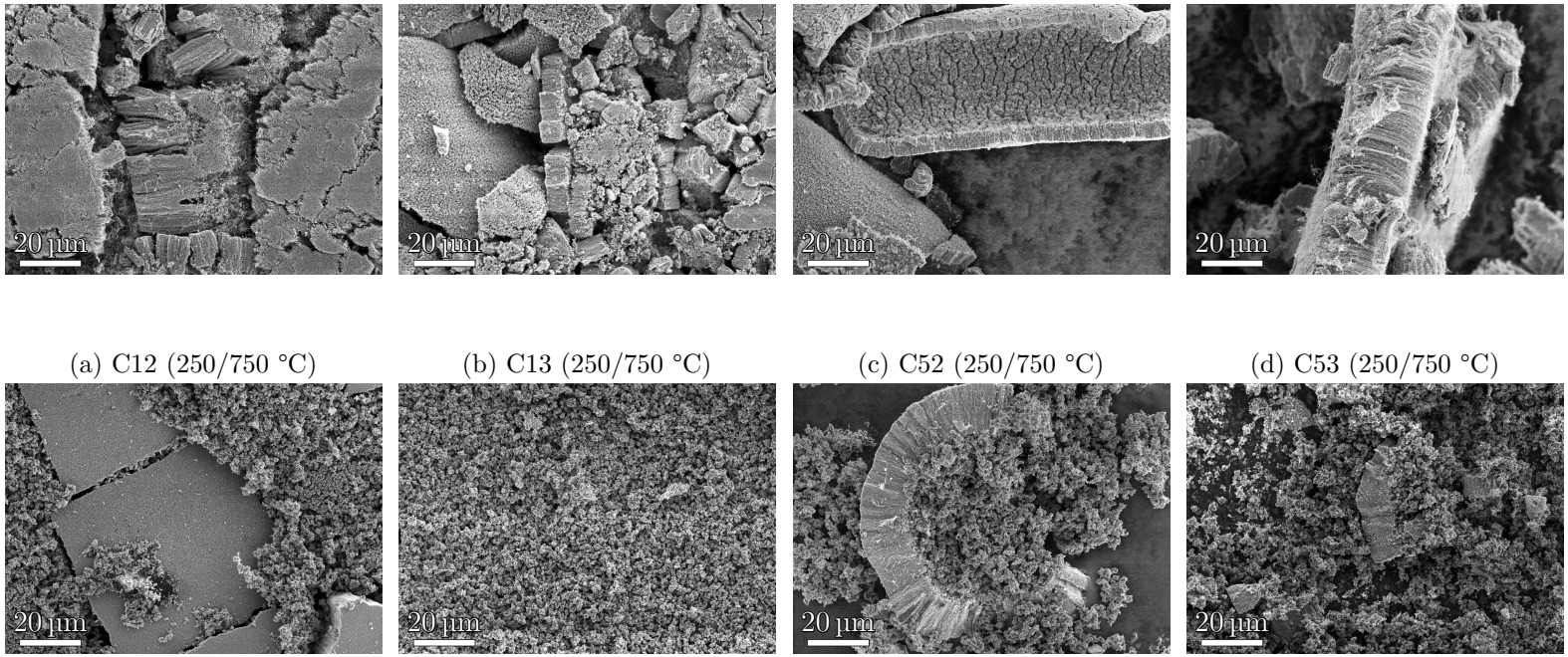
Table 2.3: The effects of different synthesis parameters on the properties of their corresponding synthesised Fe@MWCNTs. *indicates a mostly agglomerates sample. Labels: A= 200/750, B= 200/850, C= 250/750 and D= 350/850 °C for T_{sub}/T_{pyro}, 1 and 5 = 100 or 50 sccm Ar flow, respectively, and 2 and 3 = 2 or 3 cm furnace gap.



(a) A12 (2500/750 °C) (b) A13 (200/750 °C) (c) A52 (200/750 °C) (d) A53 (200/750 °C)

(e) B12 (200/850 °C) (f) B13 (200/850 °C) (g) B52 (200/850 °C) (h) B53 (200/850 °C)

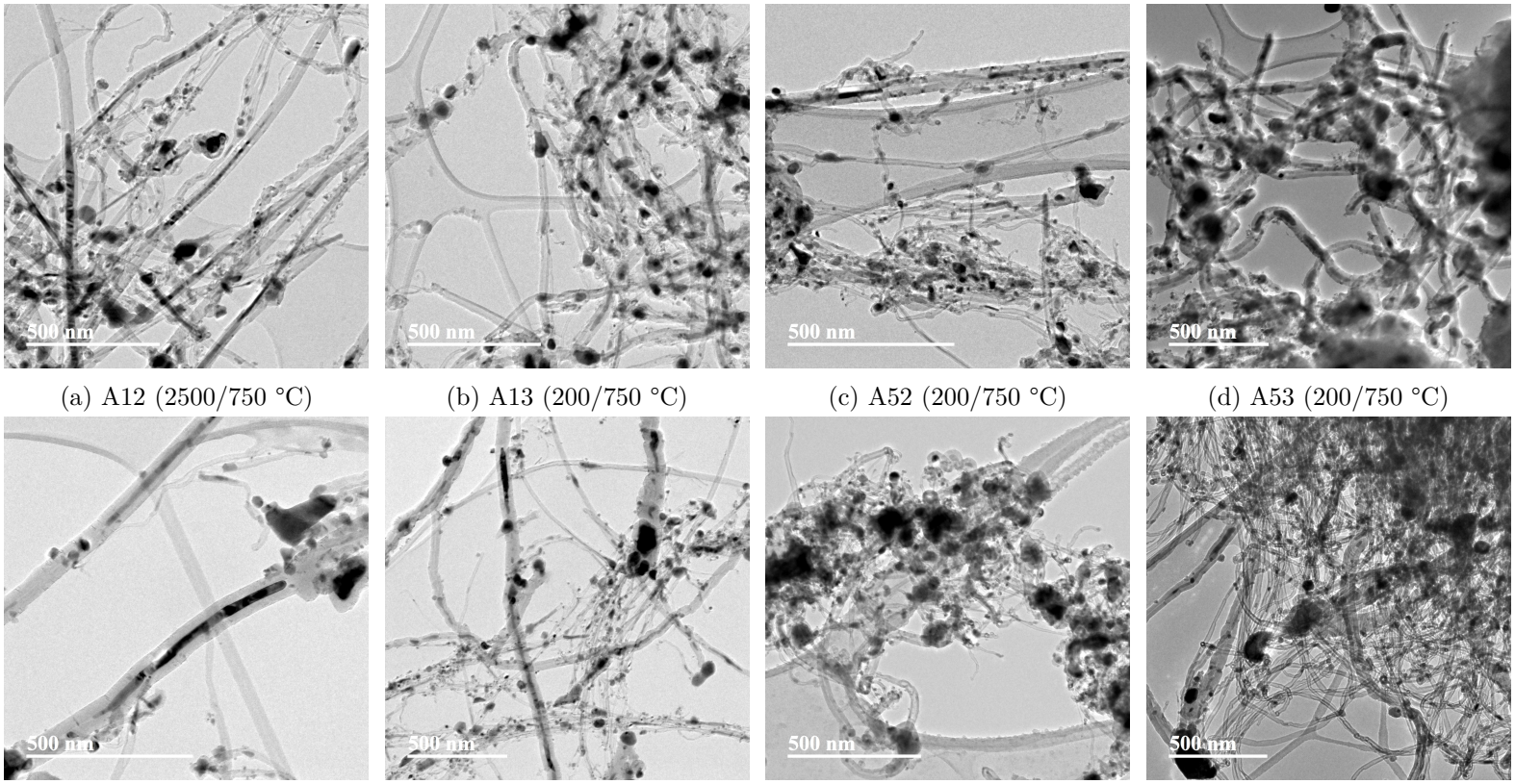
Figure 2.13: SEM images showing the material produced from syntheses monitored with MS. Syntheses were carried out with T_{sub} and T_{pyro} of 200/750 °C with a) 100 sccm, 2 cm gap, b) 100 sccm, 3 cm c) 50 sccm, 2 cm, and d) 50 sccm and 3 cm. The product for syntheses carried out with T_{sub} and T_{pyro} of 200/850 °C with e) 100 sccm, 2 cm gap, f) 100 sccm, 3 cm g) 50 sccm, 2 cm, and h) 50 sccm and 3 cm.



(a) C12 (250/750 °C) (b) C13 (250/750 °C) (c) C52 (250/750 °C) (d) C53 (250/750 °C)

(e) D12 (250/850 °C) (f) D13 (250/850 °C) (g) D52 (250/850 °C) (h) D53 (250/850 °C)

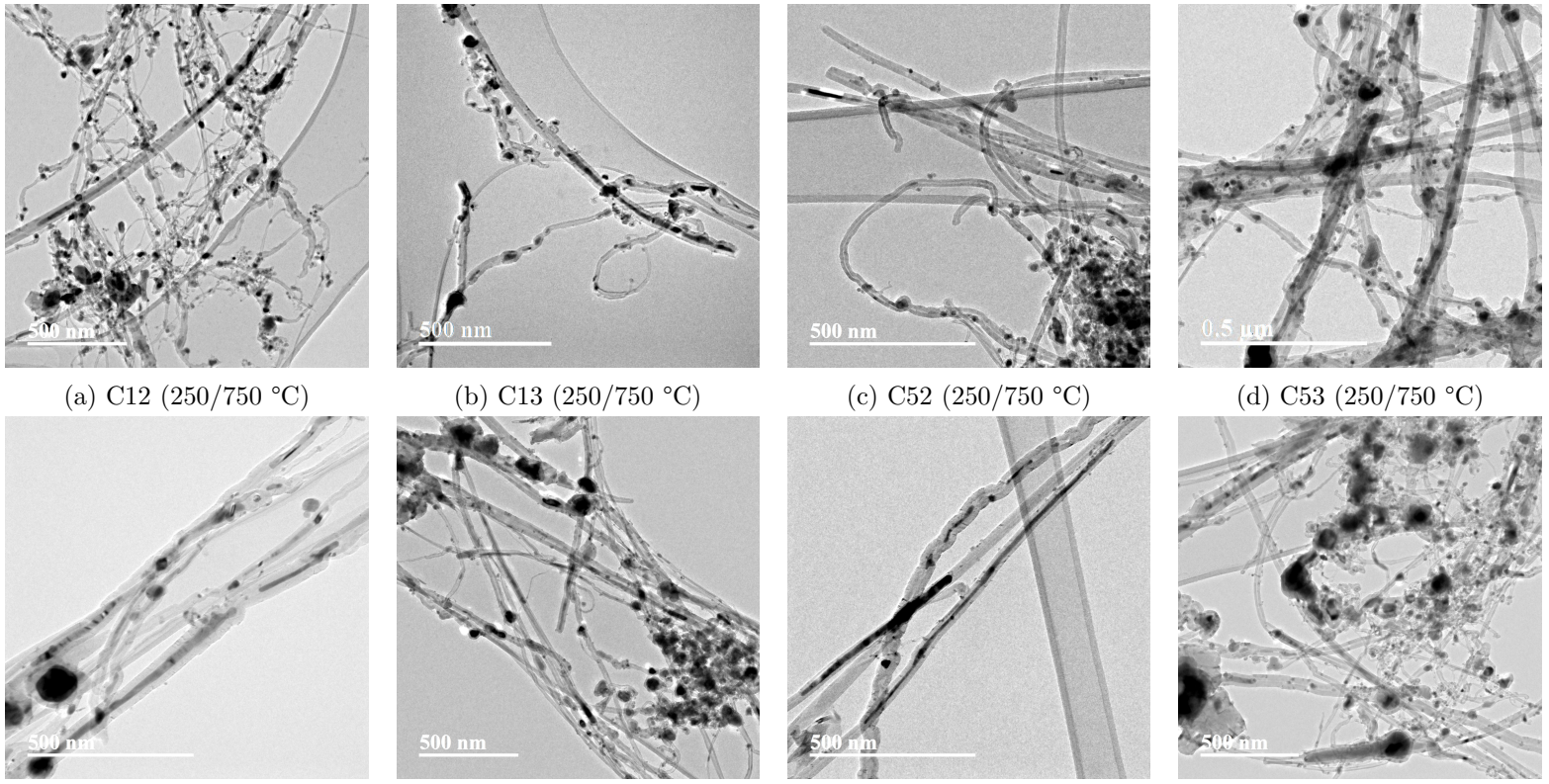
Figure 2.14: SEM images showing the material produced from syntheses monitored with MS. Syntheses were carried out with T_{sub} and T_{pyro} of 250/750 °C with a) 100 sccm, 2 cm gap, b) 100 sccm, 3 cm c) 50 sccm, 2 cm, and d) 50 sccm and 3 cm. The product for syntheses carried out with T_{sub} and T_{pyro} of 250/850 °C with e) 100 sccm, 2 cm gap, f) 100 sccm, 3 cm g) 50 sccm, 2 cm, and h) 50 sccm and 3 cm.



(a) A12 (2500/750 °C) (b) A13 (200/750 °C) (c) A52 (200/750 °C) (d) A53 (200/750 °C)

(e) B12 (200/850 °C) (f) B13 (200/850 °C) (g) B52 (200/850 °C) (h) B53 (200/850 °C)

Figure 2.15: TEM images showing the material produced from syntheses monitored with MS. Syntheses were carried out with T_{sub} and T_{pyro} of 200/750 °C with a) 100 sccm, 2 cm gap, b) 100 sccm, 3cm c) 50 sccm, 2 cm, and d) 50 sccm and 3 cm. The product for syntheses carried out with T_{sub} and T_{pyro} of 200/850 °C with e) 100 sccm, 2 cm gap, f) 100 sccm, 3cm g) 50 sccm, 2 cm, and h) 50 sccm and 3 cm.



(a) C12 (250/750 °C) (b) C13 (250/750 °C) (c) C52 (250/750 °C) (d) C53 (250/750 °C)

(e) D12 (250/850 °C) (f) D13 (250/850 °C) (g) D52 (250/850 °C) (h) D53 (250/850 °C)

Figure 2.16: TEM images showing the material produced from syntheses monitored with MS. Syntheses were carried out with T_{sub} and T_{pyro} of 250/750 °C with a) 100 sccm, 2 cm gap, b) 100 sccm, 3cm c) 50 sccm, 2 cm, and d) 50 sccm and 3 cm. The product for syntheses carried out with T_{sub} and T_{pyro} of 250/850 °C with e) 100 sccm, 2 cm gap, f) 100 sccm, 3cm g) 50 sccm, 2 cm, and h) 50 sccm and 3 cm.

Typically, lower $I_{D/G}$ ratios were observed for syntheses carried out with T_{pyro} of 850 °C, with the lowest $I_{D/G}$ ratio obtained for T_{sub} and T_{pyro} of 250 and 850 °C, respectively (Table 2.3). As agglomerates were the main product from syntheses at T_{pyro} of 850 °C, the lower $I_{D/G}$ ratio would suggest that they are graphitic, with the higher T_{pyro} allowing the C atoms to be more mobile, resulting in a decrease in defects as the C atoms are more likely to have enough energy to break and reform bonds, forming a more crystalline structure.

TEM images show the agglomerate particles were Fe coated with graphitic C (Figure 2.17). The graphitic nature of the agglomerate particles was confirmed by XRD, with the presence of the (002) plane of graphitic C at 26 2θ (Figure 2.18a). The Fe inside these agglomerates consists primarily of α-Fe, with the presence of some Fe_3C. Similar graphitic C encapsulated Fe have been reported [190–194], referred to as onion-like fullerenes or bucky-onions. These bucky-onions were produced by arc discharge [192, 194], or CVD [190, 191, 193]. Whilst no papers directly compare the $I_{D/G}$ of these nano-onions to Fe@MWCNTs, Xu *et al.* [191] reported a weak D peak for their Fe encapsulated bucky-onions, which is similar to as observed here.

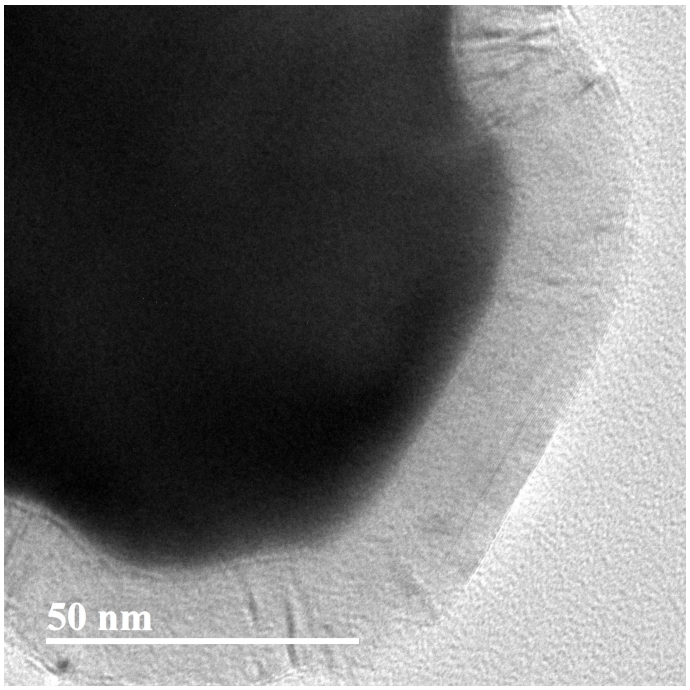
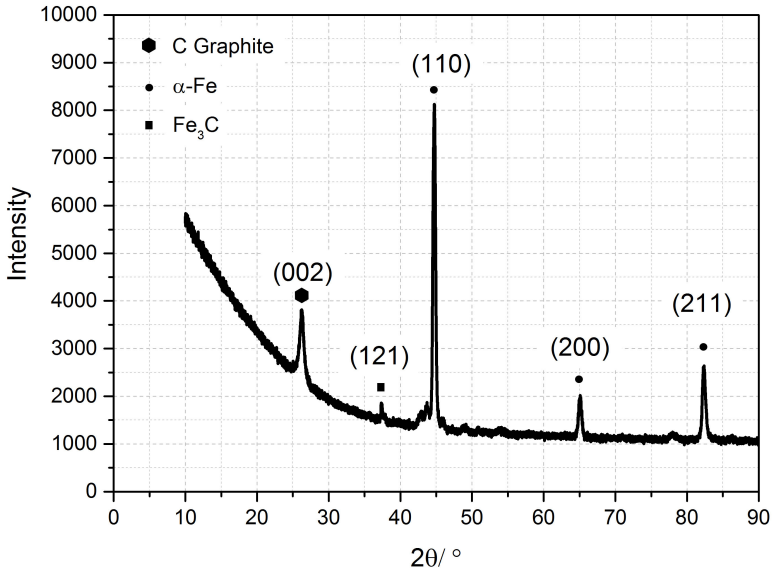
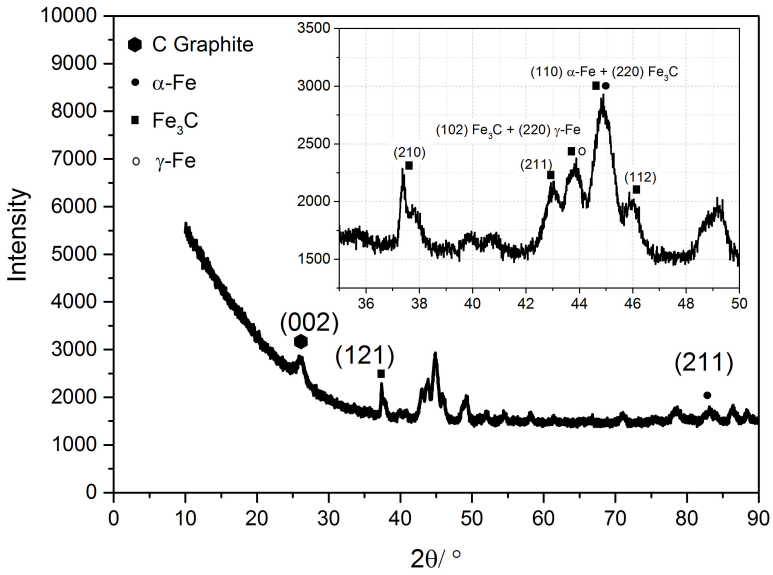


Figure 2.17: TEM image showing an example Fe NP coated in graphitic C, as confirmed by XRD.

The XRD patterns obtained for the Fe@MWCNT samples (Figure 2.18b) show the Fe-filling consists of mixtures of α-Fe, γ-Fe and Fe_3C phases (inset Figure 2.18b) [40, 113, 177]. Fe@MWCNTs with mixtures of Fe-phases and Fe_3C are well reported in the literature [40, 103, 106, 113, 177, 195–199]. In the bulk, the γ-Fe phase is only observed >860 °C and up to 6.5 wt.% C, as the γ-Fe phase transforms into α-Fe and Fe_3C below the eutectic temperature of 738 °C. However, the γ-Fe phase is detected in Fe@MWCNTs, as the phase transformation, which involves a volume dilation, is inhibited by the stiffness of the MWCNT [198]. The Fe phases in Fe@MWCNTs differs from the agglomerate Fe-particles, which mainly consists of peaks attributed to α-Fe. The graphitic C peak for the Fe@MWCNTs is less significant compared to agglomerate Fe-particles, which is reflected in the higher $I_{D/G}$ ratios observed for Fe@MWCNTs compared to samples consisting primarily of agglomerates.



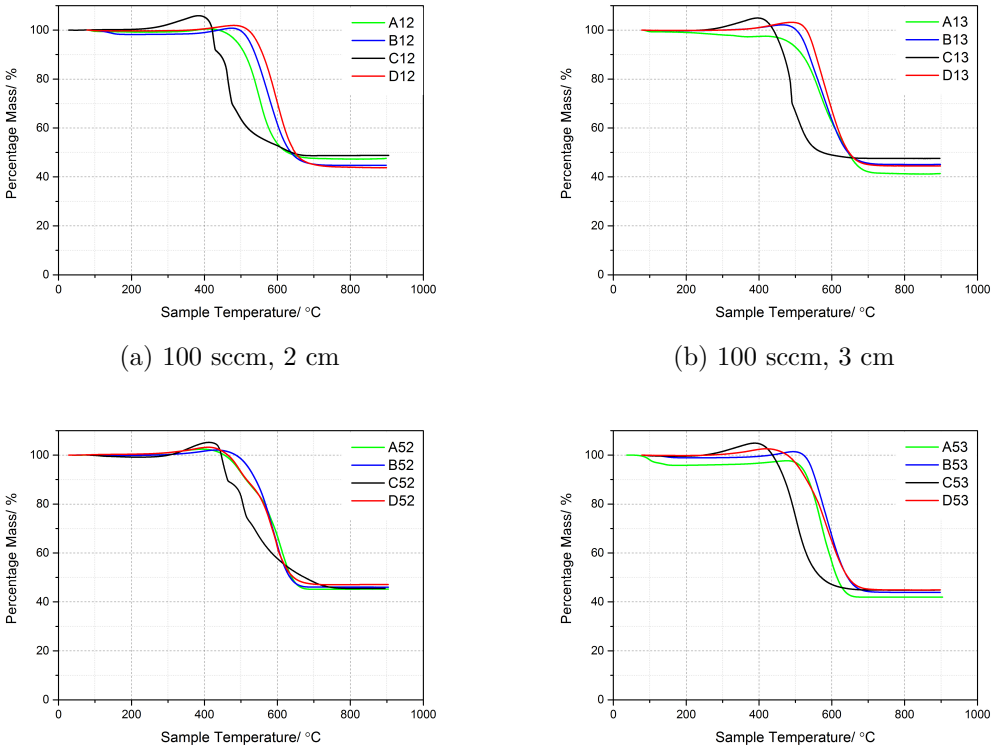
(a) Agglomerates



(b) Fe@MWCNTs

Figure 2.18: XRD patterns for a) a majority agglomerate Fe NP coated in C sample (B53) and b) a majority Fe@MWCNT sample (C53), where T_{sub}/T_{pyro} are B= 200/850 and C= 250/750 °C. The agglomerate particles consisted of α-Fe phases, whilst the Fe@MWCNTs were filled with a mixture of Fe-phases and Fe_3C.

TGA of the products from the systematic study showed similar mass loss profiles for each T_{sub} and T_{pyro} combination (Figure 2.19), with T_{sub} and T_{pyro} of 250/750 °C consistently having a lower oxidation resistance, and higher mass increase due to oxidation at *ca.* 400 °C, compared to the other furnace temperature combinations, regardless of Ar flow and furnace gap (Figure 2.19a-d, black line). For the remaining mass loss curves, there is only slight oxidation of the samples prior to mass loss.



(a) 100 sccm, 2 cm

(b) 100 sccm, 3 cm

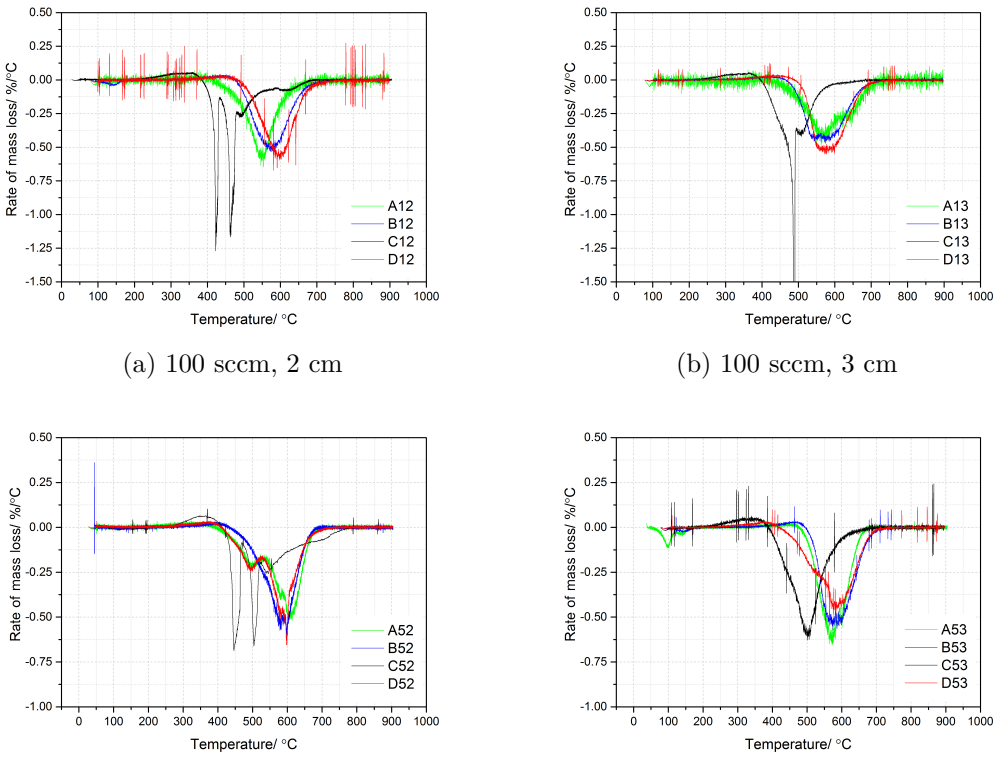
(c) 50 sccm, 2 cm

(d) 50 sccm, 3 cm

Figure 2.19: TGA graphs showing the mass loss profiles for the material produced with varying T_{sub} and T_{pyro} with a) 100 sccm Ar flow and 2 cm furnace gap b) 100 sccm Ar flow and 3 cm furnace gap, c) 50 sccm Ar flow and 2 cm furnace gap, and d) 50 sccm Ar flow and 3 cm furnace gap. The labels are as follows: A= 200/ 750, B=200/850, C= 250/750, D= 250/850 °C for T_{sub}/T_{pryo}, 1= 100, 5= 50 sccm Ar flow and 2 and 3 indicates the furnace gap in cm.

The wt.% of Fe, calculated from the residual mass of Fe_2O_3 from TGA, is similar for all experiments (17-19 wt.%, Table 2.3). However, it is unclear whether the residual Fe is from the Fe@MWCNTs or the agglomerate material. First derivative graphs of the mass loss curves show often there are two oxidation rate peaks for the agglomerates and Fe@MWCNTs Figure 2.20. The majority of the rate of mass loss curves have one distinct peak, which suggests that the clusters of C coated Fe NP and Fe@MWCNTs oxidise in the same temperature range. For syntheses carried out with T_{sub} and T_{pyro} of 250 and 750 °C,

respectively, mass loss consistently occurs at a lower temperature, which can be explained by higher $I_{D/G}$ values obtained for these samples, indicating they are more defective and hence breakdown at a lower temperature (Table 2.3). For C12 and C52 (Figure 2.20a and c, black), two peaks are observed in the rate of mass loss curves, suggesting there are two different carbon species present. The additional peak observed here could be due to a large amount of agglomerate clusters of C coated Fe NPs being present in these samples, such that two distinctive mass loss peaks are observed. The presence of the NPs are likely to influence the peaks observed in the first derivative mass loss graphs, resulting in peak broadening and the peaks being uneven, rather than a smooth singular curve. For Figure 2.20c, green and red lines, the additional oxidation peak at *ca.* 500 °C corresponds to amorphous carbon [200].



(a) 100 sccm, 2 cm

(b) 100 sccm, 3 cm

(c) 50 sccm, 2 cm

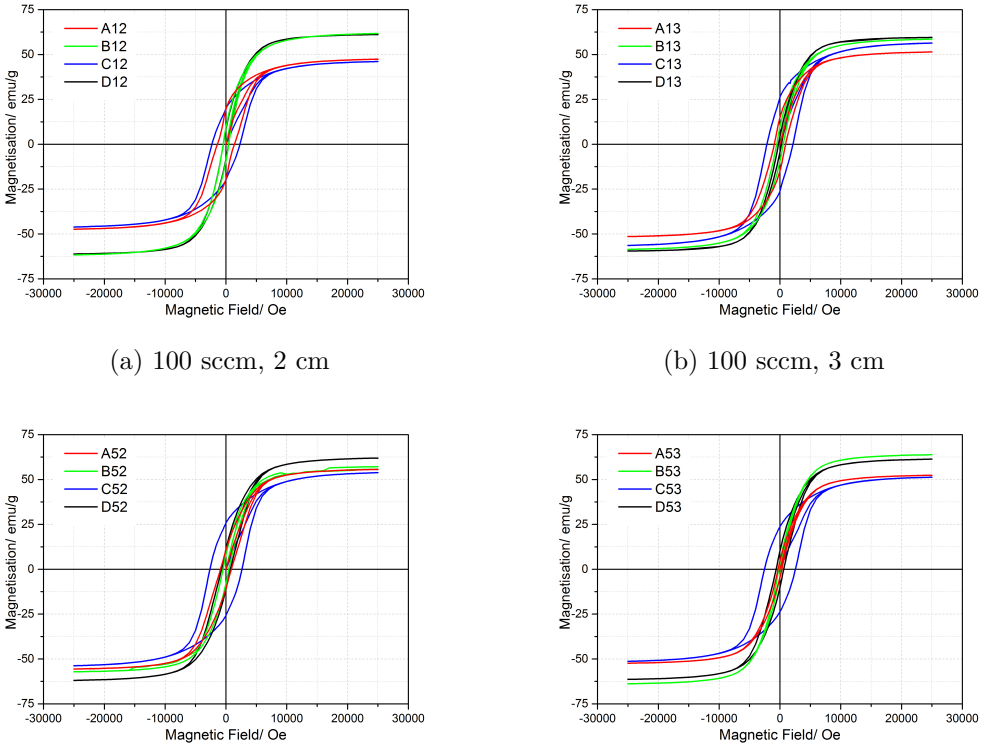
(d) 50 sccm, 3 cm

Figure 2.20: Rate of mass loss graphs for the material produced with varying T_{sub} and T_{pyro} with a) 100 sccm Ar flow and 2 cm furnace gap b) 100 sccm Ar flow and 3 cm furnace gap, c) 50 sccm Ar flow and 2 cm furnace gap, and d) 50 sccm Ar flow and 3 cm furnace gap. The labels are as follows: A= 200/ 750, B=200/850, C= 250/750, D= 250/850 °C for T_{sub}/T_{pryo}, 1= 100, 5= 50 sccm Ar flow and 2 and 3 indicates the furnace gap in cm.

Magnetic Properties of Fe@MWCNTs

The M_s and H_c of the products in the systematic study were investigated by SQUID (Figure 2.21). Dillon *et al.* [40] reported decreases in M_s with increasing T_{sub}, which contradicts with the magnetic hystereses shown in Figure 2.21. The green and black lines in Figure 2.21 corresponds to syntheses carried out with T_{pyro} 850 °C, whilst the red and blue lines correspond to a T_{750} °C. This suggests that increases in T_{pyro} result in increases in M_s, a trend that is observed across all variations in Ar flow and furnace gap. The M_s remains consistently at *ca.* 60-62 emu/g for all syntheses with T_{pyro} of 850 °C, with the exception of B52, Figure 2.21c, which has a decreased M_s of *ca.* 58 emu/g.

The materials produced with T_{sub} of 750 °C have a broader range of M_s values, which may be affected by changing the Ar flow and furnace gap. Increases in the furnace gap coincides with decreases in M_s for Figure 2.21 a to b, and c to d. With decreasing Ar flow, the M_s values increase from graphs a to c, however contradictory observations are made for graphs b to d; C13 decrease in M_s, whilst the M_s for A13 remains approximately the same. These observations may be coincidental, especially because of the contradictory results for the effect of Ar flow.



(a) 100 sccm, 2 cm

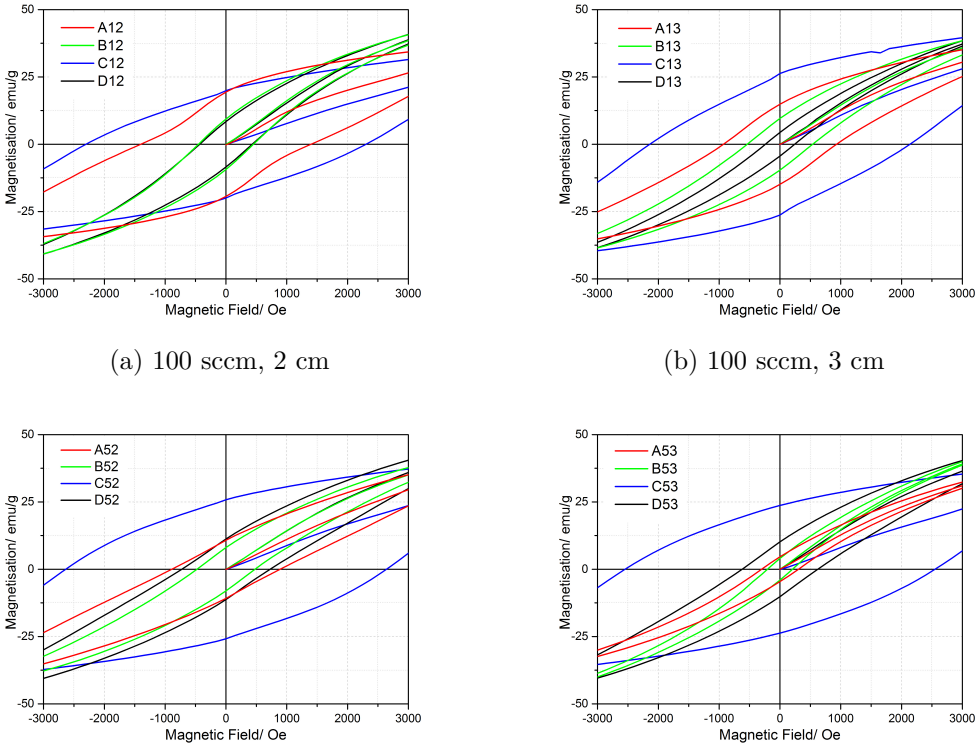
(b) 100 sccm, 3 cm

(c) 50 sccm, 2 cm

(d) 50 sccm, 3 cm

Figure 2.21: Graphs showing the magnetic hystereses syntheses carried out with Ar flows and furnace gaps of a) 100 sccm, 2 cm and b) 100 sccm, 3 cm, c) 50 sccm, 2 cm, and d) 50 sccm, 3 cm, respectively. SQUID measurements were carried out at 4 K. The labels are as follows: A= 200/ 750, B=200/850, C= 250/750, D= 250/850 °C for T_{sub}/T_{pryo}, 1= 100, 5= 50 sccm Ar flow and 2 and 3 indicates the furnace gap in cm.

Dillon also reported decreases in H_c with increasing T_{pyro} [40]. Whilst syntheses carried out at T_{pyro} of 850 °C typically had lower H_c values, the values were very similar for all temperature combinations, apart from T_{sub} and T_{pyro} combinations of 250/750 °C, which consistently had larger H_c values in all four graphs (Figure 2.22). The H_c of Fe nanowire arrays fabricated by electrodeposition in AAO fall in the range of 2100- 2300 Oe at 4 K [71]. A higher H_c of 4190 Oe was reported for ultrathin Fe arrays [67]. These H_c values are similar to the higher H_c observed for Fe@MWCNTs reported here. It has been shown that H_c increases with increasing nanowire diameter [67]. Producing nanowires by AAO has the advantage of being able to have a narrow distribution in the range of nanowires produced, as the AAO pores can be easily controlled by soaking time in phosphoric acid [67, 69]. Whilst the inner diameter of the CNT controls the diameter of the Fe nanowires within them, the is a larger inner diameter distribution for the Fe@MWCNTs produced here.



(a) 100 sccm, 2 cm

(b) 100 sccm, 3 cm

(c) 50 sccm, 2 cm

(d) 50 sccm, 3 cm

Figure 2.22: Graphs showing the coercive forces for syntheses carried out with Ar flows and furnace gaps of a) 100 sccm, 2 cm and b) 100 sccm, 3 cm, c) 50 sccm, 2 cm, and d) 50 sccm, 3 cm, respectively. SQUID measurements were carried out at 4 K. The labels are as follows: A= 200/ 750, B=200/850, C= 250/750, D= 250/850 °C for T_{sub}/T_{pryo}, 1= 100, 5= 50 sccm Ar flow and 2 and 3 indicates the furnace gap in cm.

Ref Code	**M_s/ emu/g**	**H_c Oe**	**Remanence/ G**
A52	48	1412	19
B52	62	464	9
C52	46	2293	20
D52	61	436	8
A53	52	933	15
B53	59	545	10
C53	56	2100	25
D53	59	249	4
A12	56	896	11
B12	57	489	8
C12	53	2645	26
D12	61	736	12
A13	52	298	5
B13	64	206	4
C13	51	2559	24
D13	61	626	10

Table 2.4: Values for the M_s, H_c and remanence for each sample in the systematic study. The labels are as follows: A= 200/ 750, B=200/850, C= 250/750, D= 250/850 °C for T_{sub}/T_{pryo}, 1= 100, 5= 50 sccm Ar flow and 2 and 3 indicates the furnace gap in cm.

These differences in magnetic properties, for both M_s and H_c, between the systematic study conducted here and to Dillon's work may be related to the difference in temperature combinations used; Dillon evaluated the effects of T_{sub} at a constant T_{pyro} of 950 °C, whilst a constant T_{sub} of 300 °C was used to investigate the effects of T_{pyro}, with an Ar flow of 200 sccm in all cases. Further, the effect of furnace gap is not mentioned throughout the paper, it is unclear whether the furnaces were influencing one another which could have a large effect on the results.

The hysteresis curves are likely strongly influenced by the C coated Fe NP agglomerates observed in the samples (Table 2.3). As it is not clear whether the samples analysed by SQUID in Dillon's publication contained NPs or not, it makes it difficult to compare their results to those observed here. Without separating the NPs and Fe@MWCNTs from one another, it is difficult to distinguish the contributions of each material on the hystereses observed here. It could be that by separating the NPs and Fe@MWCNTs, trends between synthesis parameters and Fe@MWCNT properties that can not be observed now will be revealed. Whilst this information is of interest on a fundamental level, the materials produced here have a magnetic response, which is the important factor for producing BPs that respond to magnetic stimuli. The SQUID measures showed that these Fe@MWCNTs display magnetic hystereses and hence are suitable for use in producing magnetic BPs.

2.4 Conclusions

In this chapter, the variables affecting the growth of Fe@MWCNTs was studied using a combination of *in situ* and *ex situ* techniques. First the effect of furnace gap on the temperatures of the sublimation and pyrolysis furnaces was studied, this is crucial to gain an understanding of the temperature profile prior to carrying out synthesis experiments. It was found that the sublimation furnace temperature was strongly influenced by the pyrolysis furnace with smaller furnace gaps. The effects of individual furnace temperatures on one another is an important factor to take into consideration for any synthesis involving more than one furnace. For all setups, understanding the furnace profile is an essential prerequisite before carrying out experiments to establish the length of the plateau region, as well as how closely the actual furnace temperature matches the programmed temperature. The ideal temperature profile for two-stage furnace setups involves having a distinct plateau region in each furnace, with a minimal temperature decrease across the furnace gap, i.e. having as small a furnace gap distance as possible, without the furnaces influencing one another. Longer plateau regions are preferential to allow the precursor molecules to experience a constant, programmed temperature for as long as possible.

In situ MS was used to compliment the *ex situ* characterisation techniques to gain an understanding of the reaction environment and the species evolved during CVD growth of Fe@MWCNTs using ferrocene. The RGA MS conditions were optimised to allow for the maximum number of MS scans within the reaction timeframe, whilst keeping a low signal-to-noise ratio. This compromise allows for high quality data to be collected whilst allowing as much information about the fragments released to be gathered. The RGA revealed that the naphthalene and benzene were the dominant high mass fragments detected at both pyrolysis temperatures. At higher T_{pyro}, cyclopentadiene fragments were not detected, likely because they reacted to form the higher mass fragments, or broke down to smaller fragments faster at the elevated pyrolysis temperature. However, naphthalene was detected for both T_{pyro}, this observation suggests that mixtures of naphthalene and ferrocene could be a good precursor combination for CVD of MWCNTs. RGA showed the importance of the lower mass fragments, ethene and methane, which continued to break down and release H_2 despite the exhaustion of ferrocene.

H_2 evolution was studied in conjunction with carrying out a systematic study to understand the effects of synthesis parameters on H_2 production. Three H_2 evolution profiles were observed within the reaction time; the evolution reached its maxima and back to initial levels within the reaction time, reached maximum within the reaction time or reached maximum after the reaction time. The profile obtained is likely controlled by a combination of Ar flow, T_{sub} and furnace gap. The H_2 evolution gives an indication of when thermocatalytic cracking of ferrocene begins and when all the hydrocarbon fragments have been exhausted, which is useful information for evaluating how long to carry out experiments for. Extending the reaction time until H_2 reaches initial levels appears to increase the mass of the Fe@MWCNTs produced, and should be explored further.

There was no strong correlation between H_2 evolution and the morphological, magnetic and graphitic properties of the product. There appeared to be no significant trends between Ar flow and furnace gap on the properties of the materials. This observation is likely to be related to the mixture of materials present within the samples. All samples were inhomogeneous and contained Fe@MWCNTs, clusters of C coated Fe NPs, as well as amorphous C.

The furnace gap is likely to influence the material produced at smaller distances, as evidenced from the variation in materials produced with a furnace gap of 0-3 cm. A T_{pyro} of 850 °C was strongly correlated to producing agglomerates of C coated Fe clusters as the main product, regardless of the other synthesis parameters. These agglomerates were confirmed by XRD to be α-Fe clusters with a graphitic coating. Conversely, the Fe@MWCNTs were filled with a mixture of Fe_3C, α-Fe and γ-Fe phases.

Performing *in situ* RGA MS in combination with *ex situ* characterisation allows for additional information to be gathered about how the synthesis parameters affect the thermocatalytic cracking of precursors. Understanding which fragments are key to MWCNT growth, and correlating this to the proposed growth mechanisms (section 1.2.4) brings us one step closer to fully understanding their growth mechanism.

Chapter 3

Producing Fe/Co@MWCNTs

In this chapter, Fe/Co filled MWCNTs (Fe/Co@MWCNTs) of varying Fe and Co composition were produced. The aim was to investigate whether creating alloy Fe/Co@MWCNTs extends the range of M_s and H_c values beyond those of Fe@MWCNTs, in a tunable manner. To understand the effects of applying current to the filling, and evaluate the suitability of using Fe/Co@MWCNTs in electronic applications, currents were applied to Fe/Co@MWCNTs, in situ in the TEM, to monitor any changes.

3.1 Introduction

The magnetic properties, such as M_s and H_c, of single metal magnetic materials are limited by the intrinsic magnetic properties of the metal. In the bulk, alloys are formed to create materials with differing magnetic properties to their single metal counterparts. Extending this concept to metal-filled MWCNTs, creating alloy metal-filled MWCNTs could allow their magnetic properties to be tuned and increase M_s and H_c beyond those possessed by Fe@MWCNTs. These tunable alloy filled-MWCNTs could be utilised in applications requiring a range of different magnetic properties within one device, for example in developing a multiple switch system, based on the work in Chapter 4. In these multiple switch systems, each switch would consist of ferromagnetic MWCNTs with different M_s, which respond to a specific external applied magnetic field, such that only some switches move into the 'on' position.

The concept of tunable magnetic properties is discussed in the context of FeCo alloys, focusing on the structure and magnetic properties are of bulk and nanoscale systems.

3.1.1 Structure of FeCo Alloy Materials

3.1.2 Bulk FeCo Alloy Materials

Alloys are materials in which the different metal atoms are metallically bonded. They can be single phase or contain a mixture of metallic phases. One of the most studied alloys for their magnetic and structural properties, is the Fe-Co system [201]. The phase diagram of the Fe-Co system (Figure 3.1) [202]shows that FeCo alloys undergo a phase change from FCC, γ, to a disordered BCC, α, structure at temperatures below the phase line at *ca.* 900 °C. Below the critical ordering temperature, T_c, the BCC phase rapidly orders to a B2, α', CsCl structure. T_c depends on Co content in the alloy, with a maximum of *ca.* 730 °C for stoichiometric FeCo. The intermetallic α' FeCo compounds are stable at ambient temperatures, between 29-70 at.% Co [203], with the ordering strongly influencing the alloys' magnetic and mechanical properties [204].

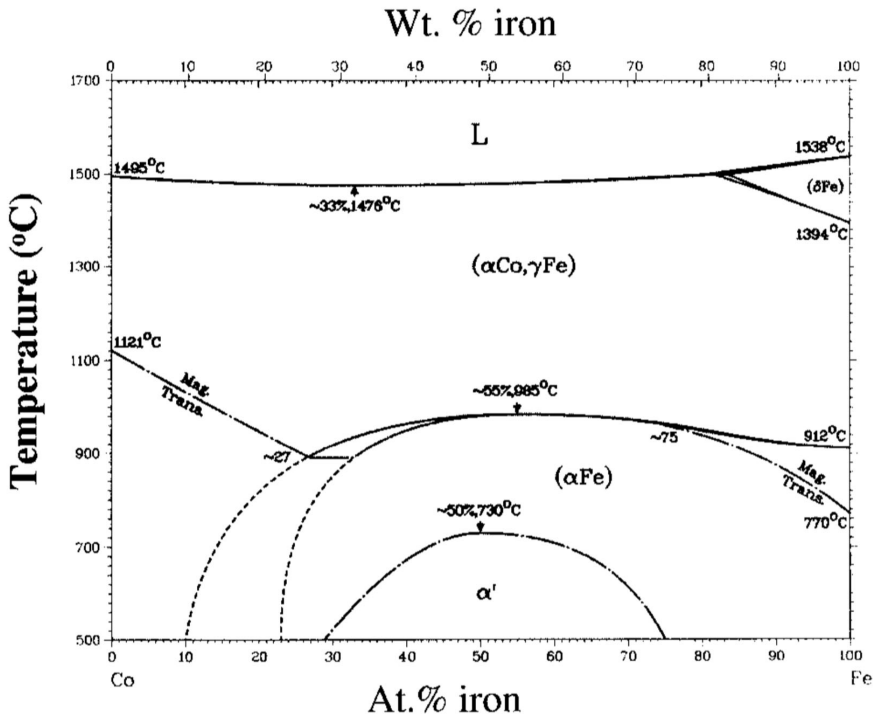


Figure 3.1: Phase diagram for Fe and Co [202]. Below 730 °C for a 50:50 Fe/Co mixture, the alloy undergoes a transition from a disordered αphase to an ordered CsCl α' phase.

3.1.3 Structure of Nanoscale Magnetic Alloy Materials

Ferrando defines nanoalloys as all metallic nanoparticles consisting of more than one metal, irrespective of chemical ordering [205]. This includes debatable, non-mixed nanomaterials, like coreshell structures, consisting of a core of one element surrounded by a shell of another [206]. In this chapter, nanoalloys are materials with a mixed elemental arrangement of atoms.

Alloy nanowires of Co-Ni and Fe-Co have been fabricated by electrodeposition into AAO templates using varying ratios of metal sulphates [73, 207, 208]. For example, Fodor *et al.* [207] used an electrolyte containing $CoSO_4$, $CoCl_2$, and Fe_4 salts in a range of ratios to form alloy nanowires of formula $Co_{1-x}Fe_x$. Whilst alloy nanowires can be created, once the AAO template is removed, the nanowires are exposed to air and quickly oxidise. Encapsulating the nanowires within CNTs protects them from oxidation.

A pioneering report on $Fe_{65}Ni_{35}$-filled MWCNTs, an Invar effect alloy, by Grobert *et al.* [13] proved that MWCNTs can be filled with alloys, and inspired research in alloy-filled MWCNTs [90, 91, 209, 210]. These $Fe_{65}Ni_{35}$-filled MWCNTs were produced by AACVD, using nickelocene and ferrocene (65:35, Fe: Ni, total 5 wt. %) dissolved in benzene, with XRD confirming the presence of Invar [13]. An AACVD approach was also used by Elias *et al.* [90], who produced monocrystalline Fe/Co@MWCNTs with nanowire lengths of 5-30 nm using 1:1 ratios of ferrocene and cobaltocene dissolved in toulene. Lv *et al.* [211] produced thin-walled MWCNTs filled with continuous FeCo, FeNi or FeCoNi nanowires by CVD using metallocene mixtures dissolved in trichlorobenzene (TCB) precursors. From these reports, it is feasible to create alloy-filled MWCNTs, however work has yet to be carried out on varying the ratio of the metals making up the alloys.

Using liquid precursors to produce alloy-filled MWCNTs drastically increases the C to metal ratio. Whilst the Cl in TCB etches away excess C, this leads to very thin MWCNT walls [211]; thicker MWCNT walls are preferable to better isolate the magnetic fillings from each other.

Using solid precursors avoids the large C to metal ratio issue. Kozhuharova *et al.* [12] produced Fe/Co@MWCNTs by CVD of ferrocene and cobaltocene (1:2) in a two-stage furnace with T_{sub} and T_{pyro} of 120-140 and 980 °C, respectively. The Fe/Co@MWCNTs were 10 μm in length, with filling lengths of a few micrometers. However, this approach

produced a range of Fe_xCo_{1-x} compositions, with an Fe concentration of 30-40 %, depending on the nanowire analysed by EDX. It is uncertain if similar variations occur in MWCNTs produced by AACVD, as none of the papers compared the metal ratio for a range of alloy-filled MWCNTs. The solid precursor approach was chosen for this chapter, due to the more favourable ratio of metal to C atoms.

3.1.4 Magnetic Properties of Alloy Materials

3.1.5 Bulk Magnetic Alloys

Magnetic properties, such as M_s, magnetic flux density, Curie temperature and H_c must be evaluated when selecting materials for magnetic applications. M_s is independent of microstructure, whilst microstructure influences H_c [204].

The M_s of pure bulk Co and Fe are 1422 and 395 emu/cm^3 at 300 K, respectively [212]. These M_s values are increased by forming FeCo alloys (Figure 3.2) [213]. Bulk FeCo alloys with 35 at.% Co have M_s of 2.45 T [203, 204] whilst bulk FeCo (50:50 at.%) has M_s values of 235 emu/g [214] and 211.3 emu/g [213], depending on the alloying process. Bardos investigated the M_s and mean magnetic moment in bcc Fe/Co alloys with 5-70 at.% Co and reported M_s values of 226.9 emu/g for 5 at.% Co, which steadily increased to a maximum of 242 emu/g for 28 at.% Co, then decreased to 211 emu/g for 70 at.% Co [215]. These findings indicate that in the bulk, controlling the alloy composition tunes M_s.

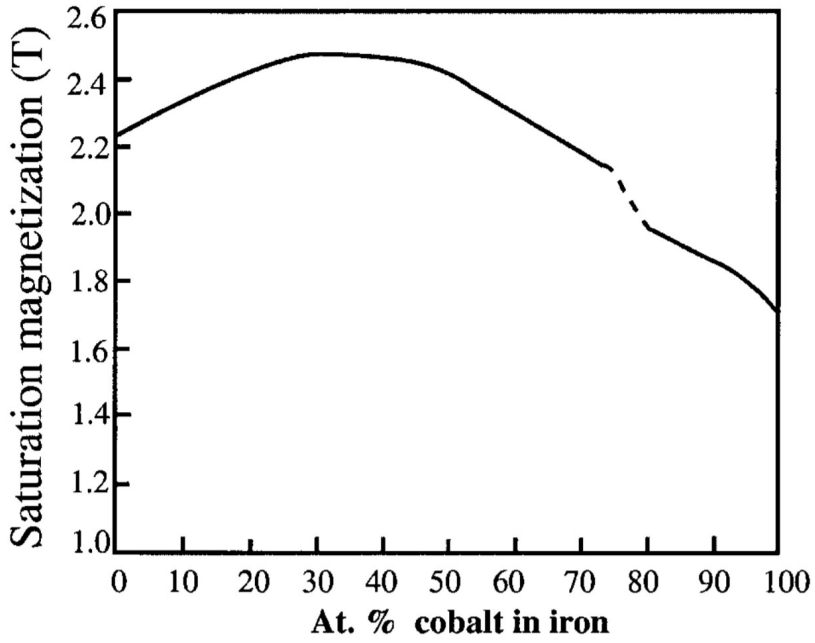


Figure 3.2: Graph showing the variation in M_s with varying Co content, showing that an alloy with *ca.* 30 at.% Co in Fe should have the highest M_s value.

3.1.6 Nanoscale Magnetic Alloys

Size effects strongly affect magnetic properties at the nanoscale, with single domain particles forming at the critical domain size, D_{cr}. The low barrier to switching magnetisation axes at the nanoscale leads to spontaneous changes in magnetisation due to thermal fluctuations [205]. These thermal fluctuation induced magnetisation reversals are undesirable for applications like magnetic data storage, where they result in data deletion [216].

The effect of nanoalloy composition on magnetic properties, focusing on alloy filled CNTs is now explored.

Monocrystalline Fe/Co@MWCNTs produced by CVD [12] and AACVD [90] possessed H_c of 126 mT and 928 Oe at room temperature, respectively. Elias *et al.* [90] stated that these Fe/Co@MWCNTs exhibit larger coercive fields at room temperature than Fe@MWCNTs, which typically have H_c of 430 Oe [41]. Whilst not directly comparable due to the synthesis methods used to produce the metal-filled MWCNTs, Elias's observation suggests that creating alloy Fe/Co@MWCNTs changes their magnetic properties, compared to single metal-filled MWCNTs. From this, it would be interesting to investigate how changing the Fe:Co ratio within these Fe/Co@MWCNTs further affects their magnetic properties.

Wang *et al.* [217] tuned the magnetic properties of Fe/Co-NP-coated Fe@MWCNTs by increasing Fe content in the Fe/Co NPs to gain softer magnetic properties. Fe@MWCNTs were coated and annealed with Fe and Co sulphates (1:1, 1:2 and 2:1), to form the NP decorated Fe@MWCNTs. Similar variations in M_s and H_c could be achieved by varying the Fe and Co content in Fe/Co@MWCNTs, as explored in this chapter. Producing Fe/Co@MWCNTs *in situ* is preferable to decorating MWCNTs with FeCo NPs, as encapsulating the Fe and Co inside the MWCNT protects them from oxidation and traps them inside the MWCNT.

Producing Fe/Co@MWCNTs with tunable M_s increases the range of electronic applications they are suited for. However, the effects of applying current to these magnetic MWCNTs must first be understood. The influence of current on Fe-filled P and N-co-doped MWCNTs was examined by Aslam *et al.* [218]. A bias was applied to the MWCNT, whilst observing any changes *in situ* with TEM. The current caused a Fe-C-N alloy to form inside the MWCNT, before joule heating destroyed the N-doped MWCNT. These results indicate that the effects of current need to be evaluated before using Fe/Co@MWCNTs in electrical applications.

In this chapter, the effect of varying ferrocene and cobaltocene precursor ratios on the Fe:Co ratio within Fe/Co@MWCNTs is investigated, with the aim of testing the hypothesis that tuning and extending the M_s and H_c of Fe/Co@MWCNTs is feasible by varying the Fe:Co in the filling. Based on the literature, using an AACVD approach can limit the amount of filling present within the MWCNTs, hence Fe/Co@MWCNTs were produced by CVD. Taking the characterisation one step further, the effect of passing current through the Fe/Co@MWCNTs on MWCNT and Fe/Co structure was assessed by *in situ* TEM. The conclusions drawn from these *in situ* measurements provide implications for the feasibility of using metal-filled MWCNTs in electrical applications.

3.2 Experimental

3.2.1 Fe/Co@MWCNT Synthesis Procedure

Fe/Co@MWCNTs were produced by CVD using the two-stage furnace described in chapter 2 (Section 2.2.2), with precursor mixtures of ferrocene and cobaltocene (Sigma-Aldrich). The as-purchased ferrocene was first purified by subliming at 80 °C. The precursors were

mixed together in an alumina crucible in a glove box, under N_2, due to the air sensitive nature of cobaltocene. A total precursor mass of 200 mg was used, with ratios of 75:25, 50:50, and 25:75 ferrocene to cobaltocene. The alumina crucible was slid into a quartz tube (2 cm diameter, 80 cm length), preloaded with quartz substrates (40x10x 5 mm, UQG Optics Ltd.). Table 3.1 shows the syntheses carried out and their reference codes.

The quartz substrates were first cleaned by a) washing with soap water and rinsed with distilled water b) sonicating for 5 minutes each in acetone, then IPA. The substrates were placed 31-43 cm along the quartz tube (Figure 3.3). The quartz tube was placed into the furnace, with a 3 cm furnace gap, and connected to the bubbler and Ar gas line. The system was purged with an Ar flow of 100 sccm for 10 minutes prior to furnace heating. The furnace temperatures were set to 250 and 750 °C for the sublimation and pyrolysis furnaces, respectively. These furnace temperatures were the best temperatures for synthesis of Fe@MWCNTs and stoichiometric FeCo@MWCNTs [90]. For all reactions, the furnace was cooled under 100 sccm of Ar to below 300 °C.

Reference Code	Ferrocene:Cobaltocene	Substrate Number
FeCo-AB	75:25	Bulk
FeCo-A1	75:25	1
FeCo-A2	75:25	2
FeCo-A3	75:25	3
FeCo-BB	50:50	Bulk
FeCo-B1	50:50	1
FeCo-B2	50:50	2
FeCo-B3	50:50	3
FeCo-CB	25:75	Bulk
FeCo-C1	25:75	1
FeCo-C2	25:75	2
FeCo-C3	25:75	3

Table 3.1: The samples produced, using different ratios of ferrocene to cobaltocene, along with their unique reference code, which is used throughout the chapter. The final number/B in the reference code refers to substrate number or bulk sample (B) scraped out the quartz tube.

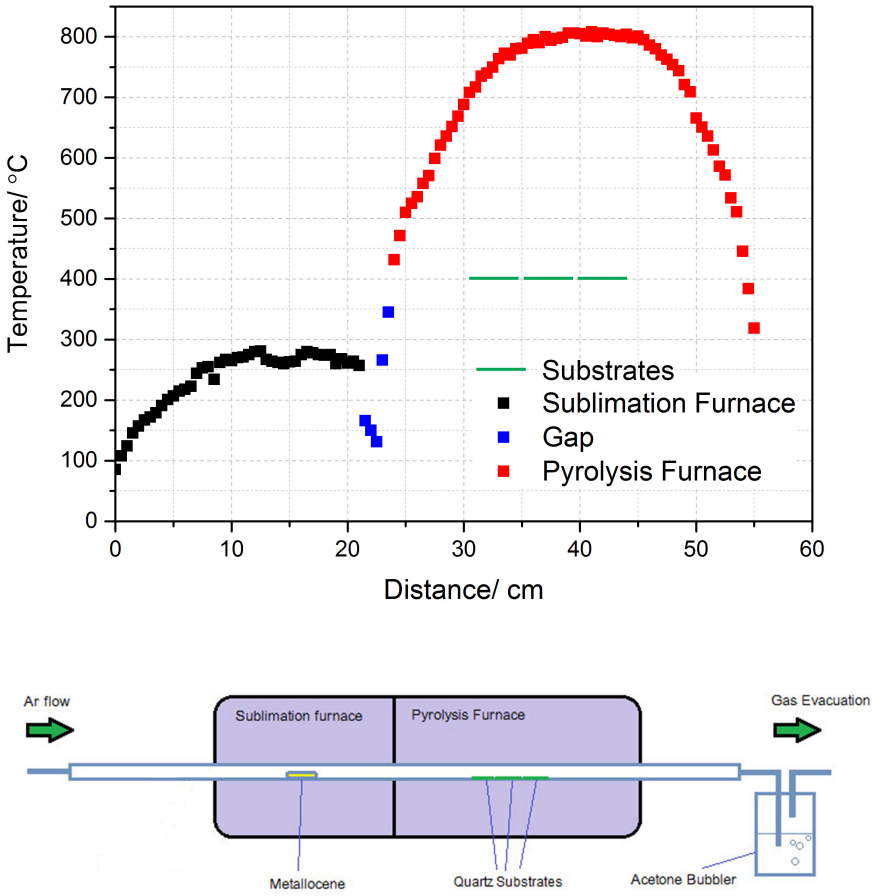


Figure 3.3: Schematic showing the position of the quartz substrates, placed 31-43 cm along the quartz tube, relative to the furnace temperature profile during the reaction, and in the full furnace setup (bottom).

3.2.2 Characterisation

The Fe/Co@MWCNT morphology was investigated using the JEOL-840F SEM operated at 5 kV and the filling in the MWCNT internal cavity was investigated by STEM and TEM using the JEOL-3000F, JEOL-ARM200F (carried out by Dr Juan Lozano), and JEOL-2100, operated at 300 kV, 200 kV and 200 kV, respectively. EDX maps confirmed the presence and distribution of Fe and Co within the MWCNTs. A Nanofactory TEM-STM holder, with a 0.25 mm Au wire as the moveable electrode, was used to investigate the effects of passing current through the Fe/Co@MWCNTs, carried out by Dr Juan Lozano. The Fe/Co@MWCNTs were mounted onto the Au wire by dipping the wire into loose Fe/Co@MWCNT powder. The Au wire was mounted on the 4-pin hat, then placed on

the sapphire piezo-electric. An additional Au wire was inserted at the other end of the TEM holder. The Nanofactory holder was placed inside the JEOL-ARM200F and the hat was moved until there was contact between the sample and the other Au wire. A bias was applied to the sample, and slowly increased. Electron energy loss spectroscopy (EELS) was conducted prior to, and after passing the current through the Fe/Co filling using *in situ* EELS analysis.

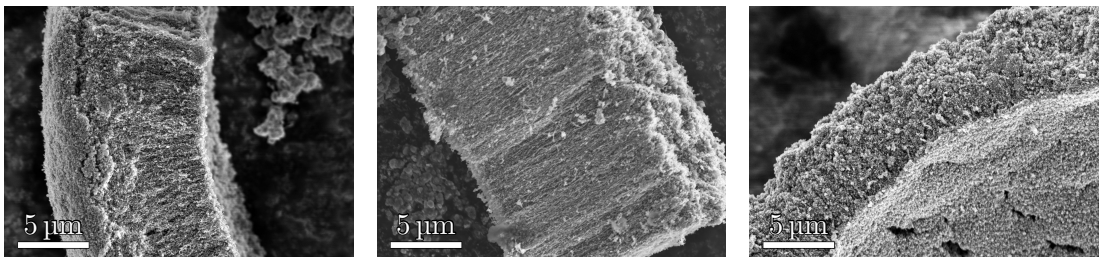
SQUID measurements and TGA were performed following the procedures described in Section 2.2.4. SQUID measurements were conducted to evaluate how changes Fe:Co in the Fe/Co@MWCNTs affected their magnetic properties, whilst TGA was carried out to establish the % filling.

Dr Phil Holdway performed X-ray powder diffraction (XRPD) (Siemens D5000 XRD) on the samples with a 2θ range of 10-100 2θ. Rietveld refinements were carried out using the TOPAS software by Miss Sarah Connolly to evaluate the abundance of different metal phases.

3.3 Results and Discussion

3.3.1 Structure and Morphology of Fe/Co@MWCNTs

All syntheses produced black, powdery deposits around the quartz tube and on the quartz substrates. SEM images of the bulk material and the deposits on the substrates are shown in Figure 3.4 and Figure 3.5, respectively, showing that MWCNTs were produced regardless of the precursor ratio. However, it was observed that the cobaltocene did not fully sublime during the 30 min reaction, indicating a slower sublimation rate for cobaltocene, compared to ferrocene. The incomplete sublimation of cobaltocene has a large impact on accurately assessing the effects of varying cobaltocene and ferrocene ratios on the magnetic properties of Fe/Co@MWCNTs produced.

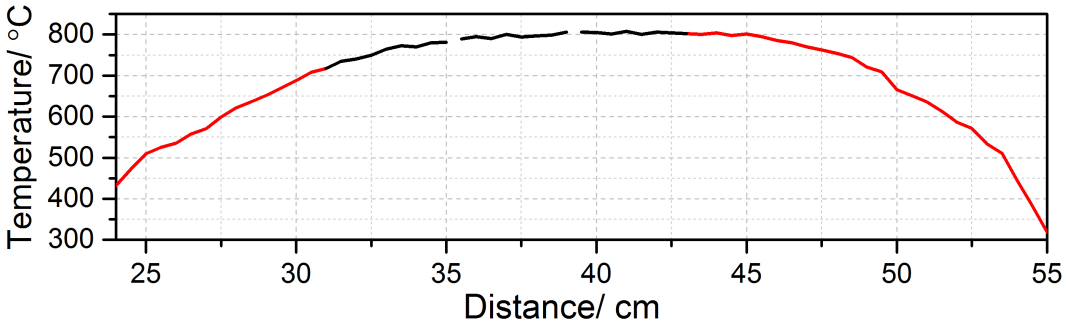


(a) FeCo-AB (b) FeCo-BB (c) FeCo-CB

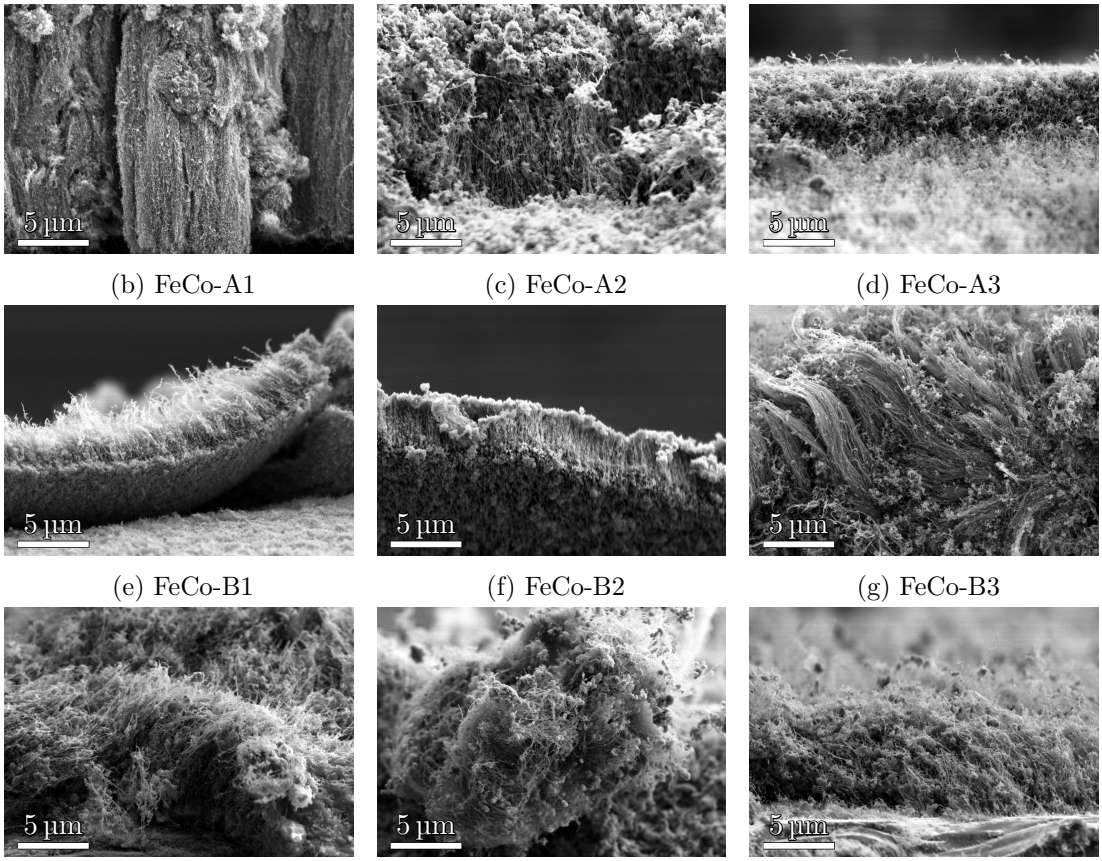
Figure 3.4: SEM images showing the bulk products from a) FeCo-AB (75:25), b) FeCo-BB (50:50), and c) FeCo-CB (25:75), where the ratios in the bracket indicate the ratios of ferrocene and cobaltocene used in the synthesis and the B indicates bulk sample.

The average Fe/Co@MWCNT lengths (Table 3.2) show the MWCNTs formed on the quartz substrates are consistently shorter than those deposited on the quartz tube. This is likely due to the layer of residual iron oxide on the quartz tubes from previous experiments, which may have assisted in catalysing MWCNT growth on the quartz tube. The range of lengths in the bulk materials is also consistently larger than for the substrate-grown material, likely because the MWCNTs are collected from the entire quartz tube length with MWCNT growth on.

The MWCNTs formed on the substrate are aligned (Figure 3.5), with less aligned MWCNTs observed for FeCo-C1-3 (Figure 3.5 h-j). Variation in the MWCNTs formed on the quartz substrates in different positions within the furnace is likely related to the local furnace temperature at the substrate location. As discussed in section 2.3.1, the furnace temperature is not constant throughout its entire length. The pyrolysis furnace temperature profile for a 3 cm furnace gap is plotted above the SEM images, along with the substrate positions, which were selected based on the growth region from trail experiments (Figure 3.5a). Only substrates 2 and 3 were in the temperature plateau region, which is likely to have some effect on the material grown. Evaluating the effect of the precise temperature on the properties of the material grown was beyond the scope of this investigation, as the focus was on understanding whether varying Fe to Co ratio within the MWCNTs affects their magnetic properties in a tunable manner. Due to the small amount of product grown on the substrates, and no significant differences across the materials produced on the substrates from a morphological perspective, only Raman was carried out on the materials grown on the substrates.



(a) Pyrolysis furnace temperature profile



(b) FeCo-A1 (c) FeCo-A2 (d) FeCo-A3

(e) FeCo-B1 (f) FeCo-B2 (g) FeCo-B3

(h) FeCo-C1 (i) FeCo-C2 (j) FeCo-C3

Figure 3.5: a) Graph showing the pyrolysis furnace temperature profile, alongside substrate position (black); the substrates are touching in the setup, but are shown separated in the graph. SEM images show the material grown on the substrates in positions b) 1, c) 2, and d) 3, for FeCoA (75:25), e) 1, f) 2, and g) 3, for FeCoB (50:50), and h) 1, i) 2, and j) 3, for FeCoC (25:75), where the ratios of ferrocene to cobaltocene used in the synthesis are in the brackets.

Reference Code	**MWCNT Average Length/ μm**	NP Average Diameter/ nm
FeCo-AB	18 ±7	65 ±45
FeCo-A1	21 ±3	-
FeCo-A2	9 ±3	-
FeCo-A3	8 ±3	-
FeCo-BB	14 ±6	17 ±10
FeCo-B1	3 ±2	-
FeCo-B2	4 ±1	-
FeCo-B3	9 ±2	-
FeCo-CB	8 ±5	39 ±28
FeCo-C1	6 ±2	-
FeCo-C2	8 ±2	-
FeCo-C3	5 ±1	-

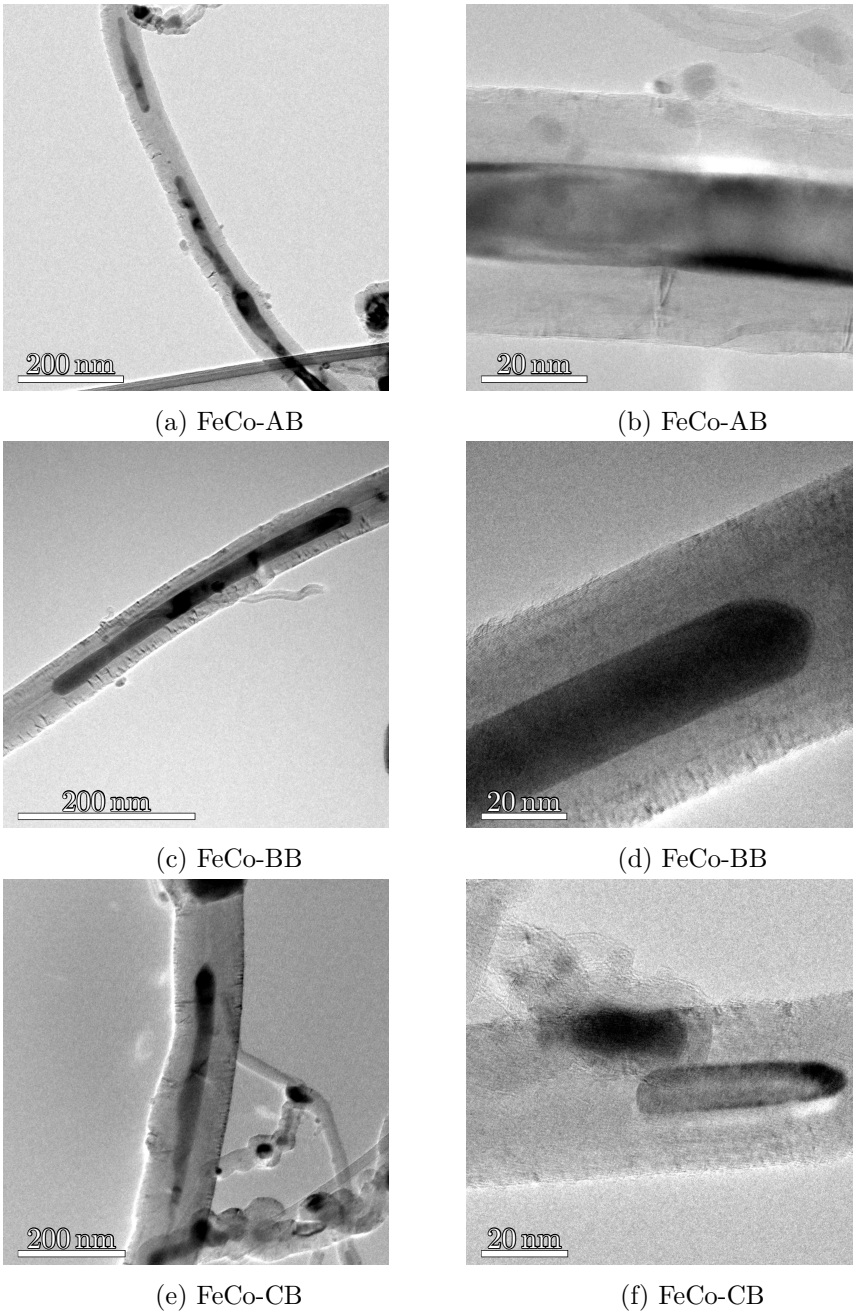
Table 3.2: The average length of Fe/Co@MWCNTs, and NP diameter, where A= 75:25, B= 50:50, and C= 25:75 ferrocene:cobaltocene ratios used in the synthesis, the substrate position is given by 1= 31-35, 2= 35-39 and 3= 39-43 cm along the quartz tube, and B= bulk sample.

3.3.2 TEM and EDX

Figure 3.6 shows representative TEM images of the filled MWCNTs produced with the different ferrocene:cobaltocene ratios, showing that MWCNTs with filled regions were successfully produced from all precursor mixtures. The mean fillings lengths were *ca.* 1.4±1 μm, 615±370 nm, and 575±440 nm for FeCo-AB, FeCo-BB and FeCo-CB, respectively. The MWCNTs were not fully filled, and the samples consisted of a mixture of empty MWCNTs, and MWCNTs with a diverse range of filling lengths.

EDX maps taken on the JEOL-2100 show an even distribution of Fe and Co within the filling, with no metal segregation for all syntheses (Figure 3.7, Figure 3.8 and Figure 3.9). The average Fe:Co ratio, given in Table 3.3, shows a large excess of Fe compared to the desired Fe:Co ratio for all cases. The large range of Fe:Co ratios observed across a range of EDX maps is reflected in the high standard deviations. Similarly, Kozhuarova reported *et al.* [12] variations in Fe:Co, with 30-40 wt.% of Fe, depending on the nanowire analysed. An excess of cobaltocene was used in their syntheses (2:1 cobaltocene to ferrocene) to

produce Fe_xCo_{1-x}, suggesting that large excesses of cobaltocene are necessary for forming Fe/Co@MWCNTs. The excess Fe within the MWCNT filling was expected as some cobaltocene remained in the crucible after the reactions. The lack of control in the Fe:Co ratio across different MWCNTs is a problem that needs to be addressed. The EDX spectra for the samples can be found in the appendix.

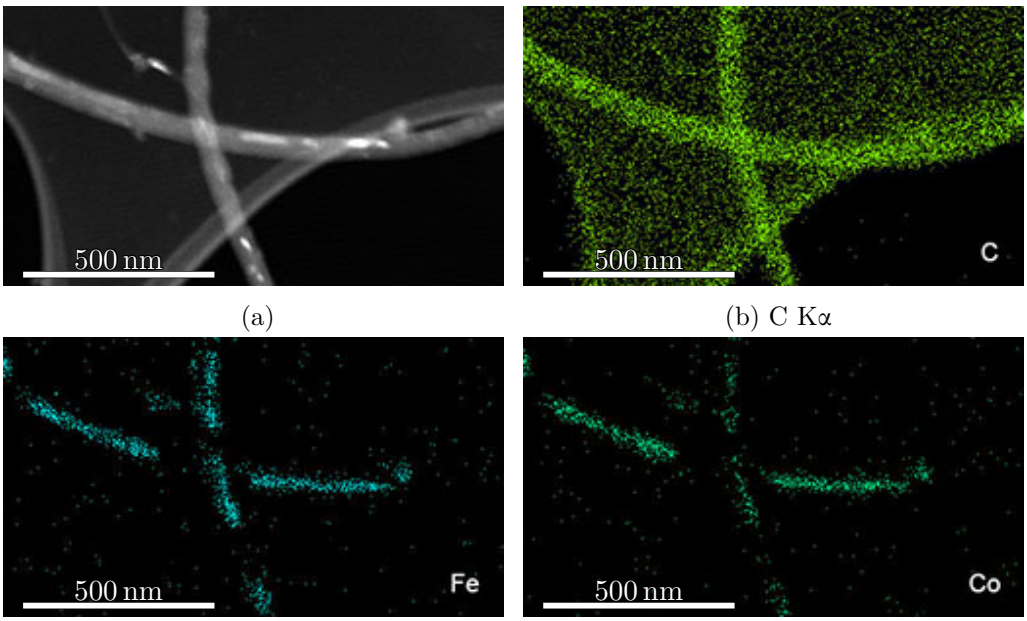


(a) FeCo-AB (b) FeCo-AB

(c) FeCo-BB (d) FeCo-BB

(e) FeCo-CB (f) FeCo-CB

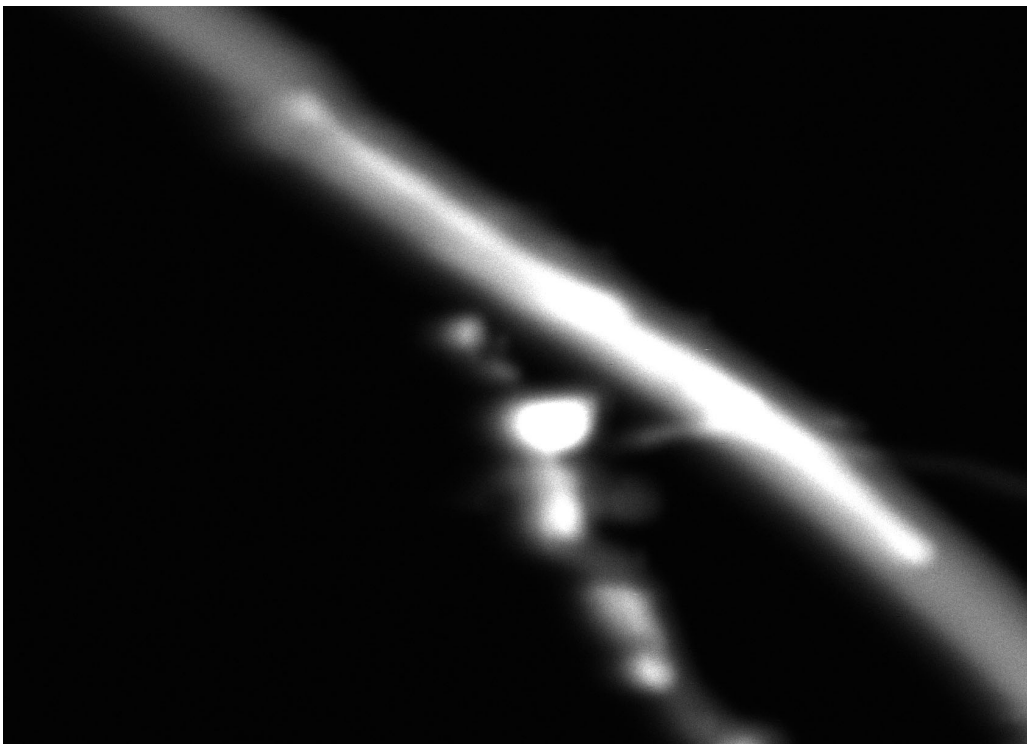
Figure 3.6: TEM image showing the filling of a Fe/Co@MWCNT produced for a and b) FeCo-AB (75:25), and c and d) FeCo-BB (50:50), e and f) FeCo-CB (25:75), with the brackets showing the ratio of ferrocene to cobaltocene used in the synthesis.



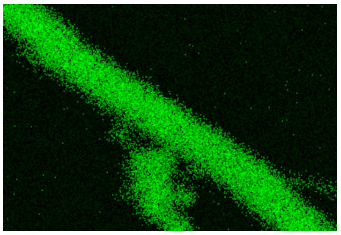
(a) (b) C Kα

(c) Fe Kα (d) Co Kα

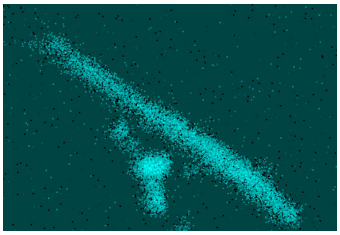
Figure 3.7: a) STEM image taken on the JEOL2100 of the site of EDX map collection. EDX maps showing the distribution of b) C, c) Fe, and d) Co within MWCNTs from FeCo-BB (50:50 ferrocene to cobaltocene synthesis). The EDX maps were taken by measuring the Kα emission for the elements listed above and show the random distribution of Fe and Co within the filled regions of the MWCNT.



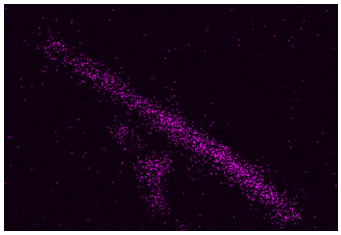
(a)



(b) C Kα

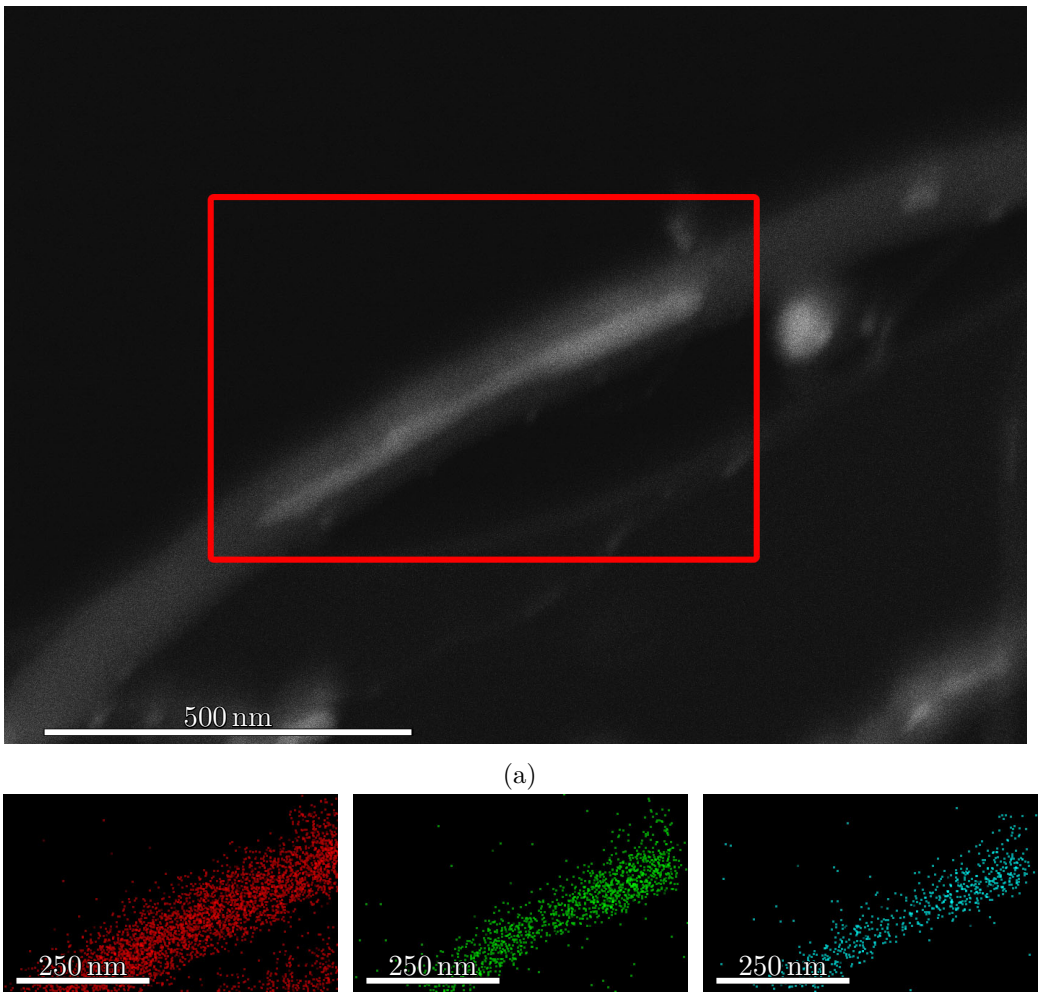


(c) Fe Kα



(d) Co Kα

Figure 3.8: a) STEM image collected from FeCo-AB sample (75:25 ferrocene to cobaltocene synthesis) and the corresponding EDX maps obtained for b) C, c) Fe and d) Co within the Fe/Co@MWCNT. The image is representative of the typical EDX maps collected for the FeCo-AB samples, which showed the even distribution of Fe and Co across the filled regions of the MWCNT. The average ratio of Fe:Co is 6:1, indicating that there was double the amount of Fe, compared to the originally intended Fe:Co ratio of 3:1.



(a)

(b) C Kα (c) Fe Kα (d) Co Kα

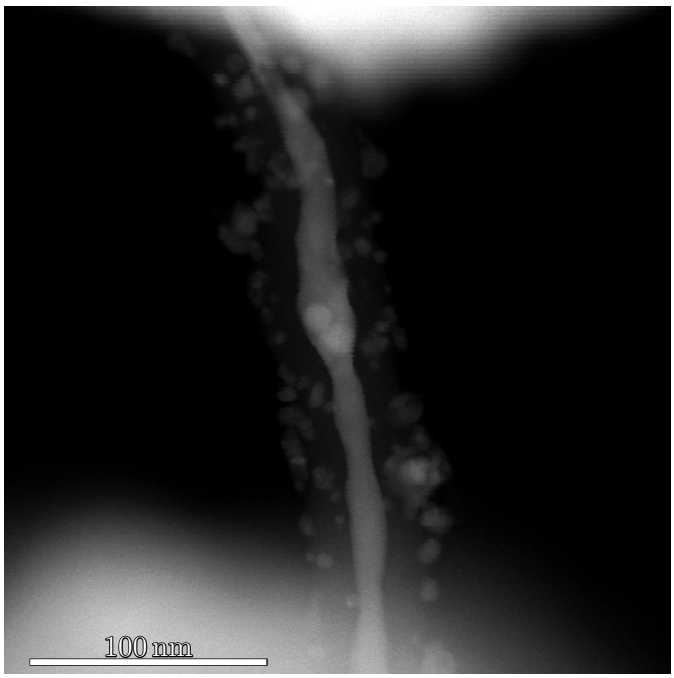
Figure 3.9: a) STEM image collected from FeCo-CB (25:75 ferrocene to cobaltocene synthesis) and the corresponding EDX maps obtained for b) C, c) Fe and d) Co within the Fe/Co@MWCNT. The image is representative of the typical EDX maps collected for the FeCo-AB samples, which showed Fe and Co is evenly distributed across the filled regions of the MWCNT. The average ratio of Fe:Co is 2.7:1, indicating that there was a large excess in the amount of Fe, compared to the originally intended Fe:Co ratio of 0.33:1.

Reference Code	Ratio Fe:Co from EDX	SD
FeCo-AB (75:25)	6:1	1.3
FeCo-BB (50:50)	2:1	2.1
FeCo-CB (25:75)	2.7:1	1.5

Table 3.3: The average ratio of Fe:Co inside the filling, as calculated from taking the average of the Fe:Co from five EDX maps taken across the sample. The ratios show that there is a large excess in Fe in all cases.

EELS maps taken at higher resolution on the JEOL-ARM200F by Dr Juan Lozano showed a MWCNT decorated with Co NPs, with an Fe core (Figure 3.10). If all the MWCNTs are Fe@MWCNTs decorated with Co NP, then the Co NPs must exclusively decorate the MWCNTs where the Fe filling was present, as no EDX maps showed the Fe or Co alone. This suggests that the Fe filling has an influence on where the Co NPs deposit, potentially due to magnetic interactions. No reports were found on synthesising Fe@MWCNTs decorated with Co NPs in one step, however, Wang *et al.* [217] decorated Fe@MWCNTs with FeCo NPs post synthesis. The paper did not suggest that the Fe filling has an influence on NP distribution, with TEM images showing the random distribution of NPs across the MWCNTs, regardless of Fe filling location.

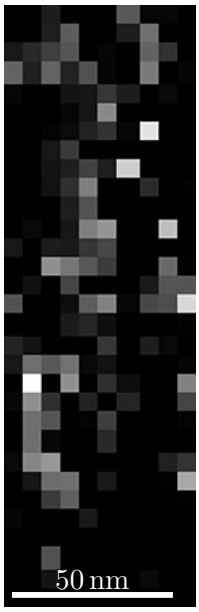
A more likely explanation is that the Co-NP decorated Fe@MWCNT imaged in the JEOL-ARM was selected by chance, rather than being representative of the entire sample. Figure 3.11 shows a typical image at lower magnification; the sample contains a mixture of MWCNTs, hllarge metal clusters, and metal NPs of varying sizes. All samples contained a similar mixture of materials. Quantifying the ratio of each of these materials within the sample was difficult, obtaining the mass of each material type would be the most useful way to assess the distribution of NPs, metal clusters and CNTs within the samples. The contribution of these byproducts on the data collected on the bulk samples by XRD, SQUID, Raman and TGA is uncertain without separating the materials from one another. This topic needs to be explored further to understand the validity of the data reported here. The red ring in Figure 3.11a shows an unusual MWCNT decorated with a large number of NPs. A higher magnification image (Figure 3.11b), shows the MWCNT has a very similar appearance to the one imaged in the JEOL-ARM. Based on Figure 3.11, it is likely that the majority of the MWCNTs have the Fe and Co within the filling. The production of Co-NP decorated Fe@MWCNTs produced here may be related to the slower cobaltocene sublimation rate; if only Co was remaining in the gaseous phase towards the end of the reaction, then Co NPs may form and deposit on the Fe@MWCNTs.



(a)

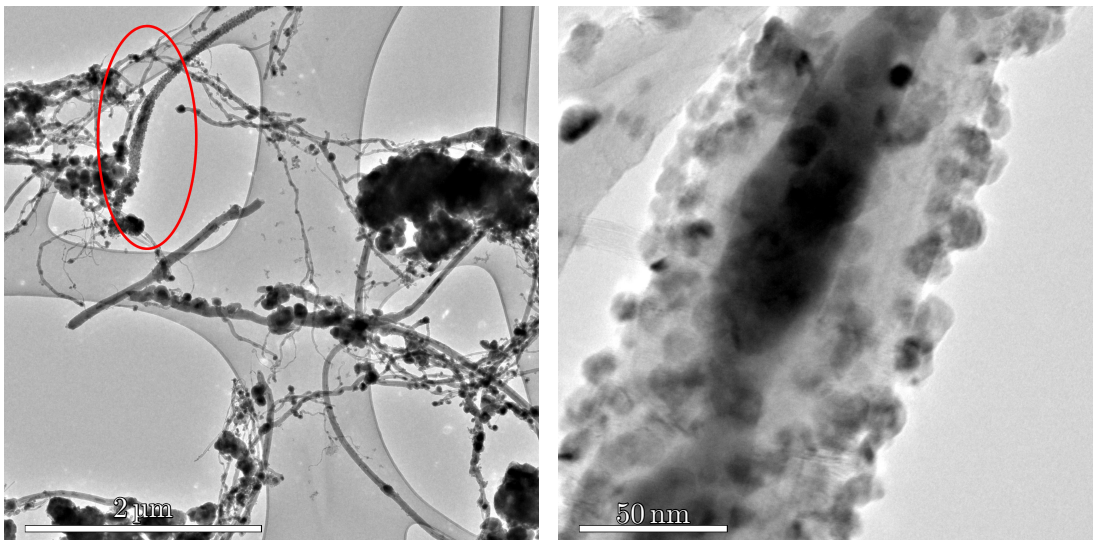


(b) Fe L edge



(c) Co L edge

Figure 3.10: a) A dark field STEM image taken of the Fe/Co@MWCNT prior to applying bias to the MWCNT. The STEM image clearly shows a filled MWCNT decorated with NPs. EELS maps showing the distribution of b) Fe and c) Co within the Fe/Co@MWCNT. Measurements were taken by measuring the the L edge for EELS. The EELS maps suggest that the MWCNT is an Fe@MWCNT, decorated with Co NPs, based on the distribution of Fe and Co within the sample. Image taken on the JEOL-ARM by Dr. Juan Lozano.

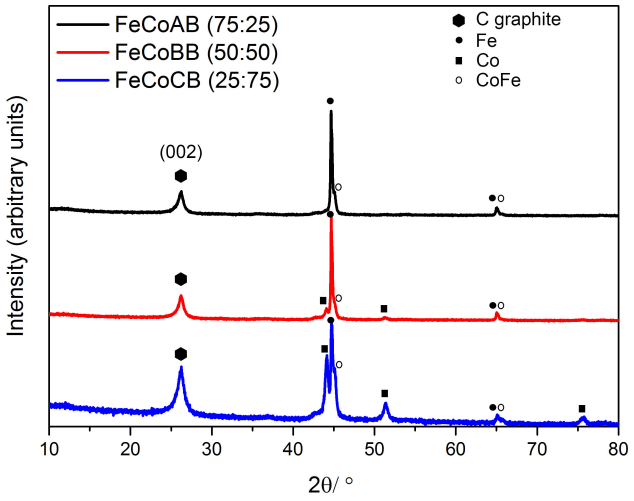


(a) (b)

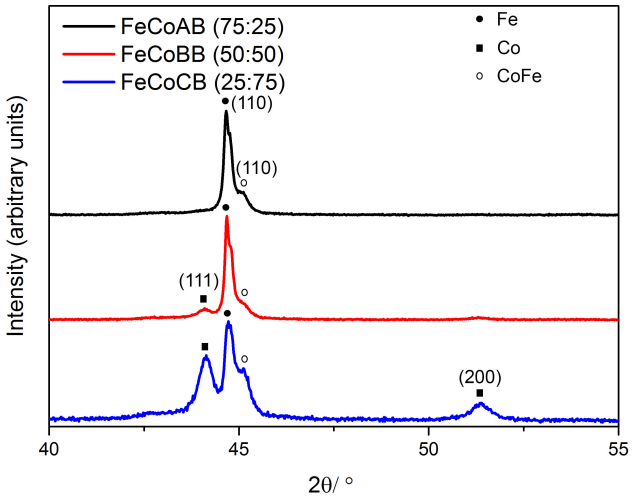
Figure 3.11: TEM images from FeCo-BB (50:50 ferrocene to cobaltocene used in synthesis) showing a) a typical image obtained at lower magnification of the sample. However, the red ring shows an unusual MWCNT, which is highly decorated in NPs. b) A higher magnification image showing the decorated MWCNT, similar to the MWCNT imaged on the JEOL-ARM200F, suggesting it was an atypical MWCNT from the sample.

3.3.3 Purity of Fe/Co@MWCNTs and Structure of Filling

PXRD pattens of the bulk materials for each synthesis showed Fe, Co, and FeCo phases (Figure 3.12). All 3 precursor ratios had peaks at *ca.* 27 2θ from the graphitic C (002) plane in MWCNTs [95], 44.2 2θ for the (110) plane in α-Fe and a small shoulder at *ca.* 45 2θ, which fits the (110) plane of FeCo [219]. The peak position at *ca.* 65 2θ overlaps for Fe and FeCo. High angle XRD measurements were taken to distinguish between FeCo and $Fe_{70}Co_{30}$, which have the same lattice parameter and space group and only differ in unit cell occupancy. These high angle measurements confirmed the FeCo alloy species was FeCo, with peaks at *ca.* 93 2θ correspond to the (211) plane of FeCo [219] (Figure 3.13). With increases in wt.% cobaltocene in the precursor, additional peaks, of increasing intensity, corresponding to Co at *ca.* 44, 52 and 76 2θ are observed.



(a)



(b)

Figure 3.12: XRD patterns for FeCo-AB (25:75 (blue)), FeCo-BB (50:50 (red)) and FeCo-CB (75:25 (black)) samples, showing a) the entire 2θ range scanned, from 10 to 80 2θ and b) a close up of the 2θ range between 40-55 2θ. The Co peaks at *ca.* 43-45 2θ increase with increasing cobaltocene ratio in the precursor.

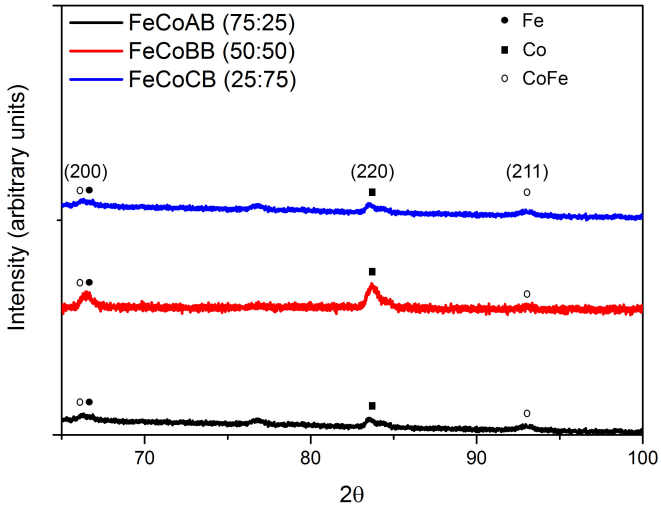


Figure 3.13: High angle XRD pattern, from 70-100 2θ, for FeCo-AB (25:75 (blue)), FeCo-BB (50:50 (red)) and FeCo-CB (75:25 (black)). The high angle measurements confirmed the presence of FeCo in the samples.

Rietveld refinement was used to calculate the wt. % of each phase within the bulk samples, revealing that the wt. % of FeCo does not significantly change with variations in precursor ratio (Table 3.4). The minor change in wt. % FeCo phase with changes in precursor ratios suggests that segregated Fe and Co phases form preferentially over FeCo alloy phases. Grobert *et al.* [13], also observed that pyrolysis of nickelocene, ferrocene powder mixtures preferentially formed segregated metal phases, rather than alloy nanowires. This preference for segregated metal phases may be caused by the differences in precursor sublimation rate influencing the mix of Fe and Co present during the reaction. Initially, there may be a higher amount of Fe present in the pyrolysis furnace, due to the faster sublimation rate of ferrocene, resulting in Fe phases forming first within the MWCNTs.

Phase	FeCo-AB/ %	FeCo-BB/ wt. %	FeCo-CB/ wt. %
FeCo	7	5	6
Fe	15	14	4
Co	1	4	10
Graphite	77	77	80
Fit	1.47	1.44	1.30

Table 3.4: The wt. % of Fe, Co and FeCo phases within the samples, calculated by Rietveld refinement, where FeCo-AB, FeCo-BB and FeCo-CB were synthesised using 75:25, 50:50 and 25:75 ratios of ferrocene to cobaltocene precursors, respectively. A good fit of the data to calculated XRD patterns was obtained for all PXRD patterns. XRD was carried out on bulk samples.

The Fe/Co values obtained from XRD, are 2.5, 1.8 and 0.5, for FeCo-AB, FeCo-BB and FeCo-CB, respectively, compared to 6.2, 2 and 2.7, respectively from EDX (Figure 3.14). The Fe/Co values the syntheses aimed to obtain were 3, 1 and 0.33 for syntheses carried out with 75:25, 50:50 and 25:75 ferrocene:cobaltocene ratios. Whilst the Fe/Co values calculated from XRD are much closer to the desired number, the Fe/Co obtained from EDX are significantly higher than desired. These large differences observed between the Fe/Co values obtained from XRD and EDX are due to the bulk versus individual MWCNT methods used. The large variations in Fe/Co measured from EDX supports the idea of metal segregation occurring because of the inconsistent amounts of Fe and Co entering different MWCNTs over the course of the reaction, leading to discontinuous fillings which further encourage metal segregation due to filling distances. Controlling the wt. % of each phase within the Fe/Co@MWCNTs is likely to be difficult, especially with the different ferrocene and cobaltocene sublimation rates. The distribution of Fe and Co within individual Fe/Co@MWCNT, as measured across multiple (*ca.* 5 images per ferrocene:cobaltocene synthesis ratio) Fe/Co@MWXNTs by EDX , suggests that varying ferrocene and cobaltocene ratios is not an accurate or producible way of synthesising Fe/Co@MWCNTs filled with controlled Fe and Co ratios. However, as applications will likely use large quantities of these Fe/Co@MWCNTs, the bulk value is arguably more important.

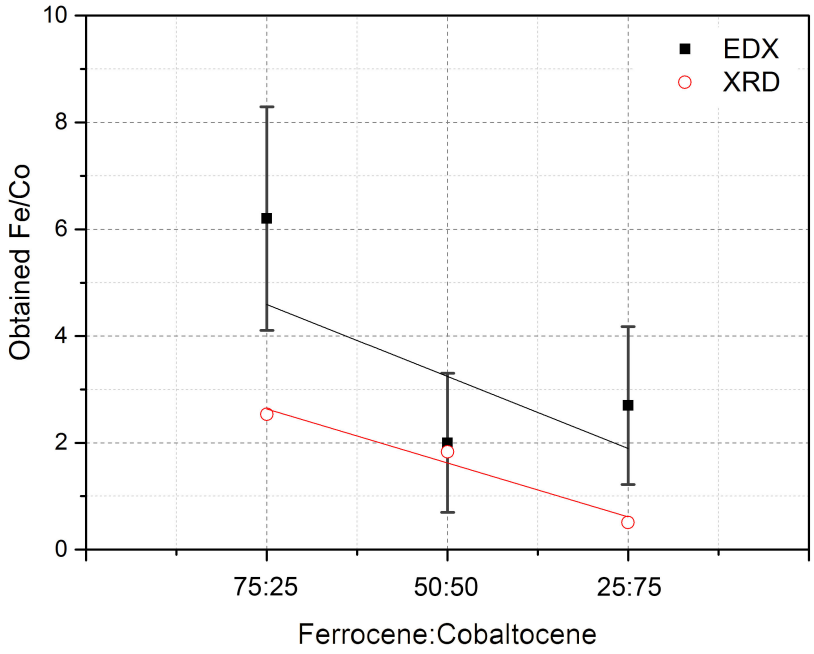


Figure 3.14: Graph showing trends in calculated Fe/Co values, obtained from EDX (black) and XRD (red), for the syntheses with varying ferrocene:cobaltocene ratio.

The % filling of the Fe/Co@MWCNTs was investigated by TGA and showed three distinctly different mass loss curves (Figure 3.15). FeCo-AB has the highest oxidation resistance, with an initial oxidation temperature of *ca.* 435 °C. Both FeCo-BB and FeCo-CB have an initial mass loss temperatures of 380 °C, with the steep gradient indicating that the initial mass loss is rapid. The mass loss rate for FeCo-BB and FeCo-CB decreases with increasing temperature, suggesting that the samples contains two classes of carbon. The initial mass loss corresponds to less graphitic C that decomposes, with the rapid mass loss indicating a narrow sample variation. This less graphitic carbonaceous material accounts for *ca.* 20 % and 30 % of FeCo-BB and FeCo-CB, respectively. The first derivative of the TGA curves showed the mass loss rate was fastest at *ca.* 500, 420 and 430 °C for FeCo-AB, FeCo-BB and FeCo-CB, respectively, indicating that a large amount of the sample was broken down at the initial decomposition temperature (Figure 3.15b-d).

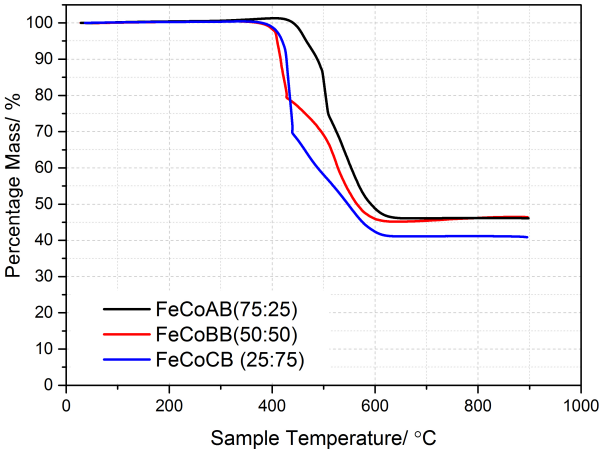
The initial % mass for all three samples remains unusually flat prior to mass decomposition. Typically, some catalyst particles oxidation occurs, resulting in a % mass increase for Fe@MWCNTs and, to a lesser extent, conventional MWCNTs samples prior to decomposition. One explanation for the % mass increase absence could be related to the presence of Co, which is more resistant to oxidation than Fe, preventing the expected increase in % mass. Similar, flat mass loss curves were obtained by Ramesh *et al.* [220] in their TGA

studies of Co@MWCNTs.

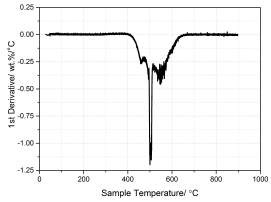
The % residual mass of FeCo-BB and FeCo-AB was *ca.* 47 %, whilst FeCo-CB had a lower metal oxide percentage of *ca.* 40 %. The lower % residual mass for FeCo-CB is likely because of incomplete cobaltocene sublimation within the reaction time. The lower amount of sublimed cobaltocene will have a larger effect on filling percentages with precursor ratios containing a higher amount of cobaltocene.

Histograms of the Fe/Co@MWCNT diameter distribution, with a group size of 10 nm, (Figure 3.16) show the variation in Fe/Co@MWCNT diameter distribution across the three precursor ratios. FeCo-BB (Figure 3.16b) had the narrowest diameter distribution, 10-90 nm, with the majority of the MWCNTs having a diameter of *ca.* 70 nm. The largest diameter distribution was observed for FeCo-AB, spanning from 10-280 nm, this sample contained some very wide CNTs, resulting in a larger diameter distribution. The diameter distribution for MWCNTs in sample FeCo-CB was 10-130 nm.

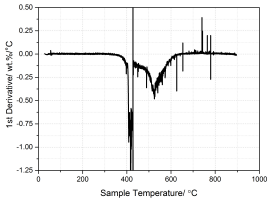
Correlating mass loss to MWCNT distribution, the mass loss at *ca.* 420 °C for FeCo-BB and FeCo-CB are likely to be the loss of defective MWCNTs, or MWCNTs with small diameters. These smaller diameter MWCNTs make up a larger proportion of measured diameters than for FeCo-AB, which may explain why there is such a sharp initial mass loss for FeCo-BB and FeCo-CB. For FeCo-AB, the much larger diameter distribution means that there is no sudden mass loss.



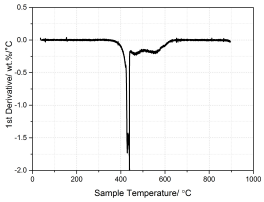
(a)



(b) FeCo-AB

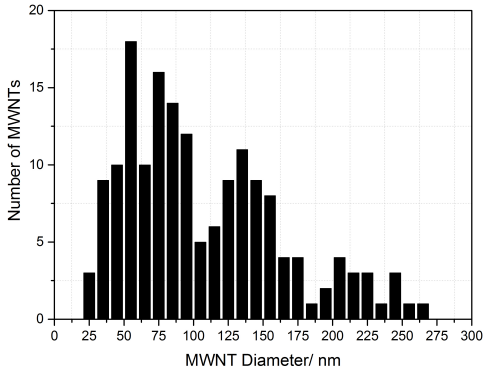


(c) FeCo-BB

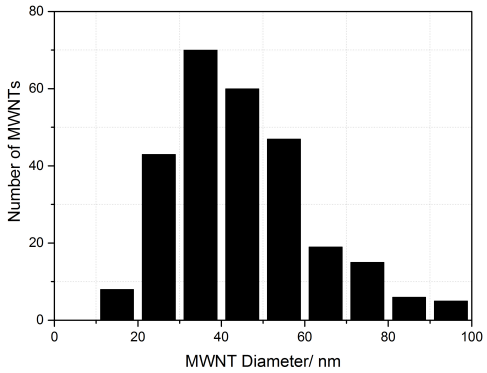


(d) FeCo-CB

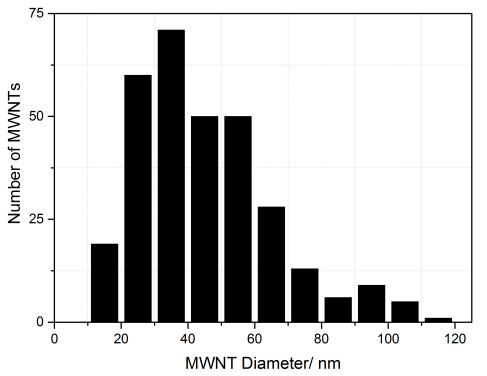
Figure 3.15: Graphs showing a) TGA mass loss curves for FeCo-AB (75:25 (black)), FeCo-BB (50:50 (red)), and FeCo-CB (25:75 (blue)). The first derivative shows changes in decomposition rate for b) FeCo-AB, c) FeCo-BB, and d) FeCo-CB. The ratio of ferrocene to cobaltocene given in brackets. TGA was carried out on bulk samples.



(a) FeCo-AB



(b) FeCo-BB



(c) FeCo-CB

Figure 3.16: Graph showing the distribution of MWCNTs produced via CVD of a) FeCo-AB (75:25), b) FeCo-BB (50:50) and c) FeCo-CB (25:25), where the ratios in the brackets show the ratio of ferrocene to cobaltocene in the precursor mixtures. It is clear the the MWCNTs in FeCo-AB have a much larger range in diameters, compared to FeCo-BB and FeCo-CB. The modal diameter range is 50-60, 30-40, and 30-40 for FeCo-AB, FeCo-BB and FeCo-CB, respectively.

The $I_{D/G}$ for the bulk material and all substrates, per experiment is shown in Table 3.5. The high $I_{D/G}$ values, between 0.5-0.79, indicate that the Fe/Co@MWCNTs produced were defective. For all precursor mixtures investigated, substrate 1 had the highest $I_{D/G}$ value, of the three substrates. This may be related to the furnace temperature profile as substrate 1 was not position in the plateau region of the furnace, leading to slight temperature fluctuations, and a lower local temperature in this region. These temperature fluctuations may have a small influence on precursor breakdown and MWCNT growth. Whilst substrates 2 and 3 are in the constant temperature range, the $I_{D/G}$ values are still high. The generally high $I_{D/G}$ values for all positions suggests that the temperatures selected for T_{sub} and T_{pyro} were not optimised. The defective nature of these Fe/Co@MWCNTs impacts their mechanical strength, which is an important factor that affects their suitability for switch applications. For switches, the moving component needs to be flexible and withstand moving from 'on' to 'off' positions repeatedly without failing.

Reference Code	$\mathbf{I_{D/G}}$
FeCo-AB (75:25)	0.55 ±0.01
FeCo-A1 (75:25)	0.69 ±0.03
FeCo-A2 (75:25)	0.57 ±0.02
FeCo-A3 (75:25)	0.58 ±0.03
FeCo-BB (75:25)	0.64 ±0.03
FeCo-B1 (50:50)	0.79 ±0.03
FeCo-B2 (50:50)	0.74 ±0.01
FeCo-B3 (50:50)	0.76 ±0.02
FeCo-CB (75:25)	0.47 ±0.01
FeCo-C1 (25:75)	0.74 ±0.04
FeCo-C2 (25:75)	0.72 ±0.04
FeCo-C3 (25:75)	0.50 ±0.02

Table 3.5: The $I_{D/G}$ obtained for different substrate positions for different ratios of ferrocene to cobaltocene precursor used during synthesis, where A= 75:25, B= 50:50, and C= 25:75 ferrocene:cobaltocene ratios used in the synthesis, the substrate position is given by 1= 31-35, 2= 35-39 and 3= 39-43 cm along the quartz tube, and B= bulk sample.

3.3.4 Magnetic Properties of Fe/Co@MWCNTs

The magnetisation curves for FeCo-AB, FeCo-BB and FeCo-CB were compared to those for Fe@MWCNTs and Co@MWCNTs at 300 and 4 K (Figure 3.17). All samples display soft, ferromagnetic behaviour at both temperatures. This soft ferromagnetic behaviour is desirable for electrical switches, as their easy magnetisation and demagnetisation means the switch will move back to its original position upon removal of the magnetic field.

The M_s and H_c values given in Table 3.6 show that M_s increases, with increasing ferrocene:cobaltocene precursor ratio. The Fe/Co@MWCNTs produced from all precursor ratios possessed higher M_s values compared to Fe@MWCNTs at both 300 and 4 K, in agreement with the trend of FeCo alloys possessing higher M_s than the pure metals [90, 213, 221, 222], however the Co@MWCNTs had comparable M_s values to FeCo-CB. The M_s of the Fe/Co@MWCNTs depends on the combination of the different phases inside the Fe/Co@MWCNTs, which complicates the comparison of their magnetic properties to Fe@MWCNTs and Co@MWCNTs, as it is difficult to attribute the contribution of each phase to the overall obtained M_s. However, Table 3.6 shows that M_s decreases with decreases in Fe:Co ratio, although this may be just coincidental. At 4 K (Figure 3.17b), the M_s of Co@MWCNTs increases by over double, from *ca.* 55 at 300 K to 105 emu/g at 4 K, this M_s at 4 K is significantly larger than those for Fe/Co@MWCNTs. It is uncertain what is causing this increase, and similar observations were not reported in the literature.

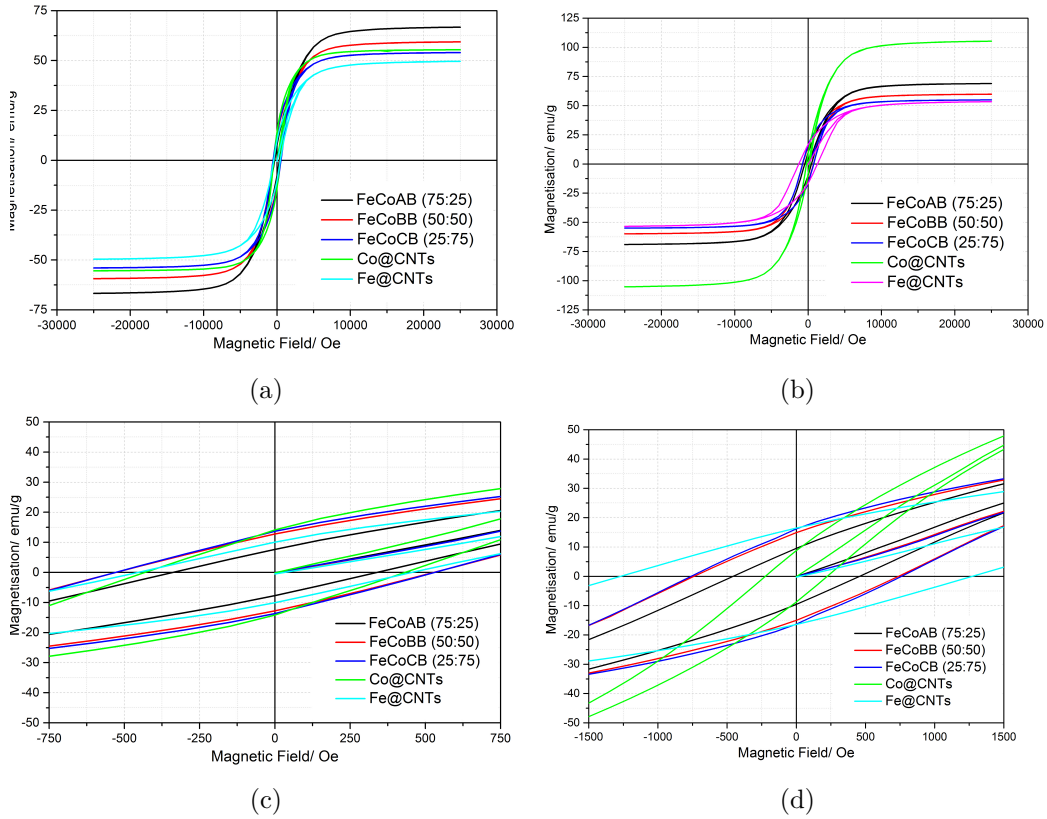


Figure 3.17: Graphs showing the hysteresis loops for Fe@MWCNTs (cyan), Co@MWCNTs (green), FeCo-AB (black (75:25)), FeCo-BB (red (50:50)), and FeCo-CB (25:75 (blue)) at a) 300 K and b) 4 K, where the ferrocene:cobaltocene precursor ratio is given in the brackets. H_c is shown more clearly for d) at 300 K and e) at 4 K.

Code/ MWCNT Type	**M_s (300 K)/ emu/g**	**M_s (4 K)/ emu/g**	**H_c (300 K)/ Oe**	**H_c (4 K)/ Oe**
Fe@MWCNTs	49	53	457	1268
FeCo-AB (2.5:1)	67	70	350	467
FeCo-BB (1.8:1)	59	59	531	752
FeCo-CB (0.5:1)	54	55	531	757
Co@MWCNTs	55	104	436	226

Table 3.6: Table showing M_s and H_c at 300 and 4 K for Fe@MWCNTs, Co@MWCNTs and FeCo-AB, FeCo-BB and FeCo-CB, where the ratio in the brackets shows the ratio of Fe:Co, as calculated from XRD. A= 75:25, B= 50:50, and C= 25:75 ferrocene:cobaltocene ratios used in the synthesis. All SQUID measurements were taken on bulk samples.

The H_c for the Fe/Co@MWCNT and Fe@MWCNT samples increased at 4 K, compared to 300 K. This increase in particularly pronounced for the Fe@MWCNTs, where H_c increases from 457 to 1268 Oe, at 300 and 4 K, respectively. Similar increases in H_c, from 450 to 2000 Oe for measurements taken at room temperature and 5 K, respectively, has previously been reported for Fe@MWCNTs [41]. For the Co@MWCNTs, the inverse is observed, with H_c decreasing by almost half, from 436 to 226 Oe, at 300 and 4 K, respectively. The H_c of FeCo-BB and FeCo-CB are higher than those for both Fe@MWCNTs and Co@MWCNTs at room temperature. However, a significantly higher H_c of 928 Oe at room temperature was reported by Elias *et al.* [90] for Fe/Co@MWCNTs. The much lower H_c observed here is likely attributed to the mixture of phases present inside the Fe/Co@MWCNTs, compared to the monocrystalline Fe/Co@MWCNTs produced by Elias [90].

The H_c of $Co_{1-x}Fe_x$ alloy nanowires produced by AAO increased with increasing Fe content, up to a maximum of 2150 Oe, for x= 0.55 [207]. This trend was not observed for the Fe/Co@MWCNTs produced by varying the ferrocene to cobaltocene ratio. Whilst the H_c does increase going from Co@MWCNTs to FeCo-CB (Fe:Co ratio of 0.5:1, as determined by XRD), FeCo-BB and FeCo-AB very similar H_c values at 300 and 4 K. This could suggest that changing the mixture of phases does not significantly impact their magnetic properties. However, as FeCo-AB displayed lower H_c, and higher M_s values compared to FeCo-BB and FeCo-CB, this is unlikely to be the case.

The mixture of Fe, Co and FeCo phases observed from XRD will impact the magnetic properties of the Fe/Co@MWCNTs, however assigning the phases within the Fe/CO@MWCNTs to the overall magnetic properties displayed is difficult. From PXRD, the % of FeCo in the MWCNTs was relatively similar, so it is likely that the differences in magnetic properties are related to the % of Fe and Co present in the sample. The lower M_s for FeCo-CB may be due to the decrease in % Fe in the sample.

Whilst producing Fe/Co@MWCNTs does lead to changes in their magnetic properties, it is difficult to reliably tune the magnetic properties of the Fe/Co@MWCNTs with the currently used method. This difficulty in tuning the magnetic properties is further enhanced by the mixture of materials present within the samples. All samples produced contained a mixture of MWCNTs and NPs, these NPs were not removed before carrying out the SQUID measurements. It is likely that the ratio of NPs to Fe/Co@MWCNTs is the most significant factor governing the observed magnetic properties of the samples. Being able to

separate the contribution of the NPs to the M_s and H_c observed here is of high importance to be able to gain a clearly idea of how changing the Fe:Co ratio within the MWCNT filling affects the magnetic properties of the Fe/Co@MWCNTs. Carrying out measurements on pure Fe/Co@MWCNTs samples should be carried out in the future.

The incomplete cobaltocene sublimation and the inability to control Fe and Co distribution within the MWCNTs means that the magnetic properties are likely to change with each synthesis. Having inconsistent magnetic properties with each synthesis is detrimental for applications, such as the multiple switch system, which rely on having a specific range of M_s or H_c values. Improving the synthesis method, or changing the approach used to tuning magnetic properties should be considered (chapter 6).

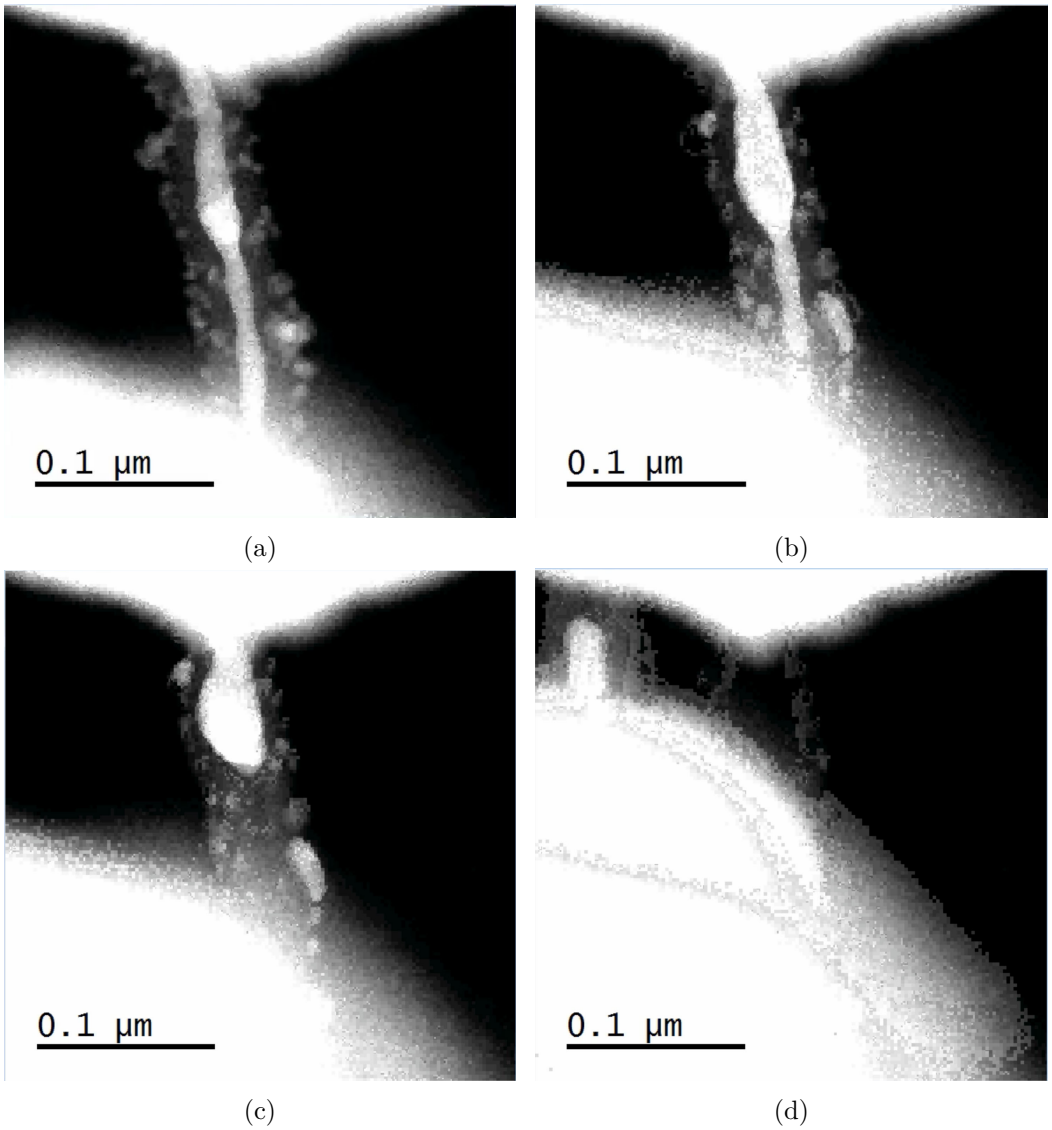
3.3.5 Evaluating the Effect of Current on Fe/Co@MWCNTs

Dr Juan Lozano carried out the *in situ* TEM measurements discussed in this section. The Fe/Co@MWCNT used for bias testing was the Co-NP decorated Fe@MWCNT imaged on the JEOL-ARM200F (Figure 3.10). Applying a bias to the Co-NP decorated Fe@MWCNT from FeCo-BB led to large changes in the distribution of Fe and Co within the MWCNT. Extracted images from the video taken whilst applying bias, show initially, little change occurs with increasing current (Figure 3.18a). With increasing current, the Co NPs decorating the MWCNT start to coalesce, forming larger NPs (Figure 3.18b). Further increase in current causes the Fe filling to move, concentrating at one end of the MWCNT (Figure 3.18c). The MWCNT distorts, as the inner diameter of the MWCNT swells to accommodate the increased concentration of Fe. Eventually, the MWCNT breaks, due to joule heating, similar to as reported by Aslam, *et al.* [218] (Figure 3.18d).

It is difficult to determine whether the changes to the Fe filling and Co NPs were influenced more by the temperature or the current, especially as it is unknown how good the contact was between the MWCNT and the Au wires at the ends of the Nanofactory holder. Unfortunately, values for the current passing through the MWCNT were not recorded and the temperature inside the MWCNT is unknown. However, the Fe filling must be molten when the filling starts to move, indicating that the temperature range inside the MWCNT must be around the melting temperature of Fe. The melting temperatures of bulk Fe and Co are 1538 and 1495 °C, respectively. Taking into account that melting point is reduced at the nanoscale, due to the larger surface to volume ratio at the nanoscale [223],

the temperature inside the MWCNT should be much lower than this. Further, the melting temperature of small particles is both size and shape dependent, with the melting temperature decreasing with decreasing particle size [224].

The melting temperature of Co NPs is likely to be lower than that of the Fe filling, due to the difference in bond strength between the two elements and finite size effects. The size of the Co NPs is much smaller than that of the Fe nanowire (Figure 3.10 on page 84), which further decreases the melting temperature of Co, compared to the bulk. Together, this explains why the Co NPs start to coalesce and move before the Fe filling.



(a) (b)

(c) (d)

Figure 3.18: *In situ* TEM images extracted from the video taken whilst passing an increasing current through an Fe@MWCNT decorated with Co NPs. The images show a) the initial structure of the MWCNT, b) the Co NPs starting to coalesce to form larger NPS, whilst the Fe filling starts to collect together, causing the inner diameter of the MWCNT to swell, c) complete movement of the Fe filling, such that it has collected in a large agglomerate at the top of the MWCNT, and d) MWCNT breakdown due to joule heating.

STEM images and EELS maps collected after applying bias to the MWCNT show the Co NPs and Fe nanowire are no longer segregated (Figure 3.19). Instead, the transition metals amassed together to form much larger NPs, with the largest NP in the STEM image being *ca.* 100 nm in diameter. EELS maps collected in the red box in Figure 3.19a for Fe and Co (Figure 3.19b-e) show the Fe and Co are now randomly distributed throughout the particles, with an estimated ratio of 63:37 ± 10 % Fe to Co for the largest particle. However, EELS maps on the particle in the green box (Figure 3.19a) mostly contain Fe, with only a small amount of Co. The random redistribution of Fe and Co after the metals had collected at one end of the MWCNT due to the applied current has led to NPs with differing Fe/Co ratios.

The Nanofactory work showed there is structural rearrangement of the Fe and Co within the MWCNT when a high enough bias is applied to the MWCNT. Unfortunately, the crystal structure of the Fe and Co could not be determined due to lattice vibrations preventing this information being obtained on such a small particle size.

Both this work and those carried out by Aslam *et al.* [218] show that applying bias to MWCNTs changes the MWCNT and filling structure. Aslam observed enhanced graphitisation of the MWCNT walls, which was not observed here. In this work, applying a sufficiently high bias caused the Co NPs and the Fe filling to rearrange, forming larger NPs containing mixed Fe and Co. Repeating these Nanofactory experiments with more representative Fe/Co@MWCNTs, whilst monitoring the current applied would provide more conclusive results on the effect of bias on Fe/Co@MWCNTs. However, these preliminary tests highlighted the need to perform *in situ* measurements to understand the effects of currents on the sample, before claiming they are useful materials for electrical applications. The suitability of using these Fe/Co@MWCNTs in electrical applications depends on the current applied, as at the lower applied currents, no changes were observed, it was only at higher currents that the filling and Co NPs started to move.

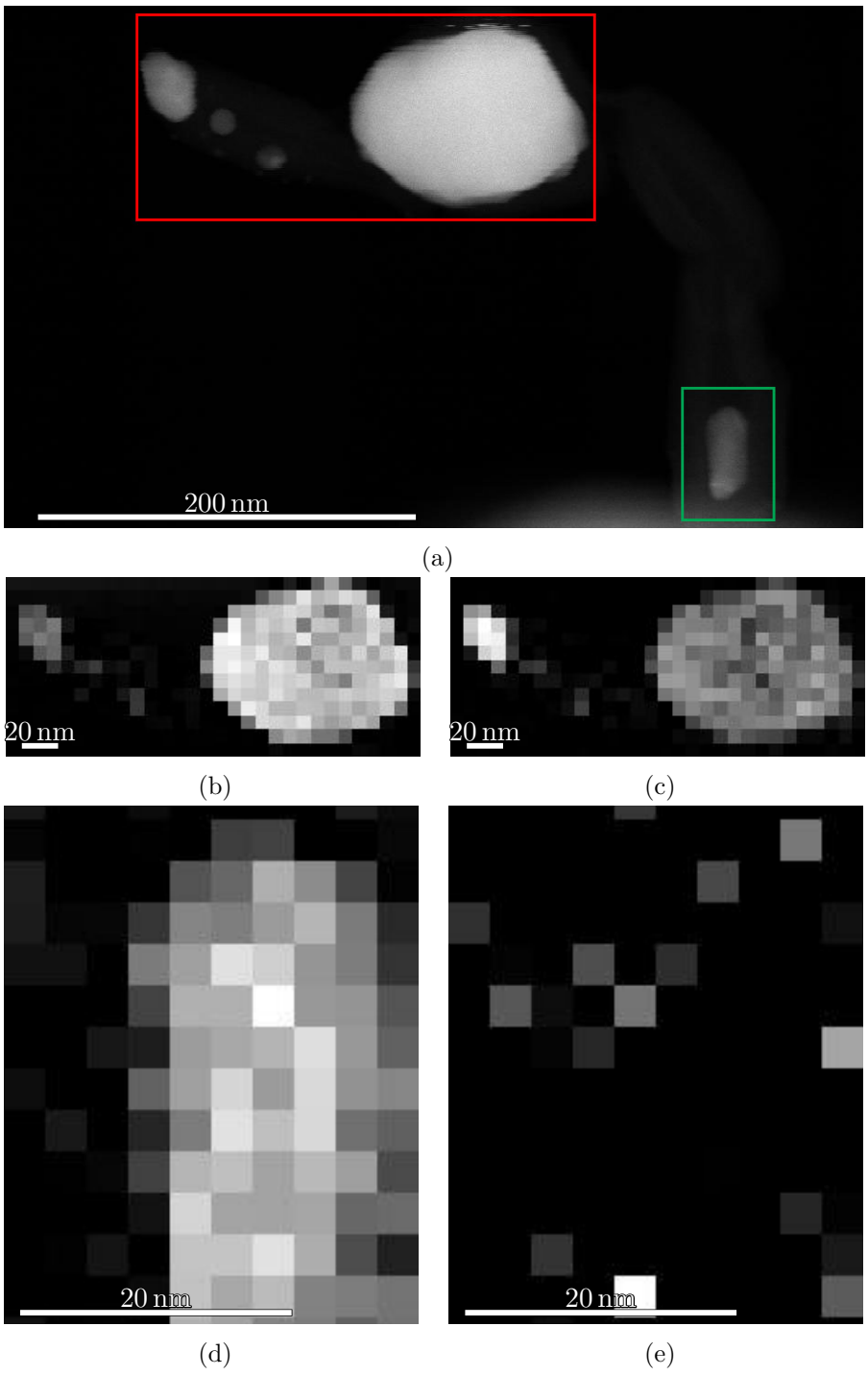


Figure 3.19: a) STEM image taken after bias was applied to the MWCNT. The red and green boxes show the two areas in which EELS maps were taken. EELS maps showing the distribution of b) Fe and c) Co within the red box, and d) Fe and e) Co within the green box. These EELS maps indicate that after applying bias, the Co NPs and the Fe filling have formed alloy NPs.

3.4 Conclusions

In this chapter, Fe/Co@MWCNTs were produced by CVD of solid precursors (ferrocene and cobaltocene). The ratios of ferrocene and cobaltocene were varied in attempt to produce MWCNTs with differing Fe and Co ratios. The aim of the investigation was to evaluate whether controlling the Fe:Co ratio inside Fe/Co@MWCNTs was a viable method of tuning their M_s and H_c.

All precursor ratios produced MWCNTs, with insignificant morphological differences for the materials deposited on substrates and on the quartz tube. However, all samples contained a mixture of Fe/Co@MWCNTs, metal NPs and large metal clusters. EDX, TEM and XRD confirmed the presence of Fe and Co, with differences in Fe/Co ratio observed from EDX across individual nanowires in the Fe/Co@MWCNTs. Whilst Fe/CoMWCNTs were successfully produced, it was observed that cobaltocene sublimed at a slower rate than the ferrocene, resulting in incomplete cobaltocene sublimation within the 30 minute reaction window. With the current set up, it is not possible to attain controllable Fe:Co ratios within the pyrolysis furnace, and hence, within the individual Fe/Co@MWCNTs. The ratio of Fe and Co within individual Fe/Co@MWCNTs, as evaluated by EDX, differed significantly from the intended ratios. XRD patterns confirmed mixed phases of FeCo, Fe and Co within the Fe/Co@MWCNTs, for all ferrocene and cobaltocene precursor ratios, with calculated Fe:Co ratios of 2.5:1, 1.8:1, and 0.5:1 for syntheses with 75:25, 50:50 and 25:75 ferrocene:cobaltocene precursor ratios. The wt. % of the FeCo phase remained approximately constant (*ca.* 6 wt. %) within the materials produced for all ferrocene:cobaltocene ratios.

Despite the incomplete cobaltocene sublimation during the syntheses, a range of M_s and H_c values were observed with varying ratio Fe:Co ratios. The Fe/Co@MWCNTs possessed higher M_s than Fe@MWCNTs and Co@MWCNTs. Evaluating the viability of tuning the M_s and H_c by controlling the Fe:Co ratio within the MWCNTs was difficult because of the slower cobaltocene sublimation rate, differing ratios of Fe and Co within individual Fe/Co@MWCNTs and the presence of a mixture of materials within the samples. As the desired ratios of Fe and Co were not achieved, accurately discerning whether changes in Fe:Co ratios within MWCNTs can reliably tune the M_s of the Fe/Co@MWCNTs was not possible. Further, it is likely that the ratio of NPs to Fe/Co@MWCNTs plays a significant role in determining the magnetic properties observed. The large variations of

Fe and Co within individual Fe/Co@MWCNTs is unacceptable for tunable materials and alternative synthesis approaches, such as AACVD, may be better suited for creating these Fe/Co@MWCNTs.

The effect of applying current to an individual MWCNT was evaluated using *in situ* TEM fitted with a Nanofactory holder. This measurement were carried out to understand how applying current affects the metal filling, which has strong implications on their suitability for electrical applications. Upon inspection, the MWCNT selected for these measurements happened to be an unusual Co-NP decorated Fe@MWCNT. Applying current to this Co-NP decorated Fe@MWCNT revealed that under high currents, the Co NPs coalesce to form larger NPs, before both the Fe-filling and the Co collect together at higher currents. Further current increases breaks the MWCNT, due to joule heating. EELS maps taken following the application of current showed the even distribution of Fe and Co within the particle formed following current-induced coalescence. This preliminary *in situ* measurement revealed the necessity of understanding how exposure to current affects the filling within the metal-filled MWCNTs before using them for electronic applications. Knowing the maximum current that can be applied before these structural changes occurs to the filling is key data that is required before taking these materials through to the application stage. This information is of particular importance for chapter 4.

Chapter 4

Manipulation of Magnetic Buckypapers

This chapter takes the Fe@MWCNTs produced in Chapter 2 to the next level by forming macroscopic papers from them, known as buckypapers (BPs), that respond to external magnetic stimuli. These ferromagnetic fabrics are formed by sandwiching Fe@MWCNTs between layers of conventional MWCNTs. The areas where the Fe@MWCNTs was deposited is controlled to create BPs with selective ferromagnetic regions. The ferromagnetic BPs showed promise as a non-metallic contact in a prototype electromechanical relay.

4.1 Introduction

Developing methods of processing CNT materials to produce macroscopic structures, such as BPs, allows for their properties to be exploited on the macroscale. One of the most reported post-synthesis methods for fabricating BPs is filtering CNT dispersions by vacuum filtration (Figure 4.1). Typically, both SWCNTs and MWCNTs are dispersed in organic solvents or water and surfactants, due to the hydrophobic nature of both SWCNTs and MWCNTs [126, 127, 143]. Vacuum filtration, widely used for SWCNT BPs and thin film production [122, 135, 136, 225–227], has been adapted to produce BPs from MWCNTs [128, 228], graphene [229, 230] and GO [231]. Making MWCNT BPs are limited by difficulties with separating MWCNTs [228], and reductions in their aspect ratios to <1000 due to the physical treatments used to disperse them [138, 232]. Whilst shorter MWCNTs are less likely to entangle and form aggregates in dispersions [138], the shorter length is

disadvantageous for forming freestanding BPs.

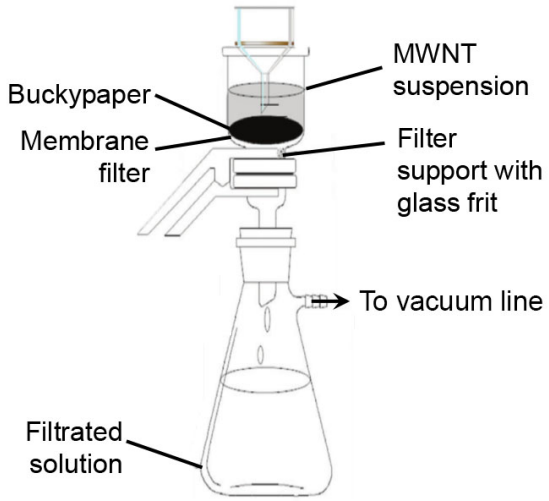


Figure 4.1: Schematic showing the set up used for vacuum filtration of the dispersions to obtain a BP.

Building on the existing research on BPs, the next step is to create responsive BPs with added functionality. These functional BPs will greatly extend the range of applications that BPs are potentially suited for [146, 233–235] due to their responsive nature. Creating BPs from Fe@MWCNTs, controllable by external magnetic stimulus, is one approach to create these responsive BPs. This controllability is desirable in applications where physically manipulating the BP is not possible, such as inside electrical devices or in corrosive solutions. One of the bottlenecks to creating responsive BPs that can be controlled and manipulated on the macroscale has been the limited availability of MWCNTs with specific properties, such as magnetic MWCNTs, in large enough quantities for BP production. However, the systematic study carried out in Chapter 2 revealed the optimised conditions for producing Fe@MWCNTs of high enough mass and quality to be processed for BP production.

Previously, BPs consisting of magnetic metal-filled MWCNTs have been produced *in situ* by AACVD, by using a precursor solution of metallocenes dissolved in dichlorobenzene (DCB) or trichlorobenzene (TCB) [236–238]. The metal-filled MWCNTs were reported to be continuously filled with metal. Whilst it has been reported that changing the Cl-containing precursor affects the M_s no explanation has been given for why using Cl-containing solvents produce BPs, rather than aligned MWCNTs.

Aligning the Fe_3C-filled MWCNTs within BPs (Figure 4.2) with the direction of the Ar flow was achieved by controlling the precursor evaporation temperature and the vapour flow rate [237]. Increasing the alignment of the MWCNTs within BP can address the low mechanical properties caused by weak Van der Waals interactions between randomly oriented tubes [239] (the mechanical properties of BPs are discussed in chapter 5). No tensile tests were conducted on these aligned Fe_3C-filled MWCNT BPs to evaluate whether increases in alignment strengthened the BPs.

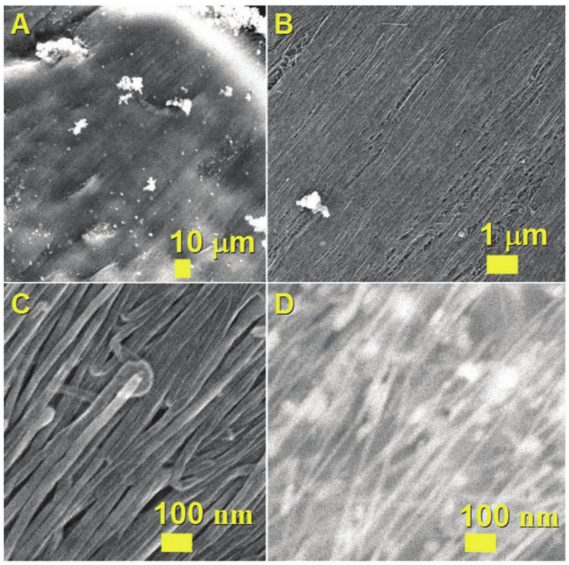


Figure 4.2: SEM images extracted from [237] showing a-c) highly aligned MWCNTs within the BP, and d) the high amount of filling.

Thus far, manipulation of magnetic BPs has only been used to prove their ferromagnetic nature, demonstrating positional control of the BP using a magnet (Figure 4.3 [236]). Magnetic BPs are viable as a flexible, non-metallic materials for the next generation of electromechanical switches. Currently, electric switches are typically either electromechanical switches or solid-state relays. Solid-state relays are expensive and heat sensitive, whilst the conventional metals used in electromechanical switches corrode over time, due to spark-induced surface oxidation. Whilst reed switches encase the contacts inside an evacuated or inert gas-filled chamber to overcome this oxidation issue, non-metallic electromechanical switches are an attractive alternative solution. These non-metallic switches are likely to have longer lifetimes because of the non-corrosive and high electrical and thermal conductivity properties of MWCNTs.

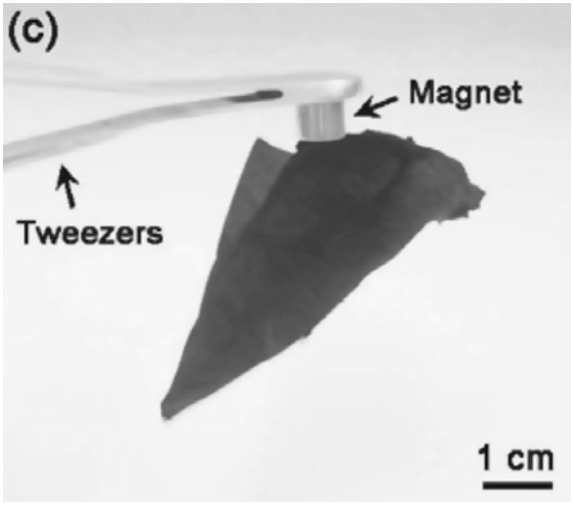


Figure 4.3: Image extracted from [236] of a magnetic BP being attracted to a magnet, showing its ferromagnetic behaviour.

The magnetic BPs produced *in situ* are limited to having the ferromagnetic metal-filled MWCNTs deposited across the entirety of the BP, which limits their movement in response to external magnetic stimulus. However, by controlling where the ferromagnetic metal-filled MWCNTs are deposited, BPs with pre-defined localised magnetic areas and hence, specific movements to external magnetic stimulation are created. In this chapter, a customisable approach to design and make tailored magnetic BPs is developed, with the magnetic response restricted to specific regions of the BP. By developing the vacuum filtration setup, sandwich structure BPs consisting of an Fe@MWCNT layer in between two conventional MWCNT layers were produced (MWCNT-Fe@MWCNT-MWCNT), with evenly distributed or localised Fe@MWCNT regions. These novel designed ferromagnetic BPs are a prerequisite for controlled BP manipulation (such as bending and folding), which are not possible for BPs with evenly distributed Fe@MWCNTs. Magnetic BP strips were incorporated into a relay prototype, as a non-metallic switch. I/V measurements, taken in air, N_2 and under vacuum, established the currents and voltages these BP switches were capable of carrying.

4.2 Experimental

The following section covers the procedures followed for growing conventional MWCNTs and Fe@MWCNTs, their processing to create ferromagnetic BPs and the method followed for performing I/V measurements and relay prototyping.

The vacuum filtration process was chosen due to the flexibility it offers in being able to deposit ferromagnetic metal-filled MWCNTs in specific locations. A visiting student, Benoit Grosjean, optimised the dispersion method for AACVD MWCNTs, with ethanol (EtOH) being the preferred dispersion medium. Figure 4.4 shows different BP types. Conventional MWCNT BPs with no smart features (Figure 4.4a) could be used as catalyst supports. Using Fe@MWCNTs creates smart BPs that respond to magnetic stimuli. Figure 4.4b show BPs with Fe@MWCNTs across the entire BP; using these BPs as catalyst supports could increase reaction rates by guiding them through solutions using magnets. Finally, BPs can be designed with localised responsive areas. These BPs can be controlled beyond their physical location, allowing them to bend and fold, depending on their design. An example structure, and the one produced in this chapter, is given in Figure 4.4c, where Fe@MWCNTs are deposited on either side of a non-magnetic central region.

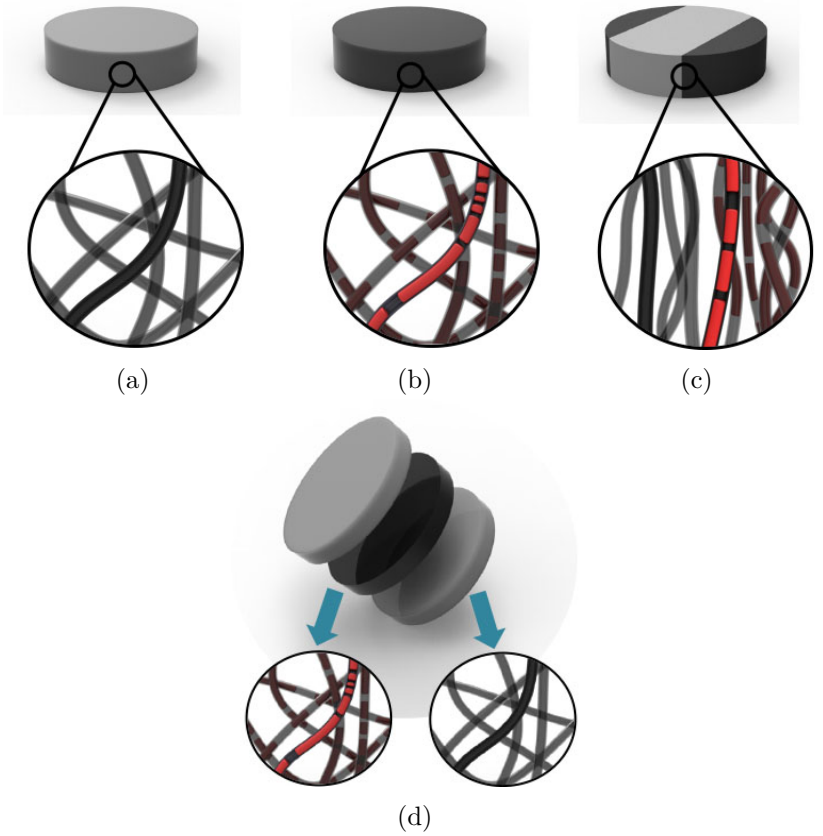


Figure 4.4: Schematics of the different types of BPs, composed of a) only conventional MWCNTs, b) Fe@MWCNTs across the entire BP surface and c) Fe@MWCNTs localised to specific regions. Schematics b and c have a sandwich structure, shown in d) a magnetic layer is deposited between two layers of conventional MWCNTs. For design c), the magnetic Fe@MWCNTs are deposited at the edges of the BP. Image produced by Jesus Acapulco.

4.2.1 MWCNT and Fe@MWCNT Synthesis

Conventional MWCNTs were synthesised by AACVD, using the protocols established by Dr Shayan Meysami [25, 30, 34]. Briefly, 5 wt.% ferrocene (Sigma Aldrich, 98 %, sublimed) was dissolved in white camphor oil (Sigma Aldrich) as the aerosol solution. A single-zone horizontal tubular furnace (Elite Thermal Systems; length 60 cm, inner diameter 4 cm) was heated to 800 °C. A quartz tube (Robson Scientific; 80 cm x 21 mm, thickness 1.5 mm) was connected to the aerosol generator (RBI Pyrosol 7901). Once the furnace was at temperature, the aerosol generator was switched on and aerosol flowed into the furnace for 15 minutes, under an Ar (BOC zero grade, 99.9999 % purity) flow rate of 1 L/min (Brooks mass flow controller). Fe@MWCNTs were produced following the method and optimised parameters described in chapter 2.

4.2.2 Magnetic Buckypaper

The following procedure was used to create BPs shown in Figure 4.4b.

150 mg MWCNTs and 100 mg of Fe@MWCNTs were placed in separate bottles with 500 ml and 300 ml of ethanol, respectively. The MWCNTs mixture were magnetically stirred on a hot plate for 20 min at room temperature. Both the conventional MWCNT and Fe@MWCNT mixtures were placed in a sonic bath (30L X-tra Basic Fisherbrand) and sonicated for 5 h. The mixture was centrifuged (Hettich Rotana 460R) for 20 mins at 3250 RPM and the supernatant for each mixture was collected in separate flasks. The precipitates were gathered in separate flasks, the same volume of solvent was added as previous and the sonication, centrifugation process was repeated twice more.

The setup shown in Figure 4.1 (Sartorius) was used to filter the CNT dispersions to form the BPs. A polycarbonate filter of diameter 47 mm and 1 μm pore size (Whatman) was placed on top of the polytetrafluroethylene (PTFE) frit and clamped in place. The vacuum was turned on, half the collected MWCNT supernatant mixture was poured through the funnel. Once filtered, the Fe@MWCNT supernatant mixture was poured into the filter, followed by the remaining MWCNT supernatant mixture after the Fe@MWCNT mixture had been filtered.

The BP was left to dry overnight then removed from the polycarbonate filter by mechanical peeling or dissolving the filter using chloroform, $CHCl_3$. $CHCl_3$ was only used if the BP was too fragile to mechanically peel off the filter. The BP was placed face down in a glass petri dish and 20 ml $CHCl_3$ was pipetted on top of the filter. The $CHCl_3$ was removed by pipetting and this process was repeated 4 times. The same procedure was carried out with EtOH following $CHCl_3$.

4.2.3 Buckypaper with Selective Magnetic Regions

Two approaches were used to create BPs with the design shown in Figure 4.4c. Fe@MWCNT pastes were created with the idea that pasting would allow more intricate patterns to be produced by piping the paste on top of pre-made conventional MWCNT BPs. A mould was designed to block the central regions of the BP; the Fe@MWCNTs were only deposited in the exposed areas.

Fe@MWCNT Pastes for BPs with Selective Magnetic Regions

Pluronic P-123 (P123), a triblock copolymer (poly(ethylene glycol)-poly(propylene glycol)-poly(ethylene glycol) ($HO(CH_2CH_2O)_{20}(CH_2CH(CH_3)O)_{70}(CH_2CH_2O)_{20}H$)) was used as the paste medium. Ratios of Pluronic P-123 (P-123) (Sigma Aldrich) and distilled water were weighed out into glass vials (Table 4.1) and sonicated (Ultrawave IND1250D sonic bath) at *ca.* 60 °C, for 2 h. 40 mg of Fe@MWCNTs was added to 4 g of P123-2 and sonicated for 2 h. Following this, the mixture was stirred by hand. Two thin conventional MWCNT BPs were produced using solutions of 37 mg conventional MWCNTs dispersed in 200 ml of EtOH, following the vacuum filtration method outlined in subsection 4.2.2. These BPs were not peeled off the polycarbonate filter paper. The BP was allowed to dry in air on the filter paper for *ca.* 1 h, following which the Fe@MWCNT-P123 mixture was pasted onto the face of one of the conventional MWCNT BPs using a spatula. The central region of the BP was covered in a thin layer of blank P123-2. The remaining conventional MWCNT BP was overlaid, face down, on top of the Fe@MWCNT-P123 covered BP, a weight was place on top to compress the three layers together and left overnight before peeling off the filter.

	% P123/ g	% H_2O/ g
P123-1	50	50
P123-2	75	25
P123-3	100	0
P123-4	70	30

Table 4.1: Masses of P123 and distilled water investigated to obtain the ideal viscosity for dispersing Fe@MWCNTs in.

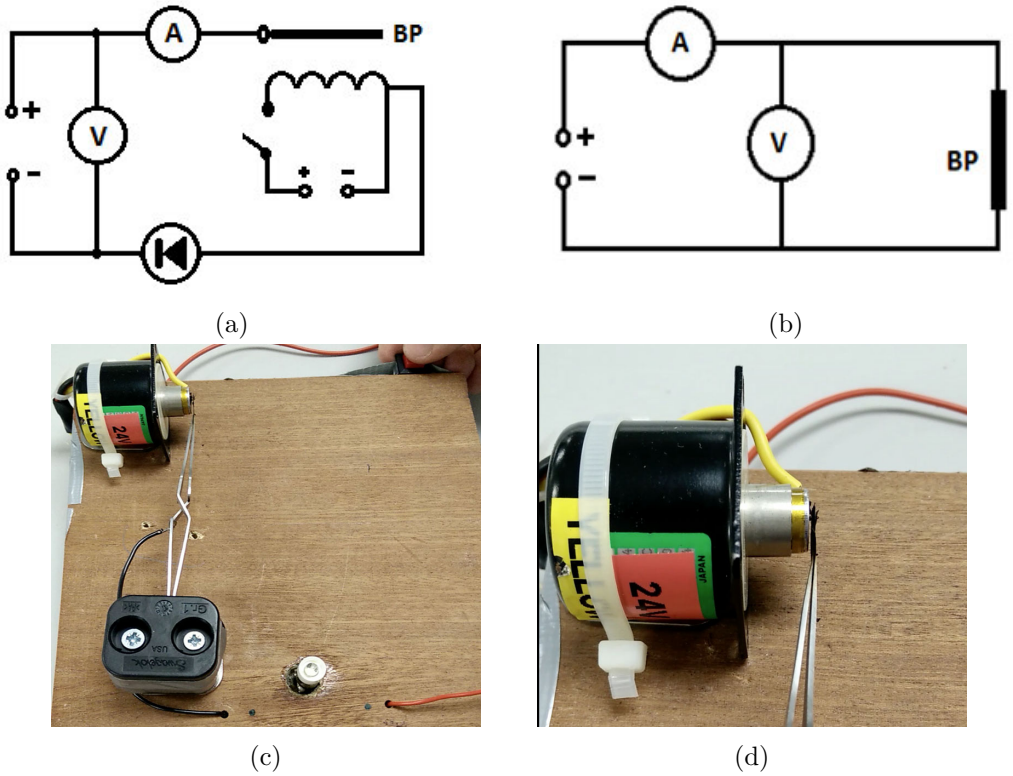
Mould Making and Designing

Moulds were made using polydimethylsiloxane (PDMS), a polymer with two components, A and B. A 10:1 ratio by weight of A to B was mixed together and centrifuged at 1250 RPM for 10 minutes to remove bubbles. This mixture was poured into the filter funnel component and cured for *ca.* 2.5 h on a hot plate at 150 °C. The cured PDMS was removed from the filter funnel and cut into the desired shape. The moulds were further developed by inserting a metal rod into the PDMS mixture during curing. During filtration, downward pressure was applied to the mould; the rod was clamped into place to maintain this pressure. The pressure improved the contact between the mould and the BP underneath it, reducing the amount of Fe@MWCNT dispersion that seeped under the mould.

The dispersion procedure (section 4.2.2) was followed for 125 mg of conventional MWCNTs and Fe@MWCNTs. BPs were produced using the vacuum filtration setup described in section 4.2.2. Half the supernatant MWCNT solution was deposited on the polycarbonate filter. The PDMS mould was placed on top of the deposited MWCNT layer. The Fe@MWCNTs dispersion was evenly poured onto the exposed areas of the MWCNT BP. The mould was removed and the remaining supernatant MWCNT dispersion was filtered. The BP was dried overnight before peeling off the filter.

4.2.4 Relay and I/V Measurements

BP strips of 5 x 15 mm were used for relay (Figure 4.5a) and I/V measurements (Figure 4.5b). For relay tests, the BP was inserted into the tweezers and a switch turned the solenoid on and off. I/V measurements were taken for conventional MWCNT BP, and annealed and non-annealed BP strips with Fe@MWCNTs distributed evenly across the entirety of the BP. For annealing, samples were heated to 650 °C under 1 SLM Ar for 5 h, and cooled to room temperature under 100 sccm Ar. Typical 5-10 I/V cycles were carried out per BP strip. The voltage was increased in 0.5 V increments, and the current recorded. All measurements were conducted inside a glovebox.



(a) (b)

(c) (d)

Figure 4.5: Schematics showing the setup used for a) testing the magnetic BP in a relay, b) I/V characteristic measurements and c and d) photos showing the switch setup used.

I/V measurements were carried out under vacuum and N_2 in an Edwards Coating Unit 12E6 carbon coater. Samples were clamped between tweezers attached to the contacts inside the carbon coater (Figure 4.6). A bell jar was placed over the top of the chamber and sealed shut. The chamber was evacuated to vacuum levels in the region of 10^{-5} mbar. I/V measurements were carried out in the same manner as in air. For the measurements under N_2, the outlet valve was connected to a N_2 cylinder and once the system was under vacuum, the outlet valve was opened to flood the system with N_2.



Figure 4.6: Photograph showing the setup used for measurements carried out under vacuum and in N_2. The sample was carefully placed between the two tweezers.

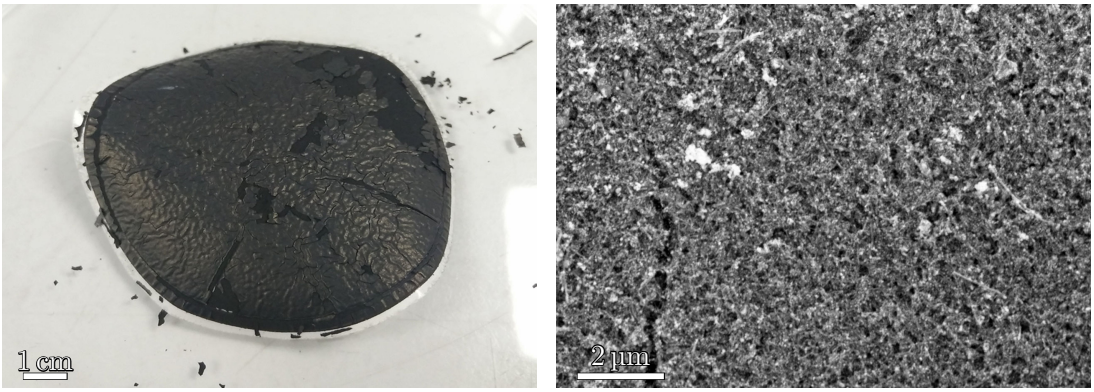
4.2.5 Characterisation

SEM images taken at 5 kV (JEOL-JSM840F field emission SEM) examined MWCNT entanglement within the BP and BP thickness was estimated from edge-on images. Raman spectra, taken in the Raman shift range of 1000-3000 cm^{-1} (Horiba LabRAM Aramis spectrometer, Laser Quantum 532nm green LASER), were collected on the BP before and after I/V measurements to establish how current affects MWCNT graphitisation. SQUID measurements (Quantum Design MPMS3 SQUID) were carried out on 1 mg BP samples at 300 K and 4 K. The applied magnetic field was applied both parallel and perpendicular to the plane of the BP.

4.3 Results and Discussion

4.3.1 Structure of Magnetic Buckypaper

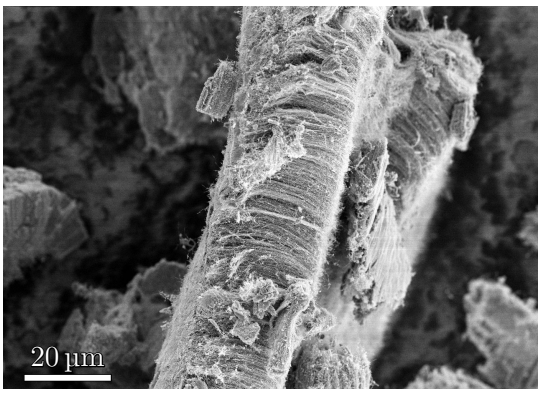
Producing BPs solely from Fe@MWCNTs, following the recipe for conventional MWCNT BPs (Section 5.2.2), was unsuccessful (Figure 4.7). The deposited Fe@MWCNTs could not be peeled from the filter paper and broke into small flakes when handled. SEM images of the Fe@MWCNT-only BP showed an arrangement of very short Fe@MWCNTs which were unable to entangle, explaining the poor integrity of solely Fe@MWCNT-BPs (Figure 4.7b). Typically, Fe@MWCNTs had lengths of 20-40 μm (Figure 4.8a), which are likely to be further shortened by the long sonication times [232].



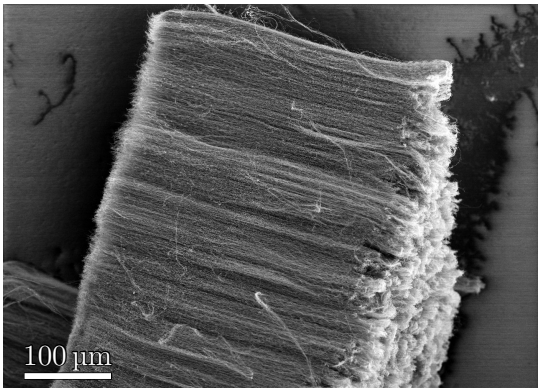
(a) (b) MWCNTs

Figure 4.7: a) Optical image of a solely Fe@MWCNT-BP. The BP flaked into small fragments and could not be peeled off the filter. b) SEM image showing the structure of the Fe@MWCNT-BP and shows a densely packed arrangement of very short Fe@MWCNTs.

To overcome poor Fe@MWCNT entanglement issues, conventional MWCNTs, of typical length >400 μm (Figure 4.8b), were incorporated to form entangled BPs. The sandwich structure (MWCNT-Fe@MWCNT-MWCNT) was selected over mixing the conventional MWCNTs and Fe@MWCNTs together to form an intermixed BP because of the added ability to select where the Fe@MWCNTs were deposited by layering the MWCNT types.



(a) Fe@MWCNTs



(b) MWCNTs

Figure 4.8: SEM images taken of a) Fe@MWCNTs and b) conventional MWCNTs, showing the difference in length between the two CNT types. The conventional MWCNTs are noticeable much longer, compared to Fe@MWCNTs.

Figure 4.9 shows optical and SEM images of the magnetic sandwich-structure BPs, which are 4 cm in diameter, with thicknesses of *ca.* 500 µm. Figure 4.9b shows entangled MWCNTs, with some agglomerate particles present. The structure of these sandwich BPs is significantly different to that of the Fe@MWCNT-only BP flakes. These ferromagnetic BPs were flexible, but not to the same extent as reported in the literature. Lv *et al.* [236] showed images of BPs folded into airplane shapes (Figure 4.3). This would not be possible with the BPs formed here, as bending the BP too much caused it to tear along the fold.

As revealed in Chapter 2, the Fe@MWCNT samples typically contain a mixture of C coated Fe NPs and Fe@MWCNTs. Whilst the sonication and centrifugation process used to produce the BP removes a large amount of these particles, the BPs are likely to still have some C coated Fe NPs present. For example, in Figure 4.9b, some of these Fe NPs are observed.

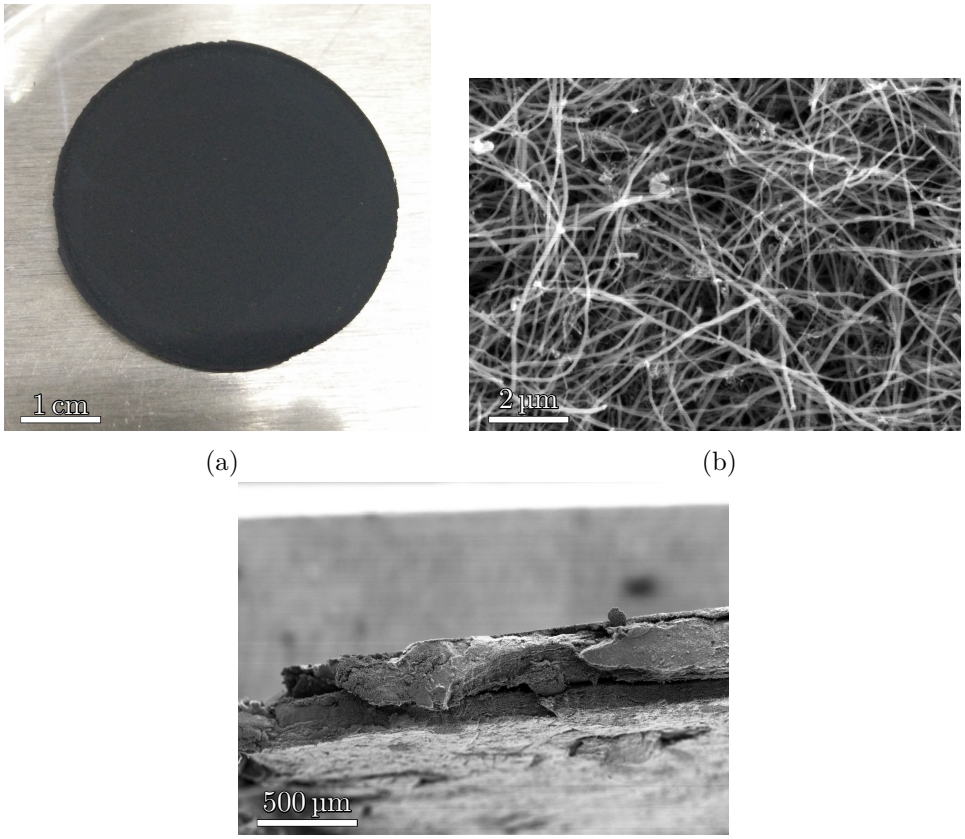


Figure 4.9: a) Optical image of a ferromagnetic BP, and SEM images showing b) the entangled MWCNTs, and c) edge-on image of a magnetic BP, used to estimate BP thickness.

4.3.2 Magnetic Properties of BP

The M_s of the BP with the magnetic field applied parallel (*ca.* 36 emu/g) and perpendicular (*ca.* 40 emu/g) to the BP are lower than for the raw Fe@MWCNTs (*ca.* 50 emu/g) (Figure 4.10). The lower M_s for the BP is most likely related to the removal of clusters of C coated Fe NPs during of the dispersion process. Figure 4.11 shows higher M_s for C coated Fe agglomerates (*ca.* 56 emu/g), compared to Fe@MWCNTs (*ca.* 48 emu/g), suggesting that removing these clusters could explain the lower M_s of the magnetic BP. Whilst no reports comparing the M_s of C-coated metal NP agglomerates to metal-filled MWCNTs have been reported, Guo *et al.* [238] produced BPs of amorphous C coated Co clusters, which had a much higher M_s (70 emu/g) than BPs formed of NiCo@CNTs (58 emu/g). These M_s are not directly comparable, due to the presence of Ni in the filling. Similarly, whilst not directly comparable due to different syntheses methods, the M_s of Co@MWCNTs produced by wet chemical approach is 62 emu/g [3], which is lower than for the C coated Co agglomerates.

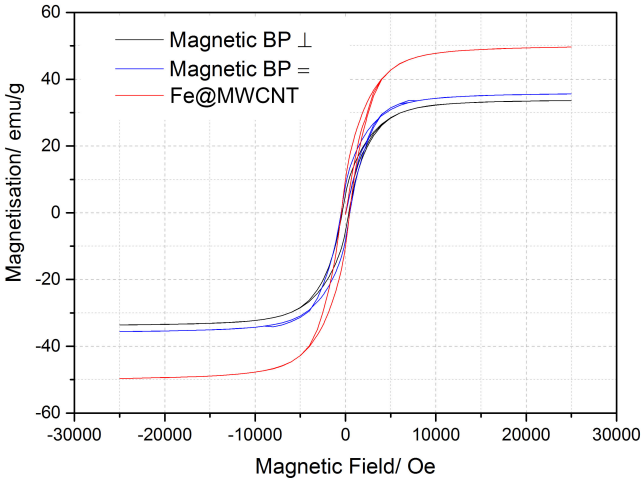


Figure 4.10: Hysteresis loops obtained at 300 K for the magnetic BPs, measured the magnetic BP both parallel and perpendicular to the applied magnetic field. The hysteresis loop for the raw Fe@MWCNTs incorporated into the ferromagnetic BP shows a higher M_s than the BP.

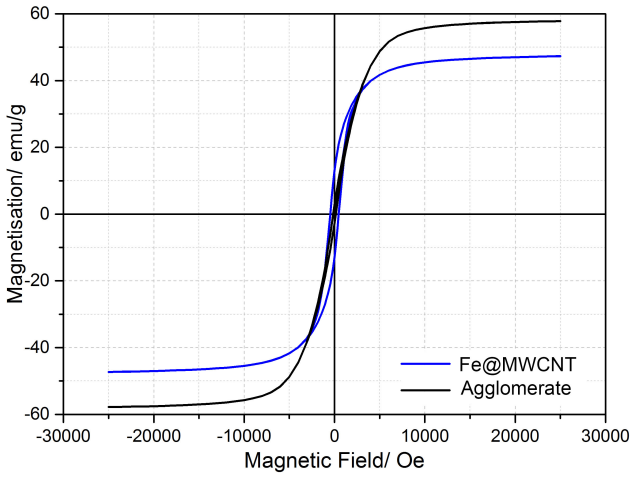


Figure 4.11: Graph comparing the magnetic hysteresis obtained from SQUID measurements carried out at 300 K, for samples containing a majority of agglomerate C coated Fe NPs (D13) and Fe@MWCNT(C53). The temperatures of T_{sub}/T_{pyro} are C= 250/750, and D= 250/850 °C.

The M_s values for ferromagnetic sandwich-structure BPs agree with those in literature, Lv *et al.* [236] reported M_s of *ca.* 40 emu/g, with the magnetic field applied perpendicular and parallel to Fe@MWCNT BP produced *in situ*. These M_s are lower than for *in situ* Fe_3C CNT BPs, which had maximum M_s values of 57.8 emu/g [237].

The coercive force of the sandwich-structure magnetic BP with the magnetic fields applied parallel and perpendicular to the plane of the BP are almost identical at 4 K, with coer-

civities of *ca.* 1200 Oe. At 300 K, coercivities of *ca.* 520 and 370 Oe were observed for the magnetic field applied parallel and perpendicular to the BP, respectively. This temperature dependent behaviour is typical for ferromagnets, where coercive force is determined by the combination of thermal fluctuation and magnetic anisotropy [41]. Lv *et al.* [236] reported similar temperature dependent coercive behaviour for their Fe@MWCNT BP at 4 K. Both Lv [236] and Guo *et al.* [238] reported a 'step-like' behaviour for magnetic fields applied parallel to the Fe@MWCNT BP at 300 K. Lv suggested that the Fe-nanowires possessed multiple domains along the tube axis direction, and these structural effects determined the coercive force [236]. Guo attributed these step-like features to the magnetisation reversal phenomenon of encapsulated crystals [238]. However, this step-like behaviour was not observed for our BPs.

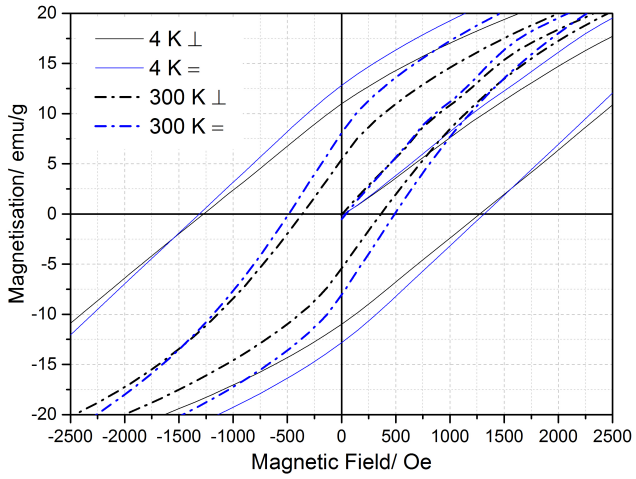


Figure 4.12: Graph showing the coercivity for the BPs with the magnetic field aligned parallel (blue) and perpendicular (black) to the BP, taken at 4 K (solid line) and 300 K (dashed line).

4.3.3 Relay and I/V Measurements

The key requirements for ferromagnetic BPs to be suitable for use in a non-metallic switch in relays are: 1) controllable magnetic BP movement using an external magnetic field, 2) the magnetic BPs must be electrically conducting. I/V measurements conducted in air, under vacuum and N_2 established the currents and voltages magnetic BPs could conduct.

I/V Measurements in Air

Preliminary tests using the setup in Figure 4.5a revealed that BP strips could carry sufficient current to power an LED that operated at 13.5 mA, at 6 V. Switching on the solenoid caused the BP to move towards it, demonstrating easy control of BP movement by the solenoid. Upon contact of the BP with the solenoid, the circuit was closed and the LED lit up, indicating the BP carried sufficient current to power the LED.

I/V measurements taken using the setup in Figure 4.5b revealed the variation in currents carried across batches of BPs, with maximum currents of *ca.* 1.7 and 0.5 A at 3.5 V for two different batches of ferromagnetic BP, FeBP1 and FeBP2, respectively (Figure 4.13). This large variation in maximum current is likely related to the inconsistent dispersibility of different MWCNTs and Fe@MWCNTs batches. Although the same protocol is followed for each synthesis, there is always batch-to-batch variation in their properties, such as defectiveness, surface chemistry and diameter and length distribution. Carrying these inconsistencies forward, differences in properties such as surface chemistry will alter how the MWCNTs and Fe@MWCNTs disperse and entangle during filtration. This entanglement and MWCNT arrangement within the BP affects how effective the current is conducted through the BP, which relies on having a good pathway for current to move through.

Typically, 5-10 cycles were carried out per BP sample to evaluate the reproducibility in I/V characteristics. Both batches of ferromagnetic BP consistently carried very similar currents at any voltage per cycle, as indicated by the small error bars, which show the shift in measured current over the cycles. With the conventional MWCNT BP, the current varied at higher voltages, suggesting that its conductance is less stable at higher voltages.

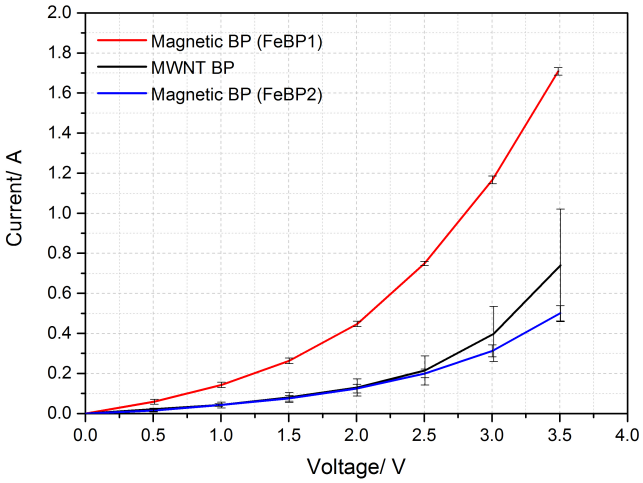


Figure 4.13: Graphs showing I/V curves obtained for conventional MWCNT BP (black) and magnetic BPs (red and blue). The two different batches of magnetic BPs are labeled FeBP1 (red) and FeBP2 (blue) for ease of discussion. Very similar I/V curves were obtained for FeBP2 and the conventional MWCNT BP, whilst FeBP1 carried much higher currents.

FeBP2 had a very similar I/V curve to the conventional MWCNT BP up to 2.5 V, whilst FeBP1 carried higher currents at any voltage. The metallic filling inside the Fe@MWCNTs could affect BP conductivity. Grimes *et al.* [240] reported decreases in MWCNT conductivity from 7.78 x 10^4 S/m to 2.22 x 10^4 S/m after annealing MWCNTs in MWCNT/polystyrene thick films at high temperatures. This decrease was attributed to removing Fe_3C particles, which acted as a conductive core, from the MWCNT cavity. Annealing graphitised and eliminated microstructural defects, which should increase conductivity, however, removing the Fe_3C particles restricted the electrons to a narrower path, leading to an overall decrease in conductivity. It is plausible that the Fe-filling in Fe@MWCNTs has a similar effect, hence FeBP1 carried higher currents compared to the conventional MWCNT BP. The lower currents carried by FeBP2 could be caused by many factors, including CNT quality, Fe-filling, entanglement, or BP thickness.

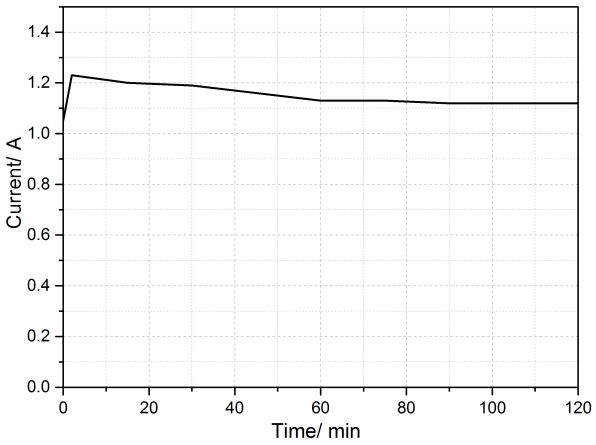
The MWCNTs in FeBP1 were less defective than FeBP2, as indicated by their lower $I_{D/G}$ (Table 4.2), which could influence the BPs' ability to carry current. The structural defects in MWCNTs can lower conductivity by increasing electron scattering [241, 242]. However, I/V studies have shown that defective MWCNTs, such as CVD produced MWCNTs and Fe@MWCNTs, in composite films displayed lower resistances compared to arc-made or annealed MWCNT-composite films [240, 243]. It is likely that a combination of factors influence the BP's ability to carry current besides quality of the MWCNTs.

BP Type	$I_{D/G}$ (Pre)	$I_{D/G}$ (Post)
MWCNT	0.37±0.01	0.45±0.02
Ferromagnetic (FeBP1)	0.43±0.05	0.46±0.09
Ferromangetic (FeBP2)	0.53±0.02	0.56±0.05

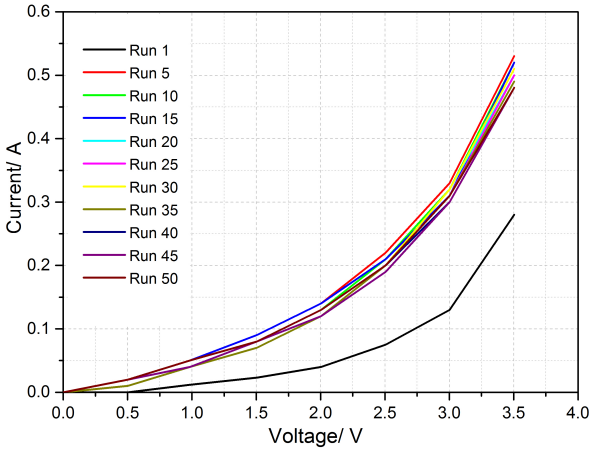
Table 4.2: The $I_{D/G}$ ratios calculated from Raman spectra for conventional MWCNT and ferromagnetic (two different batches, labeled FeBP1 and FeBP2,) BPs, taken prior to and after I/V measurements. Five Raman measurements were taken per BP sample.

All BPs display non-ohmic behaviour; the resistance decreased with increasing voltage. This non-ohmic behaviour is likely caused by tunnelling between CNT junctions at higher voltages as more charge carriers are able to overcome the tunnelling barrier between CNT walls. Similar non-linear I/V curves were reported for metallic-metallic junctions at a kink in a SWCNT, across a range of temperatures [244]. This non-ohmic behaviour was attributed to end-to-end tunnelling between the metallic segments either side of the kink. Non-linear I/V curves were also observed for tunnelling conduction between Nb or Ti contacts and a MWCNT, through a native metal oxide layer [245]. CNT defects in CVD-CNT/polystyrene films act as low-potential sites for tunnelling [243]. It is likely that tunnelling is also responsible for the non-ohmic behaviour of our BPs.

The current, monitored at 3 V, showed an initial spike to *ca.* 1.2 A, before slowly decreasing by a total of *ca.* 0.1 A over 2 h (Figure 4.14a). This current decrease could be caused by slow CNT oxidation due to prolonged current exposure. $I_{D/G}$ values of 0.42±0.05 and 0.46±0.09 were obtained before and after prolonged current exposure, respectively. The errors on $I_{D/G}$ make it difficult to conclude whether the BP become more defective following the I/V measurements.



(a)



(b)

Figure 4.14: Graphs showing a) fluctuations in current over time, and b) I/V curves obtained for magnetic BP every 5 runs of 50. The consistency of I/V curves obtained over 50 cycles, disregarding the first run, is shown.

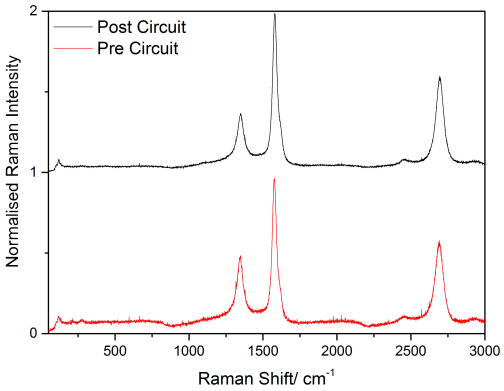
The currents carried significantly increased following the first cycle of I/V measurements for all BP samples, regardless of batch and BP type (Figure 4.14b). Current induced increases in graphitisation by CNT restructuring and defect burning could explain this behaviour. However, the $I_{D/G}$ ratio increased after I/V measurements (Table 4.2). Reasons for this increase in $I_{D/G}$ could be due to current-induced removal of remaining external Fe agglomerate particles that were not removed by sonication and centrifugation (Figure 4.8a). The Fe agglomerate particles were typically Fe clusters surrounded by a graphitic C layer, with a lower $I_{D/G}$ than Fe@MWCNT samples (section 2.3.3), hence removing these Fe clusters from the surface of the BP may explain the increase in the $I_{D/G}$ ratio.

Alternatively, the MWCNTs in the BP could be slowly oxidising in air, causing them to be more conductive by increasing tunnelling via defects [243]. Literature states that whilst oxidation in air up to 400 °C removes amorphous carbon, temperatures above this lead to defects in the tube walls forming, hence the increase in $I_{D/G}$ [246]. The BP warms up considerably during I/V measurements, as observed when removing samples from the setup. The local temperatures experienced by the MWCNTs during measurements is unknown, but can be roughly estimated to be around 700 °C at 2.3 A for FeBP1, based on black body radiation, as the BP glowed red at this current. Based on joule heating, the temperature of the BP at the currents carried at 3.5 V would likely be <400 °C (Appendix). However, this estimate does not take into account Newton's law of cooling. Using an IR thermometer in future experiments would give a better idea of local BP temperatures, leading to a better understanding of whether the local temperature would be sufficient to oxidise the MWCNTs.

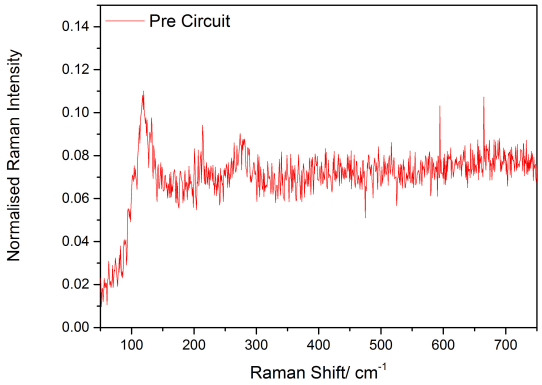
The I/V curves were highly reproducible over 50 cycles, disregarding the first cycle, with an average range of 0.15 A over the 50 cycles per voltage (Figure 4.14b). A decrease in $I_{D/G}$ ratio from 0.50±0.03 to 0.37±0.01 was observed after the 50 I/V cycles (Figure 4.15a), suggesting the BP became less defective. The MWCNTs could be restructuring and becoming more graphitised due to extended exposure to current. Aslam *et al.* [247] observed current-induced structural changes to N-doped MWCNTs, *in situ* in a TEM. They observed that initially, the current induces CNT restructuring, however at higher currents, the N-doped MWCNT broke down because of joule heating. For the BPs, too high a current causes the BP to glow red, and eventually burn, similar to the observations made when current was applied to an individual Co-NP decorated Fe@MWCNT in chapter 3. It is plausible that applying high current to the BPs could have a similar effect on the Fe-filling within the Fe@MWCNT as observed under *in situ* TEM, resulting in the Fe-filling collecting into one end of the MWCNT.

Closer inspection of the Raman spectra at low Raman shift (*ca.* 100-500 cm^{-1}) showed that small peaks present before I/V measurements at *ca.* 230 and 275 cm^{-1} were removed after measurements (Figure 4.15b and c). These peaks could be from C in amorphous C coated Fe_3O_4 [248], suggesting that applying current removed these amorphous C coated Fe_3O_4 clusters. 50 I/V cycles could remove both amorphous C and graphitic C coated Fe clusters. This, combined with increases in CNT graphitisation would lead to an overall decrease in $I_{D/G}$, if the increase in graphitisation was higher than the decrease caused by

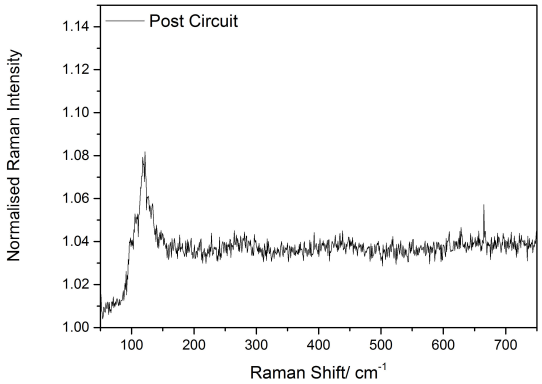
removal of the graphitic Fe agglomerates. Further investigation was not carried out due to time restraints, however this is an interesting topic for further research.



(a)



(b)



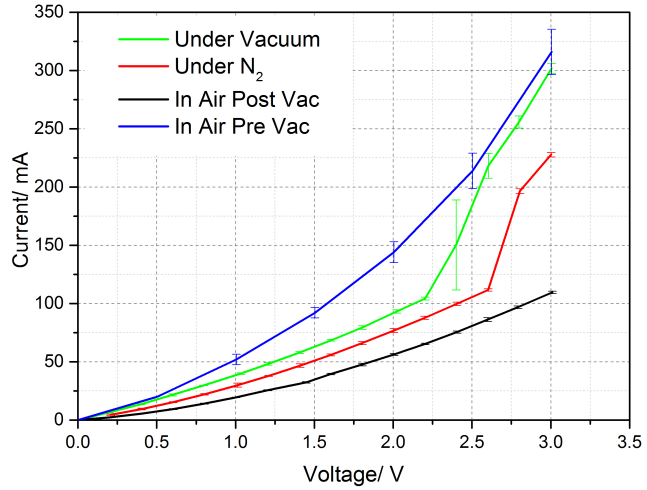
(c)

Figure 4.15: a) A comparison of the Raman spectra obtained pre (red) and post (black) I/V measurements. Close ups of the Raman spectra at low Raman shift for b) before, and c) after I/V measurements. The low angle peaks at 23-275 cm^{-1} are removed after 50 I/V measurements.

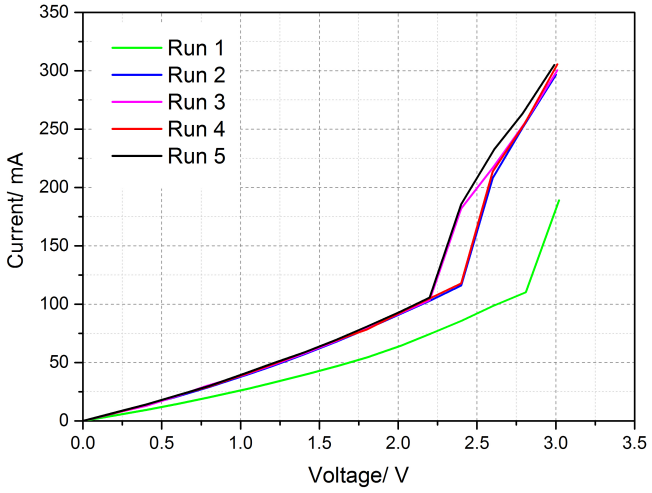
Conductivity Measurements Under Vacuum/ N_2

I/V measurements were carried out under vacuum and N_2 to imitate the inert conditions for reed switches. The BP samples carried lower currents under vacuum and N_2 than in air (Figure 4.16a). However, after subjected the same BP strip to I/V measurements under vacuum and N_2, the BP carried a lower current, when repeating the measurements in air (Figure 4.16a, black line). Additionally, the I/V curves obtained prior to placing the BP under vacuum showed non-ohmic behaviour. Measurements performed in air on the same BP after tests under vacuum showed small increases in linearity (Figure 4.16a blue and black). It can be postulated that after being under vacuum/ N_2, there is a delay in O_2 re-adsorption, which explains the less non-ohmic I/V characteristics for subsequent measurements in air. The lower currents carried by the BP following measurements under vacuum and N_2 could also be related to the delay in O_2 re-adsorption.

The I/V curves obtained under vacuum and N_2 showed reduced non-ohmic behaviour compared to in air (Figure 4.16a). The increase in linearity, compared to the I/V curves in air, suggests that for measurements under vacuum and N_2, the electron tunnelling behaviour described earlier could be suppressed. In air, both SWCNTs and MWCNTs have adsorbed species on their surface, such as O_2 and water, which can increase their conductivity [249–251]. Exposing SWCNTs to air or O_2 increased their electrical conductivity compared to under vacuum, as O_2 caused the apparent band gap of the SWCNTs to decrease [250]. A similar mechanism could occur for the MWCNTs in the BP, with a combination of thermal tunnelling effects [252] and band gap changes causing the non-linear behaviour observed for measurements taken in air. Switching the purge gas from pure N_2 to O_2 gave a similar change in conductivity as changing from vacuum to O_2, indicating that N_2 does not change CNT conductivity [250]. From these reports, the more linear I/V curves observed for measurements taken with the ferromagnetic BPs under vacuum or N_2 is likely due to removal of some of the adsorbed O_2 from the MWCNTs in the BP.



(a)



(b)

Figure 4.16: a) Comparisons of the I/V curves obtained for a Fe@MWCNT sandwich BP strip for measurements carried out in air, under vacuum and N_2 and b) graph showing the individual I/V curves obtained under vacuum over 5 cycles for **non-annealed** samples. All measurements were carried out on the same BP strip.

XRD patterns collected from the as produced BP (red) and after I/V measurements conducted under vacuum, and then in air (black) (Figure 4.17), show additional peaks, assigned to Fe_2O_3 [253]. The full width half maxima (FWHM) for the graphitic C peak at 26 2θ decreased from 0.897 to 0.794, following the I/V measurements. Combined, these observations indicate that whilst applying current increases the graphitisation of the MWCNTs, similar to as observed by Aslam *et al.* [247], this was accompanied by Fe oxidation. It is uncertain whether it was the C coated Fe clusters, or the Fe-filling inside Fe@MWCNT that was oxidised during the I/V measurements. The Fe oxidation

is undesirable for electromagnetic switches; the idea of replacing the metal contacts with Fe@MWCNTs was to avoid the oxidation issue, which leads to the metallic contacts corroding in current electromagnetic switches. Understanding if and how the Fe-filling inside the Fe@MWCNTs is being oxidised is crucial to evaluate the suitability of using ferromagnetic BPs in electromagnetic switch applications (chapter 6).

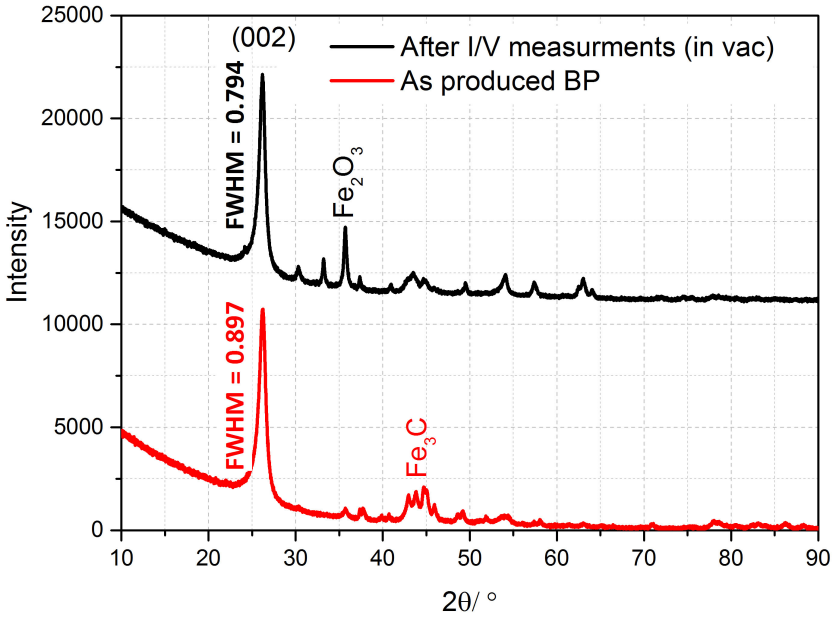
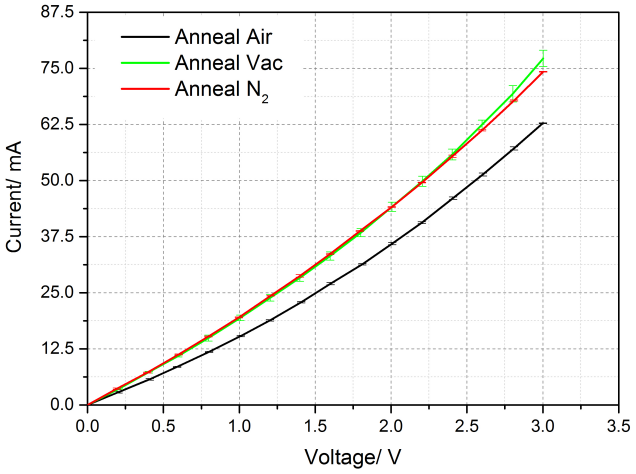


Figure 4.17: XRD patterns obtained from as produced BP (red) and following I/V measurements conducted under vacuum, then measurements in air (black), showing the formation of Fe_2O_3 following conductivity measurements.

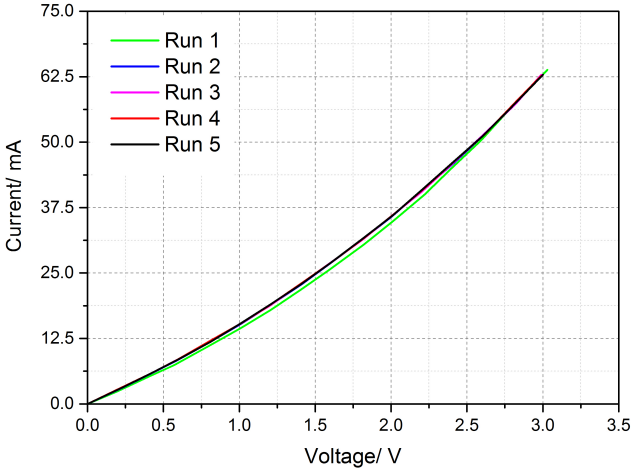
Measurements on annealed samples were performed to validate the hypothesis that annealing BP samples removes the differences in I/V curves observed between the first and subsequent cycles. An annealing temperature of 650 °C was selected based on literature; Fe@MWCNT samples were annealed at 645 and 650 °C for 15-20 h to increase α-Fe in the filling [114, 115]. BP samples were annealed for 5 h, as increasing the α-Fe content was unnecessary. Figure 4.18a shows a decrease in current carried following annealing, compared to non-annealed samples from the same BP batch. The I/V curves for the annealed sample are almost linear, with very similar I/V curves under N_2 and vacuum. The current carried by the annealed sample was lower than those of the un-annealed samples. This behaviour contradicts the expectation that annealing should increase the current carried by removing defects. The temperature chosen for annealing should be low enough to retain the conductive metal core inside the Fe@MWCNTs, so the explanation given by Grimes *et*

al. [240] is unlikely to explain the decrease in current carried. As measurements were only carried out on one annealed sample, it is uncertain whether this decrease in current carried is a representative result for annealing BP strips. Repeating the annealing procedure on a number of BP strips and carrying out I/V measurements on these will clarify this. Again, the non-ohmic behaviour decreases in vacuum, N_2 and in air, following measurements under vacuum, likely for the same reason as for the non-annealed sample.

The annealed sample displayed consistent I/V curves for all cycles (Figure 4.18b), suggesting that annealing the sample has a similar effect to passing current through the BP. However, it is difficult to determine whether the mechanism for the BP changes by annealing and applying current are the same.



(a)



(b)

Figure 4.18: a) Comparisons of the I/V curves for measurements carried out in air, under vacuum and N_2 and b) graph showing the individual I/V curves obtained over 5 cycles for **annealed** samples.

A small decrease in $I_{D/G}$, from 0.59±0.02 to 0.55±0.02, was observed before and after annealing the BP, respectively. The small $I_{D/G}$ decrease is not significant enough to show that annealing led to changes in the CNT graphitisation in the BP. The reports for annealing Fe@MWCNTs did not carry out Raman analysis [114, 115]. However, substantial increases in graphitisation of MWCNTs are reported by annealing at >1000 °C [246, 254–256]. The high annealing temperature is not comparable to the procedure used here, hence the increases in $I_{D/G}$ reported do not indicate how annealing affects $I_{D/G}$ here.

Raman spectra taken on the annealed BP following I/V measurements under vacuum showed an increase in $I_{D/G}$ to 0.63±0.12. The changes in $I_{D/G}$ before and after the I/V measurements are not significant enough to draw any conclusions. The relevance of the Raman data obtained following I/V measurements is debatable as it is uncertain whether exposing the BP to air after being under vacuum would affect the Raman data. Ideally, Raman would be carried out *in situ*, in the vacuum chamber, which was not possible with the equipment available.

4.3.4 Synthesis of BPs with Selective Magnetic Regions

A simple design (Figure 4.4c) was selected to evaluate the ability of using pastes and moulds to selectively deposit Fe@MWCNTs on conventional MWCNT BPs. Using a paste of dispersed Fe@MWCNTs could allow the past to be piped, similar to piping icing into intricate designs on a cupcake. Using a mould would be more suited for creating simple designs.

BP With Selective Magnetic Regions Created Using Fe@MWCNT Paste

P123 was selected as the medium for creating the Fe@MWCNT paste, as it is viscous, and behaves as a surfactant in solvents such as water, meaning that the Fe@MWCNTs should disperse well in it.

Sonicating P123 and water, of ratios given in Table 4.1, at 60 °C for 2 h produced homogeneous liquids, with a watery consistency, for a 50:50 ratio (P123-1) (Figure 4.19c) and gels for 75:25 (P123-2) and 70:30 (P123-4) ratios of P123:H_2O (Figure 4.19a and b). These gels contained large air bubbles, which were difficult to remove. Overall, P123-2 was closest to the desired viscosity required to create pipeable gels of Fe@MWCNTs.

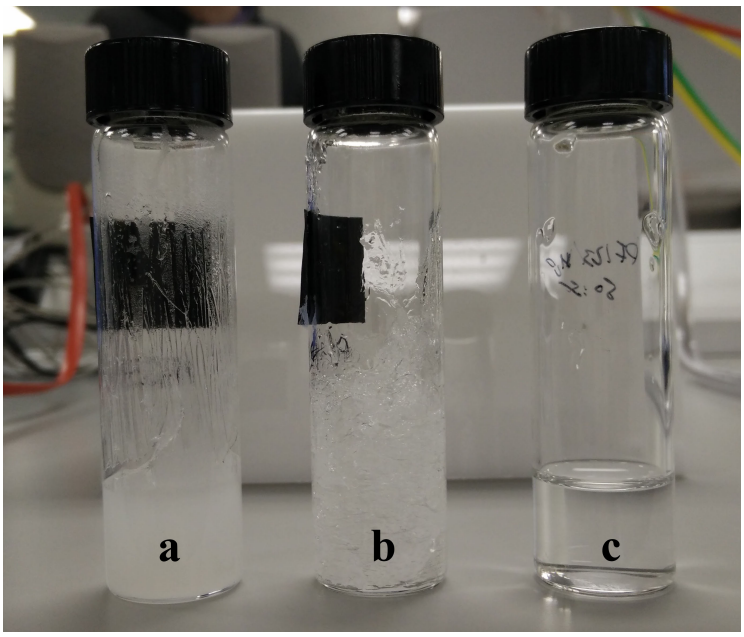


Figure 4.19: Photograph showing the mixtures of water and P123 obtained after sonication for 2 h at 60 °C where the ratios of P123 to water are a)75:25, b)70:30, and c) 50:50.

A ratio of 10 mg/g of Fe@MWCNTs:P123-2 was selected as a high concentration of Fe@MWCNTs is required to form BPs with magnetic response. Sonicating P123-2 and Fe@MWCNTs together was unable to create a homogenous mixture as the viscous nature of the P123-2 prevented the Fe@MWCNTs from infiltrating the gel. To overcome this, the mixture was stirred by hand, to form an inhomogeneous dark grey mixture.

A spatula was used to paste the Fe@MWCNT/P123-2 mixture onto the conventional MWCNT, however, the edges of the Fe@MWCNT regions were not well defined (Figure 4.20a). The P123/Fe@MWCNT mixture was difficult to spread, leading to the conventional MWCNT layer underneath tearing. Applying thin layers of paste was not possible, due to its sticky nature. The completed BP (Figure 4.20c) was shinier, compared to BPs produced with EtOH dispersions, with some excess P123 around the edges of the BP. The tear in the bottom MWCNT BP layer was no longer visible because excess P123 had infiltrated into the MWCNT layer, filling the space left by the tear in the BP.



(a) (b) (c)

Figure 4.20: Photographs showing the stages of creating a BP using the P123/Fe@MWCNT mixtures showing a) Pasting the P123/Fe@MWCNT mixture onto either side of the BP, b) pasting blank P123 (Solution 2) onto the centre of the BP, and c) the final selectively magnetic BP produced using this procedure.

The P123-BP showed improved flexibility compared to BPs produced using CNT dispersions in EtOH and was capable of being folded >90 ° without tearing. The BP only responded to magnetic stimulus in the regions where the Fe@MWCNTs had been deposited. However magnetic response was much slower compared to BPs made using MWCNTs dispersed in EtOH, due to the mass increase by incorporating the P123 polymer into the BP. These P123-BPs show some promise for increasing the flexibility of BPs; however the ability to create more intricately designed BPs with the current methodology is not possible.

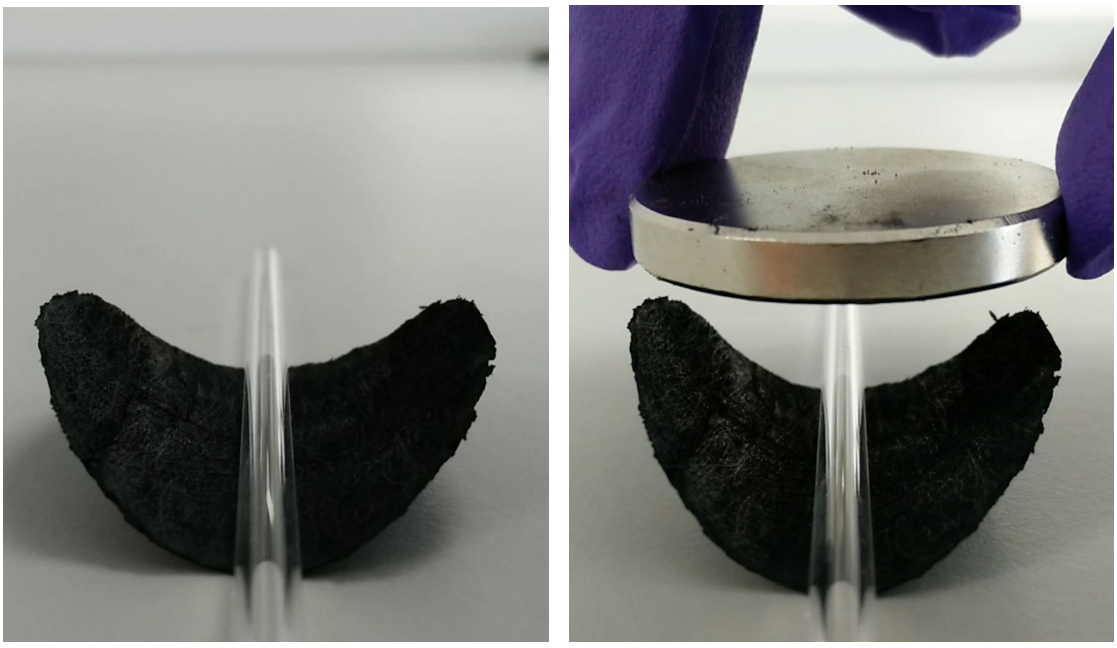
BPs with Selective Magnetic Regions Created Using Moulds

Creating the moulds from PDMS was straightforward, however the imprecise nature of cutting the PDMS meant that only crude shapes can be produced from PDMS, which limits the designs that could be produced accurately.

Initial attempts to produce BPs of the design in Figure 4.4c had limited success due to the poor contact between the MWCNT BP and the mould. The Fe@MWCNT dispersion was slowly pipetted onto the MWCNT layer to limit the amount of solution that seeped under the mould onto the central region of the BP. This process was time consuming and limited Fe@MWCNTs entanglement, which hindered the mechanical strength of the final BP. The resulting BP was very thin and could not be mechanically peeled from the filter. The BP was highly flexible whilst on the polycarbonate filter and easily folded in half, with the magnetic regions touching when exposed to magnetic stimulus. However, dissolving the

filter with $CHCl_3$ caused the BP to fall apart. The Fe@MWCNT layer separated from the conventional MWCNT layers, as confirmed using a magnet, suggesting poor entanglement between the layers.

The fragility of the BP was likely a result of the poor entanglement between the MWCNT and Fe@MWCNT layers, due to the slow filtration time. Improving the contact between the mould and the BP underneath by using the mould cured with a metal rod decreased the time required to deposit the Fe@MWCNT layers, improving the entanglement between the Fe@MWCNTs, and other layers in the sandwich structure. The rod allowed for constant pressure to be applied on the PDMS mould, meaning that the Fe@MWCNTs did not have to be pipetted onto the MWCNT BP. The BPs created using the clamped mould were mechanically cleaved off the filter with ease. The BP was flexible and only responded to magnetic stimulus in the regions where the Fe@MWCNTs were deposited (Figure 4.21). These preliminary experiments show that there is scope to create ferromagnetic BPs with the Fe@MWCNTs localised to specific regions of the BP.



(a) (b)

Figure 4.21: Images extracted from a video showing the BP reacting to stimulation with a neodymium showing a) the BP at rest, and b) the edges of the BP bending as they are stimulated by the magnet.

4.4 Conclusions

This chapter aimed to develop a versatile technique to produce BPs with a magnetic response, with control over where the Fe@MWCNTs are deposited, to create smart materials with pre-designed regions that respond to external magnetic stimulus. The BPs had a sandwich structure (MWCNT-Fe@MWCNT-MWCNT), which allowed for deposition of Fe@MWCNTs in specific areas, if desired.

SQUID measurements revealed that the M_s and H_c showed minimal differences regardless of whether the magnetic field was applied parallel or perpendicular to the BP. The M_s for the BP was lower compared to the as produced Fe@MWCNTs, this was attributed to the removal of C coated Fe clusters during processing of the Fe@MWCNTs.

Preliminary tests carried out on the prototype electric switch showed promise for using BP materials as a non-metallic switch material, capable of being manipulated by an electromagnet. I/V measurements performed in air showed that the BPs displayed non-ohmic behaviour, which is thought to be caused by tunnelling between the CNT junctions at higher voltages. The BPs were capable of reproducibly carrying the same current at a given voltage, up to 3 V, over a minimum of 50 cycles. The non-ohmic behaviour of the BP was reduced by carrying out measurements under vacuum or N_2, which may be due to the removal of O_2 from the BP surface. Fully understanding the conductivity behaviour of the BP in different environments requires further investigation. Depending on the I/V curve required for specific applications, the non-ohmic behaviour could be desirable, in which case, the BP should be used in air. Regardless of whether the measurements were conducted in air, or under inert conditions, the first I/V cycle was consistently lower than the subsequent cycles. Carrying out measurements to evaluate the contact resistances of the tweezers would also be useful, to establish their effect on the currents carried.

XRD revealed some oxidisation of the Fe to Fe_2O_3, investigating whether it was the C coated Fe clusters of the Fe-filling inside the Fe@MWCNTs will gain a better understanding of the effects of current on the ferromagnetic BP. The FWHM decreased following I/V measurements, suggesting that applying current resulted in an increase in crystallinity of the Fe@MWCNTs. The Fe oxidation has negative implications on the suitability of using these ferromagnetic BPs in switch technology, as the original benefit of using BPs was to avoid the oxidation issue with conventional metals used in electromechanical switches.

Annealing the BP prior to performing the I/V measurements resulted in all cycles displaying consistent I/V curves. This observation suggests that annealing the sample had a similar effect on the BP as passing current through the BP, although it is uncertain whether the mechanisms for the changes to the BP following annealing is the same as applying current.

Ferromagnetic BPs with Fe@MWCNTs deposited across the entire surface and with two magnetic strips were created. Two approaches were used to create the designed ferromagnetic BPs, using either a mould or a paste of Fe@MWCNTs. Both approaches produced BPs with localised Fe@MWCNT deposition, however both require further development. Using the mould was cumbersome, due to the difficulties with accurately cutting the PDMS mould and achieving good contact between the MWCNT BP and the mould. Whilst clamping the mould in place reduced the amount of Fe@MWCNT solution that seeped under the mould, there is likely to be a small amount of seepage. For the paste method, creating a homogenous Fe@MWCNT-P123-2 paste was challenging, and pasting intricate designs with the current set up would be difficult.

Despite the flaws with the approaches taken to create BPs with selective magnetic regions, this chapter has shown that ferromagnetic BPs with the Fe@MWCNTs deposited in specific regions can be created. Ferromagnetic BP movement was easily controlled using external magnetic fields, showing that there is promise in using these materials as controllable smart materials, whilst I/V measurements highlighted that individual BP samples were capable of reliably carry the currents consistently at a given voltage. The work here shows the potential of nanomagnetic macroscopic devices by exploiting strips of Fe@MWCNT BPs in a relay. Whilst magnetic nanomaterials have been proposed to be suitable a vast array of applications, such as in magnetic force microscopy tips [103, 104, 257], high bit density memory devices [73, 208] and magnetic rotary encoders [208], little work has been carried out on actually realising these applications by creating the devices. However, Mu *et al.* [231] created highly programmable 'walking' devices from graphene-oxide papers. These papers were capable of adopting pre-designed shapes and move, controlled by light or heating. The mechanism for these papers involve selectively coating certain regions of the graphene-oxide paper with polydopamine, which shrink and release water when heated or stimulated by light. This paper further reveals the potential of creating smart, responsive materials which could be used in robotics and sensing.

Chapter 5

Mechanical Properties of Buckypapers

In this chapter, BPs were produced from N-doped and conventional MWCNTs, of two different lengths per MWCNT type, with the aim of studying the effects of MWCNT type and length on the BP's mechanical properties. Tensile tests were performed in situ, in SEM, to gain further insight into the failure process and strain maps were produced from the images by digital image correlation (DIC).

5.1 Introduction

MWCNTs are known for having high stiffness and strength under axial stress, with theoretical predictions of around 1-5.5 TPa and 300 GPa for the Young's modulus and tensile strength, respectively [258, 259]. Experimental determination of the mechanical properties of MWCNTs is hindered by their small size, so indirect methods are often used. Lateral bending of arc-discharge MWCNTs, gave average tensile strengths and Young's moduli of 14.2 GPa and 126 GPa, respectively [260], whilst TEM-electrostatic deflection gave Young's moduli of 0.1-1 TPa [261]. Direct tensile tests on arc-discharge MWCNTs and SWCNTs mounted across opposing AFM tips gave tensile strengths of 150 [262], and 30 GPa [263], respectively.

The values for mechanical properties of individual MWCNTs is known to depend on their properties, Poncharal *et al.* [261] showed that increases in MWCNT diameter induces decreases in Young's modulus. Salvetat *et al.* [264] reported decreases in the average

Young's modulus from 810 GPa to 10-50 GPa for structurally ordered MWCNTs and disordered catalytic MWCNTs, respectively, showing the large effect of defects on mechanical properties.

Processing CNTs to form BPs creates macrostructures whose mechanical properties can be easily measured using conventional tensometers. Thus far, BPs are mostly produced with SWCNTs, with some reports on DWCNT [127, 139, 265] and MWCNT BPs [128, 266]. Typically, the mechanical properties of BPs (Table 5.1) are much lower than for individual CNTs. These differences between individual CNTs (SWCNT or MWCNTs) and BPs is related to stress transfer between the CNTs within the BP [265]. BPs often contain bundles of undispersed CNTs; the number and nature of the junctions between these affects the BP's mechanical properties. Stress is transferred between adjacent junctions and limits the BP's mechanical properties because of the low inter-tube shear modulus [267].

Many factors influence the mechanical properties of BPs, which can be categorised based on whether they relate to CNT or BP properties. It is very difficult to establish which factors have the largest effect on the BP's mechanical properties, especially as the literature is not directly comparable due to the vast array of differing variables. For example, reports on producing SWCNT BPs using different methods are unlikely to use SWCNTs produced using the same synthesis parameters or method, resulting in SWCNTs of differing properties hence comparing the BP production methods is unable to accurately assess the effect of the different BP production method on BP properties.

The effects of CNT properties such as CNT type, synthesis method, aspect ratio and morphological properties on BP properties have to be considered. Blighe *et al.* [265] tensile tested BPs made with SWCNTs and DWCNTs from a variety of commercial suppliers and found that SWCNT or DWCNT defect population had less of an impact on tensile strength than film morphology, i.e. entanglement. Contradictory reports state that SWCNT synthesis method is an important factor, with arc discharge SWCNT BPs possessing higher mechanical properties than HiPCO SWCNT BPs [268, 269] (Table 5.1). Arc discharge SWCNTs are typically less defective than HiPCO SWCNTs, however it is unsure whether it was the defective nature of the SWCNTs, or another property, such as SWCNT morphology, that was responsible for the higher tensile strengths and Young's modulus of the arc discharge SWCNT BP. As mentioned in Chapter 4, the aspect ratio strongly influences BP formation, hence the majority of BPs reported are created using

SWCNTs [138, 232]. Creating BPs from post hoc chemically modified MWCNTs, such as MWCNTs functionalised with carbonyl, hydroxyl or amino groups, again impacts the BP tensile strength, with polyvinylpyrrolidone (PVP) infiltrated OH-MWCNT BPs displaying tensile strengths of 15.24 MPa, compared to 6.08 MPa for PVP infiltrated MWCNT-BP [270].

BP related factors, such as density, alignment and BP production method also affect their mechanical properties. Increasing the density of SWCNT and DWCNT BPs resulted in increases in the Young's moduli from 0.22 to 1.41, and 1.41 to 3.14 GPa, respectively [271]. Similarly, increases in Young's moduli were observed for conventional MWCNT BPs, from 0.28 to 2.2 GPa with increases in BP density from 0.43 to 1.29 g/cm^3 [233]. The production method impacts entanglement, which has a strong effect on the BP's mechanical properties, with aligned BP structures typically possessing higher mechanical properties [150, 272] (Table 5.1). Again, directly comparing aligned to entangled BPs is inaccurate due to the different syntheses and properties of the CNTs, however Liu *et al.* [239] was able to directly compare aligned to entangled MWCNT sheets fabricated directly by floating catalyst CVD method. The as-grown MWCNT BP, which displayed a tensile strength of 186 ±19 MPa, were stretched by 30 % using a tensometer, then pressed under a pressure of 200 MPa to align the MWCNTs within the BP. Further stretching the BP by an additional 5 % increased the tensile strength to 598 ±36 MPa. Liu's work indicates that the degree of alignment of the MWCNTs strongly affects the BP's mechanical properties.

CNT Type	**BP Method**	**Tensile Strength/ GPa**	**Young's Modulus/ GPa**	**Ref**
SWCNT (arc discharge)	Vacuum filtration	14.3 ±2.83	3.25 ±0.89	[268]
SWCNT(HiPCO)	Oleum	8	0.03	[273]
SWCNT(HiPCO)	Vacuum filtration (Pristine)	0.01 ±0.002	0.8 ±0.1	[269]
SWCNT(HiPCO)	Vacuum filtration (10 M HNO_3)	0.074	5	[269]
SWCNT(HiPCO)	Vacuum filtration (Triton X)	0.014-0.035	0.2-2	[274]
SWCNT(HiPCO)	Vacuum filtration (SDS)	0.011	0.66	[275]
SWCNT(dual pulsed-laser vaporisation)	Cross flow filtration	0.01	1.2	[276]
Few-walled CNTs	Spinning (aligned BP)	2	90	[272]
MWCNT	Vacuum filtration	0.015	-	[277]
MWCNT	Vacuum filtration	0.002 ±0.0001	0.36 ±0.01	[270]
MWCNT (floating catalyst)	Winding drum (aligned BP)	9.6	130	[150]
MWCNT (VACNT)	Vacuum filtration	0.075	0.785	[228]

Table 5.1: Table showing the approaches used to produce BPs, the type of CNT used, and the mechanical properties for each approach. The abbreviations HiPCO stands for high pressure CO, whilst SDS stands for sodium dodecyl sulfate, a surfactant used to disperse CNTs.

Based on the sensitivity of BP properties to CNT type and functionalisation, producing BPs with other CNTs, such as doped MWCNTs, is likely to influence their mechanical properties. MWCNTs doped with N [278–281], B [280] and P [282] have been reported, however there has been little to no reports of making BPs from these doped MWCNTs. This chapter begins to address this literature gap by studying N-doped MWCNT BPs. For vacuum filtration produced BPs, the structural properties and surface chemistry of doped MWCNTs are likely to affect their dispersibility, MWCNT entanglement and BP morphology, all of which influence the BP's mechanical properties. Doping MWCNTs with N changes their surface chemistry, likely resulting in decreased hydrophobicity due to the lone pair on the N atoms, which consequently increases their dispersibility compared to conventional MWCNTs. Having a well-dispersed MWCNT solution affects the BP morphology, resulting in BPs with fewer bundles present. As mentioned, these bundles can act as microscopic defects within the BP, such that the BP has poorer mechanical properties. MWCNT entanglement depends on the aspect ratio and MWCNT length. Introducing dopants into MWCNTs affects their growth rate, for example AACVD N-doped MWCNTs grown with benzylamine grow at *ca.* half the rate of AACVD conventional MWCNTs produced with toluene [283]. This decrease in growth rate is attributed to the N atoms reducing catalyst activity and blocking the incorporation of C into the graphitic MWCNT. These shorter N-doped MWCNTs are less likely to entangle well during filtration, which will have a negative impact on the mechanical properties of the BP.

The morphological and internal structure of N-doped MWCNTs is likely to have an impact on the mechanical properties of BPs produced from them. N-doped MWCNTs are typically straighter than conventional MWCNTs (Figure 5.1b) and increases in N content result in decreases in MWCNT diameter [278]. As MWCNT diameter influences the mechanical properties of individual MWCNTs, the affect may also transfer into the mechanical properties of the BPs. The internal cavity of conventional and N-doped MWCNTs is shown in Figure 5.1c and d, respectively. N-doped MWCNTs characteristically have a stacked-cone, or 'bamboo' structure (Figure 5.1d). This stacked-cone structure is caused by the N atoms inducing curvature in the graphitic layers [280]. N atoms promote pentagon formation, which leads to cap formation and cone-stacking [284], with N having a preference for the inner walls in the compartment core [278]. The stacked-cone structure of N-doped MWCNTs is likely to make them more resilient to breaking upon bending [279], however no mechanical tests have been carried out to confirm this.

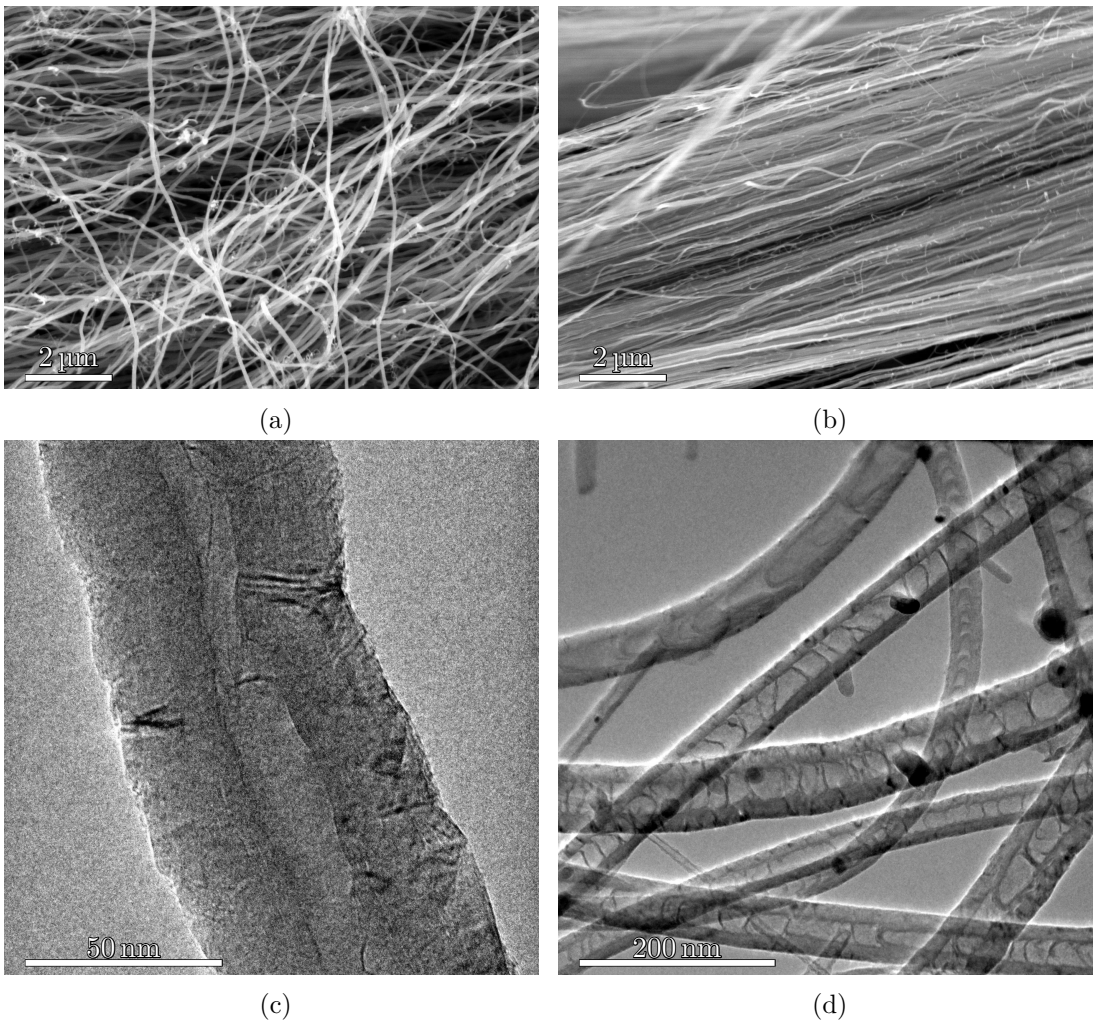


Figure 5.1: SEM images, courtesy of Dr Shayan Meysami, showing the morphology of a) conventional MWCNTs, b) N-doped MWCNTs. TEM images showing the internal structure of c) conventional MWCNTs, and d) N-doped MWCNTs.

This chapter explores the effects of CNT type (conventional or N-doped MWCNTs), and CNT length on BP structure, surface chemistry and tensile strength. Tensile tests were performed with *in situ* SEM, which provides new insight into the BP failure process. The images collected using cameras and SEM during tensile tests were analysed using DIC to obtain displacement and strain maps, which provide information on the local strains experienced within the BPs. By first studying the effects of CNT length and type on the mechanical properties individually, one can make more informed choices of which CNTs are most suited for creating BPs with a selected tensile strength. Further, the mechanical properties study can be extended to BPs consisting of more than one CNT type and length, such is the case for the ferromagnetic MWCNT BPs created in Chapter 4, and compared to BPs of each type within the mixed BPs.

5.2 Experimental

5.2.1 Preparation of MWCNTs and N-doped MWCNTs

Conventional and N-doped MWCNTs were synthesised in-house by AACVD using the procedure outlined in section 4.2.1 [25, 30, 285]. For conventional MWCNTs synthesis, a camphor precusor solution was used and syntheses were carried out for 15 and 30 mins to produce MWCNTs of short (30-50 μm) and long lengths (400-500 μm), respectively. For short N-doped MWCNTs (50-80 μm), a 5 wt. % ferrocene in benzylamine precursor was used. Longer N-doped MWCNTs (160-200 μm) samples were provided by Dr Fatma Dinc.

5.2.2 Preparation of Buckypapers

Dispersions of conventional and N-doped MWCNTs were obtained following the same procedure. 100 mg of MWCNTs was added to 500 ml ethanol (Fisher Scientific, anhydrous), and stirred with a magnetic stirrer at 1000 RPM for 20 min. Subsequently, the same procedure as outlined in Section 4.2.2 was followed to create the dispersions.

The filtration setup is described in Section 4.2.2. To make the BPs, first, half the well-dispersed supernatant was passed though the filter, followed by the final sonicated material. The remaining half of the well-dispersed supernatant was passed through the filter. The BP was dried overnight before being mechanically peeled off the polycarbonate membrane.

5.2.3 Characterisation

SEM (JEOL-JSM840F) operated at 5 kV was used to take images of the BPs before and after tensile tests to establish the effects of tensile tests on BP structure,

BP surface chemistry was studied at the Bio-Nano Electronics Research Centre (BNERC), Toyo University, with the assistance of Prof Takashi Uchida. Contact angles were measured with the Kyowa Interface Science Co. LTD Drop Master DM-701, using the FAMAS software in Sessile drop mode to collect images and calculate contact angles. A 22 G (gauge) needle was fitted onto the syringe and filled with water, ethylene glycol or hexadecane. A 28 G needle was used for formamide measurements, due to poor droplet

size control with the 22 G needle. The contact angle was calculated as the average of 5 droplets, of size 1 μml, per sample. Measurements were taken on both BP faces, with the bottom face referring to the face in contact with the filter paper during deposition. For two of the conventional MWCNT BP samples, bottom face only, a 32 G needle was used with a droplet size of 4.5 μml.

Fourier transform infrared (FTIR) spectroscopy (Bio-Rad Varian Excalibur FTS 3500) and X-ray photoelectron spectroscopy (XPS) (ThermoFisher Thermo Scientific K-Alpha+ XPS System) were performed to investigate the surface chemistry of the BPs. Dr Philip Holdway carried out the XPS measurements conducted on N-doped and conventional MWCNT BPs. The XPS spectra were analysed using the CasaXPS software.

5.2.4 Mechanical Tests and Strain Maps

Tensile tests were carried out in collaboration with Prof Clive Siviour, Dr Kalin Dragnevski and Ms Marzena Tkaczyk from the Laboratory for *In situ* Microscopy and Analysis (LIMA) in the Department of Engineering Science, Oxford University. A Carl Zeiss EVO LS15 VP-SEM equipped with a 200 N Deben tensile stage, with a 20 N load cell was used for *in situ* tensile tests. BP specimens (*ca.* 10 x 30 mm) were positioned between the jaws of the miniature-testing rig. The rig was loaded into the SEM and set to zero force. The Deben Microtest software obtained real time force vs time data in tensile mode. The BP was strained using a motor speed of 0.2 mm/min until failure, with the SEM recording the process. Images were taken at a rate of 5 frames/second using a Point Grey digital camera, with a 200 mm lens, for tabletop tensile tests. Table 5.2 shows the shorthand notation used for labelling the BP samples.

Code	Description
LCBP	Long conventional MWCNT BP
SNBP	Short N-doped MWCNT BP
LNBP	Long N-doped MWCNT BP

Table 5.2: The short hand system used to label the samples. Following the code, a number is given to indicate different batches of BP samples, e.g. LCBP1.

Frames extracted from the SEM videos, and digital images were analysed by DIC, using DaVis 8.3.0 software, to obtain displacement maps by identifying the position changes of surface features during tensile testing. DIC was carried out with the assistance of Marzena Tkaczyk. DIC uses cross correlation to measure the shift in surface features over

the course of the mechanical measurements. The images were processed by selecting an appropriate box size (measured in pixels). This box size had to be small enough to allow for the analysed images to have smooth colour transitions, whilst being large enough to observe the small feature displacements from image to image. The software assigns each box with a shade/ colour depending on how far the surface features had moved from image to image.

5.3 Results and Discussion

5.3.1 Synthesis of Doped- MWCNT BPs, and their Properties

Two lengths of N-doped and conventional MWCNTs, labeled either short or long, depending on their relative length, were used for BP production. The conventional long and short MWCNTs had lengths of *ca.* 400-500 and 30-50 μm (Figure 5.2a and b), respectively, whilst the long and short N-doped MWCNTs had lengths of 160-200 and 50-80 μm, respectively (Figure 5.2c and d). The diameters of the long and the short conventional MWCNTs were 55-90, and 35-85 nm, respectively, and 55-110 and 45-95 nm, for the long and short N-doped MWCNTs, respectively.

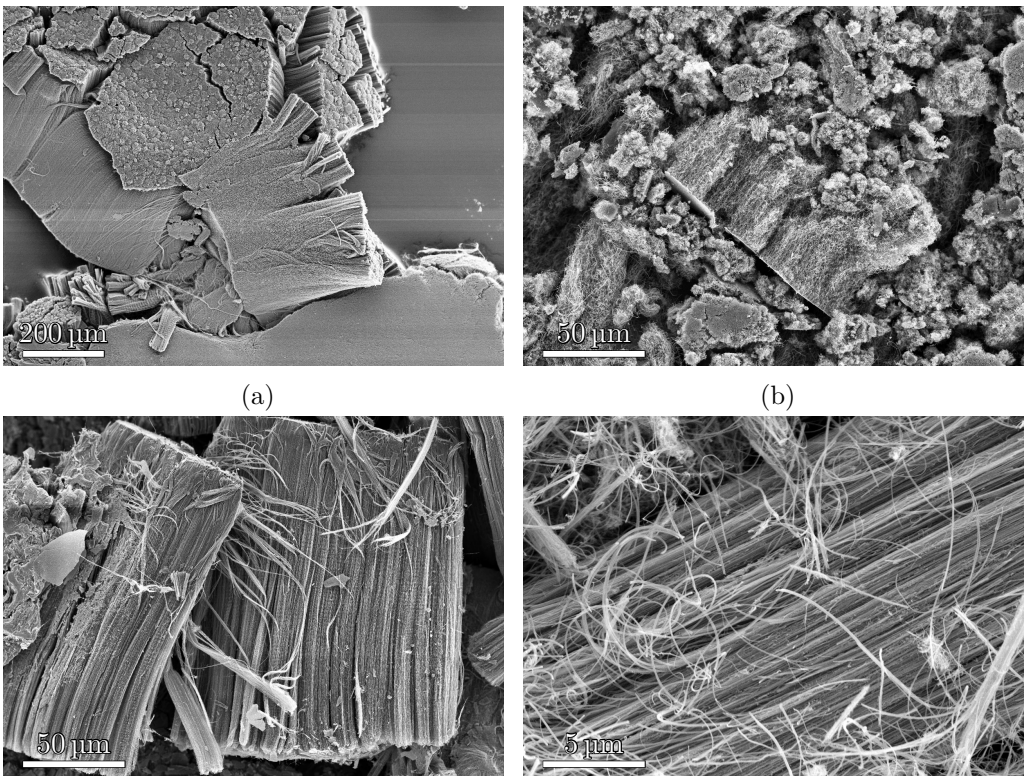
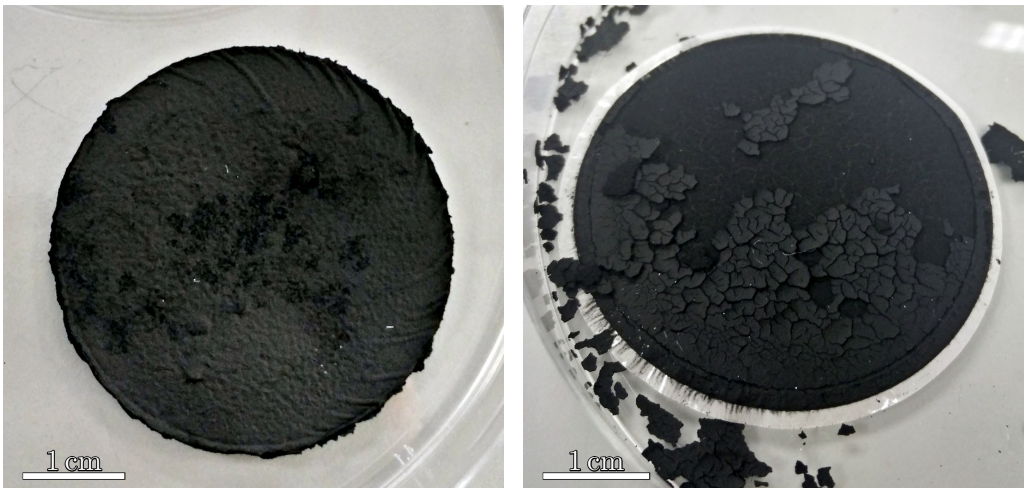


Figure 5.2: SEM images of the raw MWCNTs used for BP production. a) conventional MWCNTs (long), b) conventional MWCNTs (short), c) N-doped MWCNTs (long), and d) N-doped MWCNTs (short).

BPs produced from long conventional MWCNTs, and both long and short N-doped MWCNTs had a similar optical appearance to Figure 5.3a. On occasion, the surface of the BP had a speckled appearance, with some darker patches (Figure 5.3a). These darker patches were likely to be undispersed bundles; these bundles, typically *ca.* >40 µm in size, were observed on the BP surface under SEM. These bundles were particularly prevalent on the surface of short N-doped MWCNT BPs (Figure 5.5c and d).

BPs produced from long conventional and N-doped MWCNTs (Figure 5.4a and b, and Figure 5.5a and b) mostly consisted of well-dispersed and entangled MWCNTs, with some small bundles of MWCNTs on the surface (not shown). A minimum MWCNT length is required to produced BPs, as shorter MWCNTs are incapable of entangling well enough to produce free-standing BPs. Several attempts to produce BPs from the short MWCNTs were unsuccessful (Figure 5.3b); they fragmented after filtration to form small, fragile flakes. The surface of these short conventional MWCNT BP fragments consisted of short, disordered bundle-like clusters, which were too short and insufficiently entangled to create a freestanding BP (Figure 5.4d).The differences in the brittle short conventional MWCNT

BP fragments and the freestanding short N-doped MWCNT BPs could be related to the longer length, and aspect ratio, of the N-doped MWCNTs (length 50-80 μm), compared to the short MWCNTs (length 30-50 μm), although other factors may have influenced this, such as the defective nature of the MWCNTs. The length of the short N-doped is likely to be around the threshold minimum length, or aspect ratio, for BP formation.



(a) (b)

Figure 5.3: Optical image of a) conventional MWCNT BP produced from 'long' MWCNTs, and b) conventional MWCNT BP consisting of 'short' MWCNT on the polycarbonate filter. BPs were not successfully produced from short MWCNTs.

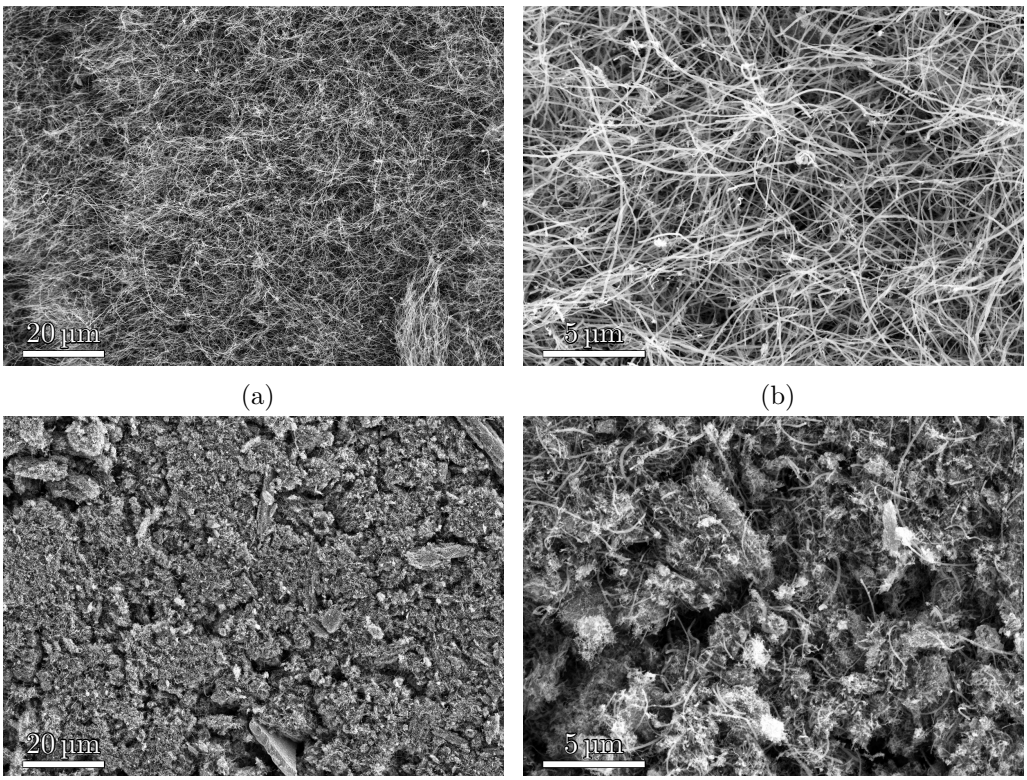


Figure 5.4: SEM images of a and b) long conventional MWCNT BP, and c, and d) attempts at producing BPs from short conventional MWCNTs, in which the majority of the surface appears to be messy bundle-like clusters.

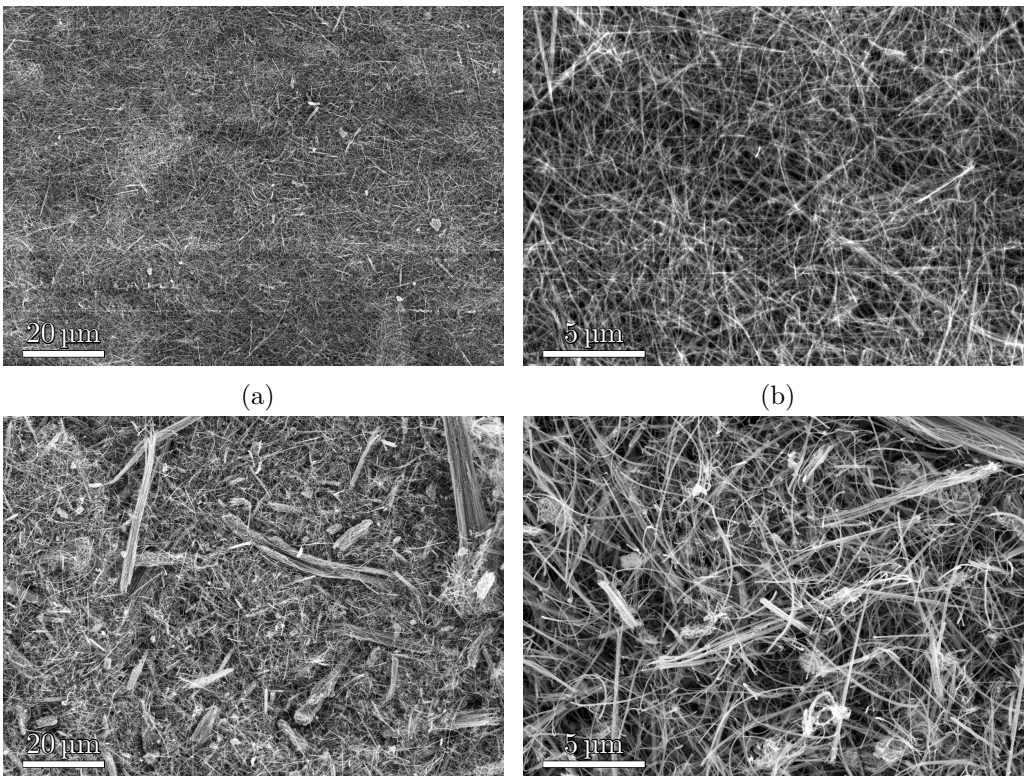


Figure 5.5: SEM images taken for a and b) long N-doped MWCNT BP sample, and c and d) a short N-doped MWCNT BP sample. The long N-doped MWCNT BPs have a more uniform distribution, whilst bundles are observed on the surface of the short N-doped MWCNT BP.

5.3.2 Contact Angle Measurements

Contact angles were carried out to understand the hydrophobic/ hydrophilic nature of the BPs. However, as the BPs consist of fibres, they are porous mats, rather than a solid surface. The porous nature of the BPs limits the validity of the surface free energy (SFE), polar and dispersive components calculated. However, the information obtained from contact angle measurements can be used qualitatively, to establish if the hydrophobic/ hydrophilic nature of the BP changes depending on MWCNT type.

Contact angles obtained for a range of solvents allowed the SFE of BPs and the corresponding polar and dispersive components to be calculated. These polar and dispersive values give an indication of the hydrophilic or hydrophobic nature of the BP surface, which gives indirect information on BP surface chemistry.

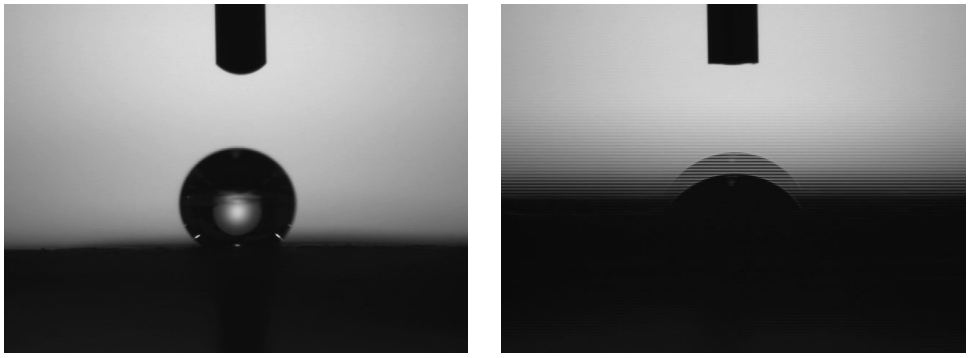
The Young's equation (Equation (5.1)) relates the surface tension of the three phases to contact angle for ideal surfaces. However, BP surface roughness and dynamic contact angles result in non-ideal behaviour. A geometric mean, extended Fowkes equation (Equa-

tion (5.2)) [286] was used to estimate the SFE, where $\cos\theta$ is the contact angle, σ is the surface tension and the superscripts D and P represent the dispersive and polar parts, respectively. The subscripts s and l represent solid and liquid, respectively.

$$\sigma_{SG} = \sigma_{SL} + \sigma_{LG}\cos\theta \tag{5.1}$$

$$\frac{\sigma_l(\cos(\theta+1))}{2\sqrt{\sigma_l^D}} = \sqrt{\sigma_s^P}\frac{\sqrt{\sigma_l^P}}{\sqrt{\sigma_l^D}} + \sqrt{\sigma_s^D} \tag{5.2}$$

The BP absorbed the majority of solvents, on both faces. This highly absorbent behaviour, whilst interesting, impeded the accuracy of the measured angles, due to a large and variable amount of the droplet being absorbed before image capture (Figure 5.6). Therefore, as the measured contact angles are highly unreliable, they can only be used qualitatively to assess the hydrophobic or absorbent nature of the sample.



(a) (b)

Figure 5.6: Representative images captured during contact angle measurements showing a) a water droplet on the surface of a BP displaying hydrophobic behaviour, b) absorbing behaviour of the BPs, typically observed for the non-water solvent droplets on the surface of a BP sample.

The average contact angles for each solvent were inserted into Equation (5.2) to produce straight line graphs, where the gradient and intercept gives the square root of the polar and the dispersive component, respectively. The sum of the polar and dispersive components is the total SFE. An example graph (Figure 5.7), shows the large errors associated with the average contact angle values, due to the absorbent nature of the BP. For some graphs, the data points did not form a straight line, which further impedes the accuracy of the calculated SFEs.

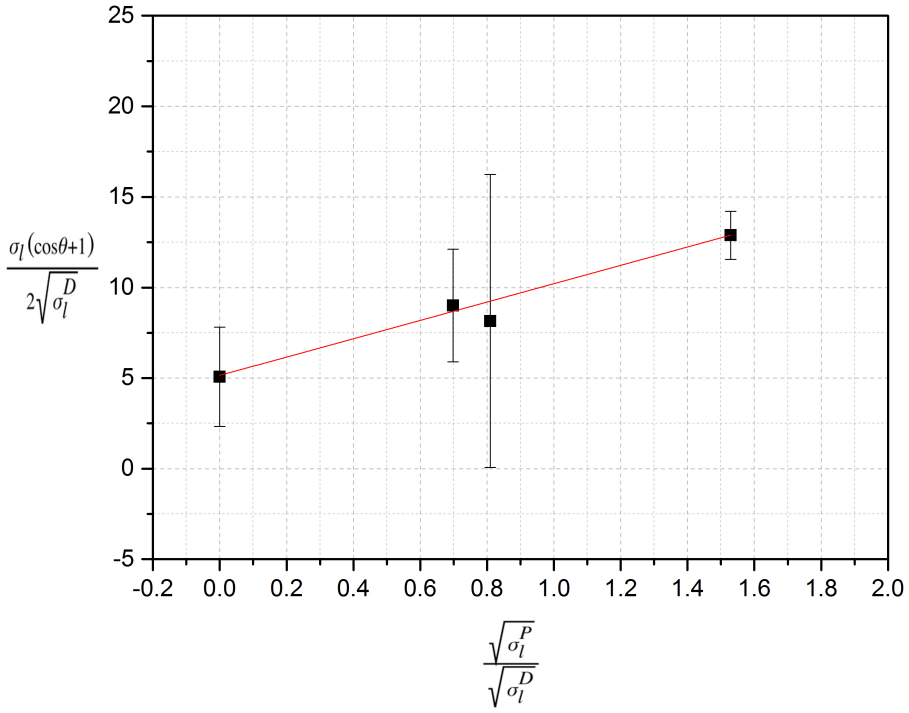


Figure 5.7: An example of the graphs used to calculate the SFE of BPs, in this case for a conventional MWCNT BP. The large errors are a result of the absorbent behaviour of the BPs.

The polar, dispersive, SFE values and their associated errors, averaged across three samples per BP type, are summarised in Table 5.3. These errors were calculated using Equation (5.3), where alpha is the error, Z is the component and A and B are variables. The standard deviation in contact angle for each solvent (5 droplets per solvent), was averaged per batch for each BP type. The errors for contact angle per solvent, and the intercept and gradient for the SFE graphs were inserted into Equation (5.3), however these values are significantly underestimated, as error for the delay in capturing droplet images cannot be quantitatively estimated.

Qualitatively, the dispersive and polar contributions to the total SFE of the N-doped and conventional MWCNT BPs differ. For conventional MWCNT BPs, the polar component dominates, indicating that the MWCNT BP is more hydrophobic than hydrophilic. The N-doped MWCNT BPs are less hydrophobic than the conventional MWCNT BPs, with similar values for the polar and dispersive components. For both BP types, there is only a marginal difference between the top and bottom faces for the calculated SFE, suggesting that the difference in surface roughness did not have a significant effect on contact angle.

$$\alpha_Z = \sqrt{(\alpha_A)^2 + (\alpha_B)^2} \tag{5.3}$$

	Total SFE/ Jm^2		**Dispersive/ Jm^2**		**Polar / Jm^2**	
BP Type	**Top**	**Bottom**	**Top**	**Bottom**	**Top**	**Bottom**
MWCNT BP	53 ±10	59 ±12	46 ±10	42 ±11	12 ±10	16 ±12
N-doped MWCNT BP	59 ±12	58 ±11	35 ±12	31 ±11	24 ±12	27 ±11

Table 5.3: The total SFE, and the corresponding dispersive and polar components for both conventional and N-doped MWCNT BPs, calculated using the Fowkes equation. Top and bottom refer to the face of the BP, where the bottom face is the BP that was in contact with the filter paper.

The Cassie-Baxter and Wenzel models describe how the contact angle of a stable liquid droplet is influenced by rough, non-ideal surfaces [287–289]. A Wenzel state describes when droplets seep into cavities on a rough surface [287]. However, the droplets on BPs surpass the Wenzel state; they spread on the BP surface, before being absorbed. This physisorption behaviour means these models cannot be used for describing droplet behaviour on the BP surface. Instead, when the liquid penetrates into the cavities in the BP, the droplet becomes unstable and collapses. The collapse of the droplet suggests that the solid/air surface tension dominates.

Different batches of BP varied in behaviour, especially for their interactions with water droplets (Table 5.4). Samples 4 and 5 (N-doped MWCNT BPs) were hydrophilic, and quickly absorbed the water droplets on both faces, whilst sample 6 showed superhydrophobic behaviour. Both faces of a BP can also behave differently; samples 1 and 2 (conventional MWCNT BPs) displayed superhydrophobic and hydrophobic behaviour, respectively on the bottom faces, whilst the top faces were hydrophilic and absorbed the water droplets. These observations suggest that the increased surface roughness of the bottom face increases the contact angle between water droplets and the BP surface.

Both N-doped and conventional MWCNT BPs were highly absorbent on both faces for the remaining three solvents, ethylene glycol (EG), formamide (F) and hexadecane (H) (average contact angles given in appendix). This highly absorbent behaviour could be utilised in spillage cleanup or water remediation, similar to using MWCNTs as impurity sponges [290–292]. Gui *et al.* [290] synthesised sponge-like MWCNT materials, formed of self-assembled interconnecting MWCNT skeletons. These MWCNT sponges had porosities >99 % and could be repeatedly compressed and expanded, without collapsing. SEM images of the sponge had a similar appearance to BPs; both are porous structures of interconnected MWCNTs. Unlike the BPs, the MWCNT sponges were structurally flexible and could be twisted without breaking. The MWCNT sponge could quickly absorb a vast range of oils and solvents, including diesel oil, chloroform and ethylene glycol. Zhu *et al.* [291] reported a maximum sorption capacity of 92.30 g/g for oil in seawater using MWCNT sponges. Our BPs may be suitable for sponge applications, and investigations into their sorption capacity, compared to MWCNT sponges, could be a topic of future research.

BP type	Sample No.	Face	Average Contact Angle/ °
MWCNT	1	T	49 ±1
MWCNT*	1	B	153 ±3
MWCNT	2	T	40 ±2
MWCNT	2	B	122 ±5
MWCNT	3	T	132 ±5
MWCNT*	3	B	152 ±3
N-doped	4	T	53 ±9
N-doped	4	B	33 ±10
N-doped	5	T	22 ±6
N-doped	5	B	45 ±14
N-doped	6	T	157 ±3
N-doped	6	B	154 ±3

Table 5.4: The average contact angle for water, recorded for three batches, of N-doped or conventional MWCNT BPs. For the 'Face' column, T and B represent top and bottom faces, representative. For samples marked with a *, the needle was switched to a 32 G needle, and a droplet of size 4.5 µml was deposited on the BP surface.

5.3.3 XPS and FTIR Spectra of BPs

FTIR and XPS were carried out to investigate the surface chemistry of the BPs. Assigned peaks for the FTIR spectra (Figure 5.8) collected for the raw MWCNTs and N-doped and conventional MWCNT BPs are shown in Table 5.5. The FTIR spectra for all samples were very similar. Misra *et al.* [293] studied N-doped MWCNTs with FTIR and assigned the peaks at 1250 and 1372 to C-N and N-CH_3 stretching vibrations, respectively. However, these peaks are present in all four samples, not just the samples containing N-doped MWCNTs, which is difficult to understand.

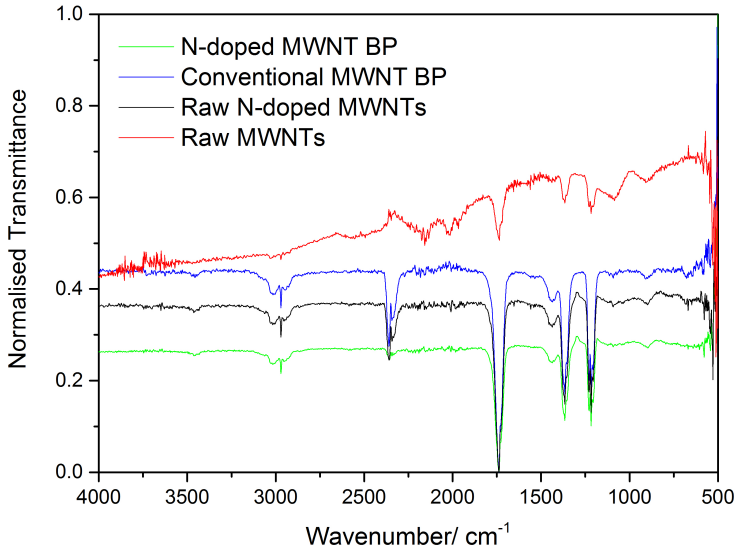


Figure 5.8: FTIR spectra obtained for raw MWCNTs, raw N-doped MWCNTs and N-doped and conventional MWCNT BPs.

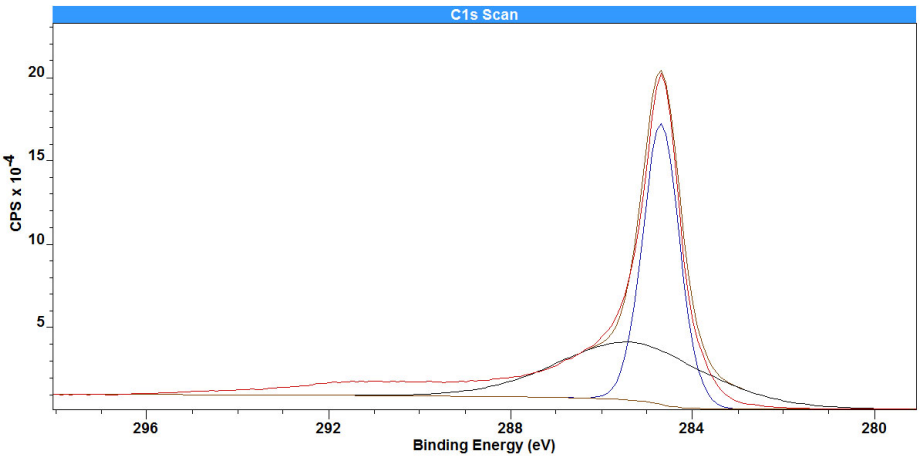
Peak Wavenumber/ cm^{-1}	Assignment
1250	C-N stretch (aromatic amines)
1370	C-H rock (alkanes)
1442	MWCNT
1740	MWCNT
2350	atmospheric CO_2
3000	C-H_x stretching of chemisorbed H_2

Table 5.5: The assignment to the key identified peaks present in all four FTIR samples.

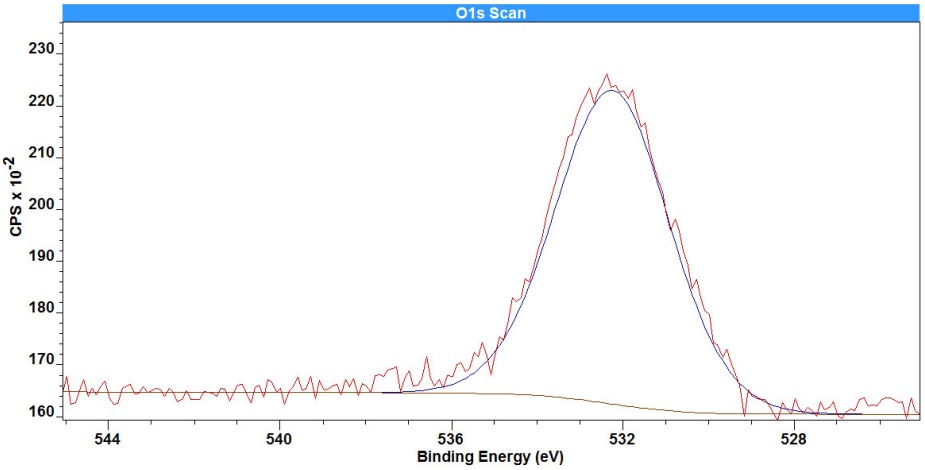
FTIR is a bulk characterisation technique that was not sensitive enough to detect differences between the N-doped and conventional MWCNTs. As the number of N dopant atoms is likely to be <5 %, XPS was carried out to investigate the surface properties of the BP samples. XPS is a surface sensitive technique, where elemental compositions are accurately measured in the range of parts per thousand.

XPS of N-doped MWCNT BPs (Figure 5.9) confirmed the presence of N, O and C, with 1.3, 2 and 96.7 at.%, respectively. The C1s peak was at 284.6 eV, with a small side band at *ca.* 285.7 eV, of ratio 54:46, respectively (Figure 5.9a). The N1s peaks (Figure 5.9c) were deconvoluted to reveal three peaks at 401.02, 398.70 and 404.89 eV, of 61:22:16, respectively. Similar peaks were reported for N-doped MWCNTs produced with acetonitrile [294], or pyridine [295] precursors. The peaks at 398.7 and 401.02 eV corresponds to N bonded to sp^3 hybridised C, and substituted N in the graphitic lattice, respectively. The peak at 404.89 could correspond to N_2 trapped between the MWCNT layers [296, 297] or tentatively to oxidised N atoms [298, 299].

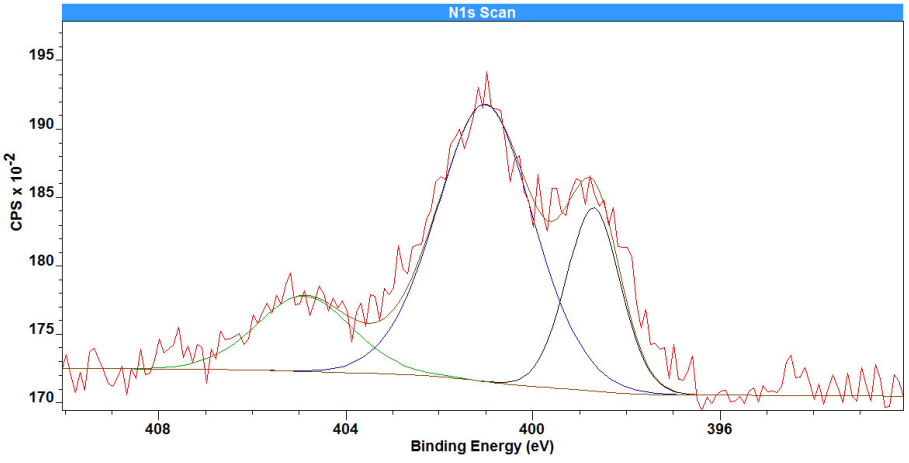
XPS detected C and O, of 99.1 and 0.9 at.%, respectively for the conventional MWCNT BPs, with peak positions of 284.6, with a side band at 285.44 eV for C1s (Figure 5.10a). XPS spectra for N-doped and conventional MWCNT BP have a singular O 1s peak, at 532.38 and 532.67 eV, respectively, with a slight shoulder at 530.86 eV for the conventional MWCNT BP. The increase in at.% O from 0.9 to 2 at.% for the N-doped MWCNT BP and conventional MWCNT BP, respectively could be related to the N-doped MWCNTs being more susceptible to oxidation [280]. However, the low at.% of O suggests that the O content is more likely from adsorbed water on the MWCNT surface, or in the XPS chamber [298]. XPS spectra in the literature report at.% of *ca.* 7.7 [298] and 0.1-3 [300–302] of residual O, for as-made N-doped and conventional MWCNT, respectively. The lack of additional bands in the C1s spectra, such as at 286.47 eV for -C-OH or C=O functional groups for both BP types again suggests that the MWCNTs do not contain any oxygen functional groups.



(a) C 1s

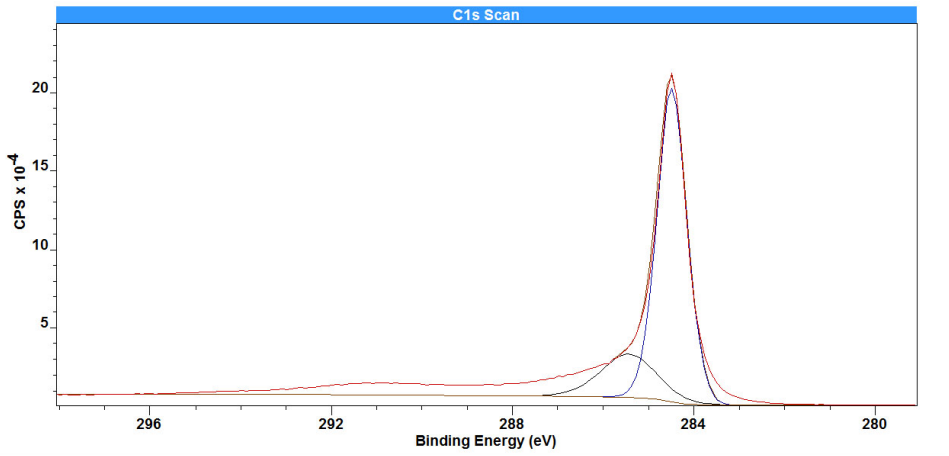


(b) O 1s

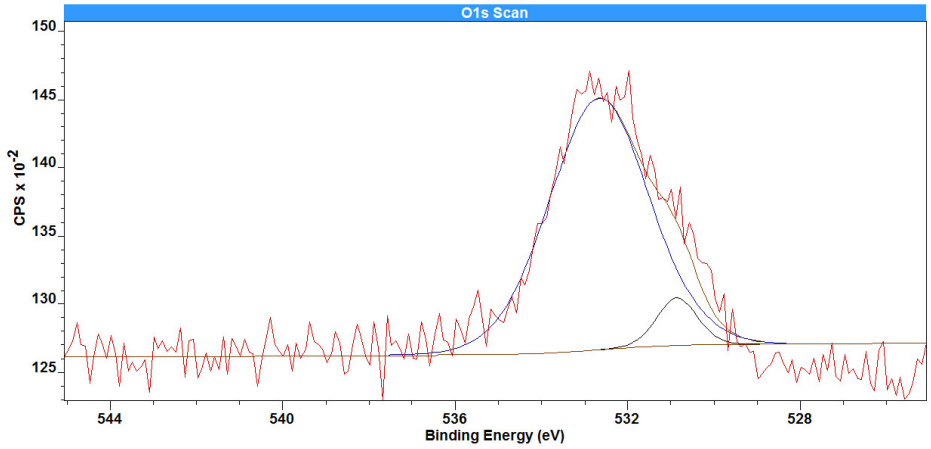


(c) N 1s

Figure 5.9: XPS spectra obtained from N-doped MWCNT BP for a) C 1s, b) O 1s, and c) N 1s.



(a) C 1s



(b) O 1s

Figure 5.10: XPS spectra obtained from conventional MWCNT BP for a) C 1s, and b) O 1s.

5.3.4 Mechanical Testing of BPs

Three samples per BP batch were tensile tested, and the force-elongation data was converted into stress and % strain graphs using the equations for stress and strain, Equation (5.4) and Equation (5.5), respectively. In Equation (5.4), F is the applied force and A is the cross-sectional area of the sample. For Equation (5.5), Δl is the change in sample length, and l_0 is the original sample length. Figure 5.11 shows representative stress-strain curves for each BP type, graphs with all curves per sample are in the appendix.

$$\sigma = \frac{F}{A} \tag{5.4}$$

$$\epsilon = \frac{\Delta l}{l_0} \tag{5.5}$$

All BPs displayed plastic deformation characteristics due to relative motion of MWCNTs within the BP. The N-doped BPs, composed of both long or short N-doped MWCNTs, failed more abruptly at the ultimate tensile stress than conventional MWCNT BPs, indicating they are more brittle. LNBP1 and SNBP2 required higher stresses to elongate them, hence the failure curves have steeper inclining gradients. SNBP1 and SNBP3 demonstrate low strain to failure of *ca.* 0.4 and 0.55 %. All batches of short N-doped BPs could withstand significantly lower % strains than conventional MWCNT BPs. This behaviour is likely caused by the short length of the N-doped MWCNTs, in combination with their straighter nature; limiting their able to entangle and reducing the pull-out length, compared to conventional MWCNTs.

The short N-doped BPs have a large number of bundles of undispersed MWCNTs on their surface, which exhibit a low shear modulus [303] and impede BP tensile strength by acting as weak points and crack nucleation sites. The high number of bundles adjacent to the fracture surface for SNBP1 and SNBP3 suggest that they have a negative impact on the mechanical properties of the BP (Figure 5.12a and b, e and f). Fewer bundles were observed at the tear edge for SNBP2 Figure 5.12c and d.

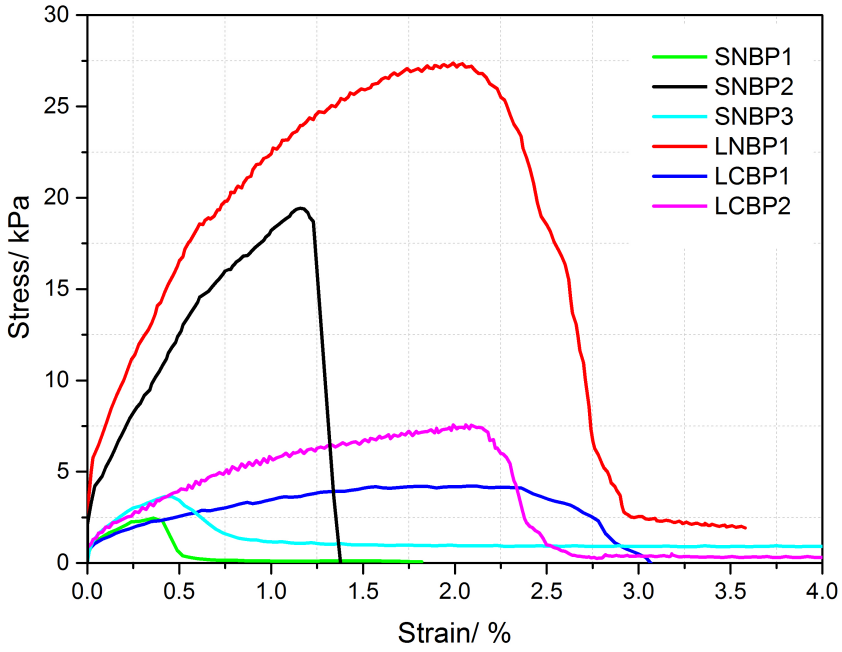
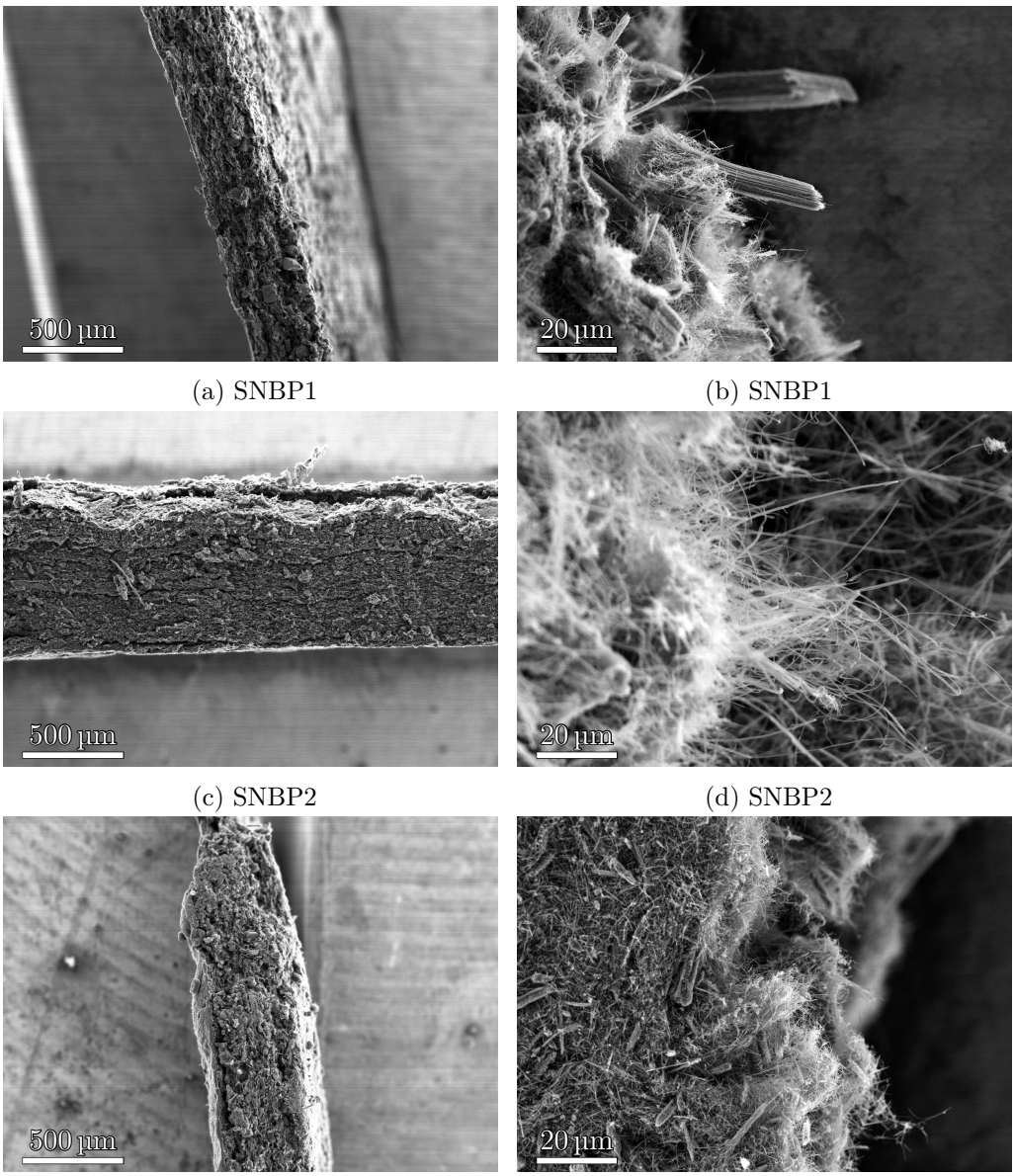


Figure 5.11: Representative stress strain curves obtained for different batches of BP samples, where L stands for long, S for short, N for N-doped MWCNT, C for conventional MWCNT. The N-doped MWCNT BPs have sharp failures, whilst the conventional MWCNT BPs are less brittle.



(a) SNBP1 (b) SNBP1

(c) SNBP2 (d) SNBP2

(e) SNBP3 (f) SNBP3

Figure 5.12: SEM images taken of the tear edge of the BPs post mechanical testing of a and b) short N-doped MWCNT BP, c and d) long N-doped MWCNT BP.

The conventional MWCNT BPs undergo more stable failures, likely related to longer MWCNT lengths and improved entanglement. The substantial increase in % strain before failure for LNBP1 also supports the theory of longer MWCNT length enabling BPs to withstand higher elongations. Similar results were reported by Sakurai *et al.* [304], where increasing the SWCNT length from 350 to 1500 µm increased the tensile strength from 27 to 52 MPa.

SEM images of the tear edge (Figure 5.12) shows the straightening and aligning of N-doped MWCNTs, compared to the entangled MWCNTs in the initial BP (Figure 5.5b). The straightening of the MWCNTs under applied stress during plastic deformation is irreversible, as evidenced by the straighter MWCNTs imaged following the tensile tests.

The length of the MWCNTs is likely to dictate the ultimate tensile strength of the BP, whilst the MWCNT type determines the BP stiffness. The increased stiffness observed in the N-doped BPs could be caused by a number of factors, including their surface chemistry, which affects the Van der Waals forces between the individual MWCNTs. The tensile strengths obtained in this chapter are likely to have been lowered by cutting the samples which introduce flaws at the edge of the BP that act as stress concentration points.

SEM videos of the tensile tests showed crack propagation during failure, with predictable tear-paths by following where the BP thinned prior to tearing (Figure 5.13). However the videos were too grainy for DIC analysis to reliably follow the directional changes in artefacts. Instead, DIC analysis was carried out on digital images. X-direction displacement maps, along with force/elongation curves are shown in Figure 5.14, Figure 5.15 and Figure 5.16. Unfortunately, as the BPs failed at the clamps for Figure 5.14 and Figure 5.15, the information that can be gained is limited. The BP strengths measured for cracks formed at the clamps are less accurate, due to localised stress at the clamps. For the long N-doped MWCNT BP (Figure 5.15), the jagged nature of the force/elongation curve is not representative of the rest of the tensile tests conducted on the sample, and could be caused by external vibrations during the measurement.

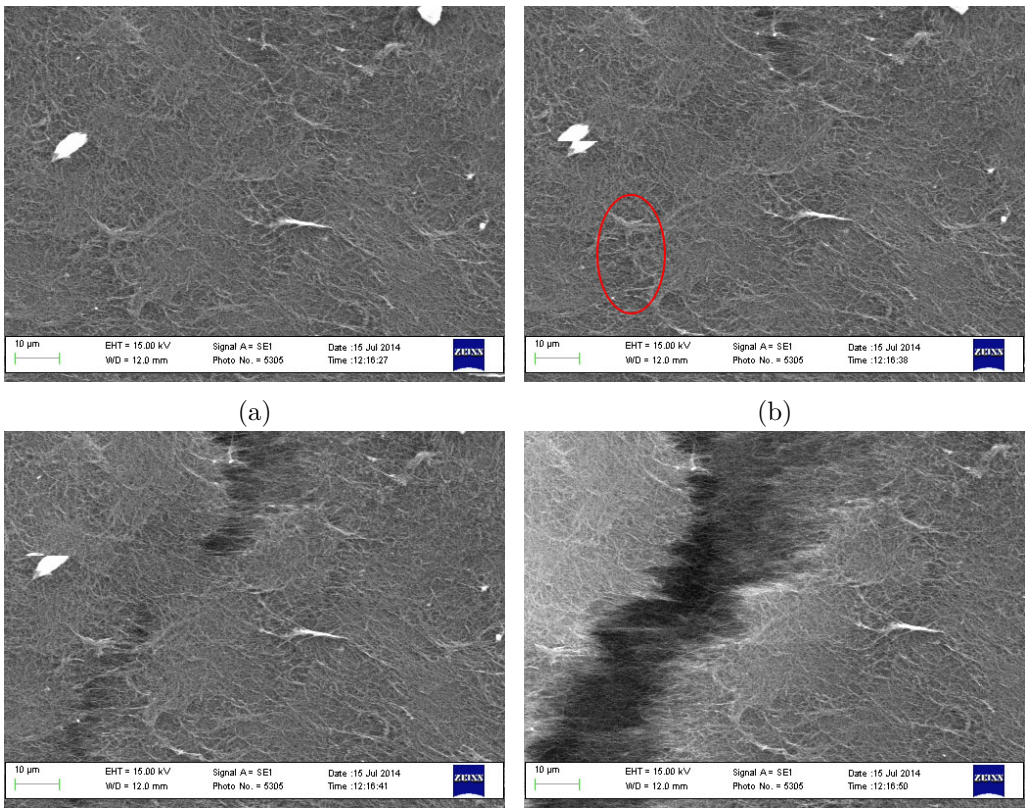
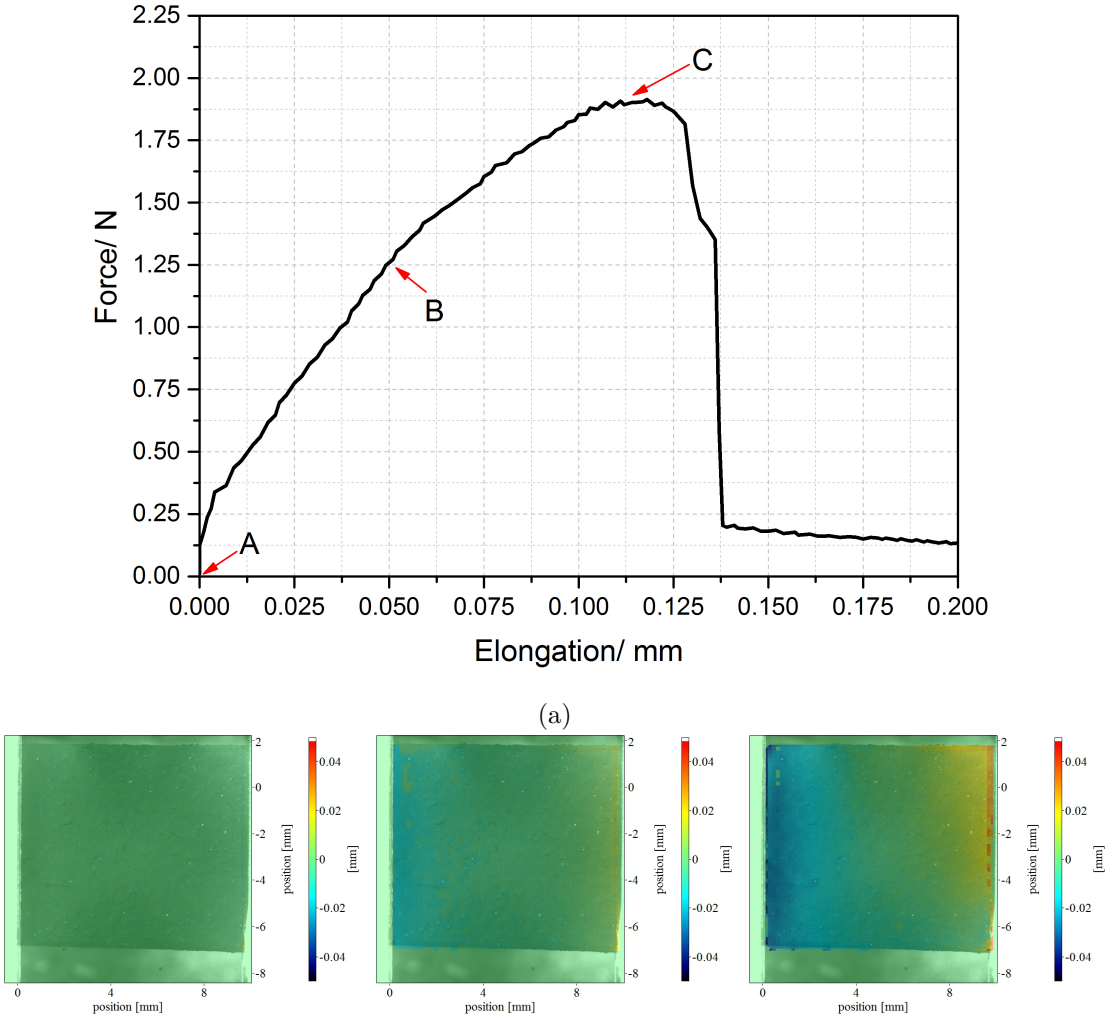


Figure 5.13: SEM images extracted from a video taken during mechanical testing carried out on a conventional MWCNT BP showing, a) The intact BP, b) the start of a tear forming and thinning of the BP (circled in red), c) further BP tearing, and d) the torn BP.

For the conventional MWCNT and long N-doped MWCNT BP (Figure 5.15 and Figure 5.16) there is a slight diagonal slant in the displacement observed for both conventional and short N-doped MWCNT BPs. This behaviour is unusual for uniaxial loading and is indicative of shear stress. The diagonal displacement is likely to be caused by slight twisting of the BP as it stretches, perhaps due to the clamps being unevenly tightened and hence allowing some slip of the BP within the holder or uneven tension across the BP before testing. 3D *in situ* mechanical tests in which x, y and z directions are filmed would be able to shed light on whether BP twisting is occurring. This diagonal slant is not observed for the short N-doped MWCNT BP (Figure 5.14), which may be due the clamp being tightened more evenly or improved sample loading.

Figure 5.17 shows the correlation coefficient images obtained by comparing image 'x' to the original image and shows that the strain is evenly distributed across the sample until the BP starts to fail. Crack formation is clearly visible in Figure 5.17e and f.

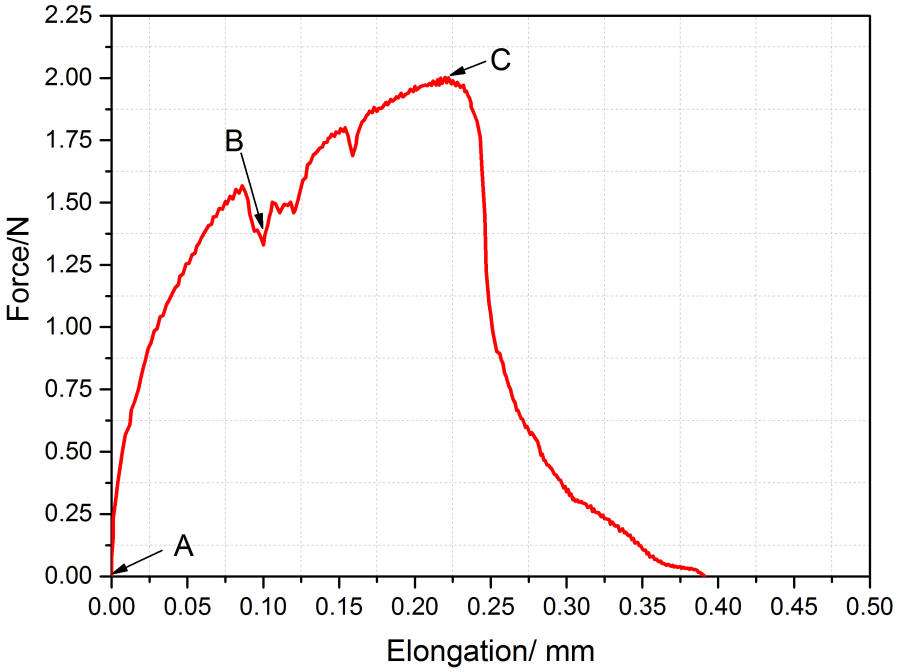
Whilst DIC is a powerful technique for analysing material behaviour [240], these displacement maps did not reveal any new information for the BPs tested. Tensile tests on dog-bone shaped samples would increase the likelihood of crack formation in the window, rather than at the clamps. DIC analysis on tensile tests on these dog-bone samples may provide more information on the local strains within the BP.



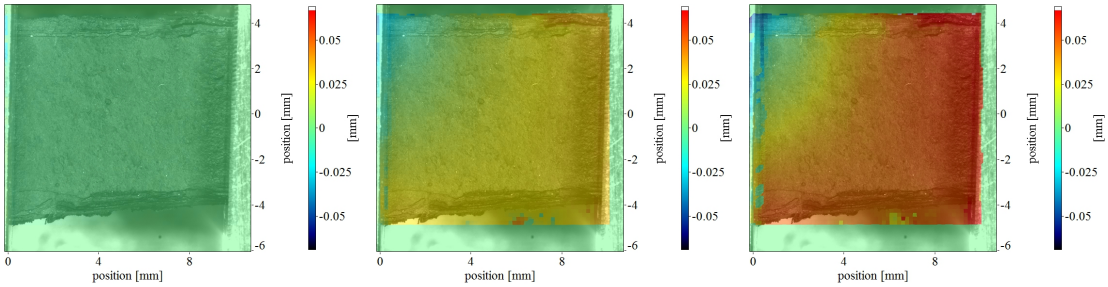
(a)

(b) Point A (c) Point B (d) Point C

Figure 5.14: a) Force/elongation curve for a short, N-doped MWCNT BP sample, showing the force required to reach BP failure. The corresponding displacement maps, obtained by DIC for b) point A, c) point B, and d) point C on the force/elongation curve.

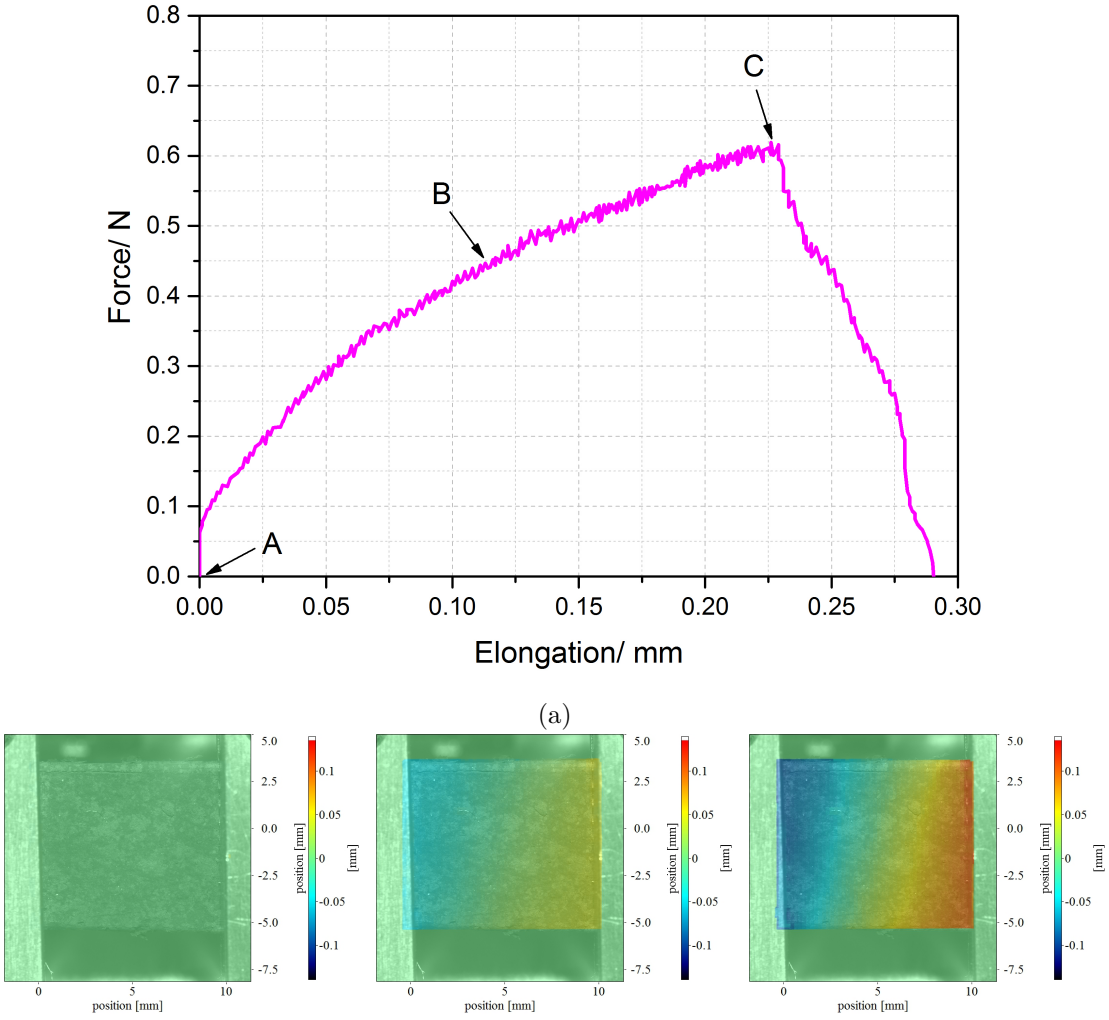


(a)



(b) Point A (c) Point B (d) Point C

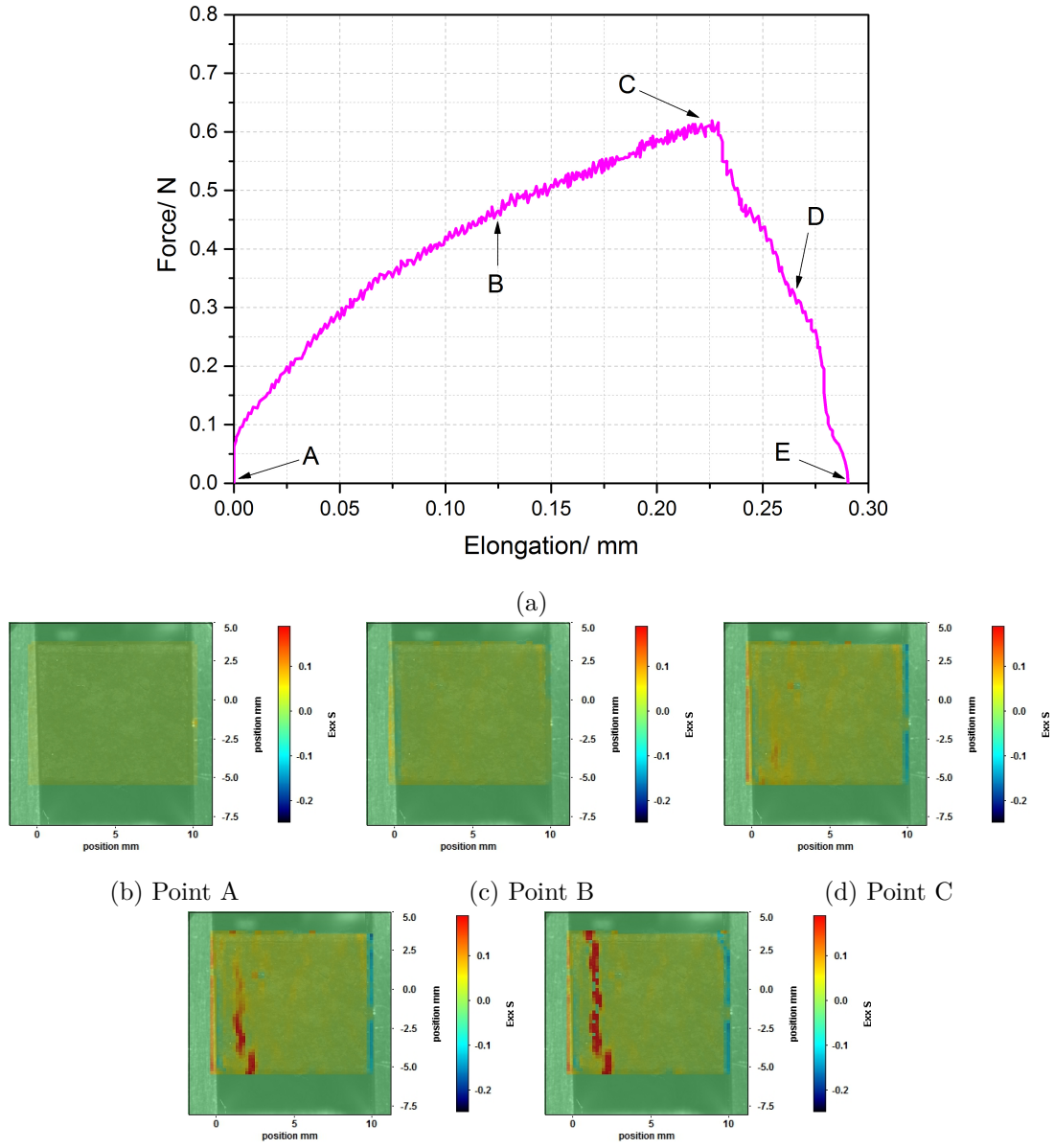
Figure 5.15: a) Force/elongation curve for a long, N-doped MWCNT BP sample, showing the force required to reach BP failure, and the corresponding displacement maps, obtained by DIC for b) point A, c) point B, and d) point C on the force/elongation curve.



(a)

(b) Point A (c) Point B (d) Point C

Figure 5.16: a) Force/elongation curve for a long, conventional MWCNT BP sample, showing the force required to reach BP failure, and the corresponding displacement maps, obtained by DIC for b) point A, c) point B, and d) point C on the force/elongation curve. The conventional MWCNT BP displays stable failure.



(a)

(b) Point A (c) Point B (d) Point C

(e) Point D (f) Point E

Figure 5.17: a) Force/elongation curve for a long, conventional MWCNT BP sample, showing the force required to reach BP failure and the corresponding correlation coefficient images, obtained by DIC for b) point A, c) point B, and d) point C, e) point D, and f) point E on the force/elongation curve.

5.4 Conclusions

In this chapter, BPs were produced from AACVD conventional and N-doped MWCNTs, of two lengths, per MWCNT type. The effect of MWCNT type and length on the mechanical properties of BPs was evaluated by conducting tensile tests *in situ* in an SEM to monitor the failure. This *in situ* approach allowed for crack propagation to be monitored and images to be collected for DIC analysis.

Freestanding BPs were produced from both long and short N-doped MWCNTs, however only long conventional MWCNT BPs could be produced, likely due to the short conventional MWCNTs (30-50 μm) being below the threshold minimum length required to produce BPs. However, other factors such as how defective the MWCNTs and the extent the length was reduced by extended periods of sonication could also have had an affect.

Contact angle measurements were conducted to indirectly gain information on the surface chemistry of the BPs. These measurements revealed the highly absorbent behaviour of the BPs, which could be further investigated to evaluate their suitability for spillage clean up applications. The conventional MWCNT BPs are more hydrophobic than the N-doped MWCNT BPs, with similar total SFEs for both BP types. XPS revealed that prolonged sonication of both types of MWCNTs did not lead to MWCNT oxidation, as confirmed by the lack of additional bands corresponding to hydroxyl or carboxyl functional groups in the C 1s peak.

Tensile tests performed on the BPs revealed that the conventional and N-doped MWCNT BPs displayed different failure behaviours; conventional MWCNT BPs underwent more stable failures whilst the N-doped MWCNT BPs had sharper failures, regardless of MWCNT length. Further, whilst BPs of the same sample displayed similar failure behaviour, different batches of the same BP type or length did not always failure in a similar manner. Three tensile tests were carried out per BP sample, with three BPs made from short N-doped MWCNTs, two BP samples consisting of long conventional MWCNTs and one BP sample formed from long N-doped MWCNTs. For each set of measurements per BP batch, the tensile behaviour of each tensile test produced a similar failure curve, however the ultimate tensile strength showed some variation, likely due to differences in CNT entanglement across the sample. The mechanical properties of the BPs are likely affected by a combination of MWCNT type, length, dispersion quality, hydrophobicity, surface

chemistry and the presence of MWCNT bundles. It is uncertain which of these factors are most important in dictating the mechanical properties of these BPs and this is a topic of further work. Fully understanding this issue is further hampered by our current ability to controllably produce nanomaterials with consistent properties. Until the synthesis of nanomaterals can be fully controlled, any processing carried out following synthesis will have batch discrepancies bought forward from the raw nanomaterial. However, the observed trends in mechanical properties suggest that MWCNT length determines the ultimate tensile stress whilst the type of MWCNT dictates BP stiffness.

SEM images of the fracture surface, after tensile testing revealed irreversible straightening of the MWCNTs during plastic deformation. A high number of bundles were found in N-doped MWCNT BPs, due to inhomogeneous dispersions produced by sonicating the MWCNTs in EtOH. These bundles may be one of the key reasons for the differences in mechanical properties between the N-doped and conventional MWCNT failure behaviour. Being able to produce bundle-free BPs would allow for a clearer indication of the effects of producing BPs from different MWCNTs types on BP failure to be evaluated.

Displacement and correlation coefficient maps produced by DIC analysis revealed limited information, as the majority of the samples failed along the clamp edges. However the correlation coefficient maps obtained for the conventional MWCNT BP sample that failed within the sample window showed that the strain was evenly distributed across the sample. Many of the displacement maps had a diagonal displacement, which was likely caused by twisting of the BP as it stretches. This behaviour could be caused by the clamps being tightened unevenly, care should be taken for future measurements to ensure that the clamps are tightened evenly.

Chapter 6

Summary and Future Research

6.1 Summary of Research

This work studied the growth of ferromagnetic metal-filled MWCNTs and took them to the next level by using them to create smart macroscopic structures. Mapping the two-stage furnace temperature profiles with various distances between the furnaces revealed the influence of T_{pyro} on T_{sub}. The furnace gap was optimised to allow for independent control of each furnace temperature, with a minimal temperature decrease in the gap. RGA, which monitored the key species detected at the exhaust of the reaction, built on the work in the literature by revealing the key fragments released during the thermocatalytic cracking of ferrocene. These RGA experiments revealed that with a T_{pyro} of 750 and 850 °C, the key fragments released were naphthalene, benzene, ethene and methane. The importance of ethene and methane for Fe@MWCNT growth was revealed; these fragments continued to break down even after the ferrocene had been fully exhausted. This suggests that ethene and methane could continue to promote Fe@MWCNT growth even after ferrocene had been fully exhausted. The systematic study, carried out in conjunction with *in situ* MS, investigated the effects of changing synthesis parameters (furnace gap, Ar flow, precursor mass, T_{sub} and T_{pyro}) on the evolution of H_2 and the materials produced. There appeared to be little correlation between evolution of H_2 and the products obtained from the syntheses, this lack of correlation was likely related to the large number of byproducts that formed, besides the Fe@MWCNTs. All samples contained a mixture of Fe@MWCNTs, C coated Fe NPs and large Fe containing clusters. The byproducts are likely to affect the data collected by Raman, TGA and SQUID. In order to gain a better idea of whether the

synthesis parameters affects, for example, the magnetic properties of the Fe@MWCNTs, the byproducts would have to be separated out from the Fe@MWCNTs. Regardless, the fact that the material produced isn't homogenous is an issue that needs to be resolved to make Fe@MWCNTs more viable as a commercial product. The maximum H_c observed in the SQUID measurements carried out here was 2293 Oe, which is falls in the range of 2100-2300 Oe for the H_c reported for nanowires grown in AAO by electrodeposition.

The feasibility of controlling Fe:Co ratio as a means to tune the magnetic properties of Fe/Co@MWCNTs was studied. Simply mixing ferrocene and cobaltocene in different ratios to use as the precursor for CVD produced MWCNTs filled with mixtures of Fe, Co and Fe/Co phases. However, due to the slow cobaltocene sublimation rate, the amount of cobaltocene entering the pyolysis furnace was not the desired amount. Despite this, the Fe/Co@MWCNTs produced with different ratios of ferrocene and cobaltocene all displayed an increased M_s compared to Fe@MWCNTs, and similar or higher M_s compared to Co@MWCNTs at 300 K. However, the increases in M_s observed are for samples that actually contained a mixture of Fe/Co@MWCNTs and NPs. Establishing the contribution of the NPs and Fe/Co@MWCNTs was not carried out, and should be investigated in the future. The slower cobaltocene sublimation rate is a key issue that needs to be addressed, alongside the issue of the large variation in Fe:Co ratio in different MWCNTs within the same batch. These observations suggest that controlling M_s simply by varying the cobaltocene:ferrocene ratio may not be the ideal method.

In situ TEM studies that involved passing current through an Fe@MWCNT decorated with Co-NPs highlighted the importance of understanding the effects of applying a bias on the structure of the metal filling before taking these materials forward in electrical applications. Whilst low currents had no obvious effects on the morphology of the Co-NP decorated Fe@MWCNT, higher currents caused the Co-NP to coalescence and eventually combine with the Fe-filling, causing the MWCNT to bulge to accommodate for the larger particle that collected at one end of the MWCNT. These results highlighted the importance of understanding the effects of current on CNTs before stating they are suitable for electronic applications, as reported in literature. Repeating these *in situ* studies on a more representative Fe/Co@MWCNT whilst monitoring the applied current is needed to gain valuable quantitative data on maximum current that can be applied before the filling starts to be affected by the current.

Taking these Fe@MWCNTs forward, macroscopic BPs were created by vacuum filtration of conventional MWCNT and Fe@MWCNT dispersions. This work built on *in situ* Fe@MWCNT BPs by creating BPs with selective regions that were susceptible to stimulation by external magnetic fields. To my knowledge, the work reported here is the first on creating a sandwich structured BP, with selective deposition of certain layers. The BPs created here are less flexible than previously reported BPs. The sandwich structure allowed for the creation of magnetic BPs with pre-designed magnetic regions, which behave in a specific manner when stimulated by an external magnetic field. These pre-designed BPs were created using two approaches; a mould or creating an Fe@MWCNT containing paste. Whilst both methods were capable of creating BPs with selectively ferromagnetic regions, both require refining to be able to deposit the Fe@MWCNTs more precisely. This work shows the potential for creating smart materials by depositing the Fe@MWCNTs in specific regions of the BP. Other approaches to do this, such as the GO-polymer papers [231] have the advantage of being highly flexible, further improving the flexibility of the BPs here will increase their mechanical lifetime before tearing.

A non-metallic electromechanical switch was prototyped with a strip of ferromagnetic BP, with the Fe@MWCNTs deposited across the entire BP, as the moving component. The switch was successful, with BP movement being easily controlled by a solenoid. I/V measurements showed that the ferromagnetic BPs displayed non-ohmic behaviour when measurements were conducted in air. However, the non-ohmic behaviour decreased when I/V measurements were taken under vacuum or N_2, likely due to the removal O_2 adsorbed on the surface of BPs in air, thus suppressing tunnelling effects. The I/V measurements were consistent and reproducible for multiple cycles, which is promising for their use in switch technology. Due to the limited accuracy of method used to cut the BPs into strips, their conductivity could not be accurately calculated. Rough estimates gave a conductivity of 98 S/m FeBP1, which is higher than 39.1 S/m for MWCNT BPs prepared by syringe filtering [305]. XRD taken before and after these I/V measurements showed there was some oxidation, with Fe_2O_3 peaks arising following these I/V measurements. This Fe oxidation is undesirable and understanding if the Fe_2O_3 is from oxidation of Fe in the C coated Fe clusters, or the Fe@MWCNTs is crucial to discern the suitability of ferromagnetic BPs for applications as non-metallic switches. To test whether it is the Fe inside the C coated Fe clusters or the Fe@MWCNTs that are oxidising, BPs consisting of only the agglomerate C coated Fe clusters or Fe@MWCNTs deposited on the MWCNT layers could be created.

Comparing the XRD taken before and after passing current through these samples would provide insight into which material was being oxidised.

Finally, tensile tests were conducted on BPs produced from conventional and N-doped MWCNTs to evaluate the effects of different types and lengths of MWCNTs on their mechanical behaviour. Whilst there have been reports on the tensile strength of BPs, these works have focused on BPs created from conventional MWCNTs and SWCNTs. Here, the mechanical strength of N-doped MWCNT BPs is compared to conventional MWCNTs, with the MWCNTs produced using the same CVD method. Tensile tests were performed *in situ* in SEM to observe crack propagation in real time, and digital images were used in DIC analysis to observe the changes in strain and displacement over the duration of the tests. The N-doped BPs displayed a more brittle failure than the conventional MWCNT BPs, whilst MWCNT length determined how much the BP can be elongated before tearing. These preliminary tests gave insight into how MWCNT type and length individually affect the mechanical properties of BPs, which is invaluable information for developing BPs with specific mechanical traits.

6.2 Future Work

The vision for furthering the work carried out in this thesis is towards the end goal of developing smart, multifunctional materials. There are still a number of challenges to be tackled before this can be achieved, including fully understanding CVD growth of Fe@MWCNTs, developing a controllable method to produce alloy metal-filled MWCNTs and improving the properties of the BPs produced.

The *in situ* MS RGA studies reported in this thesis shed light on the fragments formed from thermocatalytic cracking of ferrocene. These RGA results are a good starting point for understanding how altering the synthesis parameters, in this case T_{pyro}, affects the lifetime of the fragments and hence their detection at the exhaust. Carrying out similar RGA for the remaining parameters in the systematic study, and extending the range measured for each would provide a better insight into how thermocatalytic cracking of ferrocene is affected by each parameter. Further, the gases evolved at the reaction site can be monitored by using MS fitted with a probe that extends into the furnace [166]. Measuring the gases evolved at the reaction site could detect other gaseous species which are short-

lived and hence are not detected at the exhaust, and thus provide new insight into the chemical environment during the reaction. Combining MS with other *in situ* techniques, such as Raman, would allow for both the gaseous and solid phases to be simultaneously monitored, providing a wealth of information about events during MWCNT growth. From a combination of these techniques, the growth mechanism of Fe@MWCNTs may be further understood.

Repeating experiments with the same synthesis parameters often resulted in different materials forming, which highlights the inconsistent nature of current setups used to grow MWCNTs. Batch to batch variation is a key issue that has to be resolved before MWCNTs can be viable materials for industrial applications. Online monitoring of the species evolved during multiple CVD reactions and detailed comparisons of the abundance and nature of these species may provide insight into why a variety of materials are obtained in different repeats of the same synthesis. By gaining a full understanding of how to control the synthesis for Fe@MWCNTs, the properties of these materials can be better controlled and tuned to consistently produce high yield and quality materials.

For growth of Fe/Co@MWCNTs with controlled Fe:Co ratios, the major hurdle is the slower rate of cobaltocene sublimation compared to ferrocene; the current setup should be adapted to account for these differing sublimation rates. A new setup, in which the ferrocene is placed in a reservoir, connected to a separate gas line could be used. The reservoir is wrapped in conductive tape and maintained at a temperature of 250 °C. The cobaltocene is placed inside a a crucible, placed just outside the sublimation furnace, in a similar fashion to the currently used setup. By first establishing the sublimation rate of ferrocene at 250 °C, T_{sub} can be adjusted so that the cobaltocene sublimation rate is the same as ferrocene. Due to the extra distance between the reservoir and the pyrolysis furnace, there would be a time delay before the cobaltocene is pushed into the sublimation furnace.

To find the correct temperature to have the same sublimation rate for both ferrocene and cobaltocene, experiments would have to conducted separately for both precursors, at a range of temperatures, with the remaining mass of precursor recorded. Assuming a linear trend between sublimation rate and temperature, the corresponding temperature at which cobaltocene has the same sublimation rate as ferrocene at 250 °C can be established. Carrying out experiments with this setup at a wider range of Co and Fe ratios would clarify

whether changing the Co:Fe ratio is a viable method for tuning the magnetic properties of the Fe/Co@MWCNTs. A large selection of Fe/Co@MWCNTs per synthesis should be screened to obtain a distribution of Fe:Co ratios within the batch.

In this work, BPs were produced from different MWCNT types (ferromagnetic, N-doped and conventional MWCNTs), all of which had the common issue of bundles being present within the BP, which hamper their mechanical properties. Improving the dispersions that are filtered to make these BPs would reduce the number of bundles. As MWCNTs are highly hydrophobic, research into finding aprotic, non-polar solvents or mixtures of solvents using Hansen solubility parameters, could make the solvent-MWCNT interactions more favourable. Surfactants were not used in this chapter to avoid contaminating the BP, however these could be investigated. A more aggressive approach could be used to break up the MWCNTs such as grinding them, or using a high power sonic horn to disperse the MWCNTs, rather than a sonic bath. However, these approaches will severely shorten and damage the MWCNTs, compared to current methods, which again impacts the mechanical properties of the BP.

To further develop the BPs with pre-designed magnetic regions, the mould could be created from alternative materials, such as thin plastic sheets cut into the desired design by CAD/CAM. Changing the approach used to deposit the Fe@MWCNTs layer may remove the need for improving the contact between the mould and the MWCNT BP. Alternatively, the Fe@MWCNT solution could be spin coated on top of the conventional MWCNT BP layer with a mask applied to select the regions that the Fe@MWCNTs would be deposited on. For the ferromagnetic paste, sonicating the P123, water and Fe@MWCNTs simultaneously may lead to a more homogeneous mixture, as the gel would form with the Fe@MWCNTs already in the mixture. Further refining the ratio of P123:H_2O to create a less sticky paste that can be deposited in thinner layers or using an alternative medium to P123 would enhance the ability to apply the ferromagnetic paste to the BP. It is important to establish the feasibility and effects of removing the surfactant by heating the BP on the structure of the BP as it is likely that the surfactant would impede the conductivity of the BP.

BPs with improved mechanical and electrical properties have been reported by crosslinking the MWCNTs within the BP [153, 305]. These crosslinked BPs were created by a UV activated 1-4 addition polymerisation (Figure 6.1) [153], or 1-4-benzoquinone [305].

An alternative approach to functionalising the MWCNTs post synthesis is to produce doped MWCNTs, in which the heteroatoms are incorporated into the MWCNT structure, rather than attached to their surface. This can be achieved by first modifying the ferrocene precursor by attaching azides or amines onto the cyclopentadiene rings. Using this modified precursor in CVD with the same setup used for growth of Fe@MWCNTs may lead to the production of N-doped Fe@MWCNTs. These N-doped Fe@MWCNTs could be further functionalised and cross-linked to form stronger BPs. Similar cross-linking reactions may be possible with the N-doped MWCNTs, which should also improve the tensile strength of N-doped MWCNT BPs.

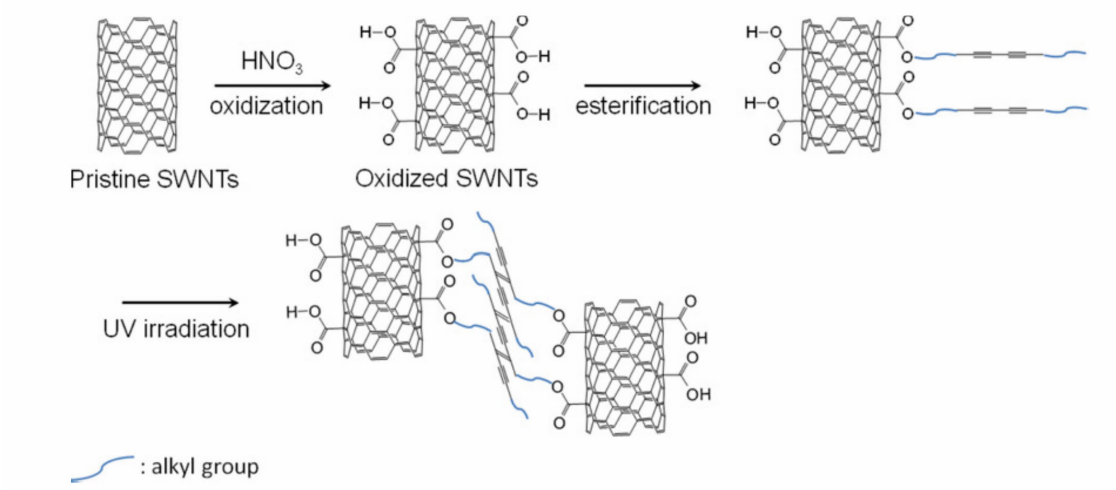


Figure 6.1: Schematic taken from [153] showing the steps involved leading up to the UV irradiation activated MWCNT conjugational cross-linking reaction.

Extending BP production to include other doped MWCNTs, such as B-doped, Si-doped and P-doped MWCNTs, and other nanomaterials, such as graphene oxide, graphene and boron nitride nanotubes (BNNTs) will create a portfolio of macroscopic papers made from different nanomaterials. Comparing the tensile tests of these additional BPs with the properties of the nanomaterial they are made from will allow for more information to be gathered about which variables have the most significant effect on mechanical properties of BPs. Furthermore, layering different types of nanomaterials would create multifunctional, smart materials. For example, depositing layers of BNNTs around a BP consisting of MWCNTs and selectively deposited Fe@MWCNT regions would create a heterostructure that is electrical insulating, yet thermally conductive, on the outside, with a core that is electrically conductive that responds to external magnetic stimuli in specific locations. These materials would be useful for applications in which electrical conductivity is only required along the BP, but not through it.

The work conducted thus far has already shown that conventional and N-doped MWCNT BPs fail at different loads. If the BPs constructed from various nanomaterials also possess different mechanical properties, layering various types of MWCNTs together could be used for stress sensor applications, with changes in conductivity being the detection mode. Performing conductivity measurements in conjunction with tensile tests to monitor how electrical conductivity of BPs are affected under strain is the next step to testing the suitability of BPs towards these stress sensor applications. Ideally, the detectable changes in conductivity will be strongly correlated to small increases in strain.

Preliminary work on understanding the biocompatibility and cytotoxicity of BPs was carried out in collaboration with BNERC. Cell proliferation tests were carried out using Alamar Blue Assays to compare the growth of two cell lines, L929 (normal) and TE2 (cancerous), on BP. Figure 6.2 shows SEM images of the cells (circled in red) on the surface of the BPs, it appears that the cells have a preference for the rougher BP surfaces. The % cell activity, compared to a control of cells grown in cell medium, showed that the cancer cells multiplied at a decreasing rate on the BPs, whilst the normal cells multiplied at a steadier rate. The % cell activity for cell lines were much lower than the cells multiplying in the cell medium, however the fact that the cells did not simply die is a promising result.

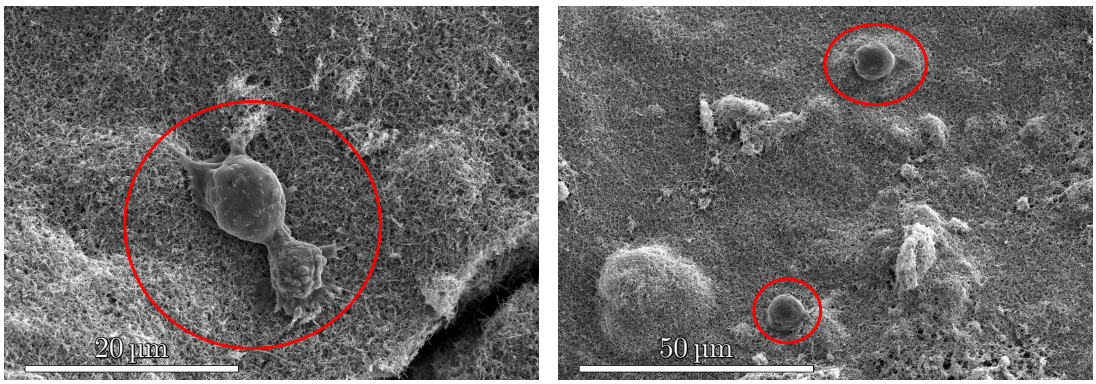


Figure 6.2: SEM images showing cells grown on the surface of ferromagnetic BPs, with the cells circled in red. The cells appear to have a preference for the slightly rougher surfaces of BPs, compared to smoother regions.

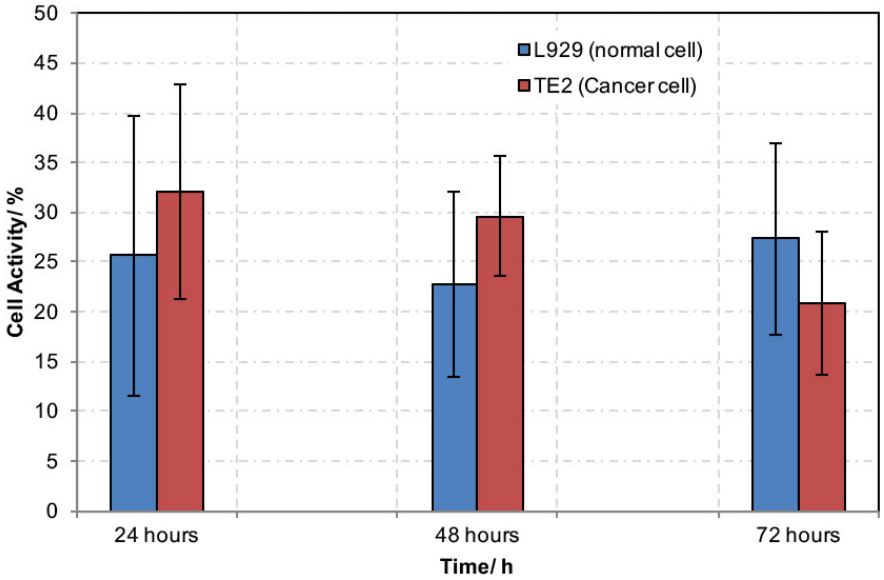


Figure 6.3: Graph showing the cell activity from Alamar Blue Assays over the course of 72 hours. The graph shows the cancer cells divide at a slower rate with increasing time, whilst the normal cells had a more steady cell division rate over the three days.

Further work currently being undertaken at BNERC aims to improve the rate of enzymatic reactions by immobilising enzymes on the surface of ferromagnetic BPs. This research builds on their previous research in which enzymes were immobilised onto magnetic particles [306, 307], these enzyme/particle hybrids formed clusters under the influence of a rotating magnetic field. The enzyme activity reached a maximum at 5-7 Hz due to the increase in enzyme-substrate collision rate [306]. At higher frequencies, the clusters were broken down into smaller clusters, which decreased their enzymatic activity. By immobilising the enzymes on to ferromagnetic BPs, the activity of enzymes should be increased, even at higher frequencies, providing the BP is able to withstand the higher rotational magnetic frequency. Theoretically, the enzymatic activity could be further increased by applying a high frequency AC magnetic field (kHz) to locally heat the BP to optimal enzyme operating temperatures via hysteresis loss heating and/or Néel effect. This exciting research could be of interest to industries that use immobilised enzymes.

Creating smart, multifunctional materials from a diverse range of nanomaterials is a promising field of research. Combining different nanomaterials to create macrostrucutures enables these materials to have tailored characteristics specific to the requirements of the target application.

Bibliography

[1] D. Golberg et al. “Copper-Filled Carbon Nanotubes: Rheostatlike Behavior and Femtogram Copper Mass Transport”. In: *Advanced Materials* 19 (2007), pp. 1937–1942.

[2] Y. Zhong et al. “Core-shell heterostructures of SnM (M=(Fe, Ni, and Cr) or Cu) alloy nanowires inside CNTs on metallic substrates”. In: *Applied Surface Science* 270 (2013), pp. 722–727.

[3] D. L. Zhao et al. “Electromagnetic and microwave absorbing properties of Co-filled CNTs”. In: *Journal of Alloys and Compounds* 505 (2010), pp. 712–716.

[4] I. Monch et al. “Synthesis and characteristics of Fe-filled multi-walled carbon nanotubes for biomedical application”. In: *Journal of Physics: Conference Series* 61 (2007), pp. 820–824.

[5] B. M. Kim, S. Qian, and H. H. Bau. “Filling carbon nanotubes with particles”. In: *Nano Letters* 5 (2005), pp. 873–878.

[6] A. N. Khlobystov et al. “Molecules in carbon nanotubes”. In: *Accounts of Chemical Research* 38 (2005), pp. 901–909.

[7] R. Sen, A. Govindaraj, and C. N. R. Rao. “Carbon nanotubes by the metallocene route”. In: *Chemical Physics Letters* 267 (1997), pp. 276–280.

[8] A. Leonhardt et al. “Synthesis, Properties, and Applications of Ferromagnetic-Filled Carbon Nanotubes”. In: *Chemical Vapor Deposition* 12 (2006), pp. 380–387.

[9] H. Reuther et al. “Investigation of the formation of Fe-filled carbon nanotubes”. In: *Journal of Physics: Conference Series* 217 (2010), pp. 012098–012112.

[10] Y. Krupskaya et al. “Magnetic study of iron-containing carbon nanotubes: Feasibility for magnetic hyperthermia”. In: *Journal of Magnetism and Magnetic Materials* 321 (2009), pp. 4067–4071.

[11] J. Hilding et al. “Dispersion of carbon nanotubes in liquids”. In: *Journal of Dispersions Science and Technology* 24 (2002), pp. 1–41.

[12] R. Kozhuharova et al. “$Fe_xCo_{(1-x)}$-alloy filled vertically aligned carbon nanotubes grown by thermal chemical vapor deposition”. In: *Journal of Magnetism and Magnetic Materials* 290 (2005), pp. 250–253.

[13] N. Grobert et al. “Alloy nanowires: Invar inside carbon nanotubes”. In: *Chemical Communications* 5 (2001), pp. 471–472.

[14] H. Morimoto et al. “Tumbling motion of magnetic particles on a magnetic substrate induced by rotational magnetic field”. In: *Physical Review E* (2008), pp. 021403–021410.

[15] H. W. Kroto et al. “C60: Buckminsterfullerene”. In: *Nature* 318 (1985), pp. 162–163.

[16] S. Iijima. “Helical microtubules of graphitic carbon”. In: *Nature* 354 (1991), pp. 56–58.

[17] Y. Ando and X. Zhao. “Synthesis of carbon nanotubes by arc-discharge method”. In: *New Diamond and Frontier Carbon Technology* 16 (2006), pp. 123–137.

[18] N. Arora and N. N. Sharma. “Arc discharge synthesis of carbon nanotubes: comprehensive review”. In: *Diamond and Related Materials* 50 (2014), pp. 135–150.

[19] V. Jourdain and C. Bichara. “Current understanding of the growth of carbon nanotubes in catalytic chemical vapour deposition”. In: *Carbon* 58 (2013), pp. 2–39.

[20] M. Jung et al. “Growth of carbon nanotubes by chemical vapour deposition”. In: *Diamond and Related Materials* 10 (2001), pp. 1235–1240.

[21] A. P. Bolshakov et al. “A novel CW laser-powder method of carbon single-wall nanotubes production”. In: *Diamond and Related Materials* 11 (2002), pp. 927–930.

[22] I. Kunadian et al. “Growth kinetic so MWCNTs synthesised by a continuous-feed CVD method”. In: *Carbon* 47 (2009), pp. 385–395.

[23] J. Kong, A. M. Cassel, and H. Dai. “Chemical vapor deposition of methane for single-walled carbon nanotubes”. In: *Chemical Physics Letters* 292 (1998), pp. 567–574.

[24] H. Ago et al. “CVD growth of single-walled carbon nanotubes with narrow diameter distribution over Fe/MgO catalyst and their fluorescence spectroscopy”. In: *Journal of Physical Chemistry B* 109 (2005), pp. 10035–10041.

[25] S. S. Meysami et al. “Aerosol-assisted chemical vapour deposition synthesis of multi-wall carbon nanotubes: III. Towards upscaling”. In: *Carbon* 8 (2015), pp. 148–156.

[26] G Che et al. “Chemical vapor deposition based synthesis of carbon nanotubes and nanofibers using a template method”. In: *Chemistry of Materials* 10 (1998), pp. 260–267.

[27] G. Eres et al. “Model for self-assembly of carbon nanotubes from acetylene based on real-time studies of vertically aligned growth kinetics”. In: *Journal of Physical Chemistry C* 113 (2009), pp. 15484–15491.

[28] M. Perez-Cabero, I. Rodriguez-Ramos, and A. Guerrero-Ruiz. “Characterization of carbon nanotubes and carbon nanofibers prepared by catalytic decomposition of acetylene in a fluidized bed reactor”. In: *Journal of Catalysis* 215 (2003), pp. 305–316.

[29] K. E. Kim et al. “Investigation on the temperature-dependent growth rate of carbon nanotubes using chemical vapour deposition of ferrocene and acetylene”. In: *Chemical Physics Letters* 401 (2005), pp. 459–464.

[30] S. S. Meysami et al. “Aerosol-assisted chemical vapour deposition synthesis of multi-wall carbon nanotubes: I. Mapping the reactor”. In: *Carbon* 58 (2013), pp. 151–158.

[31] Y. Li et al. “Growth of single-walled carbon nanotubes from discrete catalytic nanoparticles of various sizes”. In: *Journal of Physical Chemistry B* 105 (2001), pp. 11424–11431.

[32] M. Meyyappan. “A review of plasma enhanced chemical vapour deposition of carbon nanotubes”. In: *Journal of Physics D: Applied Physics* 42 (2009), pp. 213001–213016.

[33] W. Z. Li et al. “Large-scale synthesis of aligned carbon nanotubes”. In: *Science* 274 (1996), pp. 1701–1703.

[34] S. S. Meysami et al. “Aerosol-assisted chemical vapour deposition synthesis of multi-wall carbon nanotubes: II. An analytical study”. In: *Carbon* 58 (2013), pp. 159–169.

[35] M. Mayne et al. “Pyrolytic production of aligned carbon nanotubes from homogeneously dispersed benzene-base aerosols”. In: *Chemical Physics Letters* 338 (2001), pp. 101–107.

[36] C. Castro et al. “Dynamics of catalyst particle formation and multi-wall carbon nanotube growth in aerosol-assisted catalytic chemical vapour deposition”. In: *Carbon* 48 (2010), pp. 3807–3816.

[37] G. Otieno et al. “Processing and properties of aligned multi-walled carbon nanotube/aluminoborosilicate glass composites made by sol–gel processing”. In: *Carbon* 48.8 (2010), pp. 2212–2217.

[38] C. Singh et al. “Towards the production of large-scale aligned carbon nanotubes”. In: *Chemical Physics Letters* 372 (2003), pp. 860–865.

[39] C. Oncel and Y. Yurum. “Carbon nanotube synthesis via the catalytic CVD method: A review on the effect of reaction parameters”. In: *Fullerenes, Nanotubes and Carbon Nanostructures* 14 (2006), pp. 17–37.

[40] F. C. Dillon et al. “Tuning the magnetic properties of iron-filled carbon nanotubes”. In: *Carbon* 50.10 (2012), pp. 3674–3681.

[41] N. Grobert et al. “Enhanced magnetic coercivities in Fe nanowires”. In: *Applied Physics Letters* 75 (1999), pp. 3363–3365.

[42] C. N. R. Rao et al. “Large aligned-NT bundles from ferrocene pyrolysis”. In: *Chemical Communications* (1998), pp. 1525–1526.

[43] E. C. Vermisoglou et al. “Aligned carbon nanotubes with ferromagnetic behavior”. In: *Advanced Materials* 22 (2010), pp. 473–7.

[44] C. P. Deck and K. Vecchio. “Prediction of carbon nanotube growth success by the analysis of carbon-catalyst binary phase diagrams”. In: *Carbon* 44 (2006), pp. 267–275.

[45] S. Esconjauregui, C. M. Whelan, and K. Maex. “The reasons why metals catalyze the nucleation and growth of carbon nanotubes and other carbon nanomorphologies”. In: *Carbon* 47 (2009), pp. 659–669.

[46] J. Robertson. “Heterogeneous catalysis model of growth mechanisms of carbon nanotubes graphene and silicon nanowires”. In: *Journal of Materials Chemistry* 22 (2012), p. 19858.

[47] Yoshida H. et al. “Atomic-scale in-situ observation of carbon nanotube growth from solid state iron carbide nanoparticles”. In: *Nano Letters* 8 (2008), pp. 2082–2086.

[48] C. T. Wirth, S. Hofmann, and J. Robertson. “State of the catalyst during carbon nanotube growth”. In: *Diamond and Related Materials* 18 (2009), pp. 940–945.

[49] C. Muller et al. “Growth aspects of Fe-filled CNTs obtained by catalytic CVD of ferrocene”. In: *Journal of Physical Chemistry C* 113 (2009), pp. 2736–2740.

[50] S. Hofmann et al. “Surface diffusion: The low activation energy path for nanotube growth”. In: *Physical Review Letters* 95 (2005), pp. 036101–036104.

[51] S. Helveg et al. “Atomic-scale imaging of carbon nanofibre growth”. In: *Nature* 427 (2004), pp. 426–429.

[52] H. Yoshida et al. “Atomic-scale in-situ observation of carbon nanotube growth from solid state iron carbide nanoparticles”. In: *Nanoletters* 8 (2008), pp. 2082–2086.

[53] M. Lin et al. “Dynamic observation of bamboo-like carbon nanotube growth”. In: *Nano Letters* 7 (2007), pp. 2234–2238.

[54] S. Hofmann et al. “In situ observations of catalyst dynamics during surface-bound carbon nanotube nucleation”. In: *Nano Letters* 7 (2007), pp. 602–608.

[55] R. S. Wagner and W. C. Ellis. “Vapor-Liquid-Solid Mechanism of Single Crystal Growth”. In: *Applied Physics Letters* 4 (1964), p. 89.

[56] R. T. K. Baker. “Catalytic growth of carbon filaments”. In: *Carbon* 27 (1989), pp. 315–323.

[57] R. T. K. Baker et al. “Nucleation and growth of carbon deposits from nickel catalysed decomposition of acetylene”. In: *Journal of Catalysis* 26 (1972), pp. 51–62.

[58] U. Weissker et al. “Carbon Nanotubes Filled with Ferromagnetic Materials”. In: *Materials* 3 (2010), pp. 4387–4427.

[59] J. Rostrum-Nielsen and D. L. Trimm. “Mechanisms of carbon formation on nickel-containing catalyst”. In: *Journal of Catalysis* 48 (1977), pp. 155–165.

[60] G. G. Tibbetts. “Why are carbon filaments tubular”. In: *Journal of Crystal Growth* 66 (1984), pp. 632–638.

[61] J. P. Tessonnier and D. S. Su. “Recent progress on the growth mechanism of carbon nanotubes: A review”. In: *Chemistry and Sustainability* 4 (2011), pp. 824–847.

[62] X. Zhang et al. “Rapid growth of well-aligned carbon nanotube arrays”. In: *Chemical Physics Letters* 362 (2002), pp. 285–290.

[63] Y. K. Kwon et al. “Morphology and stability of growing multi wall carbon nanotubes”. In: *Physical Review Letters* 79 (1997), pp. 2065–2068.

[64] I. Kunadian et al. “Growth kinetics of MWCNTs synthesized by a continuous-feed CVD method”. In: *Carbon* 47 (2009), pp. 384–395.

[65] C. A. Ross et al. “Fabrication of patterned media for high density magnetic storage”. In: *Journal of Vacuum Science and Technology B: Microelectronics and Nanometer Structures Processing, Measurement, and Phenomena* 17 (1999), pp. 3168–3176.

[66] M. Heln et al. “Nanoscale magnetic domains in mesoscopic magnets”. In: *Science* 272 (1996), pp. 1782–1785.

[67] D. J. Sellmyer, M. Zheng, and R. Skomski. “Magnetism of Fe, Co and Ni nanowires in self-assembled arrays”. In: *Journal of Physics: Condensed Matter* 13 (2001), pp. 433–460.

[68] G. E. Possin. “A method for forming very small diameter wires”. In: *Review of Scientific Instruments* 41 (1970), pp. 772–774.

[69] D. AlMawlawi, N. Coombs, and M. Moskovits. “Magnetic properties of Fe deposited into anodic aluminium oxide pores as a function of particle size”. In: *Journal of Applied Physics* 70 (1991), pp. 4421–4425.

[70] Y. Peng et al. “Magnetic properties and magnetisation reversal of alpha-Fe nanowires deposited in alumina film”. In: *Journal of Applied Physics* 87 (2000), pp. 7405–7408.

[71] X. Y. Zhang et al. “Fabrication and magnetic properties of ultrathin Fe nanowire arrays”. In: *Applied Physics Letters* 83 (2003), pp. 3341–3343.

[72] R. Ferre and K. Ounadjela. “Magnetization processes in nickel and cobalt electrodeposited nanowires”. In: *Physical Review B* 56 (1997), pp. 14066–14075.

[73] S. Kawai and R. Ueda. “Magnetic properties of anodic oxide coatings on aluminium containing electrodeposited Co and Co-Ni”. In: *Journal of the Electrochemical Society* 122 (1975), pp. 32–36.

[74] J. Meier, B. Doudin, and J. Ph. Ansermet. “Magnetic properties of nanosized wires”. In: *Journal of Applied Physics* 79 (1996), pp. 6010–6012.

[75] R. Kitaura et al. “Fabrication of metal nanowires in carbon nanotubes via versatile nano-template reaction”. In: *Nanoletters* 8 (2008), pp. 693–699.

[76] P. M. Ajayan and Sumio Iijima. “Capillarity-induced filling of carbon nanotubes”. In: *Nature* 361 (1993), pp. 333–334.

[77] E. Borowiak-Palen et al. “Iron filled single-walled carbon nanotubes – synthesis and characteristic properties”. In: *Physica Status Solidi (b)* 243 (2006), pp. 3277–3280.

[78] C. Xu et al. “1D lanthanide halide crystals inserted into single-walled carbon nanotubes”. In: *Chemical Communications* (2000), pp. 2427–2428.

[79] A. Chu et al. “Filling of carbon nanotubes with silver, gold and gold chloride”. In: *Chemistry of Materials* 8 (1996), pp. 2751–2754.

[80] B. M. Kim, S. Qian, and H. H. Bau. “Filling carbon nanotubes with particles”. In: *Nanoletters* 5 (2005), pp. 873–878.

[81] J. Jin et al. “Magnetic Fe nanoparticle functionalized water-soluble multi-walled carbon nanotubules towards the preparation of sorbent for aromatic compounds removal”. In: *Chem Commun (Camb)* 4 (2007), pp. 386–8.

[82] E. Dujardin et al. “Capillarity and wetting of carbon nanotubes”. In: *Science* 265 (1994), pp. 1850–1852.

[83] S. C. Tsang et al. “A simple chemical method of opening and filling carbon nanotubes”. In: *Nature* 372 (1994), pp. 159–162.

[84] C. Guerret-Plecorurt et al. “Relation between metal electronic structure and morphology of metal compounds inside carbon nanotubes”. In: *Nature* 372 (1994), pp. 761–765.

[85] H. Loiseau A. Pascard. “Synthesis of long carbon nanotubes filled with Se, S, Sb and Ge by arc method”. In: *Chemical Physics Letters* 256 (1996), pp. 246–252.

[86] H. Nagata A.and Sato et al. “Magnetic properties of carbon nanotubes filled with ferromagnetic metals”. In: *Vacuum* 87 (2013), pp. 182–186.

[87] S. Hampel et al. “Growth and characterization of filled carbon nanotubes with ferromagnetic properties”. In: *Carbon* 44 (2006), pp. 2316–2322.

[88] R. Kozhuharova et al. “Well-aligned Co-filled carbon nanotubes: preparation and magnetic properties”. In: *Applied Surface Science* 238 (2004), pp. 355–359.

[89] A. Leonhardt et al. “Synthesis and properties of filled carbon nanotubes”. In: *Diamond and Related Materials* 12 (2003), pp. 790–793.

[90] A. L. Elias et al. “Production and characterization of single-crystal FeCo nanowires inside carbon nanotubes”. In: *Nano Letters* 5 (2005), pp. 467–472.

[91] R. Lv et al. “Effect of using chlorine-containing precursors in the synthesis of FeNi-filled carbon nanotubes”. In: *Carbon* 45 (2007), pp. 1433–1438.

[92] N. S. Kim et al. “Vertically aligned CNTs grown by pyrolysis of Fe Ni Co phthalocyanines”. In: *Journal of Physical Chemistry B* 107 (2003), pp. 9249–9255.

[93] Y. J. Park et al. “Effect of structures and morphologies of catalyst on growth of carbon nanotubes synthesised by CVD”. In: *AIP Conference Proceedings* 633 (2002), pp. 198–201.

[94] C. M. Tilmaciu et al. “Synthesis of superparamagnetic iron(III) oxide nanowires in double-walled carbon nanotubes”. In: *Chemical Communications* 43 (2009), pp. 6664–6.

[95] S. Liu et al. “Preparation and characteristics of carbon nanotubes filled with cobalt”. In: *Chemistry of Materials* 12 (2000), pp. 2205–2211.

[96] Z. J. Liu et al. “Preparation of Fe-filled carbon nanotubes by catalytic decomposition of cyclohexane”. In: *Synthetic Metals* 128 (2002), pp. 191–195.

[97] S. Liu et al. “Preparation and characteristics of carbon nanotubes filled with cobalt”. In: *Chemistry of Materials* 12 (2000), pp. 2205–2211.

[98] E. W. Lee. *Magnetism and introductory survey*. 1st. New York: Dover Publications Incorporated, 1963.

[99] A. Morelos-Gomez et al. “Controlling high coercivities of ferromagnetic nanowires encapsulated in carbon nanotubes”. In: *Journal of Materials Chemistry* 20 (2010), p. 5906.

[100] J. B. Wang et al. “Magnetic texture in iron nanowire arrays”. In: *Nanotechnology* 15 (2004), pp. 485–489.

[101] R. Klingeler, S. Hampel, and B. Buchner. “Carbon nanotube based biomedical agents for heating, temperature sensoring and drug delivery”. In: *Int J Hyperthermia* 24.6 (2008), pp. 496–505.

[102] F. Wolny et al. “Iron-filled carbon nanotubes as probes for magnetic force microscopy”. In: *Journal of Applied Physics* 104 (2008), pp. 064908–064913.

[103] A. Winkler et al. “Magnetic force microscopy sensors using iron-filled carbon nanotubes”. In: *Journal of Applied Physics* 99 (2006), pp. 104905–104910.

[104] F. Wolny et al. “Magnetic force microscopy measurements in external magnetic fields- comparison between coated probes and an iron filled carbon nanotube probe”. In: *Journal of Applied Physics* 108 (2010), pp. 013908–013912.

[105] F. Wolny et al. “Stable magnetization of iron filled carbon nanotube MFM probes in external magnetic fields”. In: *Journal of Physics: Conference Series* 200 (2010), pp. 112011–112015.

[106] A. G. Osorio et al. “Controlling the magnetic response of carbon nanotubes filled with iron-containing material”. In: *Materials Research Bulletin* 48 (2013), pp. 4168–4173.

[107] P/ K. Tyagi et al. “Preparation of Ni-filled carbon nanotubes for key potential applications in nanotechnology”. In: *Thin Solid Films* 469-470 (2004), pp. 127–130.

[108] C. Muller et al. “Iron filled carbon nanotubes grown on substrates with thin metal layers and their magnetic properties”. In: *Carbon* 44 (2006), pp. 1746–1753.

[109] C. Müller et al. “Incremental analysis of the magnetization behavior in iron-filled carbon nanotube arrays”. In: *Journal of Applied Physics* 103 (2008), pp. 034302–034307.

[110] Y. Lei et al. “Production of empty and iron-filled multi walled carbon nanotubes from iron-phthalocyanine polymer and their electromagnetic properties”. In: *Journal of Materials Science: Materials in Electronics* 23 (2012), pp. 921–927.

[111] F. Geng and H. Cong. “Fe-filled carbon nanotube array with high coercivity”. In: *Physica B* 382 (2006), pp. 300–304.

[112] I. Monch et al. “Ferromagnetic filled carbon nanotubes and nanoparticles: synthesis and lipid-mediated delivery into human tumor cells”. In: *Journal of Magnetism and Magnetic Materials* 290 (2005), pp. 276–278.

[113] A. Shpak et al. “Structure and magnetic properties of iron nanowires encased in multiwalled carbon nanotubes”. In: *Acta Materialia* 55 (2007), pp. 1769–1778.

[114] X. Gui et al. “Improving the filling rate and enhanced magnetic properties of carbon nanotubes by annealing and magnetic separation”. In: *Materials Research Bulletin* 43 (2008), pp. 3441–3446.

[115] A. Leonhardt et al. “Enhanced magnetism in Fe-filled carbon nanotubes produced by pyrolysis of ferrocene”. In: *Journal of Applied Physics* 98 (2005), pp. 074315–074320.

[116] Y. Feng et al. “Removal of some impurities from carbon nanotubes”. In: *Chemical Physics Letters* 375 (2003), pp. 645–648.

[117] P. X. Hou, C. Liu, and H. M. Cheng. “Purification of carbon nanotubes”. In: *Carbon* 46 (2008), pp. 2003–2025.

[118] K. Hernadi et al. “Reactivity of different kinds of carbon during oxidative purification of catalytically prepared carbon nanotubes”. In: *Solid State Ionics* 141 (2001), pp. 203–209.

[119] J. Zhang et al. “Effect of chemical oxidation on the structure of single-walled carbon nanotubes”. In: *Journal of Physical Chemistry B* 107 (2003), pp. 3712–3718.

[120] T. W. Ebbesen et al. “Purification of nanotubes”. In: *Nature* 367 (1994), pp. 522–525.

[121] Y. C. Park Y. S. ad Choi et al. “High yield purification of multiwalled carbon nanotubes by selective oxidation during thermal annealing”. In: *Carbon* 39 (2001), pp. 655–661.

[122] J. Liu. “Fullerene Pipes”. In: *Science* 280.5367 (1998), pp. 1253–1256.

[123] F. H. Ko, C. Y. Lee, and T. C. Ko C. J. abd Ch. “Purifications of multi-walled carbon nanotubes through microwave heating of nitric acid in a closed vessel”. In: *Carbon* 43 (2005), pp. 727–733.

[124] Y. Li et al. “Purification of CVD synthesized single-wall carbon nanotubes by different acid oxidation treatments”. In: *Nanotechnology* 15 (2004), pp. 1645–1649.

[125] S. W. Cranford and M. J. Buehler. “In silico assembly and nanomechanical characterization of carbon nanotube buckypaper”. In: *Nanotechnology* 21.26 (2010), p. 265706.

[126] L. Hussein, G. Urban, and M. Kruger. “Fabrication and characterization of buckypaper-based nanostructured electrodes as a novel material for biofuel cell applications”. In: *Phys Chem Chem Phys* 13.13 (2011), pp. 5831–9.

[127] Y. A Kim et al. “Fabrication of High-Purity, Double-Walled Carbon Nanotube Buckypaper”. In: *Chemical Vapor Deposition* 12.6 (2006), pp. 327–330.

[128] K. Yang et al. “Tuning electrical and thermal connectivity in multiwalled carbon nanotube buckypaper”. In: *J Phys Condens Matter* 22.33 (2010), p. 334215.

[129] H. W. Zhu et al. “Direct synthesis of long single-walled carbon nanotube strands”. In: *Science* 296 (2002), pp. 884–886.

[130] Y. L. Li, I. A. Kinloch, and A. H. Windle. “Direct spinning of carbon nanotube fibres from chemical vapor deposition synthesis”. In: *Science* 304 (2004), pp. 276–278.

[131] K. Jiang, Q. Li, and S. Fan. “Spinning continuous carbon nanotube yarns”. In: *Nature* 419 (2002), p. 801.

[132] M. Zhang, K. R. Atkinson, and R. H. Baughman. “Multifunctional carbon nanotube yarns by downsizing an ancient technology”. In: *Science* 306 (2004), pp. 1358–1361.

[133] X. Zhang et al. “Strong carbon-nanotube fibers spun from long carbon-nanotube arrays”. In: *Small* 3 (2007), pp. 244–248.

[134] G. Gruner. “Carbon nanotube films for transparent and plastic electronics”. In: *Journal of Materials Chemistry* 16 (2006), pp. 3533–3539.

[135] Z. Wu et al. “Transparent conductive carbon nanotube films”. In: *Science* 305 (2004), pp. 1273–1276.

[136] F. Hennrich et al. “Reversible modification of the adsorption properties of single-walled carbon nanotube thin films via nitric acid exposure”. In: *Physical Chemistry Chemical Physics* 5 (2003), pp. 178–183.

[137] Q. Cao and J. A. Rogers. “Ultrathin films of single-walled carbon nanotubes for electronics and sensors: A review of fundamental and applied aspects”. In: *Advanced Materials* 21 (2009), pp. 29–53.

[138] J. Hilding et al. “Dispersion of carbon nanotubes in liquids”. In: *Journal of Dispersion Science and Technology* 24 (2003), pp. 1–41.

[139] H. Muramatsu et al. “Pore structure and oxidation stability of double-walled carbon nanotube-derived bucky paper”. In: *Chemical Physics Letters* 414.4-6 (2005), pp. 444–448.

[140] H. Huang et al. “Purification and alignment of arc-synthesis single-walled carbon nanotube bundles”. In: *Chemical Physics Letters* 356 (2002), pp. 567–572.

[141] J. M. Moon et al. “High-yield purification process of singlewalled carbon nanotubes”. In: *Journal of Physical Chemistry B* 105 (2001), pp. 5677–5681.

[142] M. F. Islam et al. “High weight fraction surfactant solubilization of single-wall carbon nanotubes in water”. In: *Nano Letters* 3 (2003), pp. 269–273.

[143] R. Bandyopadhyaya et al. “Stabilisation of individual carbon nanotubes in aqueous solution”. In: *Nanoletters* 2 (2002), pp. 25–28.

[144] E. J. Wallace and M. S. P. Sansom. “Carbon nanotube self-assembly with lipids and detergent: a molecular dynamics study”. In: *Nanotechnology* 20 (2009), pp. 045101–0454107.

[145] L. Liu, W. Ma, and Z. Zhang. “Macroscopic carbon nanotube assemblies: preparation, properties, and potential applications”. In: *Small* 7.11 (2011), pp. 1504–20.

[146] Ding Wang et al. “Highly oriented carbon nanotube papers made of aligned carbon nanotubes”. In: *Nanotechnology* 19.7 (2008).

[147] Raymond L. D. Whitby et al. “Geometric control and tuneable pore size distribution of buckypaper and buckydiscs”. In: *Carbon* 46.6 (2008), pp. 949–956.

[148] L. Song et al. “Direct Synthesis of a Macroscale Single-Walled Carbon Nanotube Non-Woven Material”. In: *Advanced Materials* 16.17 (2004), pp. 1529–1534.

[149] Olivier Reynaud et al. “Aerosol feeding of catalyst precursor for carbon nanotube synthesis and highly conductive and transparent film fabrication”. In: *Chemical Engineering Journal* 255 (2014), pp. 134–140.

[150] W. Xu et al. “High-strength carbon nanotube film from improving alignment and densification”. In: *Nanoletters* 16 (2016), pp. 946–952.

[151] P. Gonnet et al. “Thermal conductivity of magnetically aligned carbon nanotube buckypapers and nanocomposites”. In: *Current Applied Physics* 6 (2006), pp. 119–122.

[152] Qunfeng Cheng et al. “High Mechanical Performance Composite Conductor: Multi-Walled Carbon Nanotube Sheet/Bismaleimide Nanocomposites”. In: *Advanced Functional Materials* 19.20 (2009), pp. 3219–3225.

[153] I. W. Chen et al. “Highly conductive carbon nanotube buckypapers with improved doping stability via conjugational cross-linking”. In: *Nanotechnology* 22.48 (2011), p. 485708.

[154] L. Zhang, G. Zhang, and S. Fan. “High-density carbon nanotube buckypapers with superior transport and mechanical properties”. In: *Nanoletters* 12 (2012), pp. 4848–4852.

[155] S. Hofmann et al. “In situ observations of catalyst dynamics during surface-bound carbon nanotube nucleation”. In: *Nanoletters* 7 (2007), pp. 602–608.

[156] S. Hofmann et al. “State of transition metal catalysts during carbon nanotube growth”. In: *Journal of Physical Chemistry C* 113 (2009), pp. 1648–1656.

[157] X. Feng et al. “In situ TEM observation of gasification and growth of carbon nanotubes using iron catalysts”. In: *Nano Research* 4 (2011), pp. 767–779.

[158] C. Mattevi et al. “In situ X-ray photoelectron spectroscopy study of catalyst-support interactions and growth of carbon nanotube forests”. In: *Journal of Physical Chemistry C* 112 (2008), pp. 12207–12213.

[159] K. Kaminska et al. “Real-time in situ Raman imaging of carbon nanotube growth”. In: *Nanotechnology* 18 (2007), pp. 165707–165713.

[160] K. Reinhold-Lopez et al. “In situ Raman monitoring of the formation and growth of carbon nanotubes via chemical vapor deposition”. In: *Procedia Engineering* 102 (2015), pp. 190–200.

[161] S. Chiashi et al. “Cold wall CVD generation of single-walled carbon nanotubes and in situ Raman scattering measurements of the growth stage”. In: *Chemical Physics Letters* 386 (2004), pp. 89–94.

[162] D. H. Kim et al. “In situ monitoring of carbon nanotube growth”. In: *Carbon* 41 (2003), pp. 579–625.

[163] S. Maruyama et al. “Growth process of vertically aligned single-walled carbon nanotubes”. In: *Chemical Physics Letters* 403 (2005), pp. 320–323.

[164] A. A. Puretzky et al. “In situ measurements and modeling of carbon nanotube array growth kinetics during chemical vapor deposition”. In: *Applied Physics A* 81 (2005), pp. 223–240.

[165] Y. Tian et al. “Thermal analysis-mass spectroscopy coupling as a powerful technique to study the growth of carbon nanotubes from benzene”. In: *Chemical Physics Letters* 388 (2004), pp. 259–262.

[166] S. S. Meysami, L. C. Snoek, and N. Grobert. “Versatile in Situ Gas Analysis Apparatus for Nanomaterials Reactors”. In: *Analytical Chemistry* 86.17 (2014), pp. 8850–8856.

[167] K. Kuwana et al. “Catalyst deactivation in CVD synthesis of carbon nanotubes”. In: *Carbon* 43 (2005), pp. 253–260.

[168] S. M. Kim et al. “SWCNT growth on Al/Fe/Mo investigated by in situ mass spectroscopy”. In: *Nanotechnology* 18 (2007), p. 185709.

[169] E. R. Meshot et al. “Engineering vertically aligned carbon nanotube growth by decoupled thermal treatment of precursor and catalyst”. In: *ACS Nano* 3 (2009), pp. 2477–2486.

[170] D. L. Plata et al. “Early evaluation of potential environmental impacts of carbon nanotube synthesis by chemical vapor deposition”. In: *Environmental Science and Technology* 43 (2009), pp. 8367–8373.

[171] Y. Tian et al. “In situ TA-MS study of the six-membered-ring-based growth of carbon nanotubes with benzene precursor”. In: *Journal of the American Chemical Society* 126 (2004), pp. 1180–1183.

[172] L. M. Dyagileva et al. “Reactivity of the first transition row metallocenes in thermal decomposition reaction”. In: *Journal of organometallic chemistry* 175 (1979), pp. 63–72.

[173] K. E. Lewis and Smith G. P. “Bond dissociation energies in ferrocene”. In: *Journal of the American Chemistry Society* 106 (1984), pp. 4650–4651.

[174] Q. Liu et al. “Synthesis of different magnetic carbon nanostructures by the pyrolysis of ferrocene at different sublimation temperatures”. In: *Carbon* 46 (2008), pp. 1892–1902.

[175] J. Sengupta and C. Jacob. “Growth temperature dependence of partially Fe filled MWCNT using chemical vapor deposition”. In: *Journal of Crystal Growth* 311 (2009), pp. 4692–4697.

[176] C. M. Seah, S. P. Chai, and A. R. Mohamed. “Synthesis of aligned carbon nanotubes”. In: *Carbon* 49 (2011), pp. 4613–4635.

[177] F. S. Boi et al. “Controlling the quantity of alpha-Fe inside multiwall carbon nanotubes filled with Fe-based crystals: The key role of vapour flow-rate”. In: *Applied Physics Letters* 105 (2014), pp. 243108–243113.

[178] M. R. Djokic et al. “An experimental and kinetic modeling study of cyclopentadiene pyrolysis: First growth of polycyclic aromatic hydrocarbons”. In: *Combustion and Flame* 161 (2014), pp. 2739–2751.

[179] National Institute of Standards and Technology. *Ferrocene*. 2017. URL: `http://webbook.nist.gov/cgi/cbook.cgi?ID=C102545&Mask=200` (visited on 10/03/2017).

[180] National Institute of Standards and Technology. *Naphthalene*. 2017. URL: `http://webbook.nist.gov/cgi/inchi/InChI%3D1S/C10H8/c1-2-6-10-8-4-3-7-9(10)5-1/h1-8H` (visited on 10/03/2017).

[181] T. Dudev and C. Lim. “Ring strain energies from ab initio calculations”. In: *Journal of the American Chemistry Society* 120 (1998), pp. 4450–4458.

[182] B. Shukla et al. “An efficient carbon precursor for gas phase growth of SWCNTs”. In: *Chemical Communications* (2009), pp. 3422–3424.

[183] Y. Zhang et al. “A new understanding of carbon nanotube growth: Different functions of carbon species”. In: *Applied Surface Science* 332 (2015), pp. 756–760.

[184] Y. Xue et al. “Synthesis of large-area, few-layer graphene on iron foil by chemical vapor deposition”. In: *Nano Research* 4 (2011), pp. 1208–1214.

[185] T. Niu et al. “Growth intermediates for CVD graphene on Cu(111): carbon clusters and defective graphene”. In: *Journal of the American Chemistry Society* 135 (2013), pp. 8409–8914.

[186] K. Kuwana et al. “Catalyst deactivation in CVD synthesis of carbon nanotubes”. In: *Carbon* 43 (2005), pp. 253–260.

[187] E. R. Meshot et al. “Engineering vertically aligned carbon nanotube growth by decoupled thermal treatment of precursor and catalyst”. In: *ACS Nano* 3 (2009), pp. 2477–2486.

[188] O. A. Louchev et al. “Diffusion-controlled kinetics of carbon nanotube forest growth by chemical vapor deposition”. In: *The Journal of Chemical Physics* 118 (2003), pp. 7622–7634.

[189] M. Baxendale and T. Peci. “Length and alpha-Fe content control of self-organised ferromagnetic nanowires encapsulated by multiwalled carbon nanotubes by low flow-rate CVD”. In: *Carbon* 98 (2016), pp. 519–525.

[190] W. Xiaomin et al. “HRTEM and Raman study of onion-like fullerenes encapsulated Fe”. In: *Journal of Physics and Chemistry of Solids* 67 (2006), pp. 871–874.

[191] B. S. Xu et al. “Several features of the iron-included onion-like fullerenes”. In: *Materials Letters* 60 (2006), pp. 2042–2050.

[192] S. Yamamuro et al. “Iron particles nesting in carbon cages grown by arc discharge”. In: *Chemical Physics Letters* 212 (1993), pp. 379–383.

[193] F. S. Boi et al. “Cm-size free-standing self-organized buckypaper of bicky-onions filled with ferromagnetic Fe_3C”. In: *RSC Advances* 7 (2017), pp. 845–850.

[194] T. Hihara et al. “Magnetic properties of iron in nanocapsules”. In: *Japanese Journal of Applied Physics* 33 (1994), pp. 24–25.

[195] C. Muller et al. “Growth studies, TEM and XRD investigations of iron-filled carbon nanotubes”. In: *Physica Status Solidi a* 203 (2006), pp. 1064–1068.

[196] T. Ruskov et al. “Mossbauer morphological analysis of Fe-filled multiwalled carbon nanotube samples”. In: *Journal of Applied Physics* 100 (2006), pp. 084326–084334.

[197] C. Prados et al. “Hysteresis shift in Fe-filled carbon nanotubes due to γ-Fe”. In: *Physical Review B* 65 (2002), pp. 113405–113409.

[198] T. Ruskov et al. “Mossbauer morphological analysis of Fe-Filled multiwalled carbon nanotube samples”. In: *Journal of Applied Physics* 100 (2006), pp. 084326–084334.

[199] N. G. Chechenin et al. “Structure phases of Fe nanoparticles in vertically aligned multi-walled carbon nanotubes”. In: *Journal of Surface Investigation. X-ray, Synchrotron and Neutron Techniques* 9 (2015), pp. 1044–1055.

[200] G. S. B. Mckee and K. S. Vecchio. “Thermogravimetric analysis of synthesis variation effects on CVD generated multiwalled carbon nanotubes”. In: *Journal of Physical Chemistry B* 110 (2006), pp. 1179–1186.

[201] I. Ohnuma et al. “Phase equilibria in the Fe-Co binary system”. In: *Acta Materialisa* 50 (2002), pp. 379–393.

[202] T. Nishizawa and K. Ishida. *Binary alloy phase diagrams*. Ed. by T. B. Massalski. 2nd ed. Vol. 2. ASM International, 1990.

[203] R. S. Sundar and S.C. Deevi. “Soft magnetic FeCo alloys: alloy development, processing and properties”. In: *International Materials Reviews* 50 (2005), pp. 157–192.

[204] T. Sourmail. “Near equiatomic FeCo alloys: constitution, mechanical and magnetic properties”. In: *Progress in Materials Science* 50 (2005), pp. 816–880.

[205] R. Ferrando. *Structure and properties of nano alloys*. Vol. 10. Elsevier, 2016.

[206] R. Ferrando, J. Jellinek, and R. L. Johnston. “Nanoalloys: From theory to applications of alloy clusters and nanoparticles”. In: *Chemical Reviews* 108 (2008), pp. 845–910.

[207] P. S. Fodor, G. M. Tsoi, and L. E. Wenger. “Fabrication and characterization of $Co_{1-x}Fe_x$ alloy nanowires”. In: *Journal of Applied Physics* 91 (2002), pp. 8186–8188.

[208] K. I. Arai, H. W. Kang, and K. Ishiyama. “Magnetic properties of Co-Fe electrodeposited alumite films”. In: *IEEE Transactions of Magnetics* 27 (1991), pp. 4906–4908.

[209] J. Wang et al. “Filling carbon nanotubes with Ni–Fe alloys via methylbenzene-oriented constant current electrodeposition for hydrazine electrocatalysis”. In: *Applied Surface Science* 270 (2013), pp. 128–132.

[210] Z. Turgut et al. “Magnetic properties and ordering in C-coated Fe_xCo_{1-x} alloy nanocrystals”. In: *Journal of Applied Physics* 83 (1998), pp. 6468–6470.

[211] R. Lv et al. “Carbon nanotubes filled with ferromagnetic alloy nanowires: Lightweight and wide-band microwave absorber”. In: *Applied Physics Letters* 93 (2008), pp. 223105–223108.

[212] L. M. Parkes et al. “Cobalt nanoparticles as novel magnetic resonance contrast agent- relaxivities at 1.5 and 3 Tesla”. In: *Contrast Media and Molecular Imaging* 3 (2008), pp. 150–156.

[213] V. A. Bautin et al. “Microstructure and magnetic properties of bulk FeCo alloys fabricated from mechanically alloying and chemically synthesised powders”. In: *Journal of Superconductivity and Novel Magnetism* 30 (2017), pp. 1281–1286.

[214] W. S. Seo et al. “FeCo/graphitic-shell nanocrystal as advanced magnetic-resonance-imaging and near-infrared agents”. In: *Nature Materials* 5 (2006), pp. 971–976.

[215] D. I. Bardos. “Mean magnetic moments in bcc Fe-Co alloys”. In: *Journal of Applied Physics* 40 (1969), pp. 1371–1372.

[216] Z. Z. Bandic and R. H. Victora. “Advances in magnetic data storage technology”. In: *Proceedings of the Institute of Electrical and Electronics Engineers* 96 (2008), pp. 1749–1753.

[217] C. Wang et al. “Synthesis and application of iron-filled carbon nanotubes coated with FeCo alloy nanoparticles”. In: *Journal of Magnetism and Magnetic Materials* 321 (2009), pp. 1924–1927.

[218] Z. Aslam et al. “Current-induced restructuring and chemical modification of N-doped multi-walled carbon nanotubes”. In: *Advanced Functional Materials* 21 (2011).

[219] K. Gandha et al. “Synthesis and characterization of FeCO nanowires with high coercivity”. In: *Nanotechnology* 26 (2015), pp. 075601–075607.

[220] B. P. Ramesh et al. “Thermogravimetric analysis of cobalt-filled carbon nanotubes deposited by chemical vapour deposition”. In: *Thin Solid Films* 494 (2006), pp. 128–132.

[221] K. Gallagher et al. “Synthesis, structure and magnetic properties of Fe-Co alloy nanocrystals”. In: *IEEE Transactions on Magnetics* 32 (1996), pp. 4842–4844.

[222] Z. H. Wang et al. “Microstructure and magnetic property of FeCo nanoparticles prepared by chemical vapor condensation process”. In: *Journal of Alloys and Compounds* 351 (2003), pp. 319–323.

[223] S. Li et al. “Effects of solvent immersion and evaporation on the electrical conductance of pre-stressed carbon nanotube buckypapers”. In: *Nanotechnology* 22.36 (2011), p. 365706.

[224] Soumyendu Roy et al. “Formation of Carbon Nanotube Bucky Paper and Feasibility Study for Filtration at the Nano and Molecular Scale”. In: *The Journal of Physical Chemistry C* 116.35 (2012), pp. 19025–19031.

[225] Jihua Gou. “Single-walled nanotube bucky paper and nanocomposite”. In: *Polymer International* 55.11 (2006), pp. 1283–1288.

[226] M. W. Rowell, M. A. Topinka, and M. D. McGehee. “Organic solar cells with carbon nanotube network electrodes”. In: *Applied Physics Letters* 88 (2006), pp. 233506–233509.

[227] L. Hu, D. S. Hecht, and G. Gruber. “Percolation in transparent and conducting carbon nanotube networks”. In: *Nano Letters* 4 (2004), pp. 2513–2517.

[228] Guanghui Xu et al. “The feasibility of producing MWcarbon nanotube paper and strong MWcarbon nanotube film from VAcarbon nanotube array”. In: *Applied Physics A* 92.3 (2008), pp. 531–539.

[229] D. Li et al. “Processable aqueous dispersions of graphene nanosheets”. In: *Nature Nanotechnology* 3 (2007), pp. 101–105.

[230] H. Chen et al. “Mechanically strong, electrically conductive, and biocompatible graphene paper”. In: *Advanced Materials* 20 (2008), pp. 3557–3561.

[231] Jiuke Mu et al. “Origami-inspired active graphene-based paper for programmable instant self-folding walking devices”. In: *Science Advances* 1.10 (2015).

[232] Y. Wang, J. Wu, and F. Wei. “A treatment method to give separated multi-walled carbon nanotubes with high purity, high crystallisation and a large aspect ratio”. In: *Carbon* 41 (2003), pp. 2939–2948.

[233] L. Zhang et al. “High-density carbon nanotube buckypapers with superior transport and mechanical properties”. In: *Nano Lett* 12.9 (2012), pp. 4848–52.

[234] Qingfeng Liu et al. “In situ assembly of multi-sheeted buckybooks from single-walled carbon nanotubes”. In: *ACS nano* 3.3 (2009), pp. 707–713.

[235] Philip D. Bradford et al. “A novel approach to fabricate high volume fraction nanocomposites with long aligned carbon nanotubes”. In: *Composites Science and Technology* 70.13 (2010), pp. 1980–1985.

[236] R. Lv et al. “In situ synthesis and magnetic anisotropy of ferromagnetic buckypaper”. In: *Carbon* 47.4 (2009), pp. 1141–1145.

[237] Filippo S. Boi et al. “Fabrication of cm scale buckypapers of horizontally aligned multiwalled carbon nanotubes highly filled with Fe 3 C: the key roles of Cl and Ar-flow rates”. In: *Chemical Communications* 52.22 (2016), pp. 4195–4198.

[238] Jian Guo et al. “Enhanced saturation magnetization in buckypaper-films of thin walled carbon nanostructures filled with Fe 3 C, FeCo, FeNi, CoNi, Co and Ni crystals: the key role of Cl”. In: *Physical Chemistry Chemical Physics* 17.27 (2015), pp. 18159–18166.

[239] Q. Liu et al. “Highly aligned dense carbon nanotube sheets induced by multiple stretching and pressing”. In: *Nanoscale* 6 (2014), 4338–4344q.

[240] C. A. Grimes et al. “Effect of purification of the electrical conductivity and complex permittivity of MWNTs”. In: *Journal of Applied Physics* 90 (2001), pp. 4134–4137.

[241] H. Dai, E. W. Wong, and C. M Lieber. “Probing electrical transport in nano materials: conductivity of individual carbon nanotubes”. In: *Science* 272 (1996), pp. 523–526.

[242] T. W. Ebbesen et al. “Electrical conductivity of individual carbon nanotubes”. In: *Nature* 382 (1996), pp. 54–56.

[243] P. C. P. Watts et al. “Are bulk defective carbon nanotubes less electrically conducting?” In: *Nano Letters* 3 (2003), pp. 549–553.

[244] Z. P. Yao et al. “Carbon Nanotube intramolecular junctions”. In: *Nature* 402 (1999), p. 273.

[245] A. Juutilainen, M. Ahlskog, and A. Volodin. “Measurements of tunneling conduction to carbon nanotubes and its sensitivity to oxygen gas”. In: *Physical Review B* 86 (2012), pp. 045405–045413.

[246] K. Behler et al. “Effect of thermal treatment on the structure of multi-walled carbon nanotubes”. In: *Journal of Nanoparticle Research* 8 (2006), pp. 615–625.

[247] Z. Aslam et al. “Carbon Nanotubes: current-induced restructuring and chemical modification of N-doped multi-walled carbon nanotubes”. In: *Advanced Functional Materials* 21 (2011), pp. 3933–3937.

[248] K. Song et al. “Comprehensive design of carbon- encapsulated Fe3O4 nanocrystals and their lithium storage properties”. In: *Nanotechnology* 23 (2012), pp. 505401–505407.

[249] P. G. Collins. “Defects and disorder in carbon nanotubes”. In: *Oxford handbook of nanoscience and technology: Frontiers and advances*. Vol. 1. Oxford University Press, 2010.

[250] P. G. Collins et al. “Extreme oxygen sensitivity of electronic properties of carbon nanotubes”. In: *Sicence* 287 (2000), pp. 1801–1804.

[251] A. Lekawa-Raus et al. “Electrical properties of carbon nanotube based fibres and their future use in electrical wiring”. In: *Advanced Functional Materials* 24 (2014), pp. 3661–3682.

[252] V. Skakalova et al. “Electronic transport in carbon nanotubes: from individual nanotubes to thin and thick networks”. In: *Physical Review B* 74 (2006), pp. 085403–085413.

[253] B. T. Hang et al. “Fe_2O_3-filled carbon nanotubes as a negative electrode for an Fe-air battery”. In: *Journal of Power Sources* 178 (2008), pp. 393–401.

[254] C. Oncel and Y. Durum. “Carbon nanotube synthesis via the catalytic method: a review on the effect of reaction parameters”. In: *Fullerenes, Nanotubes and Carbon Nanostructures* 14 (2006), pp. 17–37.

[255] A. P. Pierrot, A. L. Woodhead, and J. S. Church. “Thermal annealing effects on multi-walled carbon nanotube yarns probed by Raman spectroscopy”. In: *Spectrochimica Acta Part A: Molecular and Biomolecular Spectroscopy* 117 (2014), pp. 598–603.

[256] R. Andrews et al. “Purification and structural annealing of multi walled carbon nanotubes at graphitisation temperatures”. In: *Carbon* 39 (2001), pp. 1681–1687.

[257] F. Wolny et al. “Iron filled carbon nanotubes as novel monopole-like sensors for quantitative magnetic force microscopy”. In: *Nanotechnology* 21 (2010), p. 435501.

[258] M. F Yu et al. “Strength and breaking mechanism of multiwalled carbon nanotubes under tensile load”. In: *Science* 287 (2000), pp. 637–640.

[259] M. F. Yu et al. “Three-dimensional manipulation of carbon nanotubes under a scanning electron microscope”. In: *Nanotechnology* 10 (1999), pp. 244–252.

[260] E. W. Wong, P. E. Sheehan, and C. M. Lieber. “Nanobeam mechanics: elasticity, strength and toughness of nanorods and nanotubes”. In: *Science* 277 (1997), pp. 1971–1975.

[261] P. Poncharal et al. “Electrostatic deflections and electromechanical resonances of carbon nanotubes”. In: *Science* 283 (1999), pp. 1513–1516.

[262] B. G. Demczyk et al. “Direct mechanical measurement of the tensile strength and elastic modulus of multiwalled carbon nanotubes”. In: *Materials Science and Engineering* A334 (2002), pp. 173–178.

[263] M.-F. Yu et al. “Tensile loading of ropes of single wall carbon nanotubes and their mechanical properties”. In: *Physical Review Letters* 84 (2000), pp. 5552–5555.

[264] J. P. Salvetat et al. “Elastic modulus of ordered and disordered multiwalled carbon nanotubes”. In: *Advanced Materials* 11 (1999), pp. 161–165.

[265] F. M. Blighe et al. “On the factors controlling the mechanical properties of nanotube films”. In: *Carbon* 46 (2008), pp. 41–47.

[266] Z. Li et al. “Freestanding bucky paper with high strength from multi-wall carbon nanotubes”. In: *Materials Chemistry and Physics* 135.2-3 (2012), pp. 921–927.

[267] J. P. Salvetat et al. “Elastic and shear moduli of single-walled carbon nanotube ropes”. In: *Physical Review Letters* 82 (1999), pp. 944–947.

[268] J. Che, P. Chen, and M. B. Chan-Park. “High-strength carbon nanotube buckypaper composites as applied to free-standing electrodes for supercapacitors”. In: *Journal of Materials Chemistry A* 1 (2013), pp. 4057–4066.

[269] X. Zhang et al. “Properties and structure of nitric acid oxidised single wall carbon nanotube films”. In: *Journal of Physical Chemistry B* 108 (2004), pp. 16435–16440.

[270] Q. Liu et al. “Improvement on the tensile performance of buckypaper using a novel dispersant and functionalized carbon nanotubes”. In: *Composites: Part A* 55 (2013), pp. 102–109.

[271] S. W. Cranford and M. J. Buehler. “In silico assembly and nanomechanical characterisation of carbon nanotube buckypaper”. In: *Nanotechnology* 21 (2010), pp. 265706–265718.

[272] J. Di et al. “Ultrastrong, foldable, and highly conductive carbon nanotube film”. In: *ACS Nano* 6 (2012), pp. 5457–5464.

[273] T. V. Sreekumar et al. “Single-wall carbon nanotube films”. In: *Chemistry of Materials* 15 (2003), pp. 175–158.

[274] L. Berhan et al. “Mechanical properties of nanotube sheets: alterations in joint morphology and achievable moduli in manufacturable materials”. In: *Journal of Applied Physics* 95 (2004), pp. 4335–4345.

[275] U. Dettlaff-Weglikowska et al. “Effect of $SOCl_2$ treatment on electrical and mechanical properties of single-wall carbon nanotube networks”. In: *Journal of the American Chemistry Society* 127 (2005), pp. 5125–5131.

[276] R. H. Baughman et al. “Carbon nanotube actuators”. In: *Science* 284 (1999), pp. 1340–1344.

[277] J. Zhang et al. “Enhanced mechanical and electrical properties of carbon nanotube buckypaper by in situ cross-linking”. In: *Carbon* 63 (2013), pp. 125–132.

[278] S. Trasobares et al. “Compartmentalized CNx nanotubes: chemistry, morphology and growth”. In: *American Institute of Physics* 116 (2002), pp. 8966–8972.

[279] M. Terrones et al. “N-doping and coalescence of carbon nanotubes: synthesis and electronic properties”. In: *Applied Physics A* 74 (2002), pp. 355–361.

[280] A. A. Koos et al. “Comparison of structural changes in nitrogen and boron-doped multi-walled carbon nanotubes”. In: *Carbon* 48 (2010), pp. 3033–3041.

[281] A. A. Koos et al. “Effect of the experimental parameters on the structure of nitrogen-doped carbon nanotubes produced by aerosol chemical vapour deposition”. In: *Carbon* 47 (2009), pp. 30–37.

[282] I. O. Maciel et al. “Synthesis, electronic structure, and Raman scattering of phosphorus-doped single-wall carbon nanotubes”. In: *Nano Letters* 9 (2009), pp. 2267–2272.

[283] A. A. Koos et al. “Tailoring gas sensing properties of multi-walled carbon nanotubes by in situ modification with Si, P, and N”. In: *Carbon* 50.8 (2012), pp. 2816–2823.

[284] B. G. Sumpter et al. “Nitrogen-mediated carbon nanotube growth: Diameter reduction, metallicity, bundle dispersability,and bamboo-like structure formation”. In: *ACS Nano* 1 (2007), pp. 369–375.

[285] Antal A. Koos et al. “N-SWCNTs production by aerosol-assisted CVD method”. In: *Chemical Physics Letters* 538 (2012), pp. 108–111.

[286] M. Saito and A. Yabe. “Dispersion and polar force components of surface tension of some polymer films”. In: *Textile Research Journal* (1983), pp. 54–59.

[287] D. Murakami, H. Jinnai, and A. Takahara. “Wetting transition from Cassie-Baxter state to Wenzel state on texture polymer surfaces”. In: *Langmuir* 30 (2014), pp. 2061–2067.

[288] A. B. D Cassie and S Baxter. “Wettability of porous surfaces”. In: *Transactions of the Faraday Society* 40 (1944), pp. 546–551.

[289] D. Quere. “Wetting and Roughness”. In: *Annual Review in Materials Research* 38 (2008), pp. 71–99.

[290] X. Gui et al. “Carbon nanotube sponges”. In: *Advanced Materials* 22 (2010), pp. 617–621.

[291] K. Zhu et al. “Oil spill cleanup from sea water by carbon nanotube sponges”. In: *Frontiers of Materials Science* 7 (2013), pp. 170–176.

[292] X. Gui et al. “Recyclable carbon nanotube sponges for oil absorption”. In: *Acta Materialia* 59 (2011), pp. 4709–4804.

[293] A. Misra et al. “FTIR studies of nitrogen doped carbon nanotubes”. In: *Diamond and Related Materials* 15.2-3 (2006), pp. 385–388.

[294] L. G. Bulusheva et al. “Electrochemical properties of nitrogen-doped carbon nanotube anode in Li-ion batteries”. In: *Carbon* 49.12 (2011), pp. 4013–4023.

[295] T. Sharifi et al. “Nitrogen doped multi walled carbon nanotubes produced by CVD-correlating XPS and Raman spectroscopy for the study of nitrogen inclusion”. In: *Carbon* 50.10 (2012), pp. 3535–3541.

[296] T. Susi, T. Pichler, and P. Ayala. “X-ray photoelectron spectroscopy of graphitic carbon nanomaterials doped with heteroatoms”. In: *Beilstein Journal of Nanotechnology* 6 (2015), pp. 177–92.

[297] E. M. M. Ibrahim et al. “Synthesis, characterisation and electrical properties of nitrogen-doped single-walled carbon nanotubes with different nitrogen content”. In: *Diamond and Related Materials* 19 (2010), pp. 1199–1206.

[298] K. Fujisawa et al. “Enhanced electrical conductivities of N-doped carbon nanotubes by controlled heat treatment”. In: *Nanoscale* 3 (2011), pp. 4359–4364.

[299] J. R. Pels et al. “Evolution of nitrogen functionalities in carbonaceous materials during pyrolysis”. In: *Carbon* 33 (1995), pp. 1641–1653.

[300] T. I. T. Okpalugo et al. “High resolution XPS characterization of chemical functionalised MWCNTs and SWCNTs”. In: *Carbon* 43 (2005), pp. 153–161.

[301] I. Mazov et al. “Oxidation behaviour of multi wall carbon nanotubes with different diameters and morphology”. In: *Applied Surface Science* 258 (2012), pp. 6272–6280.

[302] G. W. Lee et al. “Structural characterisation of carboxylated multi-walled carbon nanotubes”. In: *Thin Solid Films* 516 (2008), pp. 5781–5784.

[303] C. Miko et al. “Effect of electron irradiation on the electrical properties of fibres of aligned single-walled carbon nanotubes”. In: *Applied Physics Letters* 83 (2003), pp. 4622–4624.

[304] S. Sakurai et al. “Influence of lengths of millimenter-scale single-walled carbon nanotube on electrical and mechanical properties of buckypaper”. In: *Nanoscale Research Letters* 8 (2013), pp. 546–553.

[305] J. Zhang et al. “Enhanced mechanical and electrical properties of carbon nanotube buckypaper by in situ cross-linking”. In: *Carbon* 63 (2013), pp. 125–132.

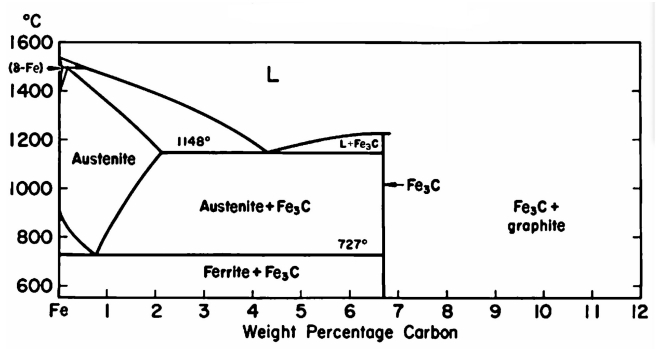
[306] T. Mizuki et al. “Activity of an enzyme immobilized on superparamagnetic particles in a rotational magnetic field”. In: *Biochemical and Biophysical Research Communications* 393 (2010), pp. 779–782.

[307] T. Mizuki et al. “Activity of lipase and chitinase immobilized on superparamagnetic particles in a rotational magnetic field”. In: *Plos One* 8 (2013), pp. 1–4.

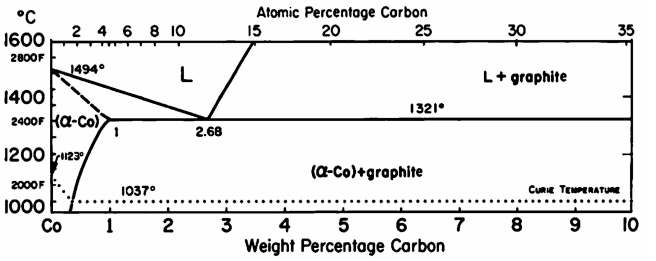
[308] L. Taylor. *Metallography, structures and phase diagrams*. 8th ed. American Society for Metals, 1973.

Chapter 7

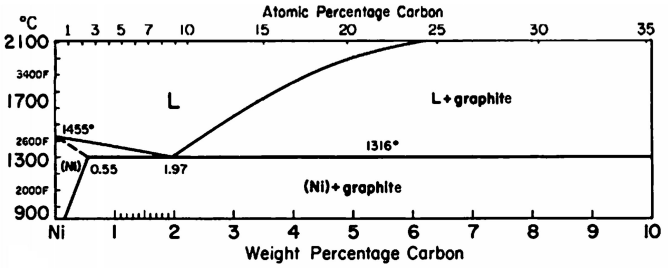
Appendix



(a) Fe

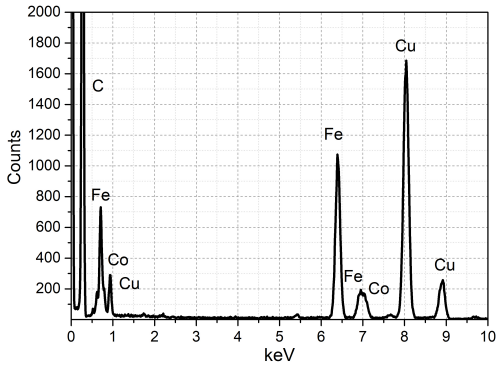


(b) Co

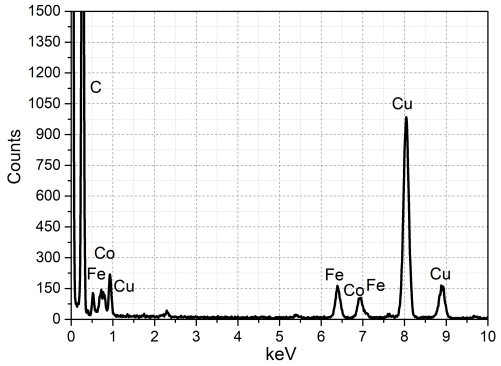


(c) Ni

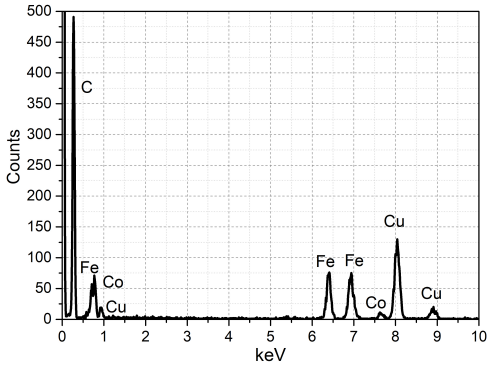
Figure 7.1: Phase diagrams for a) Fe, b) Co and c) Ni, showing the similar carbon solubilities of the three phase diagrams between 800-900 °C [44, 308].



(a) FeCo-AB

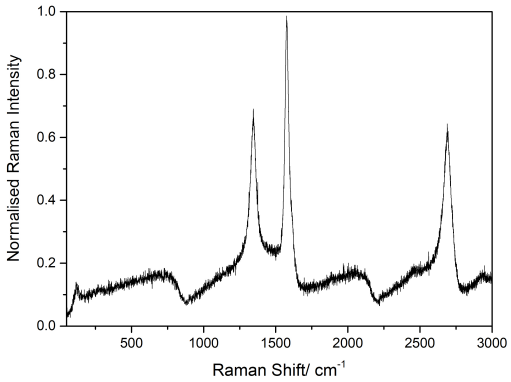


(b) FeCo-BB

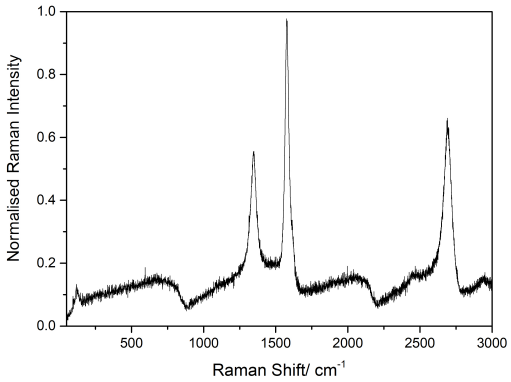


(c) FeCo-CB

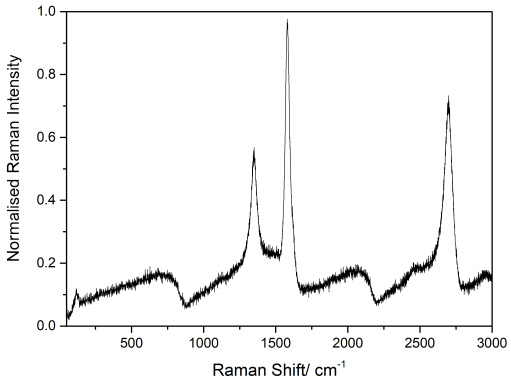
Figure 7.2: EDX spectra showing the key peaks detected from EDX of a) FeCo-AB, b) FeCo-BB, and c)FeCo-CB. Where A= 75:25, B= 50:50, and C= 25:75 ratios of ferrocene and cobaltocene used in the synthesis, and the second B= bulk sample.



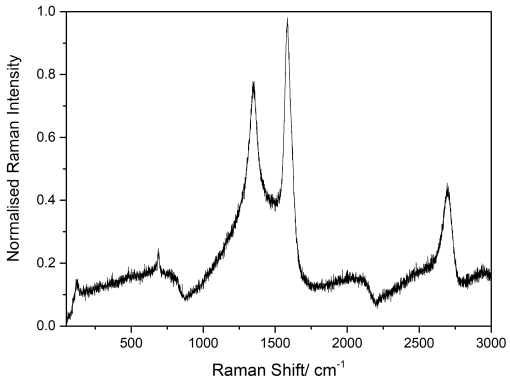
(a) FeCo-A1



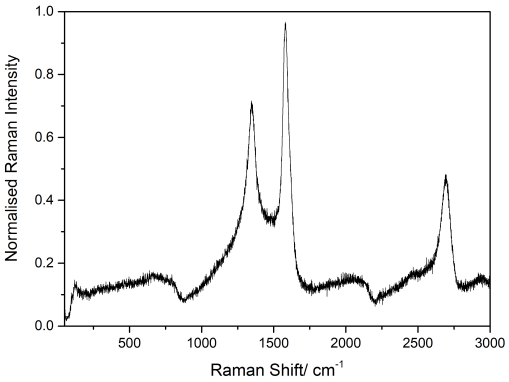
(b) FeCo-A2



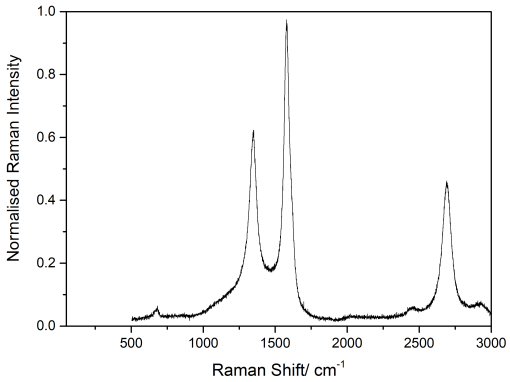
(c) FeCo-A3



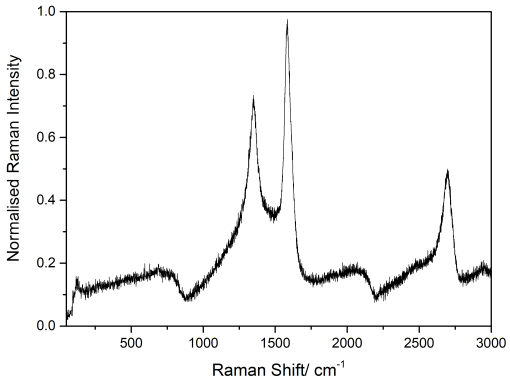
(d) FeCo-B1



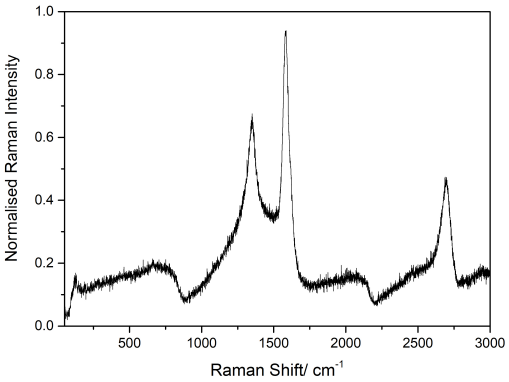
(e) FeCo-B2



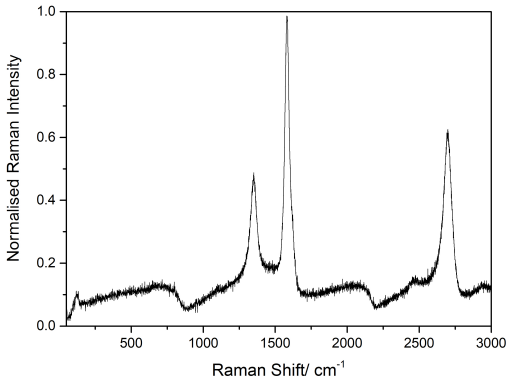
(f) FeCo-BB



(g) FeCo-C1



(h) FeCo-C2



(i) FeCo-C3

Figure 7.3: Raman spectra obtained for a)FeCo-A1, b) FeCo-A2, c) FeCo-A3, d) FeCo-B1, e) FeCo-B2, f) FeCo-BB, g) FeCo-C1, h) FeCo-C2, i) FeCo-C3, where A= 75:25, B= 50:50, and C= .25:75 ferrocene:cobaltocene ratio and 1, 2, and 3 represent the substrate position.

Chapter 4

Calculation to estimate the voltage required for BP reach 400 °C:

The joule heating current vs temperature graph is known to be a quadratic ($P= IR^2$). Assuming the most basic quadratic equation, the graph should behave following Equation 1. It is known that the graph will intercept the y axis at room temperature, which is estimated to be 300 K.

$y= ax^2 + 300$ (Equation 1)

The BP glowed red at a current of 2.27 A, and by using black body radiation, this corresponds to a temperature of *ca.* 1000 K. Inserting these values into Equation 1 gives an a value of 135.85. Plotting Equation 2 gives the quadratic curve given in Figure 7.4.

$y= 135.85x^2 + 300$ (Equation 2)

From Figure 7.4, a temperature of 400 °C (673.15 K) corresponds to a current of 1.65 A. Looking at the I/V data obtained for the BPs, the maximum currents obtained were 1.55 A, which is unlikely to translate to a local BP temperature of 400 °C.

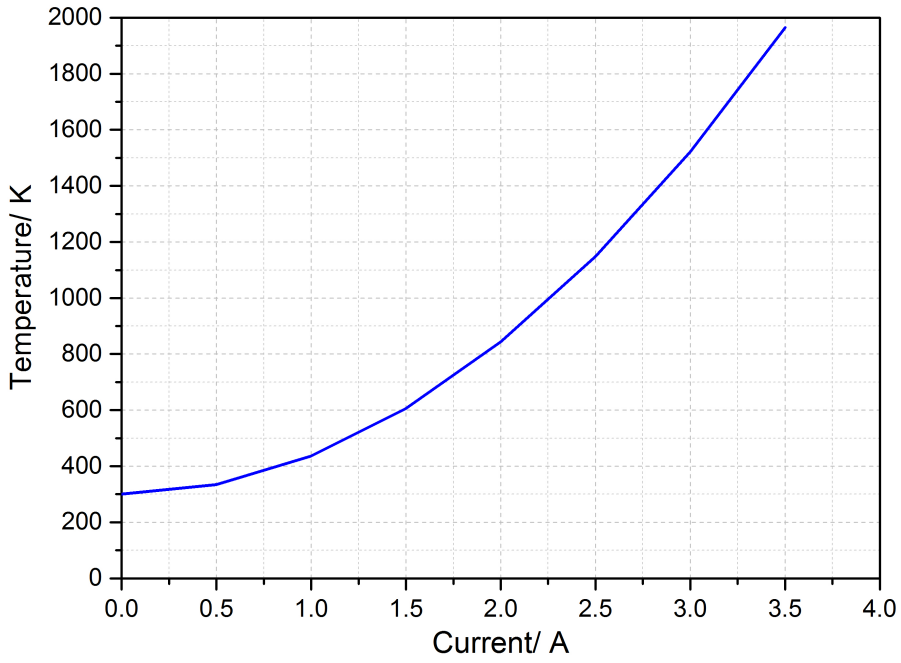


Figure 7.4: Graph showing an estimate of local BP temperature with increasing currents.

BP type	Sample No.	Face	Solvent	Average Contact Angle/ °
MWCNT	1	T	F	20
MWCNT	1	B	F	37
MWCNT	2	T	F	29
MWCNT	2	B	F	30
MWCNT	3	T	F	33
MWCNT	3	B	F	51
N-doped	4	T	F	22
N-doped	4	B	F	35
N-doped	5	T	F	38
N-doped	5	B	F	33
N-doped	6	T	F	22
N-doped	6	B	F	28

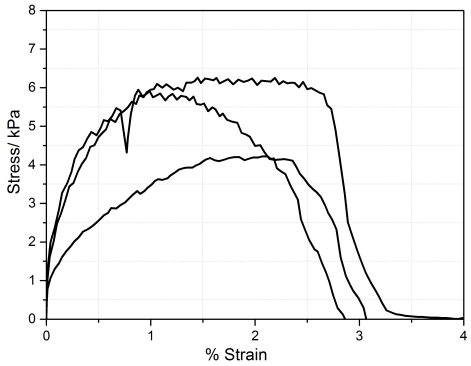
Table 7.1: Table showing the average contact angles recorded for three batches, each, of N-doped or conventional MWCNT BPs. For the 'Face' column, T and B represent top and bottom faces, representative. The solvents are denoted as EG, F and H for ethylene glycol, formamide and hexadecane, respectively. For samples marked with a *, the needle was switched to a 32 G needle, and a droplet of size 4.5 ml was deposited on the BP surface.

BP type	Sample No.	Face	Solvent	Average Contact Angle/ °
MWCNT	1	T	EG	39
MWCNT	1	B	EG	28
MWCNT	2	T	EG	33
MWCNT	2	B	EG	26
MWCNT	3	T	EG	49
MWCNT	3	B	EG	31
N-doped	4	T	EG	30
N-doped	4	B	EG	34
N-doped	5	T	EG	38
N-doped	5	B	EG	38
N-doped	6	T	EG	25
N-doped	6	B	EG	29

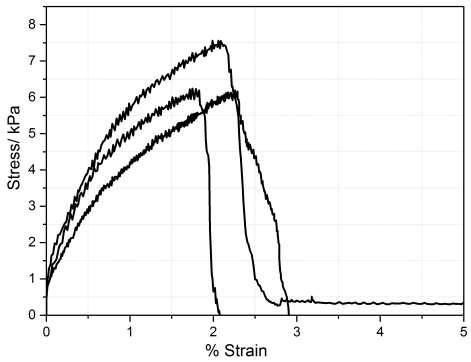
Table 7.2: Table showing the average contact angles recorded for three batches, each, of N-doped or conventional MWCNT BPs. For the 'Face' column, T and B represent top and bottom faces, representative. The solvents are denoted as EG, F and H for ethylene glycol, formamide and hexadecane, respectively. For samples marked with a *, the needle was switched to a 32 G needle, and a droplet of size 4.5 ml was deposited on the BP surface.

BP type	Sample No.	Face	Solvent	Average Contact Angle/ °
MWCNT	1	T	H	21
MWCNT	1	B	H	15
MWCNT	2	T	H	26
MWCNT	2	B	H	14
MWCNT	3	T	H	23
MWCNT	3	B	H	23
N-doped	4	T	H	24
N-doped	4	B	H	25
N-doped	5	T	H	25
N-doped	5	B	H	27
N-doped	6	T	H	27
N-doped	6	B	H	29

Table 7.3: Table showing the average contact angles recorded for three batches, each, of N-doped or conventional MWCNT BPs. For the 'Face' column, T and B represent top and bottom faces, representative. The solvents are denoted as EG, F and H for ethylene glycol, formamide and hexadecane, respectively. For samples marked with a *, the needle was switched to a 32 G needle, and a droplet of size 4.5 ml was deposited on the BP surface.

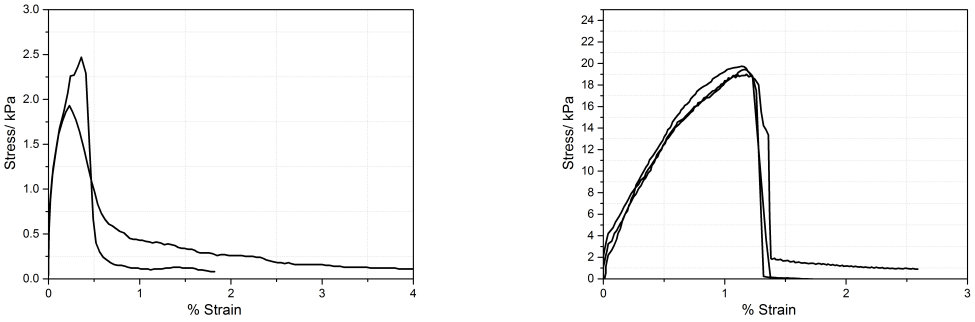


(a) Blue LCBP1



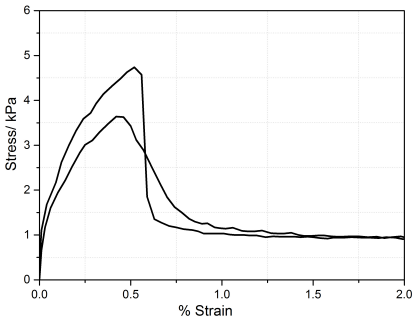
(b) Magenta LCBP2

Figure 7.5: Graphs showing the individual stress/strain curves obtained for multiple BP samples per BP batch for a) LCBP1, and b) LCBP2.

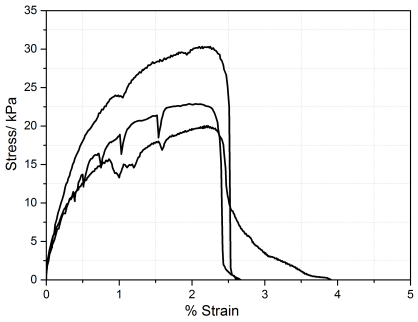


(a) Green SBBP1

(b) Black SNBP2



(c) Cyan SNBP3



(d) Red LNBP1

Figure 7.6: Graphs showing the individual stress/strain curves obtained for multiple BP samples per BP batch for a) SNBP1, b) SNBP2, c) SNBP3, and d) LNBP1.